High Enthalpy Flow Simulations for Earth and Mars Atmospheric Conditions

A thesis submitted
in fulfillment of the requirements
for the degree of

DOCTOR OF PHILOSOPHY

By

DIPANKAR DAS
ROLL NO: 136103032

Under the supervision of

Prof. VINAYAK N KULKARNI

DEPARTMENT OF MECHANICAL ENGINEERING
INDIAN INSTITUTE OF TECHNOLOGY, GUWAHATI

MARCH, 2021

Certificate

It is certified that the work contained in the thesis entitled, "**High Enthalpy Flow Simulations for Earth and Mars Atmospheric Conditions**", submitted by Dipankar Das, in the Department of Mechanical Engineering, Indian Institute of Technology Guwahati, India, for the award of degree of Doctor of Philosophy has been carried out under my supervision and that this work has not been submitted elsewhere for the award of any other degree or diploma.

Prof. Vinayak N. Kulkarni
Professor
Department of Mechanical Engineering
Indian Institute of Technology Guwahati
Guwahati-781 039, Assam
INDIA

Declaration

I declare that,

1. The work contained in this thesis is original and has been done by me under the guidance of my supervisor.
2. The work has not been submitted to any other institute for any degree or diploma.
3. I have followed the guidelines provided by the institute in preparing this thesis.
4. I have confirmed to the norms and guidelines given in the ethical code of conduct of the institute.
5. Whenever I used materials (data, theoretical analysis, figures and text) from other sources, I have given their detail in references.

Signature of student

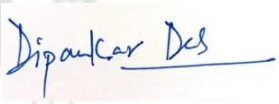

Dipankar Das
Department of Mechanical Engineering
Indian Institute of Technology, Guwahati
Guwahati-781 039, Assam
INDIA.

Acknowledgement

I express my deep sense of gratitude and indebtedness to my thesis supervisor and research guide Prof. Vinayak N. Kulkarni for his inspiring guidance and constant encouragement throughout the course of this research work. I am grateful to him for sparing his precious time and efforts throughout the entire work. I am highly obliged to him for all the insightful discussions, affection and kind suggestions, which helped me to complete the work successfully. I consider myself extremely fortunate to have him as my research guide, whose able guidance and valuable advice have helped me in every way throughout this work.

I am grateful of having an encouraging doctoral committee. I would like to thank my doctoral committee members, Prof. Subramani Kanagaraj, Prof. Anugrah Singh, Dr. Pranab K. Mondal and Dr. Ganesh Natarajan. My special thanks to Dr. Dipankar N. Basu for his valuable time and support during the absence of my guide. I am also grateful to other faculty members of the Department for their direct and indirect supports and guidance. I am also thankful to other technical and non-technical staff of Mechanical Engineering Department for their help.

A special thanks to my friend Dr. Siddesh Desai and Mr. Ashish Yadav for their help, support and companionship. I wish to record the help extended to me by my friends in all possible ways. I would like to thank Dr. Dipjyoti Baglari, Dr. Rohan Vernekar, Dr. Koushik Das, Mr. Partha P. Kemprai, Mr. Prashant Meshram and Mr. Alekh Hazarika for their constant encouragement and help.

Finally, I would like to mention my parents whose blessing and never ending supports are the real impetus that continuously motivate me to produce my best. Last but not the least, a special thanks to my wife Mousumi, for all the support she had offered during my PhD work.

Abstract

Supersonic/hypersonic flights often encounter issues like a high drag, shock and its interactions, and high-temperature effects. Thus, to design a high-speed aircraft, efficient prediction of these flow complexities is extremely important. Over the years, computational fluid dynamics has emerged as an efficient tool to simulate such flows. Given this, the present study is focused on the numerical investigation of these flow problems. Hence, a finite volume-based two-dimensional axisymmetric laminar flow solver, which accounts for reaction kinetics of Earth and Martian atmosphere is developed and validated with various numerical as well as experimental test cases. These include flow over a ramp, flow over a sphere and ramp-induced SWBLI. In addition to this real gas solver, a perfect gas solver is also employed for low enthalpy simulations.

After the successful development and validation of the in-house real gas solver, it is employed to analyze the energy deposition technique for drag mitigation in Earth and Mars atmospheric flow mediums. Here, the golden section search optimization algorithm is effectively integrated with the solver to evaluate the optimum energy deposition required to obtain the maximum power effectiveness. The study reveals the need for a comparatively more amount of energy deposition in the case of the Mars gas model to attain maximum power effectiveness. This observation is attributed to the fact that the specific heat variation for Mars atmospheric conditions is more sensitive to the temperature variation. Further, it is noted that for either flow model, the maximum power effectiveness decreases with an increase in the freestream enthalpy. This observation is found to be more prominent for the Earth atmospheric model. Thus, it is observed that the increase in the freestream enthalpy degrades the performance of the energy deposition-based drag reduction technique for both the flow mediums.

Further, the investigation is continued to analyze the real gas effects on the Mach reflection studies in Earth and Mars atmosphere. The low enthalpy simulations reveal the Mach reflection in both the flow mediums. Further, for either flow medium, it is noted that the increase in freestream enthalpy decreases the Mach stem height and as the enthalpy crosses a threshold value, the transition to the regular reflection occurs. This is because of noticeable real gas effects for the higher enthalpy simulations. To quantify the observation, the shock polar diagrams are also incorporated which reveals the mechanism for these transitions.

In further studies, the detailed physics associated with shock/shock interactions on various double wedge geometries and freestream enthalpies are explored. For this purpose, reacting as well as the perfect gas simulations are performed in Earth and Mars atmospheric mediums. Significant differences in the flow structures are noticed between the perfect and reacting gas outcomes. The reasons for these discrepancies are identified and discussed. Further, it is noted that for the same geometry, the interaction type changes with the variation in freestream enthalpies. Thus, it is observed the increase in enthalpy provided the same effects as that of reducing the second wedge angle.

In continuation, the real gas effects on shock/expansion wave interactions in different geometries are also investigated. The initial outcomes of perfect gas simulations are found to be in good agreement with the analytical inviscid results. The real gas simulation at different freestream enthalpies shows a drastic modification in the flow structures. It is noted that an increase in the freestream enthalpy has a decreasing effect on the post-shock Mach number and an increasing effect on the post-expansion wave Mach number. Further, the peak pressure ratio is noted to be on the lower side for higher enthalpy cases.

Later, ramp-induced shock wave boundary layer interaction (SWBLI) study in Earth and Mars atmosphere has been carried out. For this purpose, hypersonic laminar flow simulations are performed with the in-house real gas solver. The effects of variation in wall temperature, freestream enthalpy, Mach number on the intensity of SWBLI are explored. For both flow mediums, the separation size is found to be directly proportional to the wall temperature and inversely proportional to the Mach number and freestream enthalpy. Here, the percentage change in the separation size is always found to be more for the Mars gas model. Further, the difference in separation length for the same wall to total temperature ratio is found to be insignificant for either flow medium. The present investigation confirms that, for both planetary conditions, sufficiently large leading-edge bluntness can be a useful tool to mitigate the boundary layer separation. Further, the outcomes of the simulations are utilized to revise correlations to predict the upstream influence location and separation size for the Earth atmosphere and devise new correlations for the Mars atmosphere.

Contents

List of Figures

List of Tables

Abbreviations

CFD	-	Computational fluid dynamics
DSMC	-	Direct Simulation Monte Carlo
I-SWBLI	-	Impingement based shock wave boundary layer interactions
MR	-	Mach reflection
RR	-	Regular reflection
R-SWBLI	-	Ramp induced shock wave boundary layer interactions
SICD	-	Shock induced combustion device
SS	-	slip surface
SWBLI	-	Shock wave boundary layer interaction

Nomenclature

a	-	Constant (a = 1 for 2-D axisymmetric, a = 0 for 2-D problem)
C_i	-	Mass concentration of species i (kg/m^3)
C_{pi}	-	Specific heat of species i at constant pressure (J/kmolK)
C_w	-	Chapman-Rubesin parameter
D_{im}	-	Effective binary diffusivity of species i (5×10^{-5} m^2/s)
e	-	Internal energy (J/kg)
e_i	-	Internal energy of species i (J/mol)
E	-	Total energy (J/kg)
F_{lb}	-	Proportionality constant for length of separation relation
F_{ui}	-	Proportionality constant for upstream influence relation
F_I	-	Inviscid flux vector in x direction
F_v	-	Viscous flux vector in x direction
G_I	-	Inviscid flux vector in y direction
G_v	-	Viscous flux vector in y direction
H_{st}	-	Mach stem height (m)
$h^o_{f_i}$	-	Heat of formation of species i (J/mol)
L	-	Location of energy spot from stagnation point (mm)
L_b	-	Separation length
L_c	-	Length of the flat plate (m)
L_{ui}	-	Extent of upstream influence measured from ramp foot to the upstream influence location (m)
L_1	-	Length of the first wedge (m)
L_2	-	Length of the second wedge (m)
M	-	Mach number
M_∞	-	Freestream Mach number

M_o	-	Mach number at the edge of boundary-layer
MW_i	-	Molecular weight of species *i*
N	-	Number of species
p	-	Pressure (Pa)
P_{incp}	-	Incipient pressure (Pa)
P_∞	-	Freestream pressure (Pa)
Q_l	-	Lower limit of energy source strength (W)
Q_u	-	Upper limit of energy source strength (W)
Q_1, Q_2	-	Intermediate values of energy source strength (W)
Re_∞	-	Freestream per unit Reynolds number (m^{-1})
r	-	Radius of bluntness (mm)
R_u	-	Universal gas constant
S	-	Reaction source term
S_I	-	Invsicid source term
S_v	-	Viscous source term
T	-	Temperature (K)
T_e	-	Temperature at the boundary-layer edge (K)
T_w	-	Wall temperature (K)
T_o	-	Total temperature (K)
T_∞	-	Freestream temperature (K)
u	-	Component of velocity in x direction (m/s)
$\bar{u}_i$	-	Diffusion velocities in *x* direction (m/s)
$\bar{v}_i$	-	Diffusion velocities in y direction (m/s)
U	-	Solution or conservative vector
v	-	Component of velocity in x direction (m/s)
x_o	-	Upstream influence location measured from the leading edge (m)
X	-	X-coordinate (m)
Y	-	Y-coordinate (m)
$\propto$	-	Incident shock wave angle

β	-	Reflected shock wave angle
γ	-	specific heat ratio
ρ	-	Density (kg/m^3)
δ_o	-	Boundary-layer thickness at the upstream influence location (m)
Δy_{min}	-	Minimum Δy near wall (m)
Δx_{minle}	-	Minimum Δx at the leading edge (m)
Δx_{minju}	-	Minimum Δx at the flat plate- Ramp junction (m)
$\tau_{xx}, \tau_{yx}, \tau_{yy}, \tau_{\theta\theta}$	-	Shear stress components (N/m^2)
θ	-	Angle (degree)
θ_1	-	First wedge angle (degree)
θ_2	-	Second wedge angle (degree)
θ_{max}	-	maximum deflection angle (degree)
μ	-	Viscosity (Ns/m^2)
μ_1	-	Forward Mach angle
μ_2	-	Backward Mach angle

Dedicated to my Mother and Father

Chapter 1: Introduction

1.1 Introduction

Historically, the idea of flying like birds has always instigated researchers to build manned flights. At the very beginning, the design idea was to imitate birds by attaching a wing-like structure around the arms. After many unsuccessful attempts, the idea of "*ornithopters*" came into existence, where the flapping of wings is performed by some mechanical device. The initial design of such *ornithopters* can be found in the fifteenth-century articles of Leonardo da Vinci. Later on, the idea of lighter than air vehicles lead to the invention of hot air balloons and the first manned flight was achieved in the year 1783. The hot air balloons were followed by the invention of the glider. Nevertheless, the foundation of modern-day flights i.e. heavier-than-air flight was first conceptualized by Sir George Cayley in the latter part of the eighteenth century. He was the first person to introduce the idea of fixed-wing for lift and a separate propulsion system. Subsequently, Orville and Wilbur Wright achieved the first successful flight of powered aircraft on December 17, 1903. This accomplishment ensured the rapid development in the field of powered aircraft in the next decade and by the year 1913 societies in different parts of the globe started using these flying machines for the public as well as military purposes. Likewise, enhancements continued, and desire to fly faster-enabled mankind to achieve its first supersonic flight by 1947 and the first successful moon mission by 1969.

These advancements in aviation history opened up different challenges to the researchers as the design parameters to be considered while designing an aircraft are dissimilar in different flow regimes. These flow regimes are differentiated in terms of Mach number, i.e. if the Mach number is less than unity the flow is labeled as subsonic, and if it is greater than unity the flow is considered to be supersonic. However, one can always argue about the value of Mach number to be considered to differentiate between the supersonic and hypersonic flow regimes. Nevertheless, flow above Mach five is considered as hypersonic flow in general. Though in recent times mankind has progressed a lot in the field of high speed flights yet researchers are working hard to enhance the existing technologies and innovate new ones. In this line, present study is focused on some major challenges faced during high speed flights.

1.2 Hypersonic flows and real gas effects

In fluid dynamics, one of the usual practices is to assume the working fluid to be calorically perfect gas. This assumption holds well while the temperature is low. However, at higher temperatures such an assumption may lead to erroneous results as the *real gas effects* (also called *high-temperature effects*) such as temperature-dependent specific heat, dissociation reaction, ionization, etc. becomes prominent. Considerations of such real gas effects typically become important in the hypersonic regime due to high viscous dissipation and higher post-shock temperature. For example, in Earth atmosphere at 1atm pressure, usually, the deviation from calorically perfect gas assumptions starts at around 800K, the dissociation of O_2 starts at around 2000K; O_2 is almost completely dissociated as the flow field temperature reaches 4000K, at this temperature the dissociation of N_2 starts, which dissociates completely as the flow field temperature reaches 9000K, above which the ionization starts [**1**]. Further, the magnitude of change due to real gas effects depends upon the type of reacting flow. The reacting flows can be classified as frozen, equilibrium, and non-equilibrium flow. In Frozen flow, the reaction rates are so slow that, flow passes over the body way before the reaction can take place. In other words, the reaction time scale is too large compared to the flow time scale. In contrast, when the reaction time scale is too small compared to the flow time scale the flow is termed as equilibrium flow. Here, the reactions get activated and terminated in a very short time interval. In non-equilibrium flow, the reaction time scale and flow time scale are of the same order. Here, the chemical reactions initiated in the flow field remain incomplete while passing over the body.

1.3 Earth and Mars atmospheres

Earth atmosphere is a boon for mankind. In fact, all the life in mother Earth is mostly possible for its existence. The atmosphere provides us with invaluable oxygen, water, etc. and protects us from harmful ultraviolet rays, from extreme cold by retaining heat near the Earth surface, etc. The list is endless. However, the same atmosphere stands as a major hurdle in the development of high-speed aircraft as the different gases present in the atmosphere act as the source of fluid friction, thereby causing drag and heating loads. Further, for the possible life forms in the nearby planet and natural satellites, there has been a surge in the moon and Mars missions such as ‘Chandrayan’, ‘MOM’, Viking, ‘Mars Odyssey’, ‘Mars InSight lander’ etc. and a

significant number of expeditions are planned across the globe in near future. Hence, the researcher community has a huge challenge ahead to make these expeditions successful and more efficient. Having said this, it is of utmost importance to have a detailed understanding of the atmospheric conditions of these satellites and planets as the different flow complications associated with such flight missions are dependent on the medium of the flow. The present study is focused on the investigations in Earth and Mars atmospheric conditions. Earth atmosphere consists of mainly N_2 (≈78.09%) and O_2 (≈20.95%) and a smaller percentage of other gases such as argon, carbon dioxide, etc. and Mars atmosphere is mainly filled with CO_2 (≈96.85%), N_2 (≈2.7%) and small percentage of argon. Further, the higher speed associated with such interplanetary flights guarantees higher flow field temperature leading to dissociation of these molecules to various other forms (N, O, NO for Earth and CO, C, N, O_2, O, NO for Mars). This difference in compositions leads to different performance in Earth and Mars atmosphere. Therefore, it is of prime importance to rigorously test such Mars expedition aircraft in both the atmospheric conditions.

1.4 Major issues in hypersonic flows

In a hypersonic flow regime, certain flow phenomena like thin shock layer, viscous interactions, entropy layers, high-temperature flows, etc. become more important. Hence, any missile, rocket, or space vehicle exposed to hypersonic flow experiences many flow complications like shock wave boundary-layer interactions, high drag, shock/shock interactions, high-temperature flow, excessive heating, etc. Therefore, a thorough understanding and study of these complications are necessary for designing a safe and cost-effective hypersonic aircraft. Given this, investigations for following important aspects are planned in the present studies.

1.4.1 Higher drag force and associated remedies

One of the major challenges faced during a hypersonic flight is the aerodynamic heating. Installation of cooling system [**2**,**3**] and blunt nosed profile are the most commonly used solutions by the aerodynamicist to tackle this problem. But, a blunt nosed profile increases the wave drag which leads to more fuel consumption and thus results in higher flight cost. Therefore, there is a need to devise drag reduction techniques. Hence, many researchers carried out investigations in this field. Among those, implementation of multistep after body [**4**] and attaching a forward facing

spike at the stagnation point [**5**] are termed as passive drag reduction techniques. However, heat addition in front of the blunt body by surface coating of chromium [**6**], laser induced air-spike [**7**,**8**], counter-flow jet ejection from the stagnation point [**9**,**10**] and deposition of energy upstream of the spacecraft [**11**,**12**] are accounted as the active drag reduction techniques. Combination of both, active and passive means of drag reduction has also been explored in the literature [**13**]. Further, energy deposition based drag reduction is the focal point of present studies since it has potential to act as a prominent flow control technique at hypersonic speeds [**14**]. In this method, the energy can be deposited at an upstream location in the form of electromagnetic wave, laser, microwave, electric arc discharge, etc. The deposited the energy acts as a disturbance, which recasts the shock and as a result, the surface pressure gets reduced drastically. The schematic of such an energy deposition based drag reduction technique is shown in Fig. 1.1**.** Different aspects of this technique are reported in the open literature.

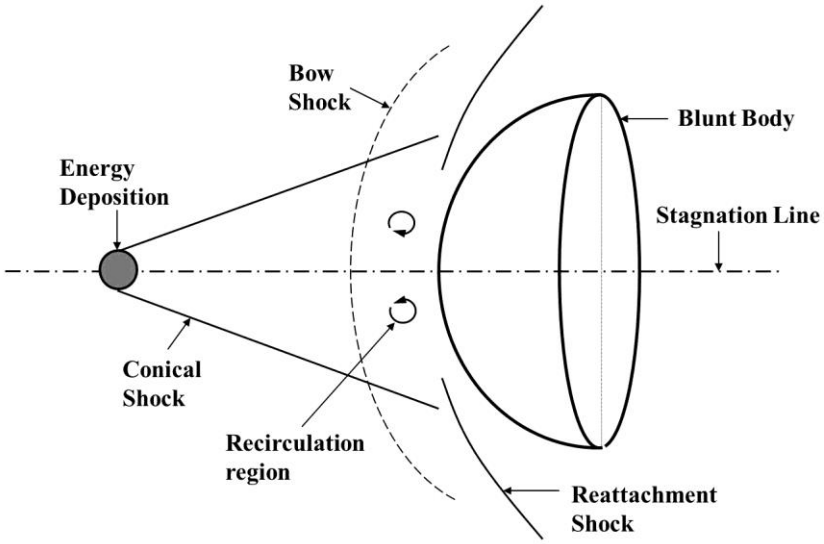

Figure 1.1: Schematic diagram of energy deposition based drag reduction technique.

Satheesh and Jagadeesh [**15**] studied the energy deposition based drag reduction technique for hypersonic flow over a 60º half angle blunt cone. Experiments were performed for air and argon environment at hypersonic Mach number of 6 and 9.1 respectively. The energy was deposited at an upstream location through electric arc discharge. It was found that the effect of energy deposition is comparatively more for argon than air environment. Additionally, it has been

reported that the interaction of hypersonic flow with the electric arc creates an unsteady flow field. Subsequently, Erdem et al. [**16**] investigated the effect of arc discharge based energy deposition upstream of a 15º half angle truncated cone at Mach 5. Experiments were performed to analyze the effect of amount of truncation and location of energy deposition. They reported location for maximum efficiency to be at 0.9 of diameter of the truncated face. Miller et al. [**17**] used the energy deposition technique to alter the flow filed and there by suppress the sonic boom. The technique was found to be viable for energy deposition at upstream as well as around the body. Riggins et al. [**18**] numerically investigated energy deposition based drag reduction technique for flow over cylindrical and spherical body at Mach 6.5 and 10. The energy was deposited at the stagnation line upstream of the blunt body. From their parametric study, they found 30% reduction in drag and power effectiveness up to 33. Macheret et al. [**14**] in their computational study demonstrated the usefulness of energy deposition technique to tackle the spillage issue in scramjet inlet by creating a virtual cowl upstream of the cowl lip. They reported optimum reduction in spillage for energy deposition at or just below the cowl line. Ogino et al. [**19**] carried out numerical investigations on drag reduction by single pulse energy deposition ahead of a sphere in the supersonic flow. They found that, the reduction in drag is directly proportional to the radius of blast wave core and square of the Mach number. Similar pulse energy deposition based study was also reported by Sangtabi et al. [**20**]. John and Kulkarni [**21**] numerically analyzed the effect of energy deposition upstream of a sphere of radius 30mm in Mach 8 flow. Different parametric studies were carried out to analyze the effect of strength, location and size of the energy spot. However their work is confined to calorically perfect gas assumption. Recently, Ganesh and John [**22**] carried out concentrated energy deposition based drag reduction study for hypersonic flow over blunt body. A perfect gas Euler solver was employed for the purpose and the study was focused on determining the optimum energy deposition location. They noticed the presence of more than one minimum drag locations. Apart from the above discussed experimental [**15**,**16**] and numerical studies with perfect gas assumption [**14**,**17**,**18**,**19**,**20**,**21**,**22**] few researchers also employed real gas solvers to investigate this drag reduction technique. Knight et al. [**23**] developed a three dimensional time-dependent inviscid solver to study the effects of microwave energy deposition upstream of a hemispherical body exposed to Mach 2 flow. Their real gas solver for air environment incorporates 23 species and 238 reactions. The discharge is considered to be of spherical shape and is located along the stagnation line at a distance 1.5 times of diameter of the

sphere. The interaction of the plasma generated by energy deposition and blunt body shock was studied and reduction in stagnation pressure has been observed. Further, It was also mentioned that a substantial dissociation of O_2 occurs which leads to formation of O throughout the interaction. Similarly, Siddesh et al. [**24**] considered real gas effects for their parametric study on energy deposition based drag reduction. It was concluded that the absolute value of strength of energy spot required for attaining the peak power efficiency increases with the increase in stagnation enthalpy. However, the non-dimensional value of energy strength remains almost same for all stagnation enthalpies considered. It was found that the peak power efficiency is in a narrow band of non-dimensional energy strength. However no efforts were made to estimate the exact value of energy strength corresponding to the peak power efficiency.

1.4.2 Shock reflection

A schematic diagram of shock reflection phenomena (regular reflection) is shown in Fig. 1.2. Here, the upstream supersonic flow in the region (1) with Mach number M_1 gets deflected by an angle equivalent to the wedge angle (θ) and an attached oblique shock (I) inevitably gets formed. This shock (I) impinges on the wall at point B. Downstream of the shock, the flow is denoted by region (2) with Mach number M_2. The flow conditions in this region are uniquely defined by the M_1 and θ from the oblique shock relations [**25**]. Now, since the flow in point B must be parallel to the wall, region (2) flow must be deflected upward by an angle θ. This can only be achieved by another shock stationed at point B, with sufficient strength to deflect the flow with Mach number M_2 by an angle θ. Hence, a reflected shock (R) is formed at point B. the strength of shock R and its downstream (Region (3)) flow properties are uniquely defined by M_2 and θ. It is important to note that the incident shock angle ($\propto$) and reflected shock angle (β) are not equal due to the disparity in their respective shock strength. Further, in case the reflected shock does not have enough strength to deflect the region (2) flow parallel to the wall then, instead of a regular reflection, a Mach reflection occurs. In that case a Mach stem gets formed and remains attached to the reflecting wall. Further, it introduces a triple point in the flow filed at the common interesting location of the incident shock, reflected shock, and Mach stem.

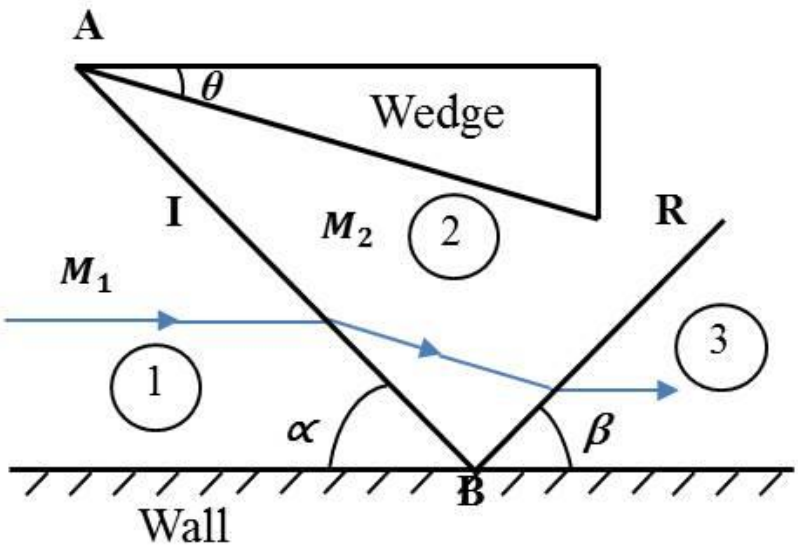

Figure 1.2: Schematic diagram of shock reflection phenomena (Regular reflection).

Various researchers have performed experimental, theoretical as well as numerical studies in shock wave reflection phenomena. The studies were focused on the transition between regular reflection (RR) and Mach Reflection (MR), hysteresis effects on the transition, Mach stem height variation, etc. Hornung and Robinson [**26**] performed an experimental investigation to determine the transition criteria from regular to Mach reflection for a wedge generated shock which is reflected from a flat opposite wall. The transition criteria were determined for flows in a range of Mach numbers from 2.8 to 5. They reported that at steady state, the transition occurs at Von-Neumann criteria and this observation is correct for both increasing and decreasing shock angles. Similarly, Chpoun et al. [**27**] experimentally investigated the transition of RR↔MR for Mach 4.96 flow over a straight reflecting surface. The hysteresis effects and steady regular reflection in the dual solution regions were observed. Ivanov et al. [**28**] carried out experimental as well as numerical study to investigate the effect of three-dimensionality on the transition criteria of Regular to Mach reflection. Good agreement between the experimental and numerical results was noticed. Subsequently, a theoretical investigation on the transition between a regular reflection and Mach reflection is given by Wu et al. [**29**]. They argued that, in regular reflection, as the incident shock is reflected from the wall, a small Mach stem (named as the geometrical stem) inevitably gets formed above the boundary-layer and hence, a contact discontinuity exists in regular reflection also.

Many researchers emphasized on the hysteresis phenomena on the RR↔MR transitions. Lvanov et al. [**30**] numerically analyzed the hysteresis effect on RR↔MR transitions using the Direct Simulation Monte Carlo (DSMC) method. It was found that, the transition of RR→MR occurs at detachment criteria whereas MR→RR transition happens at smaller angles. Similarly, Ivanon et al. [**31**] also used DSMC method for their study of shock wave reflection phenomena. They focused on the effect of external disturbance on the possible RR↔MR transitions in the region of dual solution. It was concluded that RR is more sensitive to the external disturbances than MR. Later; Ben-Dor [**32**] summarized the hysteresis phenomena in the transition of regular to Mach reflection and vice-versa in their study. Tao et al. [**33**] developed a theoretical method to investigate the viscous effects on the hysteresis phenomena of steady-state shock reflection. Further, the efficiency of the model is confirmed with numerical and experimental results.

Investigation associated with Mach stem sizes and shapes are also part of the open literature. Azevedo and Liu [**34**] presented an analytical formulation to predict the Mach stem height for a wedge geometry subjected to a supersonic flow of Mach number ranging from 2.8 to 5. They predicted stem heights are which are lower than the experimental results. Li and Ben-Dor [**35**] proposed an analytical model to predict the flow field of steady-state Mach reflections. Mach stem heights for different freestream Mach numbers were calculated and found to be in satisfactory agreement with experimental and numerical results. Their remark was, for a given freestream Mach number; the Mach stem height is solely dependent on the geometry set-up. Further, they noticed chocked flow just before the disappearance of Mach stem. Similarly, Mouton and Hornung [**36**] developed a theoretical model to predict the Mach stem height and its growth rate. The authenticity of the model is confirmed with two and three-dimensional numerical simulations. Bibin et al. [**37**] carried out inviscid simulations to predict the Mach stem height for a wedge configuration using different flux splitting schemes. Rusanov scheme was noted to be the most suitable to predict the Mach stem height. Their results also over predicted the Mach stem height as that of Vuillon et al. [**38**]. Recently, Wu et al. [**39**] numerically investigated the effect of wall temperature on Mach stem deformation. The k-ω turbulence model was employed for the purpose. They reported significant deformations in Mach stem with an increase in wall temperature above 400K. Furthermore, Hu et al. [**40**] confirmed the existence of an overall Mach reflection consisting of two inverse Mach reflections through their computational study. Semenov et al. [**41**] performed a series of experiments to classify pseudo-steady state reflection of shock

waves over a wedge. The classifications were made based on the shape of reflected shock, Mach stem and contact discontinuity and seven new types of shock wave reflection were proposed. Kemm [**42**] discussed the proper initial conditions, boundary conditions, and computational domain size to obtain double Mach reflection for inviscid flow.

Apart from the above mentioned experimental, theoretical and numerical studies, few researchers also emphasized on the real gas effects to investigate this phenomenon. Shi et al. [**43**] numerically investigated the influence of high temperatures on the protrusion of Mach stem using a non-equilibrium flow solver. In addition, a theoretical study was also performed. They proposed that the protrusion of the Mach stem is mainly due to the forward moving wall-jet. Li and Yang [**44**] theoretically investigated the transition criteria for Regular to Mach reflection. The results from the theoretical analysis were confirmed by the numerical results of a real gas flow solver.

1.4.3 Shock/shock interaction

Shock waves get naturally induced whenever the path of supersonic or hypersonic flow is obstructed. This shock can further interact with a boundary-layer [**45**,**46**], expansion waves [**47**], as well as other shocks [**48**,**49**], and significantly modifies the flow field. One of the examples is an interaction between the shocks generated from fuselage and wing of an aircraft. The existence of such interactions may source serious design issues like high thermal loads [**49**,**50**] high surface pressure [**51**,**52**] etc. Therefore, the investigation of this phenomenon became one of the vital areas among researchers.

In 1968, Edney [**48**] classified the shock/shock interaction into six types based on his experimental investigation of the interaction between an oblique shock and a bow shock induced by a blunt body. Here, the types of interactions are decided by the location of the impingement. Following this, various researchers attempted experimental and numerical investigations for blunt-body configurations. Most of them focused on quantifying the amplification of heat transfer and pressure on the body in the vicinity of interaction [**49**,**50**,**51**]. Boldyrev et al. [**49**] performed experiments in air as well as carbon dioxide (CO_2) medium to quantify the thermal loads on a blunt body arising due to Type III and IV interactions. They reported comparatively higher amplification in peak heat flux in CO_2 than air medium. Later, Grasso et al. [**52**] analyzed Type III and IV interactions for air stream through theoretical as well as experimental studies for blunt

bodies. In this study, the highest intensity of thermal load was observed for Type IV interaction case. Similarly, Chettle et al. [**53**] also carried out an experimental investigations for Type IV interaction upstream of a hemispherical body exposed to hypersonic flow. Moreover, the unsteady nature of the flow field generated by shock/shock interactions [**54**,**55**,**56**,**57**,**58**,**59**] was also studied by many researchers.

Apart from these, investigations were also carried out for double wedge geometries where the interaction occurs between the shocks formed by the first and second wedges. Here, the first wedge generates the impinging shock and the second wedge generates an attached oblique or a detached bow shock based on the flow conditions. The pattern of such interactions depends on various parameters such as Mach number (M), specific heat ratio (γ), first wedge length to second wedge length ratio (L_1/L_2), and the wedge angles (θ_1,θ_2). Though the patterns resulting from these interactions can be categorized into Edney's classifications yet the physical mechanism of their appearance can be significantly different due to different geometrical constraints. One of the pioneering studies related to this class was performed by Bertin and Hinkle [**60**]. They made comparisons between the experimental and theoretical outcomes where an excellent agreement was noted for the Type VI interaction. Later, Schrijer et al. [**61**] used the particle image velocimetry (PIV) method to capture the flow structure of different shock/shock interactions produced by double wedge geometries. They found PIV to be a suitable technique for flow visualization. Olejniczak et al. [**62**] performed numerical investigations for hypersonic flow over different geometries assuming air as a perfect gas. The Type VI, V, and IV interactions were studied along with a new unique interaction named as Type IVr. Subsequently, Wright et al. [**63**] focused on the Type V and VI interaction formed by double cone geometries for the freestream of Mach number 8. Good agreement between the experimental and perfect gas solver results was reported at lower Reynolds numbers. Later, Ben-Dor et al. [**64**] analyzed the transition between regular reflection (RR) and Mach reflection (MR) for Type V interactions for supersonic flow over double wedge configurations. The hysteresis effect and self-induced oscillations were found in the shock structures for the second wedge angle $42^o< \theta <43^o$. Few others also attempted to study similar cases [**65**,**66**,**67**] and revealed that the transition occurs (RR↔MR) at higher Mach number [**65**]. They also observed the existence of abnormal Mach reflection in Type V interactions [**66**]. Hu et al. [**67**] proposed a geometrical transition criterion (GTC) for RR↔MR in Type V interaction. They noticed a weak relation between the Mach number and the proposed GTC.

Subsequently, Durna et al. [**68**] numerically worked for the Type V interaction induced by Mach 7 air-stream ahead of double wedge configuration. They noted a steady-state flow field below a threshold value (45º-50º) of the second wedge angle, irrespective to the appearance of the bow shock in the interaction. Later, they [**69**] confirmed the existence of oscillation between the steady and unsteady state at a second wedge angle greater than 47^0. Recently, Xiang et al. [**70**] numerically investigated the effects of the wedge and sweep angles on shock/shock interaction phenomena in double wedge geometries. They found a significant effect of wedge angles on shock structure. Tchuen et al. [**71**,**72**] considered the real gas effects for their numerical investigation of Type IVr, IV and V interactions obtained at air medium. They observed substantial changes in flow structures especially in the post-shock regions due to the presence of real gas effects in the flow field. Likewise, few others investigated the transition of Type V and Type VI interaction using shock polar method and verified using non-equilibrium flow solver results [**73**,**74**]. Tumuklu et al. [**75**] employed real gas solver to analyze Type V interaction. The simulations were performed in air as well as nitrogen medium at Mach 7 with stagnation enthalpy of 8 MJ/kg. Their conclusion was that the time required to attain the steady-state for air is less compared to the nitrogen medium.

1.4.4 Shock wave-expansion fan interaction

When supersonic flow passes through a convex corner an expansion fan is generated**.** The expansion fan is made of infinite number of Mach waves bounded by the forward Mach line and rearward Mach line as shown in Fig. 1.3. The forward Mach angle, μ_1 is given by $\sin^{-1}\left(\frac{1}{M_1}\right)$ and backward Mach angle, μ_2 is given by $\sin^{-1}\left(\frac{1}{M_2}\right)$, where, M_1 and M_2 are Mach number upstream and downstream of the expansion fan respectively. Here, the expansion fan is centered at corner A and the oncoming flow is smoothly deflected across the expansion fan until it becomes parallel to the downstream surface. Furthermore, the entire expansion process is isentropic in nature. In contrary to an oblique shock, the flow gets accelerated and the flow properties across the expansion fan change smoothly. The static properties like pressure (p), temperature (T) and density (ρ) decrease across the expansion fan.

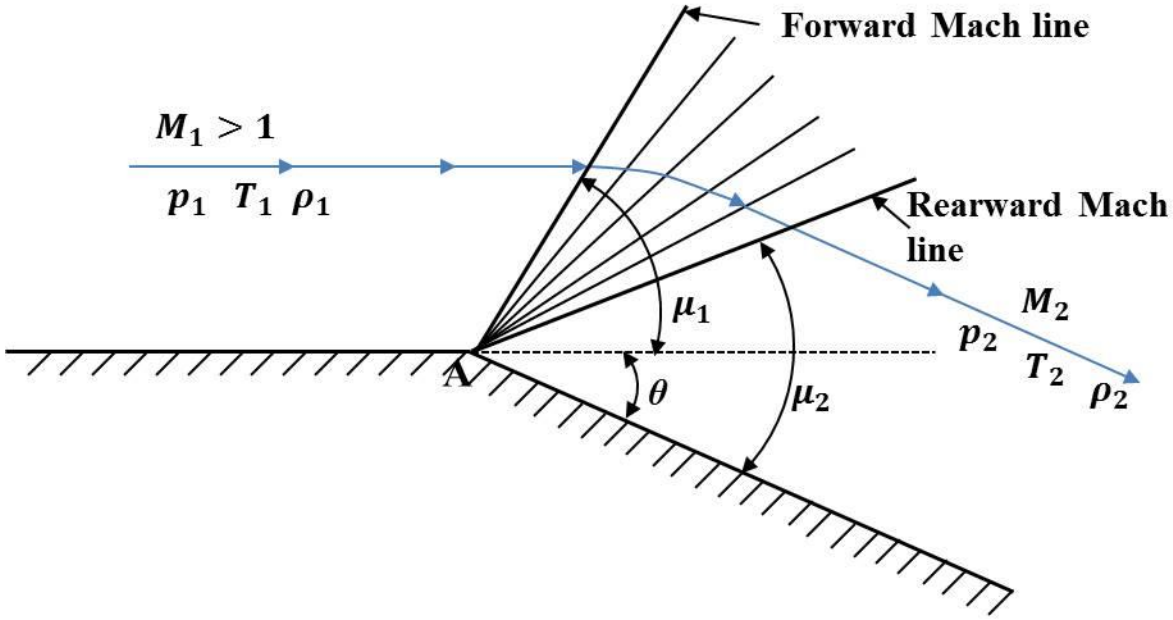

Figure 1.3: Schematic representation of an expansion fan.

Investigations for expansion fan are considered by many researchers over the years. Experimental, numerical, as well as theoretical studies can be found in the open literature. The investigators focused on understanding the flow structures (arising out of this interaction), effects on boundary-layer separation, effects on Mach reflection, etc. Back in 1969, Sullivan [**76**] theoretically investigated the laminar boundary-layer and expansion wave interaction. The effects of the interaction process on the upstream influence, transverse pressure gradient (in the vicinity of expansion corner) and the interaction of boundary-layer with the external flow (at a downstream location) were investigated. Among these, the effect on the downstream interaction was reported to be the maximum. Subsequently, Koziak and Sullivan [**77**] performed a series of experiments to investigate the effect of expansion corner on the hypersonic laminar boundary-layer. They reported a strong interaction between the corner generated expansion waves and the boundary-layer. Chew [**78**] experimentally investigated the effects on a shock wave boundary-layer interaction due to the presence of an expansion corner in the vicinity of the interaction. Experiments were performed for 1.8 to 2.5 Mach flow; impinging shock with 2º, 4º and 6º deflection angles were used for the study. It was reported that the existence of the expansion corner has significant effects on the pressure distribution and flow separation size. Further, these effects were prominent for instances where the shock impinges before (upstream) the expansion

corner. Chung and Lu [**79**] experimentally investigated the behavior of shock when it impinges at upstream, at and downstream location of an expansion corner. The expansion corner considered for the study is 2.5º or 4.25º and the shocks are generated either by a wedge of 2º or 4º. They reported significant effects on the upstream influence location due to the presence of expansion corner. A similar study of the effect of shock impinging at different locations near the expansion corner was carried out by White and Ault [**80**]. The experimental study was mainly performed to generate a data set for shock wave/boundary-layer interactions in the vicinity of an expansion corner for comparison with the numerical results. For this purpose, the shocks were generated using wedges of 10º, 12º and15º angles and the respective expansion waves are created by an expansion corner of the same magnitude. The study reveals that, the separation bubble size gets affected (reduced) by the presence of the expansion corner only when the edge of the bubble is very near to the corner. Hawboldt et al. [**81**] experimentally investigated the effects on the laminar boundary-layer separation due to presence of a convex corner. Wedges of 5º and 10º were used for shock generations and the same angle convex corners were employed for expansion wave generation. The study suggested that, though the expansion corner cannot completely nullify the separation, yet it can significantly reduce the separation size, especially when the external shock impinges exactly at the expansion corner. Li and Ben-Dor [**82**] carried out an analytical study for interaction of shock wave and centered expansion wave of opposite family. To find an expression for the shape of the interaction region they considered it to be a second order polynomial and with this assumption presented an analytical expression for it. Abate et al. [**83**] carried out shock and expansion wave interaction study experimentally and theoretically. They presented a study on shock waves undergoing sudden expansion and this study was used to design a shock induced combustion device (SICD). Chung [**84**] performed an experimental investigation on shock wave/expansion wave interaction in a supersonic flow. It was reported that the expansion corner significantly affects the upstream influence location and downstream pressure ratio. Further, it was observed that the increasing corner angle has decreasing effects on the downstream and peak pressure ratio. Sanderson [**85**] investigated the interaction between an oblique shock undergoing Mach reflection and expansion wave considering two-dimensional Euler equations. Hillier [**86**] numerically investigated the interaction of expansion wave and an incident oblique shock of opposite family. It was found that the presence of expansion waves significantly changes the criteria for occurrence Mach reflection. Similarly, the influence of shock wave/expansion wave

interaction on the transition criteria of regular to Mach reflection is reported by Yao et al. [**87**]. Zhang et al. [**88**] carried out theoretical as well numerical study to investigate the behavior of cowl shock/boundary-layer interaction due to the presence of expansion waves generated at a convex corner of the ramp used for the shock generation. They reported that when the cowl shock impinges near the expansion corner the interactions process between the shocks and expansion waves actually suppress the boundary-layer separation. Similarly, Silnikov et al. [**89**] proposed an analytical model for expansion wave/ oblique shock interactions studies and verified the model with numerical results. Narayanan and Verma [**90**] carried out an experimental study to investigate the effects of variation in wedge angle, expansion angle and shock impinging location on the boundary-layer separation. They reported the upstream movement of the separation point with an increase in the wedge angle. Further, it was found that; pressure peak reduces with the downstream movement of impinging location and increase in expansion angle. Recently, Nel and Skews [**91**] highlighted the usefulness of the Schlieren flow visualization tool to capture the detailed flow structure of a shock wave/expansion wave interaction in their wind tunnel test.

1.4.5 Shock wave boundary-layer interaction

An object in viscous supersonic or hypersonic flow experiences a shock wave and certainly boundary-layers formed in the vicinity of the surface. Due to the obvious presence of these two flow phenomena and their interaction in many practical applications such as wing-body junctions, engine inlets, etc. various unintended flow features like flow separations, boundary-layer readjustment, high heat transfer rate, etc. inherently get induced. Therefore, from the designer's perspective, it becomes very important to understand the physics associated with shock wave boundary-layer interaction (SWBLI) phenomena. Broadly, these interactions are classified into two categories- one with normal shock and another with oblique shock. Again, Oblique shock interaction is divided into two categories- impingement based shock wave boundary-layer interactions (I-SWBLI) and ramp induced shock wave boundary-layer interactions (R-SWBLI). In I-SWBLI, the externally induced oblique shock penetrates a boundary-layer developed over another surface and gets reflected. Whereas, in R-SWBLI, oblique shock generated by ramp interacts its boundary-layer. A schematic diagram of such types of interactions is shown in Fig. 1.4**.** Here, due to the presence of the compression corner, the oncoming supersonic or hypersonic flow gets deflected abruptly leading to the formation of an oblique shock stationed at ramp foot.

Hence, in the downstream region of this shock, the flow velocity decreases, and the pressure increases drastically. This pressure rise propagates upstream of the shock through the subsonic region of the boundary-layer resulting in a thicker boundary-layer. Further, this boundary-layer thickening may lead to flow separation. As the flow separation occurs, the oblique shock positions itself at an upstream location which is labeled as separation shock and reattaches at a downstream location. These shocks again interact to form a new shock further downstream as shown in the figure. It is worth mentioning that, this flow separation is not guaranteed in every case. The flow separation occurs only when the ramp angle is greater than a certain value defined by the *incipient separation* angle. Further, this incipient separation angle is generally a function of Mach number, Reynolds number, wall temperature, etc. However, even if there is no flow separation the effect of the oblique shock is always felt upstream of it and the location at which such influence is felt is termed as upstream influence location (L_{ui}). Usually, this point is determined by the location at which the surface pressure starts to rise. Further, in the separation region pressure remains constant which is called as plateau pressure. Beyond the flow reattachment, pressure again increases. Finally, another important terminology in the study of SWBLI phenomena is the separation length (L_b), which is defined as the streamwise distance between the flow separation point and the reattachment point.

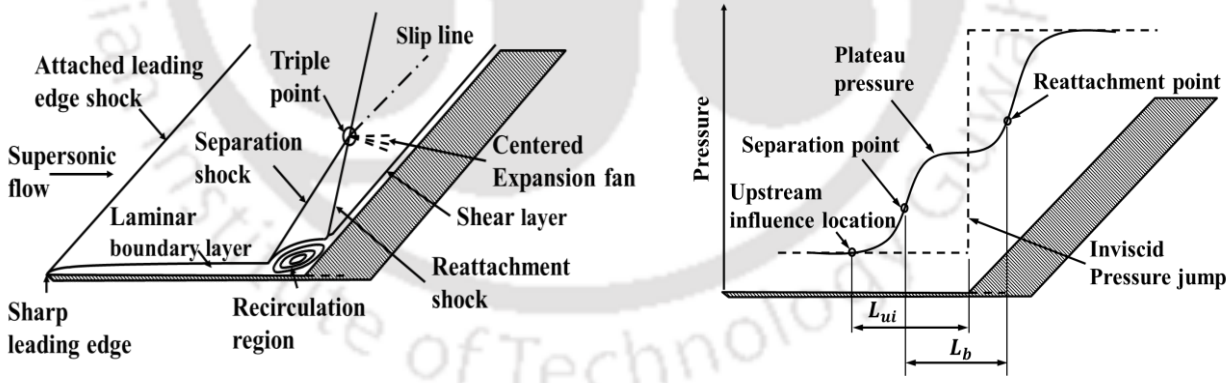

Figure 1.4: Schematic diagram of a Ramp based SWBLI along with surface pressure distribution.

Experimental work on the shock wave boundary-layer interaction (SWBLI) started back in 1940s [**92**,**93**,**94**]. However, most of the investigations were performed for flow mostly in the subsonic regime with some supersonic pockets. Later on, in the early 1950s [**95**,**96**,**97**,**98**] systematic study on the phenomena started in purely supersonic flow with an aim to investigate the effects of various parameters such as Mach number, Reynolds number, shock strength, etc.

One of the most noted investigations in the field of shock/shock interactions is of Chapman et al. [**99**]. They carried out numerous experiments and theoretical analyses for different flow models in subsonic and supersonic regimes. They observed that few characteristics of separated flow neither depend on the shape of the geometry nor on the mode of inducing such separation. It is reported that, in the supersonic regime, for both laminar and turbulent separation, the pressure rise doesn't depend on how the separation is induced. Few more important observations are: laminar and turbulent separations are mostly steady and barely depend on Reynolds number and with an increase in Mach number the laminar separated mixing layer stabilizes. Later on, Kuehn [**100**] analyzed the turbulent interactions for various configurations such as compression corner; curve surfaces etc. in supersonic flow of Mach 1.6 to 4.2. The investigation emphasizes the effects of Reynolds number and Mach number on incipient separation. It was observed that variation in Mach number significantly affects the magnitude of pressure required for incipient separation. Again, the effects of Reynolds number are found to be significant only when Mach numbers are high and Reynolds numbers are low. Furthermore, he proposed to estimate the incipient separation point by surface pressure measurement instead of skin friction measurements. Followed by this, Needham [**101**] developed a heat transfer measurement based methodology to predict incipient separation. However, both these methods were found inadequate in predicting small separation bubbles. Subsequently, Needam and stollery [**102**] formulated a correlation to estimate the incipient separation angle based on their experimental outcomes.

Most of the investigations in the 1960s were limited to the supersonic regime. However, by the dawn of next decade, researchers started to investigate this phenomenon in the hypersonic regime. One of the first to consider SWBLI in hypersonic flow is Holden [**103**]. He performed a series of experiments to analyze the effect of Mach and Reynolds number on flow separation over a compression corner. The range of Mach number and Reynolds number considered for the investigations were 14 to 20 and 2000/in. to 14000/in. respectively. Besides, the effect of leading edge bluntness was also studied. Increase in separation length was noticed for increase in Reynolds number whereas a decrease in separation length was noticed as Mach number increases. Again it was concluded that, with the introduction of leading edge bluntness the pressure, heat transfer and the wedge angle required for incipient separation can be reduced significantly. Furthermore, another important observation was the rapid increase in upstream influence with an increasing wedge angle for hypersonic flow as against a steady increase in supersonic flow. Bloy

and Georgeff [**104**] carried out an experimental investigations of laminar SWBLI in hypersonic flow. The experimental results were compared with theoretical results and found to be in good agreement. In addition, they proposed a correlation for hypersonic incipient separation. Back and Cuffel [**105**] investigated shock-wave/turbulent boundary-layer interaction. The focus of their investigations was the effect of surface cooling and heating on the separation length. One of the important observations reported is the decrease in the separation region with surface cooling. Hayakawa and Squire [**106**] emphases on the effects of upstream interaction state on the downstream interactions. The experiments were performed for Mach number ranging from 1.8 to 2.9 and wedge angle of 8º to 14º. The equilibrium state of the boundary-layer ahead of the interaction was intentionally changed by injecting air through a porous wall. For all Mach numbers considered in the investigation, upstream influence was noted to increases with an increase in injection rates and wedge angle. Few researchers also carried out investigation of SWBLI experimentally as well as numerically such as the investigations for two-dimensional configurations by Marini [**107**] and for blunted con-flare by Dieudonne et al. [**108**]. Holden [**109**] presented experimental data related to SWBLI in the hypersonic flow regime for cone/cone and cylindrical geometries. The main motive behind his work was to have experimental data for validation of numerical codes. Neuenhahn and Olivier [**110**] performed an experimental study to analyze the laminar SWBLI phenomena for a double wedge geometry immersed in hypersonic flow. The effects of leading edge bluntness and wall temperature were investigated. It was mentioned that, for higher wall temperature the separation length is higher. Recently, Hongyu et al. [**111**] studied the unsteadiness in R-SWBLI by means of plasma jet at an upstream location. The intention was to test the feasibility of such intentional disturbance in the flow to reduce/eliminate the adverse effects of SWBLI and as intended, the method was found to be adequate. A similar effort to control boundary-layer transition was also performed by Szwaba et al. [**112**].

Apart from experimental findings discussed above, many researchers have carried out numerical studies to analyze the SWBLI phenomena. Among them, one of the initial reporting in this field is of Carter [**113**] for the laminar SWBLI phenomena for a supersonic flow (Mach 3) over a two dimensional 10º compression corner. Subsequently, MacCormack and Baldwin [**114**] put forward a time-accurate second order numerical method for the turbulent SWBLI phenomena in the year 1975. Again, Hung and MacCormack [**115**] presented a numerical scheme for solving

two-dimensional Naviers stoke equations for laminar flow over a wedge. Simulations were performed in supersonic as well as hypersonic flow regimes for different wedge angles ranging between 15º to 24º. The results were compared with previously reported experimental values and found in good agreement. It was stated that, for hypersonic flow, the leading edge shock inclusion is important, as this shock may interact with the compression corner shock and lead to a significant rise in surface pressure. Balleur et al. [**116**] used two different approaches namely global and coupled approach to investigate the viscous-inviscid SWBLI phenomena in high Reynolds number flow. In the global approach, a single set of equations (Naviers-Stokes) was solved for both viscous as well as inviscid domain. Whereas, in the coupled approach two different sets of equations were considered for each domain. In this approach, the simulations in both the domains were performed simultaneously and the boundary condition at the interface for the inviscid domain was obtained by solving the viscous domain. Similarly, Rudy et al. [**117**] and Garsso et al. [**118**] presented numerical techniques to solve for laminar and turbulent SWBLI phenomena in the hypersonic flow regime.

In addition to the above-discussed investigations, many numerical investigations were focused on different parametric studies on SWBLI. Grasso and Marini [**119**] investigated the ramp induce SWBLI in hypersonic flow. The effects of the deflection angle and leading edge bluntness in the separation length were investigated. It was concluded that with an increase in ramp angle the separation region tends to increase whereas with the addition of bluntness in the leading edge the separation region decreases. Subsequently, Marini [**120**] investigated the effects of ramp angle, wall temperature and asymmetry on SWBLI for hypersonic flow over a flat plate-ramp configuration. They reported larger separation length and plateau pressure for the axisymmetric case as compared to the two-dimensional one. Again, it was concluded that with the increase in wall temperature the separation region increases. This observation about the wall temperature was further confirmed by Savino and Paterna [**121**] in their study of SWBLI in hypersonic flow over a blunted cone-flare configuration. In line with this, John et al. [**122**] reported that the separation region increases with an increase in wall temperature and ramp angle and decreases with increase in Mach number and freestream stagnation enthalpy. Additionally, they also explored the effects of wall to total temperature ratio and found that it depends on the ratio of these two temperatures and not on their individual magnitudes. John and Kulkarni [**123**] performed a numerical investigation to evaluate the effects of leading edge bluntness on ramp induced SWBLI. It was

found that there exists a critical radius of bluntness above which the separation region decreases as compared to the case of no bluntness. Few researchers also proposed correlations to predict separation bubble size [**119**,**124**], extent of upstream influence [**124**] etc. It is worth mentioning that, all of the above numerical studies were performed with a perfect gas assumption. Very few investigators focused on the impact of real gas effects on SWBLI phenomena. Among them, Jahantigh et al. [**125**] considered real gas effects in their study of SWBLI phenomena. Simulations were performed for different ramp angles and it was found that with an increase in ramp angle the separation size increases. Further, Davis and Sturtevant [**126**] also highlighted the consideration of non-equilibrium flow model to study the effect of high enthalpy flow on SWBLI**.** Clemente et al. [**127**] used a five-species non-equilibrium flow model containing 17 reactions for their study of SWBLI around a 20º open flap. Recently, Hao and Wen [**128**] focused on the effects of vibrational non-equilibrium on SWBLI for double-cone geometries.

1.5 Work plan for present study

Due to the significant number of Mars expeditions planned in near future, researchers around the world should contribute immensely to the success of these expeditions. In general, these flights fly at hypersonic speed and are always associated with various flow complications like a high drag, high thermal load, boundary-layer separation, etc. Furthermore, in comparison to costly experiments CFD (computational fluid dynamics) is a cost-effective tool for investigating such flow complications. Many researchers have carried out simulations with perfect gas assumptions. However, for higher flow field temperature, this perfect gas model is inappropriate as the real gas effects such as specific heat variation, dissociation reactions, ionization, etc. became prominent at higher temperatures. Therefore, it is advisable to use a real gas solver for simulating high enthalpy flows.

Various researchers reported energy deposition based drag reduction technique in the open literature. It is concluded that there is peak power effectiveness corresponding to a particular value of deposited energy [**21**]. However, none of the investigations considered to measure the optimum energy to be deposited for peak power effectiveness. Further, it must be noted that the reported studies are for only Earth atmospheric conditions (air). Hence, it is desirable to use a formal optimization technique to attain the optimum energy corresponding to maximum power effectiveness in both Earth and Mars atmospheric conditions.

The design of a space transportation system demands proper predictions of thermal and structural loads. In supersonic and hypersonic flight, the shape and structure of shock wave, expansion fan etc. defines these loads. Due to the sharp leading edges present in different components of these systems, different types of shocks, expansion fans etc. are induced. Further, these shocks may interact with other shock or some expansion fans or get reflected. This leads to changes in the flow field. Many aspects of the shock reflection phenomenon such as transition between regular (RR) and Mach reflection (MR), hysteresis effects and Mach stem growth rate etc. were explored by different investigators. Most of the numerical studies considered perfect gas solver and very few considered the real gas effects in their investigations [**43**,**44**] of this flow phenomenon. Furthermore, all these investigations are limited to air medium. Again, it has been noticed that the effect of freestream enthalpy on the transition criteria for RR↔MR is left untouched. Hence, it is essential to investigate the transition criteria (RR↔MR) at higher enthalpies in different flow mediums. The majority of the literature associated with shock/shock interactions are confined to air flow medium and only a handful endeavored into the other medium like nitrogen [**75**] and carbon dioxide [**51**]. Furthermore, limited number of literatures considered [**71**,**72**,**73**,**74**,**75**] real gas effects. Again, in the case of shock/expansion wave interaction, it has been noticed that the majority of the studies are concerned only about the effects in air flow medium. Hence, it is desirable to perform investigations of these flow interactions considering real gas effects in Earth and Mars atmospheric conditions.

Literature related to shock wave boundary-layer interactions (SWBLI) studies showed that there are active and passive techniques to control it and is governed by different flow parameters. In addition, few investigations reported correlations to predict the important flow features such as the amount of flow separation, upstream influence location etc. considering perfect gas simulations results. Furthermore, most of the parametric studies used perfect gas assumption and very few researchers accounted for real gas effects [**125**,**126**,**127**,**128**]. It has been noticed that these studies are mainly confined to air flow medium and important flow mediums like carbon dioxide are left unexplored. Therefore, it is essential to explore the effects of various flow parameters in SWBLI in a carbon dioxide medium with real gas effects. Besides it is important to revisit the previously obtained correlations considering real gas effects in air medium and model new correlations for carbon dioxide medium.

In view of the above discussions, the work plan for present investigation is

1. Development of an unstructured finite volume based Navier-stokes reacting gas flow solver for simulating hypersonic flight conditions in Mars environment.
2. Validation of the in-house developed solver with various two-dimensional and axisymmetric cases.
3. Examinations of the performance of energy deposition based drag reduction technique in Earth as well as Mars flight conditions and estimate the optimum energy deposition for peak power effectiveness using a standard optimization technique.
4. Assessment of the transition criteria for regular to Mach reflection in different flow mediums at various freestream enthalpies.
5. Aerothermodynamics analysis of different shock/shock interactions induced by double wedge geometries in Earth and Mars atmospheric conditions.
6. Assessment of real gas effects on shock/expansion wave interaction for different geometries.
7. Comparison of the effect of different parameters on shock wave boundary-layer interactions in Earth and Mars Atmospheres. Subsequently, propose correlations for upstream influence location and extent of flow separation.

1.6 Objective of the present study

The major objectives of the present investigation are

1. To develop an unstructured finite volume-based reacting gas flow solver for simulating hypersonic flight conditions in the Mars environment.
2. To validate the in-house developed solver with various test cases.
3. To examine the energy deposition-based drag reduction technique in Earth and Mars flight conditions by estimating the peak power effectiveness with the golden section search optimization method.
4. To analysis the transition between regular and Mach reflection with variation in freestream enthalpies in different flow mediums.
5. To analysis different shock/shock interactions patterns induced by double wedge geometries in Earth as well as Mars atmospheric conditions.

6. To assess real gas effects on flow field involving shock and expansion fan for different geometries.
7. To perform parametric studies on shock-wave boundary-layer interactions in Earth and Mars Atmospheric conditions and compare the outcomes of these flow mediums. Subsequently, propose correlations for the extent of flow separation and upstream influence location.

1.7 Organization of Thesis

1. Chapter 2 deals with the details of numerical formulation and validation of the in-house developed real gas solver.
2. Chapter 3 discusses the performance of energy deposition technique in Earth and Mars environment. Besides, the details of the optimization method and its integration with the solver to measure the optimum energy deposition for peak power effectiveness are provided in this chapter.
3. In chapter 4, the effect enthalpy variation on transition criteria for Regular to Mach reflection is discussed.
4. Chapter 5 focuses on various shock/shock interaction induced by double wedge geometries in Earth and Martian atmosphere.
5. Chapter 6 deals with real gas effects on the shock/expansion wave interactions.
6. In chapter 7, comparative study of effects of various parameters on laminar SWBLI in Earth and Mars atmospheric conditions are discussed.
7. The present investigations are summarized in chapter 8, highlighting the important findings and future scopes.

Chapter 2 : Numerical Formulations

Overview

This chapter presents the numerical formulations used to simulate compressible flow at low as well as high enthalpy. The cell-centered finite volume formulation opted for the present solver is discussed in detail. The flux calculations (inviscid and viscous) and different boundary conditions implemented in the solver are the part of this chapter. Further, the various flow models employed for the investigation and their validation are also discussed herein.

2.1 Introduction

The present study aims at solving different two-dimensional and axisymmetric problems related to high-speed flow in Earth and Mars atmosphere. For the energy deposition-based drag reduction study two-dimensional axisymmetric geometry is considered whereas for Mach reflection, shock/shock interaction, shock expansion fan interaction and shock wave boundary layer interaction studies two-dimensional geometries are considered. Here, viscous simulations are performed for the shock wave boundary layer study and the rest of the problems consider in-viscid flow. Further, for all cases, the study is performed in both Earth and Mars atmospheric mediums. Therefore, a finite-volume based two-dimensional (axisymmetric) real gas solver is employed for the study. The solver is the one developed by Desai et al. [**24**,**129**,**130**,**131**]for simulating Earth atmospheric conditions, which is further extended for simulating Mars atmosphere specifically for the present study. In addition, perfect gas simulations are performed by the solver developed by John et al. [**21**,**122**,**123**,**124**]. The following sections provide the detail of the solvers.

2.2 Governing equations

Computational fluid dynamics (CFD) is a technique to predict the fluid-flow phenomena by solving the governing equations with the aid of suitable numerical methods. It is a cost-efficient choice as compared to costly experiments. Over the years, with the advancement in computer capabilities, it has emerged as an integral part of the design industries, especially for high-speed aircraft like missiles, spacecraft etc. Basically, the solution methodology involves the Euler or the Navier-stokes (N-S) equations as the governing equations. However, for efficient prediction of flow features at high enthalpy conditions, the consideration of real gas effects such as

specific heat variation, chemical reactions etc. become important. Hence, to account for the reacting gas, the species continuity equation has to be coupled with the N-S equations and solved jointly. The reactive Navier-Stokes equations for two dimensional axisymmetric laminar viscous compressible flows in vector form can be expressed as

$$\frac{\partial U}{\partial t}+\frac{\partial F_I}{\partial x}+\frac{\partial G_I}{\partial y}+S+a(S_I-S_v)=\frac{\partial F_v}{\partial x}+\frac{\partial G_v}{\partial y} \qquad (2.1)$$

Where,

$$U=\begin{pmatrix}\rho\\ \rho u\\ \rho v\\ \rho E\\ C_1\\ .\\ .\\ C_{N-1}\end{pmatrix} \qquad F_I=\begin{pmatrix}\rho u\\ \rho u^2+p\\ \rho uv\\ (\rho E+p)u\\ uC_1\\ .\\ .\\ uC_{N-1}\end{pmatrix} \qquad G_I=\begin{pmatrix}\rho v\\ \rho uv\\ \rho v^2+p\\ (\rho E+p)v\\ vC_1\\ .\\ .\\ vC_{N-1}\end{pmatrix}$$

$$F_v=\begin{pmatrix}0\\ \tau_{xx}\\ \tau_{xy}\\ u\tau_{xx}+v\tau_{xy}-q_x-\sum_{i=1}^{N}h_iC_i\bar{u}_i\\ -C_1\bar{u}_1\\ .\\ .\\ -C_{N-1}\bar{u}_{N-1}\end{pmatrix} \qquad G_v=\begin{pmatrix}0\\ \tau_{xy}\\ \tau_{yy}\\ u\tau_{xy}+v\tau_{yy}-q_y-\sum_{i=1}^{N}h_iC_i\bar{v}_i\\ -C_1\bar{v}_1\\ .\\ .\\ -C_{N-1}\bar{v}_{N-1}\end{pmatrix}$$

$$S=-\begin{pmatrix}0\\ 0\\ 0\\ 0\\ S_1\\ .\\ .\\ S_{N-1}\end{pmatrix} \qquad S_I=\frac{1}{y}\begin{pmatrix}\rho v\\ \rho uv\\ \rho v^2\\ (\rho E+p)v\\ vC_1\\ .\\ .\\ vC_{N-1}\end{pmatrix}$$

$$S_v = \frac{1}{y}\begin{pmatrix} 0 \\ \tau_{xy} - \frac{2}{3}y\frac{\partial(\mu v/y)}{\partial x} \\ \tau_{yy} - \tau_{\theta\theta} - \frac{2}{3}\mu\left(\frac{v}{y}\right) - \frac{2}{3}y\frac{\partial(\mu v/y)}{\partial y} \\ u\tau_{xy} + v\tau_{yy} - q_y - \frac{2}{3}\frac{\mu v^2}{y} - \frac{2}{3}y\frac{\partial(\mu v^2/y)}{\partial y} - \frac{2}{3}y\frac{\partial(\mu uv/y)}{\partial x} - \sum_{i=1}^{N} h_i C_i \bar{v}_i \\ -C_1\bar{v}_1/y \\ . \\ . \\ -C_{N-1}\bar{v}_{N-1}/y \end{pmatrix}$$

Here, U is the solution or conservative vector, F_I, G_I and F_v, G_v are convective and viscous flux vectors in x and y directions respectively, S is the reaction source term, S_I and S_v represent the invsicid and viscous source term respectively and a is a constant which takes a value of 0 (for 2-D cases) or 1 (for axisymmetric cases) depending on the problem considered. Further, ρ is density, p is pressure, T is temperature and u and v are velocities in x and y directions respectively. Here, E is total energy $\left(E = e + \frac{1}{2}(u^2 + v^2)\right)$ where, e is internal energy $\left(e = \sum_{i=1}^{N} e_i \frac{C_i}{\rho MW_i}\right)$. In this equation, e_i is the molar internal energy of the species $\left(e_i = h_{f_i}^0 + \int_{T_R}^{T} C_{pi}dT - R_u T\right)$. Where, C_i, MW_i, $h_{f_i}^0$ and C_{pi} respectively represents the mass concentration, molecular weight, heat of formation and specific heat at constant pressure. Further, R_u is the universal gas constant, and 'N' is number of species. The stress terms are $\tau_{xx} = \mu\left(\frac{4}{3}\frac{\partial u}{\partial x} - \frac{2}{3}\frac{\partial v}{\partial y}\right)$, $\tau_{xy} = \mu\left(\frac{\partial u}{\partial y} + \frac{\partial v}{\partial x}\right)$, $\tau_{yy} = \mu\left(\frac{4}{3}\frac{\partial v}{\partial y} - \frac{2}{3}\frac{\partial u}{\partial x}\right)$ and $\tau_{\theta\theta} = \mu\left[\frac{-2}{3}\left(\frac{\partial u}{\partial y} + \frac{\partial v}{\partial x}\right) + \frac{4v}{3y}\right]$. Here, $\bar{u}$ and $\bar{v}$ represents the diffusion velocities in x and y direction respectively and are calculated by using the Fick's law, i.e. $Y_i\bar{u} = D_{im}\frac{\partial Y_i}{\partial x}$, $Y_i\bar{v} = D_{im}\frac{\partial Y_i}{\partial y}$, where D_{im} is a constant.

The present solver considers the polynomial expression to account for the variation in specific heat, thermal conductivity and viscosity with temperature as specified by Gordon and McBride [**132**]. Finally, the equation of state is used for the closure of the system, where the pressure is calculated by totaling the individual partial pressure of the species.

$$p = R_u T \sum_{i=1}^{N} \frac{C_i}{MW_i} \tag{2.2}$$

Temperature in the above expression is obtained from internal energy, Newton-Raphson iterative method is used for the purpose.

$$\rho e = \sum_{i=0}^{N} \frac{C_i}{MW_i} \left(h_{f_i}^0 + \int_{T_R}^{T} C_{pi} dT \right) - p \tag{2.3}$$

The following section provides the details of chemical kinetics incorporated in the present real gas solver.

Furthermore, the sonic velocity (frozen) for chemical non-equilibrium case is given by [**133**]

$$a^2 = \left(\frac{\partial p}{\partial \rho}\right)_s = p_\rho + p_e \, {}^{p}/_{\rho^2} + \sum_{i=1}^{N-1} \frac{C_i p_{C_i}}{\rho} \tag{2.4}$$

Where *a* is the speed of sound; *p, ρ, e, and* C_i are pressure, density, specific internal energy, and mass concentration for species *i* respectively. Further, $p_\rho, p_e and\ p_{C_i}$ are partial derivative of *p* with respect to *ρ, e,* and C_i with other variables held fixed.

Further, the above equation (Eq. 2.3) can be reduced to [**134**]

$$a^2 = \frac{p}{\rho}\left(1 + \frac{R}{C_v}\right) \tag{2.5}$$

2.3 Chemical Kinetics

The reversible reaction mechanism for '*N*' number of species can be written as

$$\sum_{j=1}^{N} v'_{ij} n_j \leftrightarrow \sum_{j=1}^{N} v''_{ij} n_j \tag{2.6}$$

Here, the indices *i* and *j* denote the number of reactions and the number of species respectively. In this equation, v'_{ij} and v''_{ij} are specifies stoichiometric coefficients for the reactants and products in the i^{th} reaction of the species *j*. The molar concentration of the j^{th} species

is given by $n_j = \frac{C_j}{MW_j}$. Further, the reaction rate constant is obtained by using the Arrhenius rate equation, which is given as (for the i^{th} reaction)

$$k_i = A_i T^{m_i} e^{\frac{-E_i}{RuT}} \tag{2.7}$$

Here, A_i and m_i are constants and E_i is the activation energy.

The current real gas solver is capable of simulating Earth as well as Mars atmospheric conditions. When simulated for the reacting air flow or Earth atmospheric conditions, it accounts five species (N_2, O_2, N, O, and NO) and eleven chemical reactions among them, whereas for the Mars atmospheric or carbon dioxide flow case it accounts eight species (N_2, O_2, N, O, NO, CO_2, CO and C) and ten chemical reactions. Again, the rate of change of molar concentration of a particular species is obtained by accounting the changes at all reaction steps,

$$S_j = MW_j \sum_{i=1}^{N_R} \left(v''_{ij} - v'_{ij}\right) \left(k_{fi} \prod_{l=1}^{N} {n_l}^{v'_{il}} - k_{bi} \prod_{l=1}^{N} {n_l}^{v''_{il}} \right) \tag{2.8}$$

Here, k_{fi} and k_{bi} represents the forward and backward rate constant for reaction i. The reactions and reaction-rate constants considered for Air and Mars environment are given in Table 2.1 and 2.2 respectively. The reaction kinetic data for the Earth atmosphere is taken from the Dunn and Kang [**135**]. However, the range of temperatures present work deals with is not high enough for ionization to occur. Hence, ionization and its associated reactions are not considered herein. Similarly, the kinetic data considered for the Mars environment are taken from Kay and Netterfield [**136**] excluding the ionization.

Table 2.1: Chemical reactions and specific reaction-rate constants in the chemical non-equilibrium calculations Earth Atmosphere.

No	Forward Reaction	k_{fi}(cm^3/mole sec)	k_{bi}(cm^3/mole sec)
1	$O_2 + M - > 2O + M(N)$	$3.6 \times 10^{18} T^{-1.0} e^{-5.95 \times 10^4 / T}$	$3.0 \times 10^{15} T^{-0.5}$
2	$N_2 + M - > 2N + M(O)$	$1.9 \times 10^{17} T^{-0.5} e^{-1.13 \times 10^5 / T}$	$1.1 \times 10^{16} T^{-0.5}$
3	$NO + M - > N + O + M(O_2)$	$3.9 \times 10^{20} T^{-1.5} e^{-7.75 \times 10^4 / T}$	$1.0 \times 10^{20} T^{-1.5}$

4	$O + NO- > N + O_2$	$3.2 \times 10^{9} T^{1} e^{-1.97\times10^{4}/T}$	$1.3 \times 10^{10} T^{1} e^{-3.58\times10^{3}/T}$
5	$O + N_2- > N + NO$	$7.0 \times 10^{13} e^{-3.8\times10^{4}/T}$	1.56×10^{3}
6	$N + N_2- > N + N + N$	$4.085 \times 10^{22} T^{-1.5} e^{-1.13\times10^{5}/T}$	$2.27 \times 10^{21} T^{-1.5}$
7	$O_2+ O- >2O + O$	$9.0 \times 10^{19} T^{-1.0} e^{-5.95\times10^{4}/T}$	$7.5 \times 10^{16} T^{-0.5}$
8	$O_2 + O_2- >2O + O_2$	$3.24 \times 10^{19} T^{-1.0} e^{-5.95\times10^{4}/T}$	$2.7 \times 10^{16} T^{-0.5}$
9	$O_2 + N_2- >2O + N_2$	$7.2 \times 10^{18} T^{-1.0} e^{-5.95\times10^{4}/T}$	$6 \times 10^{15} T^{-0.5}$
10	$N_2 + N_2- >2N + N_2$	$4.7 \times 10^{18} T^{-0.5} e^{-1.13\times10^{5}/T}$	$2.72 \times 10^{16} T^{-0.5}$
11	$NO +M- > N + O +M(O)$	$7.8 \times 10^{22} T^{-1.5} e^{-7.55\times10^{4}/T}$	$2.0 \times 10^{20} T^{-1.5}$

Table 2.2: Chemical reactions and specific reaction-rate constants in the chemical non-equilibrium calculations Mars atmosphere.

No	Forward Reaction	k_{fi} (cm^3/mole sec)	k_{bi} (cm^3/mole sec)
1	$O_2 +M- >2O +M$	$9.1 \times 10^{18} T^{1.0} e^{-5.937\times10^{4}/T}$	$9.0 \times 10^{15} T^{-0.5}$
2	$N_2 +M- >2N +M$	$2.5 \times 10^{19} T^{-1.0} e^{-1.132\times10^{5}/T}$	$1.5 \times 10^{18} T^{-1.0}$
3	$NO +M- > N + O +M$	$4.1 \times 10^{18} T^{-1.0} e^{-7.533\times10^{4}/T}$	$3.5 \times 10^{18} T^{-1.0}$
4	$CO + M- > C+ O +M$	$4.5 \times 10^{19} T^{-1.0} e^{-1.289\times10^{5}/T}$	$1.0 \times 10^{18} T^{-1.0}$
5	$CO_2 + M- > CO+O+M$	$3.7 \times 10^{14} e^{-5.25\times10^{4}/T}$	$2.4 \times 10^{15} e^{-2.184\times10^{3}/T}$
6	$N_2+O-> NO + N$	$7.4 \times 10^{11} T^{0.5} e^{-3.794\times10^{4}/T}$	$1.6 \times 10^{11} T^{0.5}$
7	$NO + O- >O_2 + N$	$3.0 \times 10^{11} T^{0.5} e^{-1.946\times10^{4}/T}$	$9.5 \times 10^{9} T^{1.0}$
8	$CO + O- >C + O_2$	$2.7 \times 10^{12} T^{0.5} e^{-6.945\times10^{4}/T}$	$9.4 \times 10^{12} T^{0.25}$
9	$CO_2 + O- >CO + O_2$	$1.7 \times 10^{13} e^{-2.65\times10^{4}/T}$	$2.5 \times 10^{12} e^{-2.4\times10^{4}}$
10	$CO + N- >NO + C$	$2.9 \times 10^{11} T^{0.5} e^{-5.363\times10^{4}/T}$	$2.6 \times 10^{10} T^{0.5}$

2.4 Finite volume method-*cell centered approach*

The finite volume discretization technique is one of the most widely used, as it is based on the integration of conservative forms of governing equations. In the finite volume method the governing equations are discretized by first dividing the physical space into a number of arbitrary polyhedral control volumes and then approximating the surface integral by the sum of the fluxes crossing the individual faces of the control volume. The shapes and position of the control volume concerning the grid can be defined in mainly two ways *i.e* cell-centered approach/scheme and cell-vertex approach/scheme. In the cell-centered scheme, the flow quantities are stored at the centroid of the grid cells. Whereas, in the cell-vertex scheme, the flow quantities are stored at the grid points. The control volume can then either be a union of the entire cell sharing the grid points or some volume centered on the grid point. Figures 2.1(a) and 2.1(b) represent the cell-centered approach and cell-vertex approach respectively. In the solver employed for the present investigation cell-centered approach is used. This solver can handle both structured as well as unstructured meshes as it is written in the unstructured format.

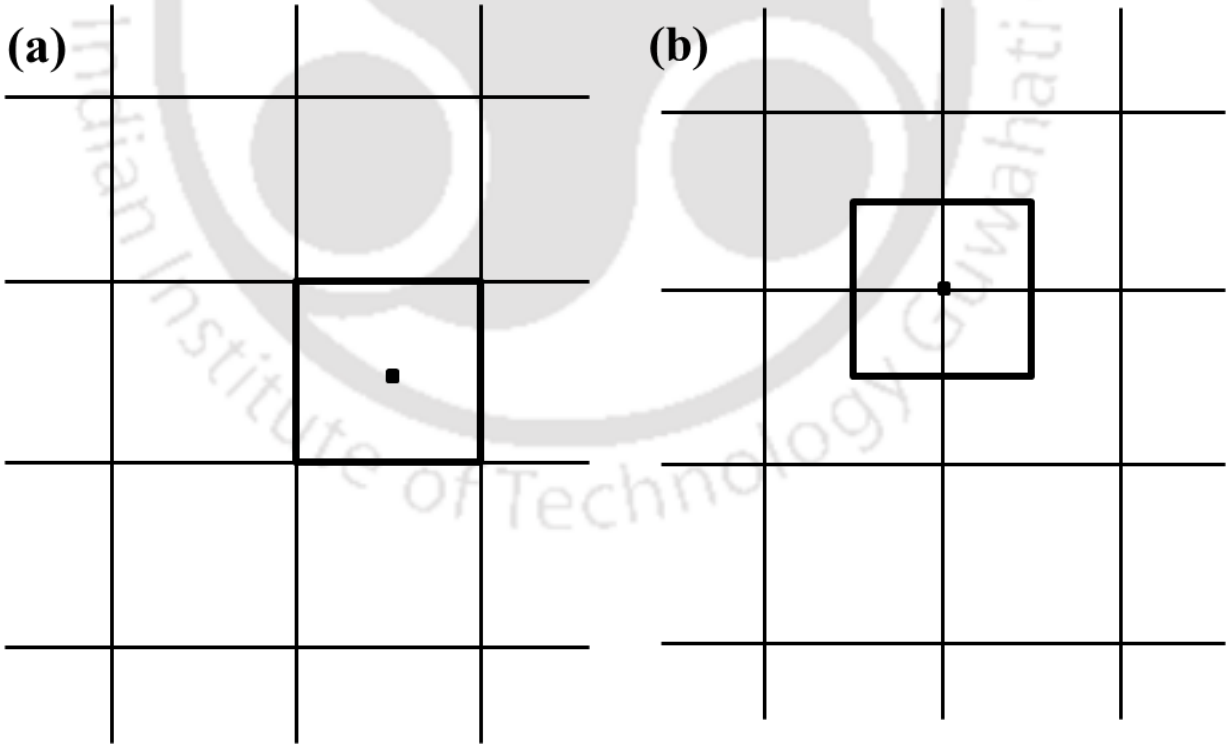

Figure 2.1: Representation of (a) cell centered and (b) cell vertex FVM scheme.

The volume integral of the Eq. (2.1) can be represented as

$$\int_{\Omega} \left(\frac{\partial U}{\partial t} + \frac{\partial F_I}{\partial x} + \frac{\partial G_I}{\partial y} - \frac{\partial F_v}{\partial x} - \frac{\partial G_v}{\partial y} + S + \alpha(S_I - S_v)\right) d\Omega = 0 \qquad (2.9)$$

Rearranging the above equation, we have

$$\int_{\Omega} \frac{\partial U}{\partial t} d\Omega = -\int_{\Omega} \left(\frac{\partial (F_I - F_v)}{\partial x} + \frac{\partial (G_I - G_v)}{\partial y} + S + \alpha(S_I - S_v)\right) d\Omega \qquad (2.10)$$

Now, left hand side of the above equation is

$$\int_{\Omega} \frac{\partial U}{\partial t} \partial\Omega = \frac{\partial}{\partial t} \int_{\Omega} U \, d\Omega$$

$$\int \frac{\partial U}{\partial t} \partial\Omega = \frac{d(\bar{U}\Omega)}{dt}$$

$$\int_{\Omega} \frac{\partial U}{\partial t} \partial\Omega = \Omega \frac{d\bar{U}}{dt} \qquad (2.11)$$

Where, $\bar{U} = \frac{\int_{\Omega} U d\Omega}{\int_{\Omega} d\Omega}$

Now, considering the right hand side of equation (2.10) we have,

$$\int_{\Omega} \left(\frac{\partial (F_I - F_v)}{\partial x} + \frac{\partial (G_I - G_v)}{\partial y} + S + \alpha(S_I - S_v)\right) d\Omega$$

$$= \int_{\Omega} \left(\nabla . (H_I - H_v) + S + \alpha(S_I - S_v)\right) d\Omega \qquad (2.12)$$

Where, $H_I = [F_I \quad G_I]$, $H_v = [F_v \quad G_v]$ and $\nabla = \left[\frac{\partial}{\partial x} \quad \frac{\partial}{\partial y}\right]$

Now, let us consider $H = H_I - H_v$

Therefore, from gauss divergence theorem we have,

$$\int_{\Omega} (\nabla . H) d\Omega = \int_{S} H . \hat{n} \, dS \qquad (2.13)$$

Where, $\hat{n} = [n_x \quad n_y]$

Here, $\hat{n}$ is the outward unit normal and its x and y component are represented by n_x and n_y respectively.

Further, Eq. (2.13) can be written as

$$\int_S H.\hat{n}\, dS = \sum_{J=1}^{n_f} H_J\, \hat{n}_J \Delta S_J = \sum_{J=1}^{n_f} H_{\perp J} \Delta S_J \qquad (2.14)$$

Here, for two-dimensional cases, ΔS_J is the face length of the control volume and $H_\perp$represent the total normal flux contributed by both viscous (H_v) as well as inviscid (H_I) fluxes. Hence,

$$H_\perp = H_{I\perp} - H_{v\perp} \qquad (2.15)$$

Where,

$$H_{I\perp} = \begin{bmatrix} \rho u_\perp \\ \rho u u_\perp + p n_x \\ \rho v u_\perp + p n_y \\ (\rho e + p) u_\perp \\ C_1 u_\perp \\ \vdots \\ C_{N-1} u_\perp \end{bmatrix} \qquad H_{v\perp} = \begin{bmatrix} 0 \\ n_x \tau_{xx} + n_y \tau_{xy} \\ n_x \tau_{yx} + n_y \tau_{yy} \\ n_x \Theta_x + n_y \Theta_y \\ 0 \\ \vdots \\ 0 \end{bmatrix}$$

Here, $u_\perp$is the contravariant velocity and can be written as

$$u_\perp = u.n_x + v.n_y \qquad (2.16)$$

In the energy equation, work done by viscous force and heat conduction are shown as

$$\Theta_x = u\tau_{xx} + v\tau_{xy} - q_x - \sum_{i=1}^{N} h_i C_i \bar{u}_i$$
$$\Theta_y = u\tau_{yx} + v\tau_{yy} - q_y - \sum_{i=1}^{N} h_i C_i \bar{v}_i \qquad (2.17)$$

Similar mathematical handling of the source terms in Eq. (2.10) as that of Eq. (2.11) yields

$$\int_\Omega \left(S + \propto (S_I - S_v)\right) d\Omega = \Omega \bar{S}_c + \alpha\, \Omega \bar{S} \qquad (2.18)$$

Where, $\bar{S} = \bar{S}_I - \bar{S}_v$

Therefore, from Eq. (2.11), (2.14) and (2.18) the modified integral form of the governing Eq. (2.10) can be rewritten as follows

$$\Omega_i \frac{d\bar{U}_i}{dt} + \sum_{J=1}^{n_f} H_{\perp J} \Delta S_J + \Omega_i \bar{S}_{ci} + \alpha \Omega_i \bar{S}_i = 0$$

$$\frac{d\bar{U}_i}{dt} = -\frac{1}{\Omega_i} \sum_{J=1}^{n_f} H_{\perp J} \Delta S_J - \bar{S}_{ci} - \alpha \bar{S}_i = R(\bar{U}_i) \qquad (2.19)$$

The above equation is the semi-discretized form of the governing equation.

2.5 Spatial discretization

The time marching solution of the Eq. (2.19) demands the calculations of the residual $R(\bar{U}_i)$. This is achieved by evaluating the convective and viscous fluxes at every face of the control volume. Hence, the methodology employed for evaluating these face-fluxes determines the solution accuracy. The methodology/schemes adopted for the flux calculations are discussed below.

2.5.1 Calculation of convective fluxes

For calculations of convective fluxes many upwind schemes such as Van-Leer scheme, Steger–Warming scheme, Rusanov scheme, Roe scheme, AUSM scheme etc. exists. These schemes broadly fall under two categories i.e. flux-vector splitting (FVS) and Flux difference splitting (FDS) schemes. All these schemes have their own merits and demerits. However, due to its robustness and accuracy, AUSM scheme [**37**,**137**] is one of the widely used schemes. In view of this, for the present study, the convective fluxes are computed using the Advection Upstream Splitting Method (AUSM)-delta hybrid [**138**] scheme, which is suitably extended to consider the non-equilibrium effects.

Here, the interface flux is given by

$$H_{I_\perp} = (M_n)_{I+\frac{1}{2}} \begin{Bmatrix} \rho a \\ \rho a u \\ \rho a v \\ (\rho E + p) a \\ C_i a \end{Bmatrix}_{L/R} + \begin{Bmatrix} 0 \\ p n_x \\ p n_y \\ 0 \\ 0 \end{Bmatrix}_{I+\frac{1}{2}}$$

Where,

$$(M_n)_{I+\frac{1}{2}} = M_{L^-} + M_{R^+}$$

$$(P)_{I+\frac{1}{2}} = p_{L^+} + p_{R^-}$$

$$(.)_{L/R} = \begin{cases} (.)_L & if \ \ (M_n)_{I+\frac{1}{2}} \geq 0 \\ (.)_R & otherwise \end{cases}$$

The pressure terms are calculated as follows

$$p_{L^+} = \begin{cases} p_L & if\ \ M_L \geq +1 \\ \dfrac{p_L}{4}\,(M_L+1)^2(2-M_L) & if\ \ |M_L| < 1 \\ 0 & if\ \ M_L \leq -1 \end{cases}$$

$$p_{R^-} = \begin{cases} 0 & if\ \ M_R \geq +1 \\ \dfrac{p_R}{4}\,(M_R-1)^2(2+M_R) & if\ \ |M_R| < 1 \\ p_R & if\ \ M_R \leq -1 \end{cases}$$

To avoid zero advection Mach number $(M_n)_{I+\frac{1}{2}}$ is modified in AUSM-delta as

$$\left|(M_n)_{I+\frac{1}{2}}\right| = \begin{cases} \left|(M_n)_{I+\frac{1}{2}}\right| & if\ \left|(M_n)_{I+\frac{1}{2}}\right| > \delta \\ \dfrac{(M_n)^2_{I+\frac{1}{2}} + \delta^2}{2\delta} & if\ \left|(M_n)_{I+\frac{1}{2}}\right| \leq \delta \end{cases}$$

2.5.2 Solution reconstruction for spatial accuracy

The solution with upwind schemes necessitates the computation of flow properties on both sides of the faces. For the first order accurate solution, this can be achieved by simply extrapolating the cell centroid properties to the face centers. However, enhancement in the accuracy of the results demands the adoption of a higher-order extrapolating technique. For the current study, the piece-wise linear reconstruction strategy proposed by Barth and Jespersen [**139**] is adopted to achieve the second-order spatial accuracy. This technique assumes the linear piece-wise distribution of the solution in the control volume. Hence, the left and right flow variables are given as follows,

$$U_{left} = U_{I_{cell}} + \psi\,(\nabla U_{I_{cell}}.\vec{r}_{left})$$

$$U_{right} = U_{J_{cell}} + \psi\,(\nabla U_{J_{cell}}.\vec{r}_{right})$$

Here, $\nabla U_{I_{cell}}$is the gradient of any flow property *U* at the cell center, which is defined as,

$$\nabla U_{I_{cell}} = \left[\frac{\partial U}{\partial x} \quad \frac{\partial U}{\partial y}\right]^T$$

Further, $\vec{r}_{left}$ and $\vec{r}_{right}$ are the normal vectors pointing towards the face centroid from the cell centroid as represented in fig. 2.2.

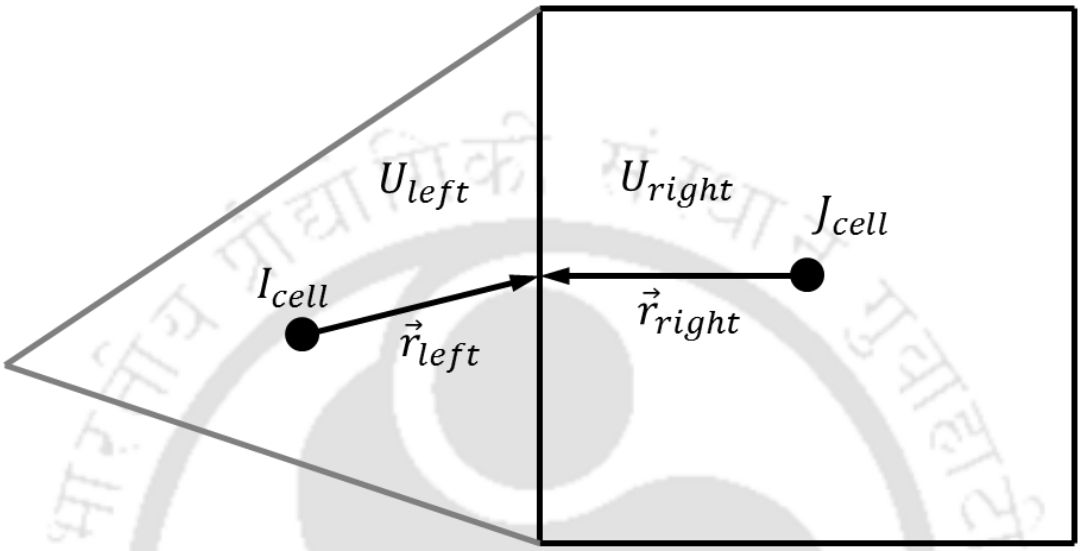

Figure 2.2: Linear reconstruction for the cell centered scheme.

Here, ψ is the limiter function. The absence of a limiter causes oscillations in the vicinity of discontinuities in the solution of second or higher-order schemes. This is commonly referred to as monotonicity loss. The use of a limiter generates non-increasing maxima and non-decreasing minima thereby ensuring monotonicity while reconstruction of left and right variable values. Due to its added advantage of the increase in convergence rate Venkatkrishnan limiter [**140**] is incorporated in the present solver. In this method, the limiter function is evaluated as

$$\psi = \begin{Bmatrix} \frac{1}{\Delta_2}\left[\frac{\left(\Delta_{1,max}^2 + \varepsilon^2\right)\Delta_2 + 2\Delta_2^2\Delta_{1,max}}{\Delta_{1,max}^2 + 2\Delta_2^2 + \Delta_{1,max}\Delta_2 + \varepsilon^2}\right] & if\ \Delta_2 > 0 \\ \frac{1}{\Delta_2}\left[\frac{\left(\Delta_{1,min}^2 + \varepsilon^2\right)\Delta_2 + 2\Delta_2^2\Delta_{1,min}}{\Delta_{1,min}^2 + 2\Delta_2^2 + \Delta_{1,min}\Delta_2 + \varepsilon^2}\right] & if\ \Delta_2 < 0 \\ 1 & if\ \Delta_2 = 0 \end{Bmatrix}$$

Here, $\Delta_{1,max} = U_{max} - U_{I_{cell}}$ and $\Delta_{1,min} = U_{min} - U_{I_{cell}}$. Where, U_{min} and U_{max} are the minimum and maximum of cell *I* and all adjacent cells *J*.

i.e.

$$U_{max} = max(U_{I_{cell}}, max_{J_{cell}} U_{J_{cell}})$$

$$U_{min} = min(U_{I_{cell}}, min_{J_{cell}} U_{J_{cell}})$$

Further, Δ_2 and ε^2 are evaluated as $\Delta_2 = \nabla U_{I_{cell}} . \vec{r}_{left}$ and $\varepsilon^2 = (K\Delta h)^3$. Where, *K* is a constant and Δh is the square root of the area in two-dimensional cases. The convergence rate and accuracy of the solution achieved with the Venkatakrishnan's limiter basically depends on the value of *K*. here, *K=0*, denotes full limiting, resulting in degradation in convergence rate. Whereas, a larger value of *K* lowers the solution accuracy. Therefore, care must be taken while choosing the value of *K*. For the present investigation, *K* is usually taken as 2. Here, the computation of the parameters involved in the limiter function demands extra time and storage i.e although the limiter used [**140**] improves solution accuracy and convergence significantly, the computational cost of calculating this limiter function is relatively high. However, these pitfalls of the limiter are accepted in order to improve solution accuracy and convergence rate.

2.5.3 Calculation of viscous fluxes

For viscous flux calculation at the face centroid, initially, the flow variables and their first derivative must be evaluated at the same location. To keep the data structure simple, the same control volume considered in convective flux calculation is used for viscous flux calculations as well. Here, the flow variables at the face centers are obtained by averaging the left cell and right cell values of the same quantity as shown below

$$U_{IJ_{face}} = \frac{1}{2}\left(U_{I_{cell}} + U_{J_{cell}}\right)$$

Further, to evaluate the derivative of the flow variables at the face centers, initially the derivative is calculated at the cell centroid using the gauss divergence theorem [**141**]

i.e.

$$\int_{\Omega} \nabla U \, d\Omega = \int_{S} U\hat{n} \, dS = \sum_{j=1}^{n_f} U_j . \vec{S}_j$$

Here, U is any variable and $\hat{n}$ is the outward surface normal of faces of the control volume Ω. Further, j represents the face index; n_f is the number of faces of a cell.

Therefore, assuming the ∇U to be constant over the control volume, we have

$$\nabla U = \frac{1}{\Omega}\left(\sum_{j=1}^{n_f} U_j.\vec{S}_j\right)$$

After obtaining the derivatives at the cell centroids, the same is calculated at the nodes by taking the average of all cells sharing the node. Finally, the values are evaluated at the face centers by taking the average of the node values.

2.6 Boundary Conditions

The selection of boundary conditions can make or break the solutions of a numerical investigation. Therefore, care must be taken while implementing it. The present study deals with different configurations subjected to supersonic and hypersonic flow. Further, both viscous and inviscid flow problems are considered in the study. In view of this, various boundary conditions considered in the present investigation are discussed below

2.6.1 Inviscid wall (free-slip) boundary condition

The absence of viscosity in inviscid flow allows the fluid to slip over the wall. Therefore, the tangential component of the velocity is non-zero at the boundary. Further, as the inviscid wall is considered to be impermeable, the normal component of velocity has to be zero. This suggests that the velocity adjacent to the inviscid boundary is tangent to the wall.

i.e.

$$\vec{V}.\hat{n} = 0$$

Where, $\vec{V}$ is the velocity and $\hat{n}$ is the unit normal vector.

Again, the normal flux crossing the wall in a symmetry boundary condition is zero. Therefore, though the symmetry and inviscid wall boundary conditions are physically different, they are mathematically the same. Here, the mirror or ghost cell approach is employed to implement the boundary condition.

Mirror or Ghost cell approach

In this approach, the tangential velocity and thermodynamics terms are extrapolated from the interior cells. Pressure can either be calculated by solving the momentum equation or can be

directly extrapolated from the interior cells. Further, the normal velocity component is handled separately. One of the main advantages of this approach is that it allows the execution of interior schemes on the boundary. A schematic of a ghost cell approach is shown in fig. 2.3 and mathematical relations are given below.

$$u_{normal_{ghost}} = -u_{normal_{interior}}$$

$$u_{parallel_{ghost}} = u_{parallel_{interior}}$$

$$p_{ghost} = p_{interior}$$

$$\rho_{ghost} = \rho_{interior}$$

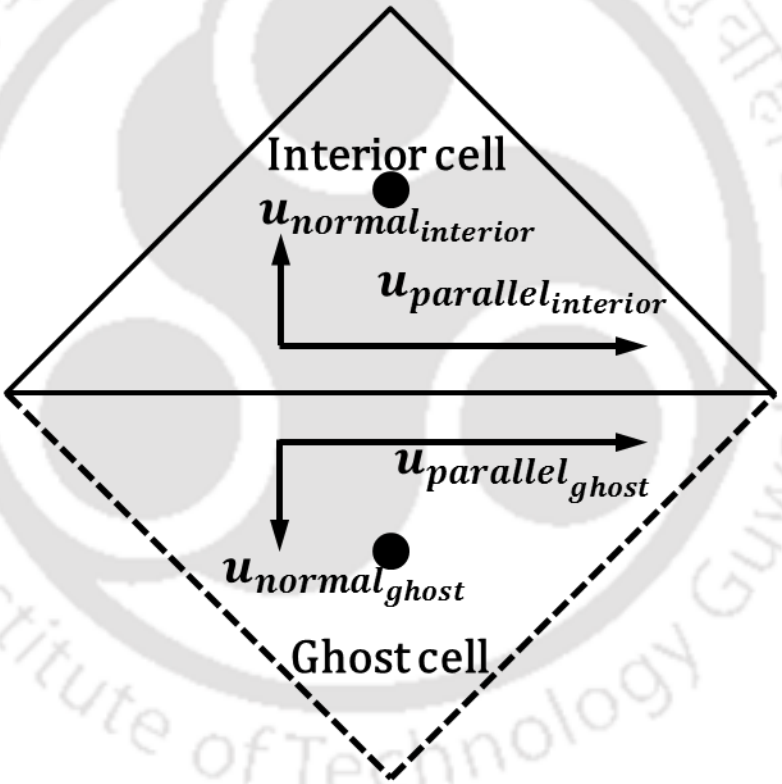

Figure 2.3: representation of Mirror or Ghost cell approach.

2.6.2 Viscous wall or no-slip boundary condition

The no-slip condition for the viscous wall approves zero normal as well as tangential velocity at the wall. Further, the present study considers isothermal wall boundary condition. Hence, the temperature is fixed at a given constant temperature and mass fractions are fixed at a known value. Again, the pressure is extrapolated from the immediate interior cell.

2.6.3 Supersonic inlet

The characteristic theory [**142**] confirms that all eigenvalues have an identical sign for supersonic inlet conditions. Hence, for this boundary condition, the flow quantities are set to the corresponding freestream values of a typical supersonic/hypersonic ground test or flight condition.

2.6.4 Supersonic outlet

For the problems considered in the present study, the flow leaving the computational domain is mostly supersonic. Therefore, a supersonic outlet boundary condition is incorporated, where there is no upstream influence of the outgoing flow. For example in the case of isentropic flow through a convergent-divergent nozzle having a supersonic/hypersonic outlet, decrement in the nozzle exit pressure does not change the mass flow rate, pressure, temperature etc. in the nozzle. Hence, any value of the exit pressure below the critical value, which is required for the flow to be isentropic, can give us the same flow variable variation in the nozzle. Hence, all the flow quantities at the boundary are extrapolated from the immediate interior location.

2.7 Temporal discretization

Along with spatial discretization, temporal discretization is carried out to obtain the system of algebraic equations from the governing partial differential equations. Basically, two types of approaches are employed for temporal discretization *viz*. explicit and implicit approaches. Both approaches have their own merits and demerits. Comparatively, an explicit approach is easier to implement. Further, the computational time per iteration is lesser and generally preferred for time-accurate solutions. However, in this approach, the maximum time step size is limited by the stability criteria. This smaller time step size may result in very high overall computational time especially in cases involving viscous flows. In contrast, the implicit approach is unconditionally stable. Hence, there is no restriction in the choice of the time step. Therefore, the solution can be

obtained at a lesser computational time. However, this approach is difficult to implement and due to greater time step size may not always be efficient in obtaining a time-accurate solution. Having said this, a mainly explicit approach is used for the present study. However, in the chemistry model, the larger source term changes the flow variables rapidly. The changes caused by the source term occur at much smaller time scales than those caused by the flow equations. This significantly increases the stiffness of the governing equations [**143**]. Therefore, explicit discretization of the source term would necessitate a very small time scale, resulting in a very high computational time or, in some cases, failure to find a correct solution [**144**]. To mitigate this, the source term is discretized with an implicit approach as proposed by Bussing and Murman [**145**]. Now, recalling Eq. (2.19), we have

$$\frac{d\bar{U}_i}{dt} = -\frac{1}{\Omega_i}\sum_{J=1}^{n_f} H_{\perp J}\Delta S_J - \bar{S}_{ci} - \alpha\bar{S}_i = R(\bar{U}_i)$$

Discretizing the above equation

$$\frac{\bar{U}_i^{n+1} - \bar{U}_i^n}{\Delta t} = -\frac{1}{\Omega_i}\left(\sum_{J=1}^{n_f} H_{\perp J}\Delta S_J\right)^n - {\bar{S}_{ci}}^{n+1} - \alpha{\bar{S}_i}^n \qquad (2.20)$$

Now, Linearizing the chemical source term by Newton's method

$${\bar{S}_{ci}}^{n+1} = {\bar{S}_{ci}}^n + \left(\frac{\partial\bar{S}_{ci}}{\partial\bar{U}}\right)^n \Delta\bar{U} + O(\Delta\bar{U})^2 \qquad (2.21)$$

Now, putting the value of ${\bar{S}_{ci}}^{n+1}$ in equation (2.20), we have

$$\frac{\bar{U}_i^{n+1} - \bar{U}_i^n}{\Delta t} = -\frac{1}{\Omega_i}\left(\sum_{J=1}^{n_f} H_{\perp J}\Delta S_J\right)^n - \left[{\bar{S}_{ci}}^n + \left(\frac{\partial\bar{S}_{ci}}{\partial\bar{U}}\right)^n \Delta\bar{U}\right] - \alpha{\bar{S}_i}^n \qquad (2.22)$$

$$\frac{\bar{U}_i^{n+1} - \bar{U}_i^n}{\Delta t} + \left(\frac{\partial\bar{S}_{ci}}{\partial\bar{U}}\right)^n \Delta\bar{U} = -\frac{1}{\Omega_i}\left(\sum_{J=1}^{n_f} H_{\perp J}\Delta S_J\right)^n - {\bar{S}_{ci}}^n - \alpha{\bar{S}_i}^n \qquad (2.23)$$

$$\frac{\bar{U}_i^{n+1} - \bar{U}_i^n}{\Delta t} + \left(\frac{\partial\bar{S}_{ci}}{\partial\bar{U}}\right)^n (\bar{U}_i^{n+1} - \bar{U}_i^n) = -\frac{1}{\Omega_i}\left(\sum_{J=1}^{n_f} H_{\perp J}\Delta S_J\right)^n - {\bar{S}_{ci}}^n - \alpha{\bar{S}_i}^n \qquad (2.24)$$

$$\frac{\bar{U}_i^{n+1} - \bar{U}_i^n}{\Delta t}\left[I + \Delta t\left(\frac{\partial\bar{S}_{ci}}{\partial\bar{U}}\right)^n\right] = -\frac{1}{\Omega_i}\left(\sum_{J=1}^{n_f} H_{\perp J}\Delta S_J\right)^n - {\bar{S}_{ci}}^n - \alpha{\bar{S}_i}^n \qquad (2.25)$$

Here, I and $\frac{\partial \bar{S}_{ci}}{\partial \bar{U}}$ are the identity and Jacobian matrix respectively. Further, the Jacobian matrix is evaluated as follows

$$\frac{\partial S_{ci}}{\partial U} = \begin{bmatrix} 0 & 0 & 0 & 0 & 0 & 0 & 0 & 0 \\ 0 & 0 & 0 & 0 & 0 & 0 & 0 & 0 \\ 0 & 0 & 0 & 0 & 0 & 0 & 0 & 0 \\ 0 & 0 & 0 & 0 & 0 & 0 & 0 & 0 \\ \frac{\partial S_1}{\partial \rho} & \frac{\partial S_1}{\partial (\rho u)} & \frac{\partial S_1}{\partial (\rho v)} & \frac{\partial S_1}{\partial (\rho E)} & \frac{\partial S_1}{\partial C_1} & . & . & \frac{\partial S_1}{\partial C_{N-1}} \\ \frac{\partial (.)}{\partial \rho} & \frac{\partial (.)}{\partial (\rho u)} & \frac{\partial (.)}{\partial (\rho v)} & \frac{\partial (.)}{\partial (\rho E)} & \frac{\partial (.)}{\partial C_1} & . & . & \frac{\partial (.)}{\partial C_{N-1}} \\ \frac{\partial (.)}{\partial \rho} & \frac{\partial (.)}{\partial (\rho u)} & \frac{\partial (.)}{\partial (\rho v)} & \frac{\partial (.)}{\partial (\rho E)} & \frac{\partial (.)}{\partial C_1} & . & . & \frac{\partial (.)}{\partial C_{N-1}} \\ \frac{\partial S_{N-1}}{\partial \rho} & \frac{\partial S_{N-1}}{\partial (\rho u)} & \frac{\partial S_{N-1}}{\partial (\rho v)} & \frac{\partial S_{N-1}}{\partial (\rho E)} & \frac{\partial S_{N-1}}{\partial C_1} & . & . & \frac{\partial S_{N-1}}{\partial C_{N-1}} \end{bmatrix}$$

Here, only the diagonal terms are considered and the rest terms are neglected as suggested by Bussing and Murman [**145**] and Joarder [**134**]. This eliminates the need to inverse the matrix and hence, reduces the per iteration computational time. However, these lead to minor discrepancies in the species concentration calculation. Again, different terms in the matrix can be obtained as follows

$$\left.\frac{\partial S_j}{\partial T}\right|_{C_{i,i=1,2..N-1}} = W_j \sum_{i=1}^{N_R} (v''_{ij} - v'_{ij}) \left[\frac{K_{fi}}{T} \left(m_{fi} + \frac{E_{fi}}{R_u T} \right) \prod_{l=1}^{N} n_l^{v'_{il}} - \frac{K_{bi}}{T} \left(m_{bi} + \frac{E_{bi}}{R_u T} \right) \prod_{l=1}^{N} n_l^{v''_{il}} \right]$$

$$\left.\frac{\partial S_j}{\partial \rho u}\right|_{\rho, \rho E, C_{i,i=1,2.....N-1}} = -\frac{u}{\rho C_v} \left.\frac{\partial S_j}{\partial T}\right|_{C_{i,i=1,2.....N-1}} \quad (2.26)$$

$$\left.\frac{\partial S_j}{\partial \rho E}\right|_{\rho, \rho u, C_{i,i=1,2.....N-1}} = \frac{1}{\rho C_v} \left.\frac{\partial S_j}{\partial T}\right|_{C_{i,i=1,2.....N-1}} \quad (2.27)$$

$$\left.\frac{\partial S_j}{\partial C_i}\right|_{\rho,\rho u,\rho E} = W_j \sum_{k=1}^{N_R}\left[(v''_{ki}-v'_{ki})\left(\frac{v'_{ki}K_{fk}}{C_i}\prod_{l=1}^{N} n_l^{v'_{kl}} - \frac{v''_{ki}K_{bk}}{C_i}\prod_{l=1}^{N} n_l^{v''_{kl}}\right)\right] - \frac{(e_i-e_N)}{\rho C_v}\left.\frac{\partial S_j}{\partial T}\right|_{C_{i,i=1,2....N-1}} \quad (2.28)$$

Therefore, with successive time marching the flow variables at the $(n+1)^{th}$ time level can be calculated by the known properties at n^{th} level from equation (2.25).

2.8 Flow models

Present investigation considers low as well as high enthalpy simulations at different flow mediums to demonstrate the effects of real gas in flow-field modifications. Hence, different flow models are considered in the present study. The following subsections give a brief overview of these flow models.

2.8.1 Perfect gas model

This flow model is based on the calorically and thermally perfect gas assumption. The perfect gas solver employed herein is the one developed by John et al. [**21**,**123**,**124**,**122**] . Here, the thermodynamic properties are correlated by the ideal gas equation (Eq.2.29)

$$p = \rho RT \quad (2.29)$$

Here, *p, ρ, T* is the pressure, density and temperature respectively and *R* represents the characteristic gas constant. Again, the specific internal energy *e*, enthalpy *h* and sonic speed *a* are evaluated as

$$e = \frac{RT}{(\gamma-1)}; h = \frac{\gamma RT}{(\gamma-1)}; a = \sqrt{\frac{\gamma p}{\rho}} \quad (2.30)$$

Here, γ represents specific heat ratio, which is independent of temperature and is considered 1.4 and 1.28 for Air and carbon-dioxide medium respectively.

Further, the viscosity calculation is based on the Sutherland's law for viscosity [**146**], which can be mathematically expressed as

$$\mu = \mu_{ref}\left(\frac{T}{T_{ref}}\right)^{3/2}\left(\frac{T_{ref}+S}{T+S}\right) \quad (2.31)$$

Here, μ is the dynamic viscosity and μ_{ref} is viscosity at the reference temperature T_{ref}. Further, S is the Sutherland's constant (110.56).

2.8.2 Real gas flow model

A high-speed flight often creates high-temperature regions where perfect gas assumptions become invalid. Hence, for better prediction of the flow-fields, simulation for such cases involving high enthalpy flows must be performed with a real gas solver instead of a perfect gas solver. The real gas solver employed for the present investigation is capable of simulating Earth and Mars atmosphere. The solver used for the Earth atmospheric simulation is the one considered by Desai et al. [**24**,**129**,**130**,**131**]. The real gas solver discussed in this chapter is the extension of the same. The extended version of the solver incorporates the reaction kinetics of both Earth as well as Mars atmosphere and is capable of simulating both the atmospheric condition.

2.9 Validation of the real gas solver

A final aspect in the development of any CFD solver is the validation process. Hence, the present in-house developed real gas solver is validated and tested against various numerical as well as experimental results. Here, separate inviscid and viscous cases are opted for the validation to confirm accuracy in each case.

2.9.1 Flow over a Ramp

Initially, inviscid steady-state simulations for supersonic/hypersonic flow over a ramp of different angles are performed to validate the in-house solver for test cases without reaction in the Martian atmosphere. When supersonic or hypersonic flow encounters a ramp, then the flow streamlines are deflected and an oblique shock is formed. There exist a unique relation between θ, β and M. The deflection angle θ can be specified as a unique function of M_1 and β as stated below [**25**].

$$tan\,\theta = 2cot\beta\left[\frac{M_1^2\sin^2\beta - 1}{M_1^2(\gamma + \cos 2\beta) + 2}\right] \quad 2.32$$

Where θ is the ram angle, β is the oblique shock angle; M_1 is the freestream Mach number and γ is the freestream specific heat ratio. Simulations are performed for three ramp angles (10º, 20º and 30º) and three Mach numbers (4, 5 and 7). The freestream conditions used for all those simulations have pressure 199.45 Pa and temperature 131.70 K. The computational domain along with boundary conditions used for 10º ramps is shown in the Fig. 2.4. For all cases, computational domain is meshed with uniform mesh of size 280x150.

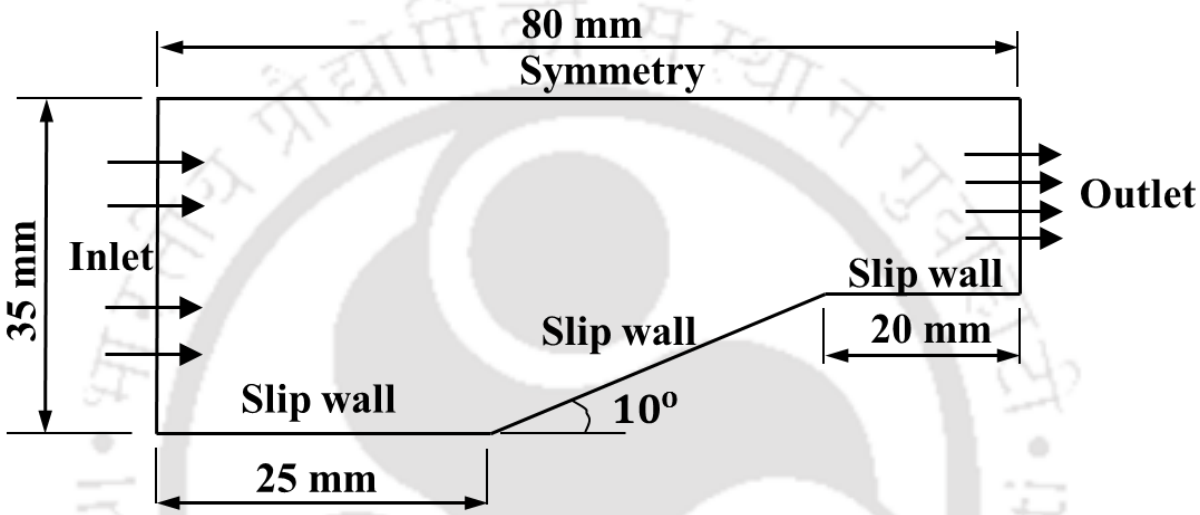

Figure 2.4: Computational Domain for flow over 10º ramp.

The pressure contour obtained from the simulation for Mach 4 and Mach 7 conditions is shown in Fig. 2.5 and the developed oblique shock can be clearly seen in the same figure**.** For the validation purpose, shock wave angle (β), pressure ratio and temperature ratio obtained from in-house solver for low enthalpy test conditions are compared with the analytical predictions [**25**]. This comparison is given in Table 2.3. From the table, it evident that the results of the in-house solver are in good agreement with the analytical predictions. For example, for the 10° ramp case, the error in predicting the shock wave angle is between 0.27% to 2.15%. Similarly, for the 20° case it is between 1.14% to 2.155%, while for the 30° it is 0.08% to 1.63%. Therefore, it can be concluded that in-house solver is validated successfully.

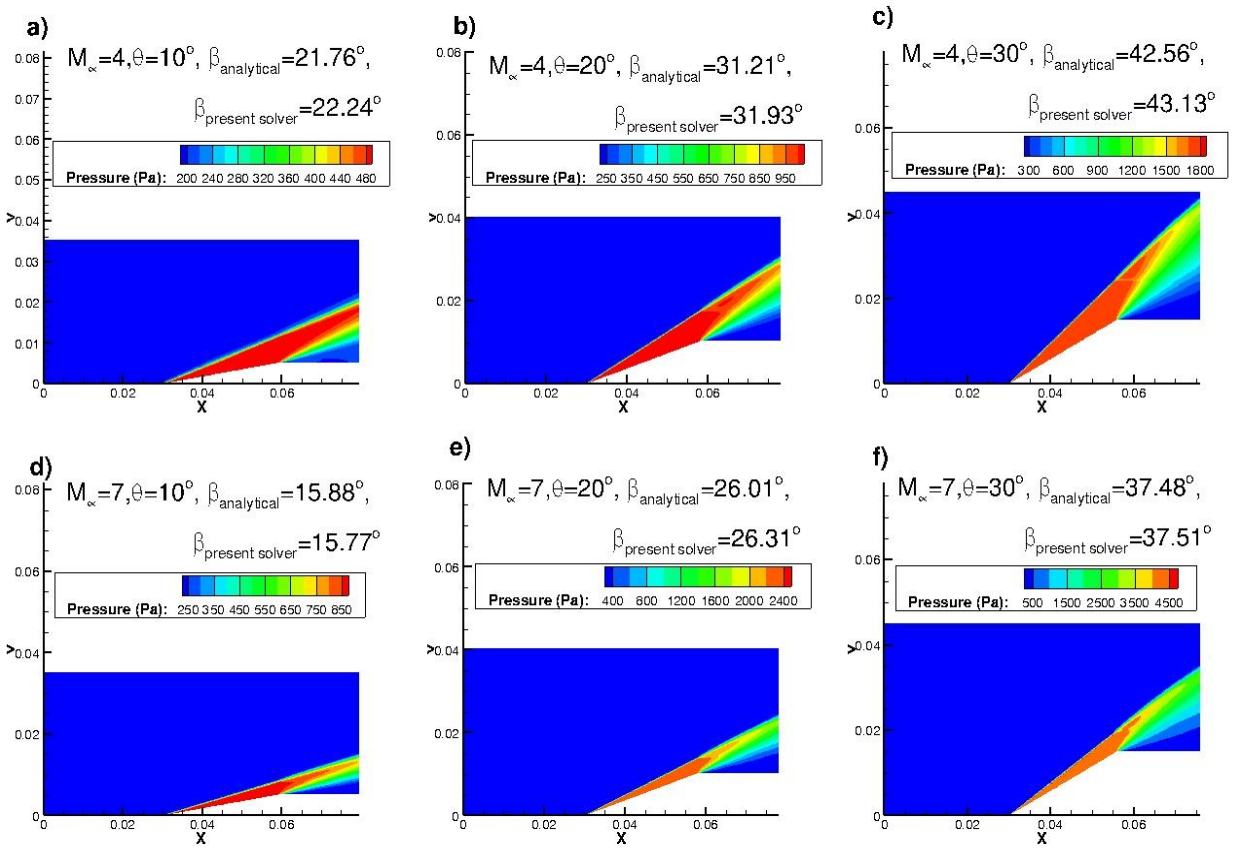

Figure 2.5: Pressure contours for Mach 4 and 7 flow over a ramp- Mars atmosphere.

Table 2.3: Shock wave angle, pressure ratio and temperature ratio at different deflection angles and Mach numbers - Mars atmosphere.

Ramp Angle	Mach Number	Shock wave angle (β)		Pressure ratio		Temperature ratio	
		Analytical	In-house Solver	Analytical	In-house Solver	Analytical	In-house Solver
10º	4	21.76	22.24	2.35	2.40	1.22	1.28
	5	18.90	18.85	2.82	2.95	1.29	1.38
	7	15.88	15.77	4.00	4.04	1.45	1.55
20º	4	31.21	31.93	4.70	4.92	1.54	1.67
	5	28.55	29.13	6.29	6.41	1.74	1.76
	7	26.01	26.31	10.46	11.24	2.26	2.53
30º	4	42.56	43.13	8.09	8.74	1.96	2.21
	5	39.86	40.52	11.41	12.24	2.38	2.64
	7	37.48	37.51	20.24	20.49	3.47	3.67

2.9.2 Flow over a sphere

Steady state inviscid simulations are carried out for flow of carbondioxide (CO_2) over a 10 mm diameter sphere in order to validate the present solver for reacting flow situations. Two test cases of velocity 2.122 Km/sec and 3.810 Km/sec are considered herein. The details of test conditions, given in the literature [**147**] and accounted for present simulations, are listed in Table 2.4. In the literature reported findings, non-dimensional shock stand off distance measured during experiments was compared with the CFD simulations based on two-temperature non-equilibrium model. Therefore, shock stand-off distance (Δ) obtained from present simulations, normalized with respect to the sphere radius (R), is compared with those experimental and computational results in Table 2.5. Encouraging agreement can be noticed in this table. For example, for the C10-1 case, the difference in the in-house results and experimental value of Liao et al. [**147**] is only 0.63% while it is 0.89% with the reported numerical results. The Fig. 2.6 shows the comparison of shock structure obtained from in-house solver with that of the literature [**147**] and it also asserts an excellent agreement. Again, the Pressure ratio (P_2/P_1) and temperature ratio (T_2/T_1) across the normal shock along the stagnation line are compared with analytical values in Table 2.6. Here, region 1 corresponds to flow upstream of the shock and region 2 corresponds to flow just downstream the shock. The analytical values are calculated from the normal shock relations [**25**]. From the table, it can be seen that though the pressure ratios are in acceptable range but the temperature ratios are significantly different. This is because of the real gas effects as the dissociation reaction become prominent in those temperatures. To demonstrate this fact, simulations are performed for low total temperature conditions by changing freestream temperature alone and keeping all other freestream parameter constant. It can be seen that, for lower total temperature simulations, the temperature ratio as well as pressure ratios approach the

corresponding analytical values. The minor difference this comparison is accounted to the fact that, simulations consider the change in specific heat values with temperature but the analytical expressions are derived for calorically perfect gas. Hence, it can be concluded that the in-house solver for Mars atmosphere has potential to simulate high temperature chemical reactions.

Table 2.4: Test conditions accounted for solver validation. **[**147**]**

Test	Flight speed (Km/sec)	Ambient pressure (KPa)	Ambient Temperature (K)
C10-1	2.122	12.300	292.10
C10-3	3.810	4.2100	292.70

Table 2.5: Comparison of the shock stand-off distance obtained from the In-house solver with that of the Liao et al. [**147**]

Test	Normalized shock stand-off Distance (Δ/R)		
	Liao et al. (2017)		In-house solver Numerical
	Experimental	Numerical	
C10-1	0.0795	0.0783	0.0790
C10-3	0.0553	0.0604	0.0590

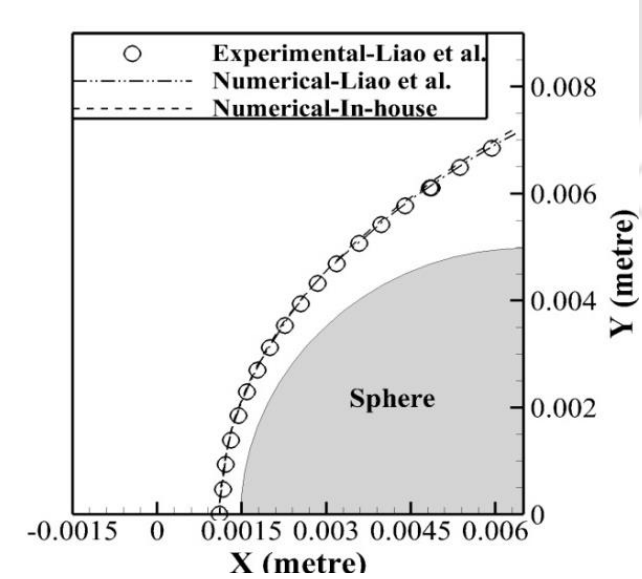

Figure 2.6: Comparison of the shock structure obtained from the In-house solver with that of the Liao et al. for Test C10-1 [**147**].

Table 2.6: Comparison of the Pressure ratio and Temperature ratio obtained from the In-house solver with that of the Analytical values **[**25**]**.

Freestream Temperature(K)	Freestream Mach no.	Freestream Pressure (Pa)	P_2/P_1		T_2/T_1	
			Analytical	In-house	Analytical	In-house
292.1	7.95	12300	70.84	73.33	9.68	7.22
100	7.95	12300	70.84	72.09	9.68	8.90

2.9.3 Ramp induced SWBLI test case

Viscous flow simulations for Earth atmosphere are performed to reproduce the experimental results of Mallinson [**148**]. The opted geometry consists of 0.085m long flat plate (L_c) and 18º ramp of 0.095m length as shown in Fig. 2.8. The initial conditions such as freestream Mach number (M_∞), freestream static temperature (T_∞), freestream static pressure (P_∞), freestream per unit Reynolds number (Re_∞) and wall temperature (T_w) considered for the purpose are listed in Table 2.8. Stanton number and surface pressure distribution obtained are compared with experimental results of Mallinson [**148**] and numerical results of Olejniczak & Candler [**149**] and of Deepak et al. [**150**] in Fig. 2.9. Here, the abscissa is normalized by the flat plate length (L_c) hence, the compression corner is located at X/L_c=1. The presently obtained Stanton number and pressure distributions agree very well with the literature reported real gas simulations of Olejniczak & Candler [**149**]. Upstream shift of upstream influence location and larger separation size are evident for the perfect gas simulations of Deepak et al. [**150**] due to absence of real gas effects [**131**]. Further, the experimental data is seen to agree very well with the real gas simulations up to the reattachment point, and downstream of this location, the values of numerically predicted heat flux peak and pressure peak are noticed to deviate from the experimental prediction. This discrepancy, which was also noticed by Deepak et al. [**150**] and Olejniczak & Candler [**149**] is expected to be due to turbulent reattachment as claimed in the literature.

Table 2.7: Initial conditions for validation with the experimental results [Mallinson **[**148**]**]

Atmosphere	M_∞	T_∞ (K)	P_∞ (Pa)	Re_∞ (m^{-1})	T_w (K)	Mass fractions
Earth	9.1	160	730	3220000	300	N_2- 0.78; O_2- 0.22

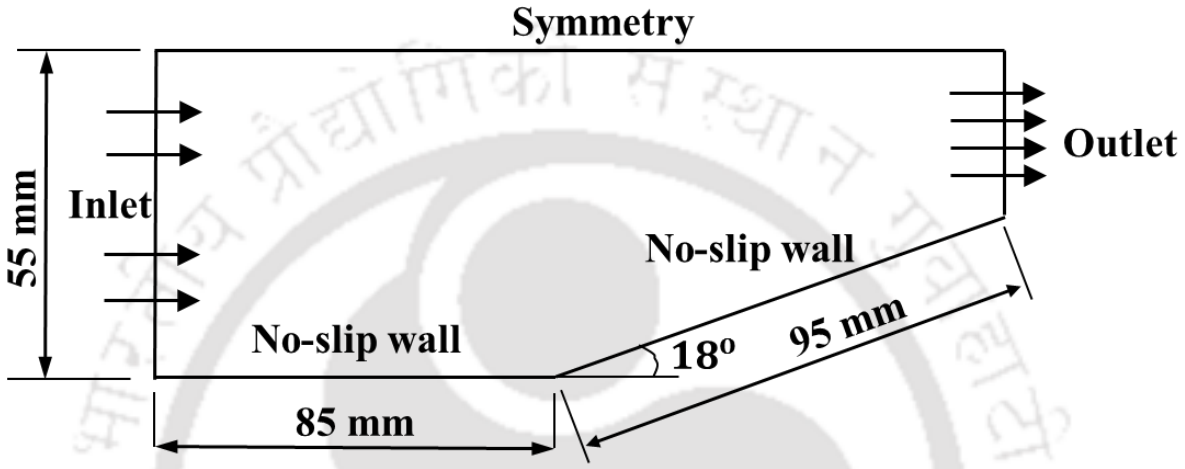

Figure 2.7: Computational domain along with the boundary conditions used to simulate the flow over ramp test case.

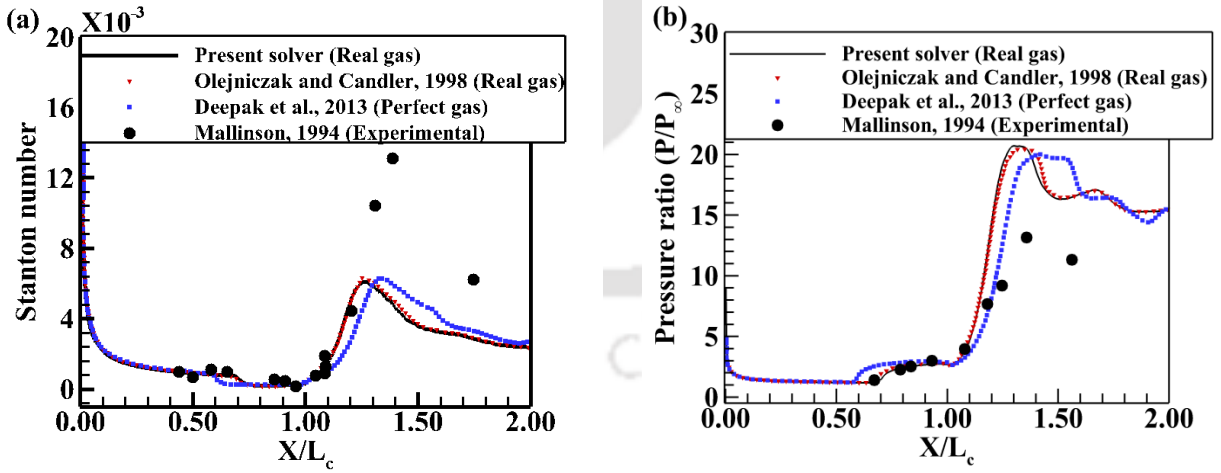

Figure 2.8: Comparison of surface properties obtained by In-house solver for Earth atmosphere with experimental results of Mallison **[**148**]** and numerical results of Olejniczak & Candler **[**149**]**; and Deepak et al. **[**150**]** (a) Stanton number; (b) Pressure distribution.

2.10 Conclusion

The cell-centered finite volume based two-dimensional (Axisymmetric) real gas solver capable of simulating Earth and Mars environment is successfully developed and tested with different test cases. To validate the solver for inviscid steady-state simulations in the Martian atmosphere at low enthalpy conditions, the supersonic/hypersonic flow over a ramp case is considered and the predictions are found to be in very good agreement with the analytical findings. Similarly, for a high enthalpy case, a carbon-dioxide flow over a sphere of radius 10 mm is taken into consideration. An excellent match is observed between the present simulation results and the reported experimental as well as numerical results. Further, for viscous flow, a ramp induced SWBLI problem is simulated. The computed pressure and Stanton number variation are compared with the literature reported experimental as well as numerical findings and are found to be in good agreement. These findings confirm that the present in-house developed solver is capable of performing steady state simulations in inviscid as well as viscous flow at low and high enthalpy conditions efficiently.

Chapter 3 : Performance Assessment of Energy Deposition Based Drag Reduction Technique for Earth and Mars Flight Conditions

Overview

In the present chapter, energy deposition based drag reduction technique is numerically investigated for Earth and Mars atmospheric conditions using in-house real gas Euler solver. Golden section search algorithm is successfully integrated with this CFD solver to evaluate the optimum amount of energy to be deposited for maximum power effectiveness. During these studies for spherical configuration, it has been noticed that, the amount of energy deposited corresponding to maximum power effectiveness is more for Mars case than the Earth case. Higher temperature dependence of specific heat for carbon dioxide than air is accounted to be responsible for this observation. Further, maximum power effectiveness is marked to be lower for carbon dioxide flow as compared to that for air flow. It has also been noticed that the performance of this technique gets lowered with increase in stagnation enthalpy of the flow, in either cases, with remarkable drop in case of air.

3.1 Introduction

The main hurdles faced in designing of hypersonic flights are the high drag and immense heating loads. To tackle the high heating load issues, back in the 1950's the use of blunt nose configurations came into practice as it was established that the stagnation point heat flux is inversely proportional to the square root of the nose radius. However, the blunt-nosed profile increases the wave drag which leads to more fuel consumption resulting in higher flight costs. Therefore, in subsequent time many drag reduction techniques were proposed such as attaching a forward spike [**5**], energy deposition at the upstream location [**11**,**12**], counter-flow jets [**9**,**10**]**,** etc. The present study focuses on energy deposition based drag reduction, which is an active method.

From the literatures (Chapter 1) related to energy deposition based drag reduction technique, it is noted that, various aspects of the energy deposition based drag reduction technique are explored by the researchers. Major focus of some explorations was to find optimum energy

deposition loaction [**14**,**16**,**22**]. Some studies also revealed the mechanisms of drag reduction due to enrgy deposition and effect of different parameters on it [**17**,**18**,**19**,**21**]. Further, it has also been noted that the power effectiveness of the deposited energy would be maximum only for a particular deposition amount. But, consideration of a formal optimization methodology, to arrive at the optimum amount of energy, is seen to be unattained. Hence, it is desirable to device a methodology to obtain the optimum strength of the energy spot for the known freestream conditions and geometry using a reliable optimization technique. Besides this, use of close to optimum solutions attained using numerous simulations or experiments are related to the Earth atmosphere or with air flow only. It is highly desirable to assess the usefulness of this drag reduction method in case of carbon dioxide medium or the Mars atmosphere. Different initiatives of Mars exploration all over the globe [**151**] provide the necessary impetus to explore energy deposition studies in Mars atmosphere. Therefore, major objective of present studies is to carry out a comparative assessment of this technique with air and carbon dioxide mediums or for the Earth and the Mars atmospheric conditions respectively. Thus, proposed integration of optimization process in the high fidelity framework would give the practical difference in maximum power effectiveness and optimum amount of energy required to deposit for air and carbon dioxide flow conditions. In continuation to this, studies for high enthalpy effect are also planned for both the planetary conditions. In view of this, in-house CFD solver, which accounts for reactions and specific heat variation with temperature, is employed to achieve the desired goals. The high fidelity optimization framework and the results are discussed in following sections.

3.2 Optimization Process and Its Integration with CFD Solvers

Many conventional or advanced soft computing techniques are available in the literature which can be thought for the present integration with CFD solver. But, considering simplicity and effectiveness, bracketing method namely “golden section search method” is considered herein. Broadly, algorithm of the golden section search method can be classified into two parts. One part deals with bracketing the lower and upper limits of the manima/maxima to be determined. Then second part follows an iterative process within those limits to estimate the desired optimum value of the objective function.

One of the objectives of present investigations is to determine the peak power effectiveness, which is defined by Eq. 3.1.

$$P = \frac{(D_0 - D)U_\infty}{Q} \tag{3.1}$$

Here, D is the drag force with energy deposition, D_0 is the drag force without energy deposition case, U_∞ is the freestream velocity and Q is the absolute strength of energy spot. For the present study, power effectiveness is the objective function whose maximum value needs to be calculated. In this phase, the in-house CFD solver, coupled with the golden section search method, are employed to obtain the peak power effectiveness for different cases. The detailed algorithm of this integration is shown in Fig. 3.1. As discussed in the algorithm, first of all, lower (Q_l) and upper (Q_u) limits of energy source strength, which bracket the peak power effectiveness, are evaluated. Then two intermediate values of source strengths (Q_1 and Q_2) are calculated. Simulations are carried out for these (Q_l, Q_u, Q_1 and Q_2) energy source strengths and corresponding drag values are computed by integrating the surface pressure. Further, the power effectiveness for the known source strength (Q) is calculated using Eq. 3.1. Then the Power Effectiveness value P_1 corresponding to Q_1 amount of heat addition and P_2 corresponding to Q_2 amount of heat addition are compared with each other. If $P_1 > P_2$, the region on the left hand side of 'Q_2' is eliminated and lower limit is updated as Q_l=Q_2. The upper limit is maintained same and the second intermediate point Q_2 is updated to take value of Q_1. Finally, the value of first intermediate point 'Q_1' is re-calculated. If $P_2 > P_1$, the region on the right of 'Q_1' is eliminated and the upper limit is updated as Q_u=Q_1. The lower limit is maintained same and the first intermediate point 'Q_1' is updated to take value of 'Q_2'. Then, the value of second intermediate point 'Q_2'is re-calculated. The process continues until $Q_u - Q_l < \varepsilon$. Here, 'ε' is the stopping criteria and is usually a very small number. When the stopping criterion is attained, the required maximum is considered to be at $\frac{Q_u+Q_l}{2}$. In the present case, stopping criterion is maintained as about 1 Watt. Thus, CFD simulations are carried out for both Earth and Mars atmospheric conditions and also for different freestream stagnation enthalpies.

3.3 Results and Discussion

In the present study, hypersonic flow over a sphere of radius 30mm is considered. For energy deposition cases, energy source is fixed on the stagnation streamline, upstream of the

stagnation point, having its center at a distance equal to the diameter of the sphere (60mm). This source is considered to have uniform intensity over a spherical region of radius 1mm. The schematic diagram describing the configuration, computational domain and associated boundary conditions is shown in the Fig. 3.2 (a).

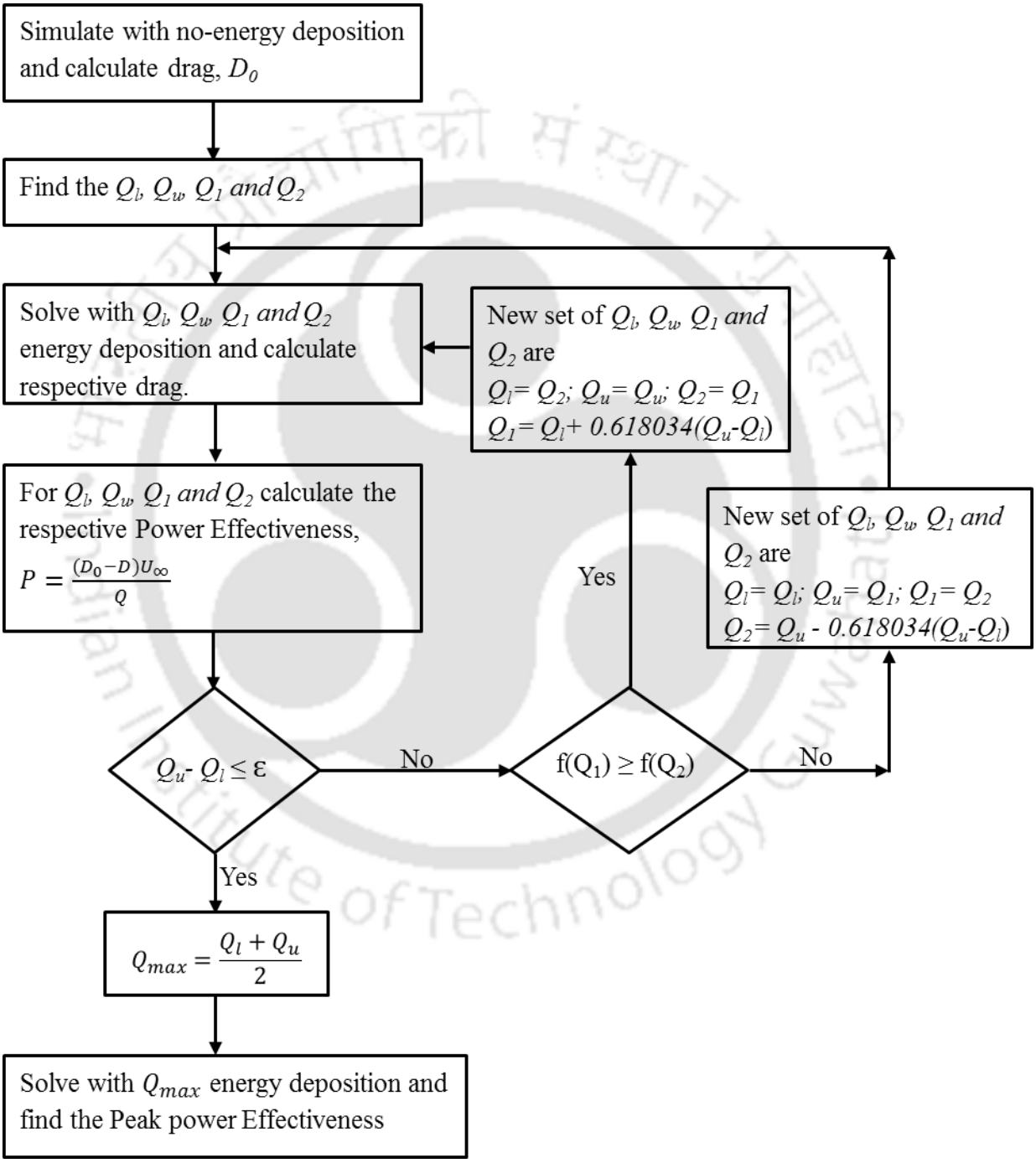

Figure 3.1: Algorithm used to find the peak power effectiveness.

3.3.1 Effect of heat addition in Earth and Mars atmosphere

Initially inviscid steady state simulations are carried out for 5.5W of energy deposition in air medium with different grids. Figure 3.2 (b) and (c) respectively show the surface pressure distribution and residue history for different grid sizes. It can be seen from this figure that, there is not much change in the pressure distribution after 250x120 grid resolution. Hence, mesh of size 250x120 (Δx_{min}=0.0004m and Δy_{min}=0.00039m) is opted. Such mesh independence results are considered for further analysis. The choice of the freestream conditions is listed in Table 3.1.

It is known that the high speed flow over a blunt nosed configuration produces bow shock in front of the object, which leads to high drag. Energy deposition ahead of such configurations alters the flow field and recasts the shock structure which in turn establishes an upstream low pressure recirculation region ahead of the body. Due to these alterations, pressure distribution on the surface of the object changes and it leads to reduction in drag. However, the amount of drag reduction depends on the reformed shock strengths for known flow properties and given strength of energy spot. In view of this, Earth as well as Mars atmospheric conditions are considered for the present study.

As discussed earlier, Golden section search method, in integration with CFD solvers, is used for the optimization. For this purpose, the algorithm illustrated in Fig. 3.1 is adopted. The first step towards this method is to find the lower (Q_l) and upper (Q_u) limit values of the energy source strength which bracket the peak power effectiveness. It has been found that, the lower limit (Q_l) for both Earth as well as Mars atmosphere is 5.5W. But the upper limit (Q_u) for Earth and Mars atmosphere are 9.5 W and 17.5W respectively. Considering these values as the initial lower and upper limits, CFD simulations are further continued. However, Mach contours, for some intermediate strength of energy spot, in case of simulations for Mars atmosphere, are shown in the Fig. 3.3. It is evident from the contour that, for lower strength of the energy spot, appearances of the oblique shock gets delayed. Further, the shock attachment point on the surface of the sphere is found to be upstream for lower energy spot strength. It can also be seen from the figures that the separation bubble formed in the presence of re-casted oblique shocks is smaller in case of energy spot of lower strength and this restructuring results in comparatively higher value of pressure in the recirculation region. Furthermore, from the surface pressure distribution shown in Fig. 3.3(b), it is evident that, for lower value of energy spot strength, the

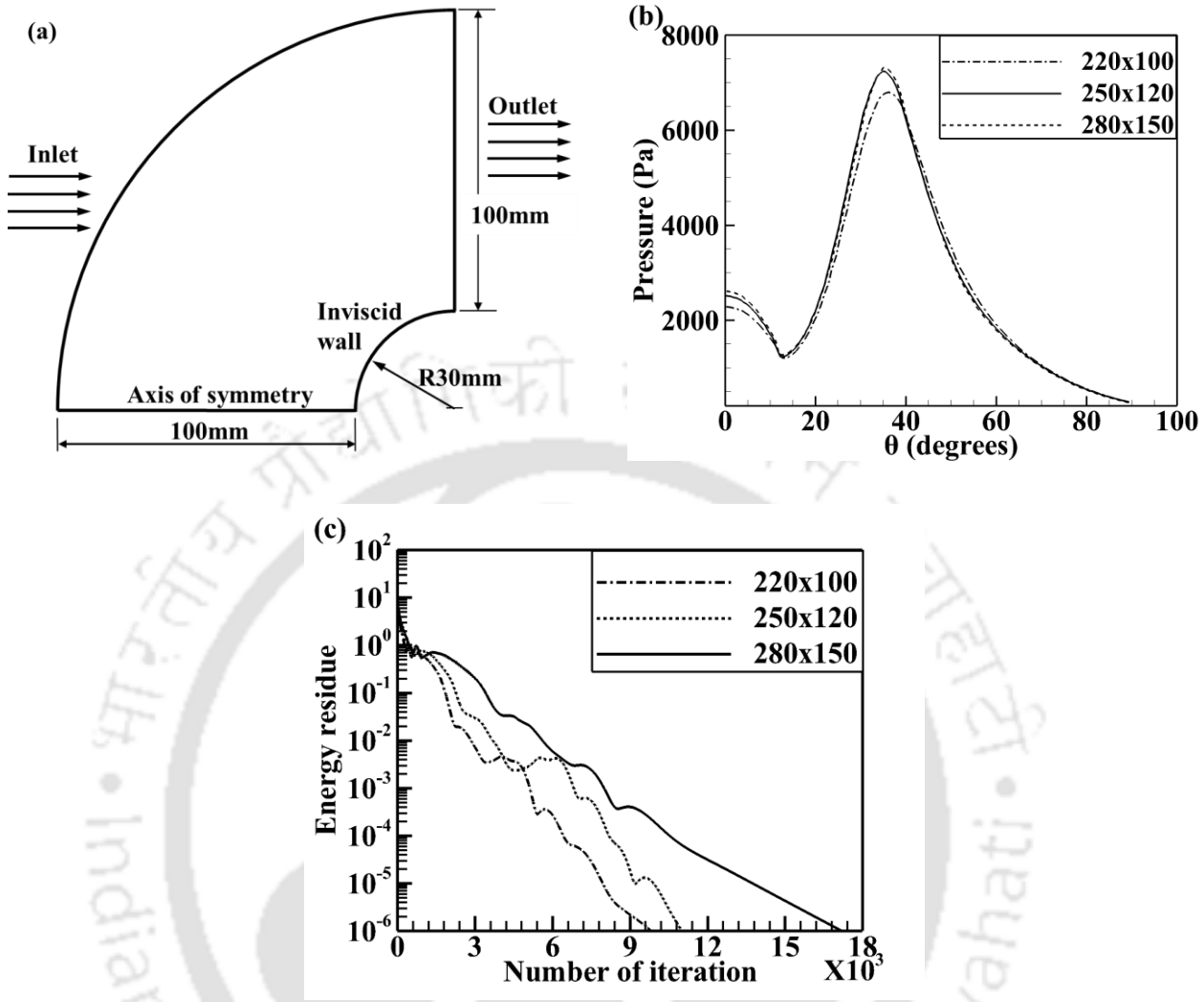

Figure 3.2: (a) Schematic of computational domain and (b) Surface pressure distributions (c) residue history for different grid sizes.

Table 3.1: Details of the freestream conditions used for Energy deposition case.

Atmosphere	Mach number	Pressure (Pa)	Temperature (K)
Earth atmosphere	8	89	113
Mars atmosphere	8	89	113

pressure at the shock attachment point is higher. Again, from Fig. 3.3 (c), it is noted that the amount of drag reduction increases with the increase in the absolute amount of energy deposition.

A similar conclusion can be drawn from the Mach contours, surface pressure distribution, and Drag reduction plot for Earth atmosphere shown in Fig. 3.4 (a) (b) and (c) respectively.

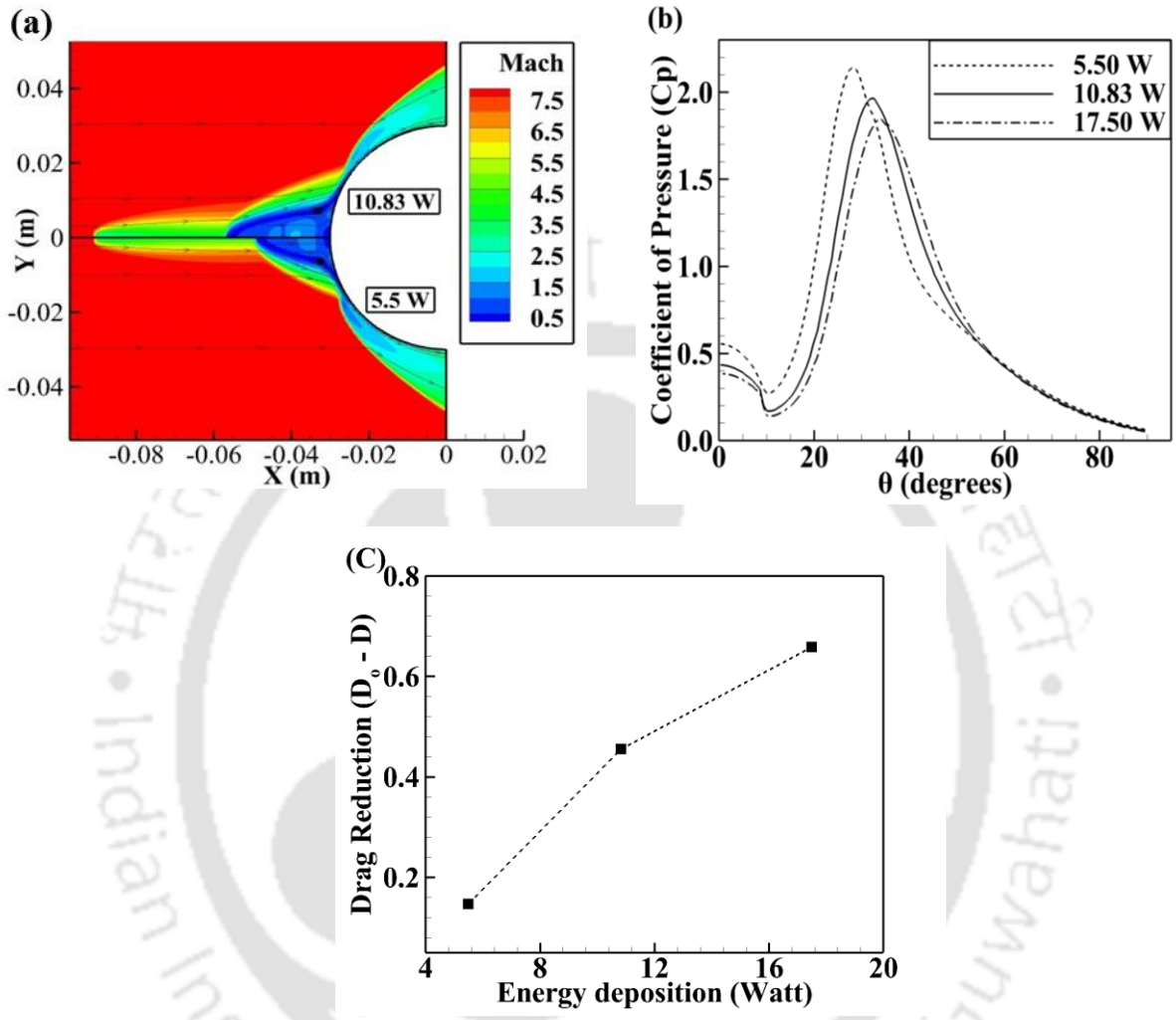

Figure 3.3: Comparison of properties at different energy spot strength obtained with Mars atmospheric simulations; (a) Mach contour, (b) Pressure distribution and (c) Drag reduction.

Figure 3.5(a) and (b) respectively show the variation of power effectiveness with the strength of energy source, obtained finally from present high fidelity integration for Mars and Earth atmosphere. It can be noticed here that, the amount of drag reduction increases with increase in energy spot strength for both the cases.

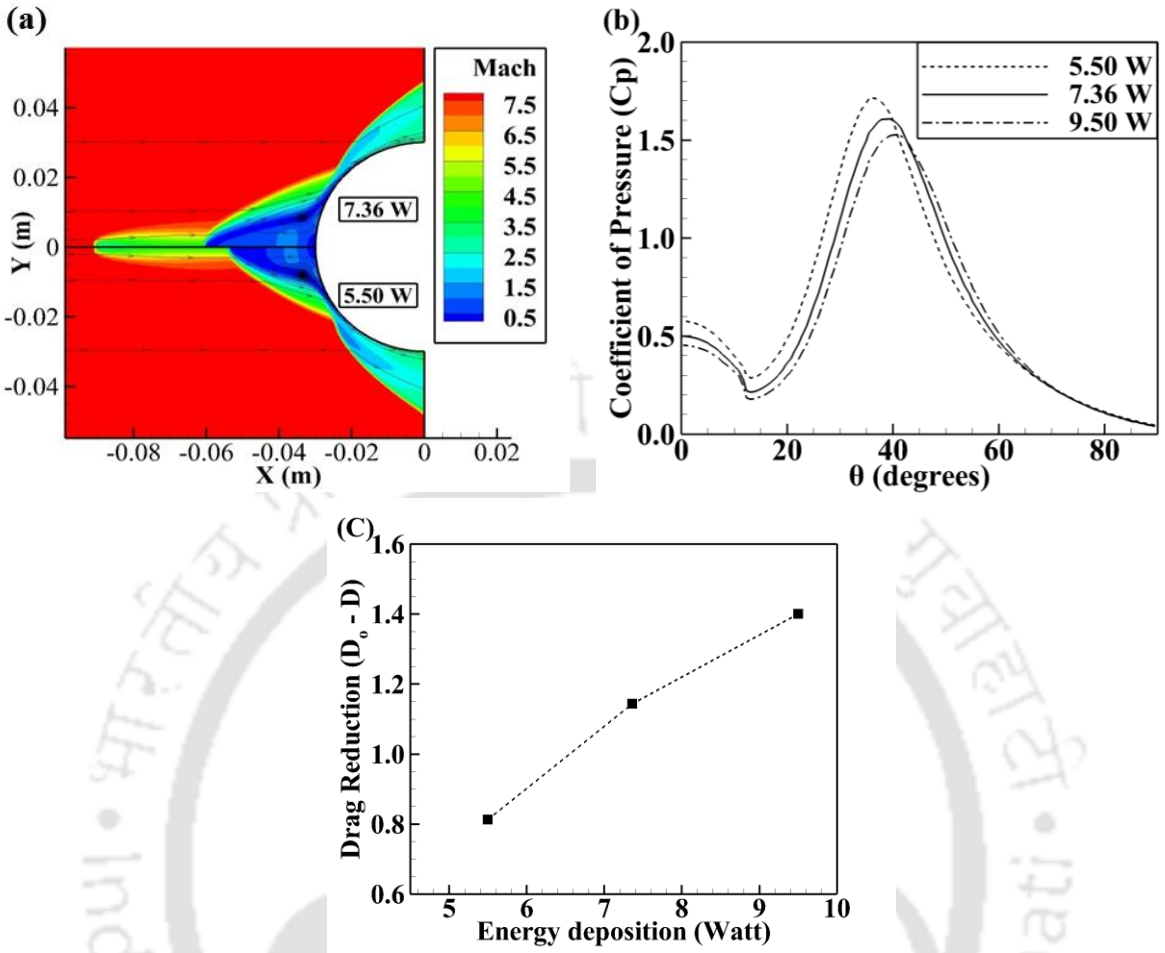

Figure 3.4: Comparison of properties at different energy spot strength obtained with Earth atmospheric simulations; (a) Mach contour, (b) Pressure distribution and (c) Drag reduction.

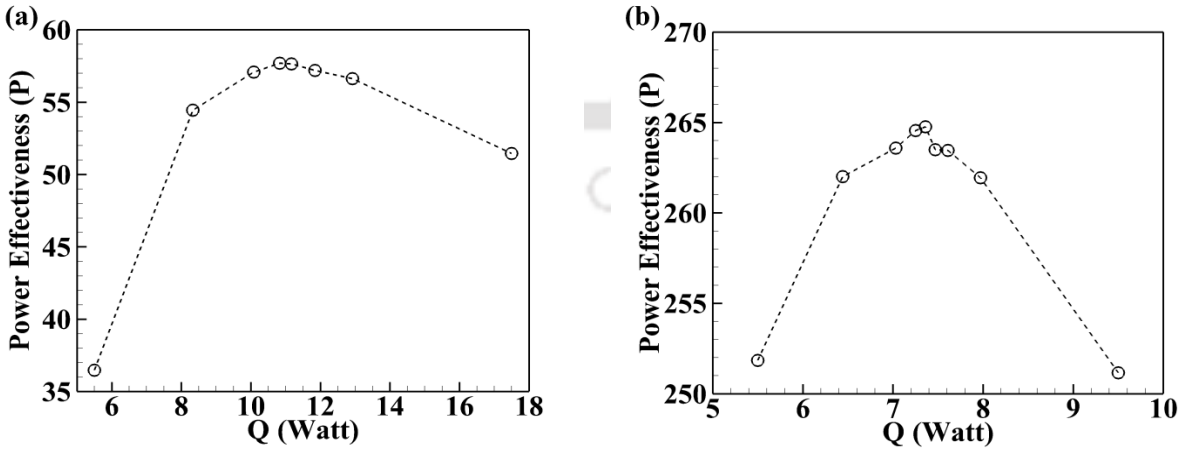

Figure 3.5: Variation of power effectiveness with strength of energy source used as lower and upper limits (a) Mars atmosphere and (b) Earth atmosphere.

However, power effectiveness (P), which portrays practical use of deposited energy in reducing the drag, increases with initial increment in strength of the energy source until it attains a peak value for particular source strength. But then, it starts to decrease with further increment in the strength of the source. Thus, optimum value of power effectiveness and its respective energy spot strength is computed successfully as an outcome of present integration. It has been found that the peak power effectiveness for Mars atmosphere case is 57.69 and the corresponding strength of the energy source is 10.83W. The peak power effectiveness for Earth atmosphere case is found to be higher than the Mars atmosphere case i.e. 264.76. However, the absolute strength of energy spot required to attain the same is lower for air and is found to be 7.36W. Although, added energy introduces dissociation reactions in each case, most of the flow is found to be recombined before reaching the stagnation point. Therefore, the observed difference in requirement of absolute energy in order to attain the peak power effectiveness is attributed to the difference in value of specific heat for Earth and Mars atmospheres at a given temperature. Due to this fact, the temperature rise for Mars atmosphere case is less compared to the Earth atmosphere case (Fig. 3.6(a)), for same freestream parameters and same strength of energy spot (10.83W). So, the disturbance created due to the energy deposition is comparatively lesser strong with carbon dioxide medium and it leads to higher approach Mach number (Fig. 3.6(a)) as compared to air medium. Such high Mach number flow, downstream of the energy spot, fetches high drag, which can be justified from the surface pressure variation and drag reduction plots shown in Fig. 3.7. So, the Mars atmospheric case demands higher value of absolute energy strength to achieve better power effectiveness. Furthermore, for the same value of energy source strength, the freestream velocity for Mars atmosphere case (1367.93m/s) is less than the Earth atmospheric case (1703.94m/s). Hence, for Mars atmosphere case, amount of drag reduction as well as the freestream velocity is comparatively less. Therefore, from the expression of power effectiveness, for the same hot spot strength or denominator in both the cases, the numerator is comparatively small for Mars atmosphere case. Hence, the power effectiveness of the Mars atmosphere case is less compared to the Earth atmosphere case for same strength of energy source.

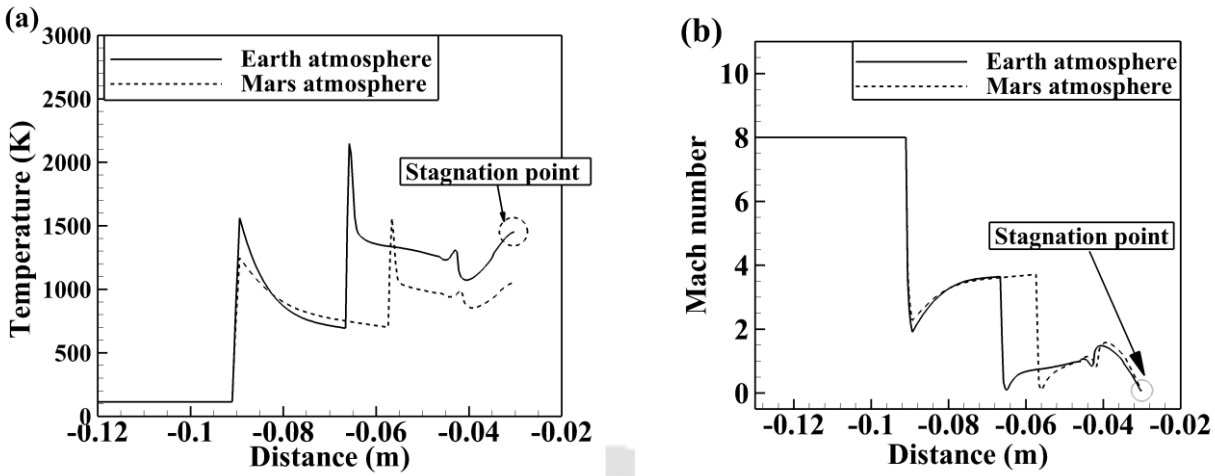

Figure 3.6: Variation of different properties along the stagnation line for 10.83 W of energy deposition (a) Temperature and (b) Mach number.

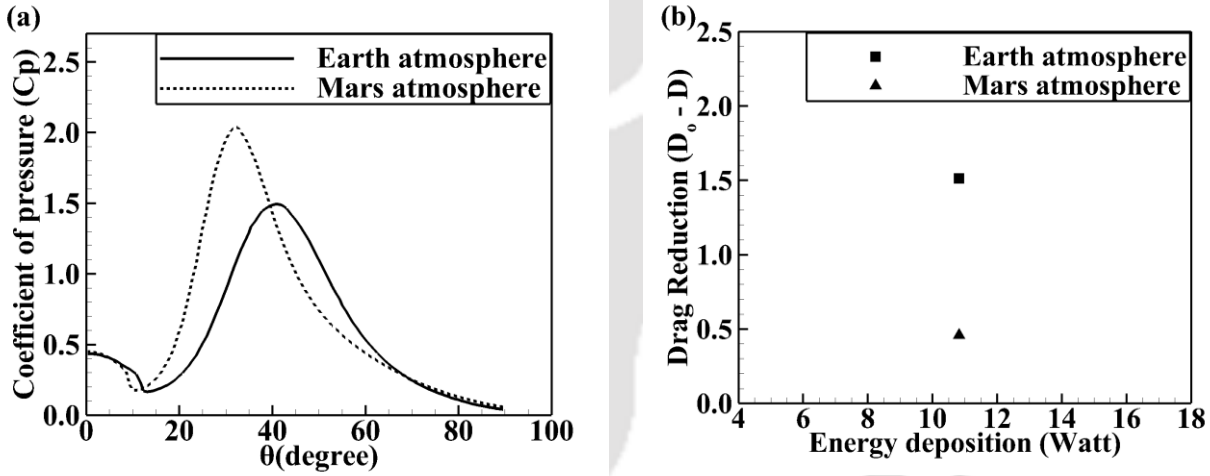

Figure 3.7: (a) Surface pressure distribution and (b) Drag reduction for different flow medium with 10.83W of energy deposition.

3.3.2 Effect of freestream stagnation enthalpy

Present study is extended to investigate the effect of stagnation enthalpy on the energy deposition based drag reduction technique. Simulations are carried out at different stagnation enthalpies for both Earth and Mars environments. The stagnation enthalpies are varied in a range of 1.56MJ/kg to 10.80MJ/kg for Earth atmosphere and 1.03MJ/kg to 6.83MJ/kg for Mars atmosphere. This variation is achieved by changing the freestream temperature alone and keeping the other freestream parameters like Mach number and pressure same as that mentioned in Table

3.1. Upper limit of this variation is set by accounting the maximum allowable temperature limit for specific heat variation.

Simulations for each stagnation enthalpy case are performed with the high fidelity approach given in Fig. 3.1. Therefore, outcome of all these computations is the peak power effectiveness and corresponding energy spot strength for every freestream stagnation enthalpy. The absolute strength of energy spots required to attain the peak power effectiveness at different enthalpies is plotted in Fig. 3.8(a). The peak power effectiveness obtained from the present simulations is plotted against their respective stagnation enthalpies in Fig. 3.8(b).

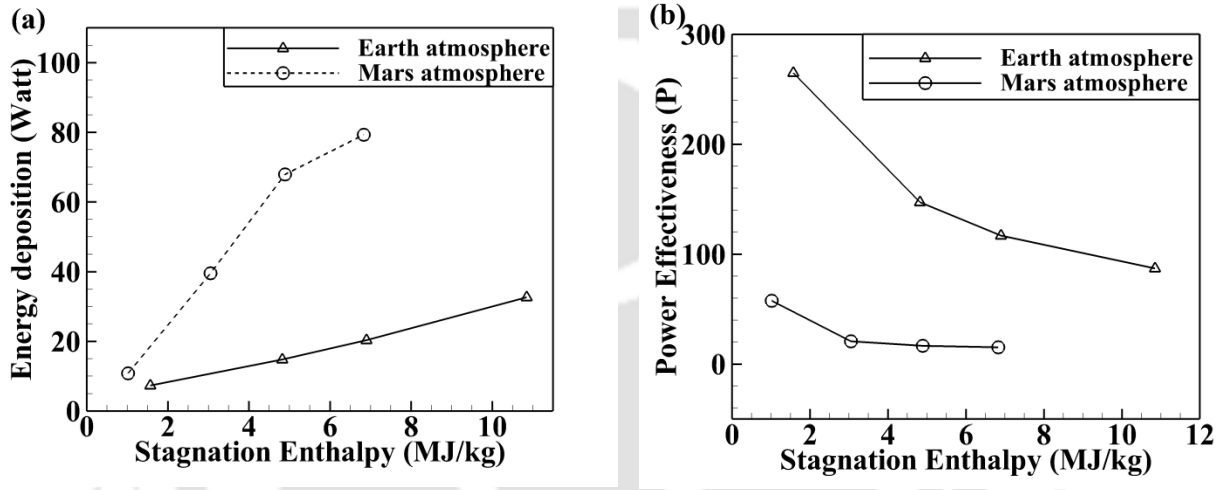

Figure 3.8: Effect of variation in enthalpy on (a) Absolute energy spot strength required to attain the peak power effectiveness and (b) Peak power effectiveness.

It is evident from the Fig. 3.8(b) that, for both Earth and Mars atmospheres, the peak power effectiveness decreases with increase in stagnation enthalpies. This is mainly due to the fact that, in general, for the same amount of heat addition, the power effectiveness decreases with increase in stagnation enthalpies. Figure 3.9 shows the variation of power effectiveness with stagnation enthalpies for 7.36W of energy addition in case of air medium. These trends can be well interpreted in one more way using the intensity of disturbance created due to the energy addition. Such energy spot intensity can be quantified in terms of temperature rise at the hot spot location. So, in the same figure, the non-dimensional peak temperature of the hot spot is plotted against their respective stagnation enthalpies. It is evident from the Fig. 3.9 that the temperature rise is less for higher values of stagnation enthalpy. Therefore it forms a weaker disturbance. As a result of this, Mach number downstream of the energy spot remains high, (Fig. 3.10(a)) and

pressure on the sphere surface increases (Fig. 3.10(b)); which eventually reduces the percentage drag reduction. This explanation for one sample heat source strength is sufficient to analyze the effect of stagnation enthalpy on optimum strength of energy spot (fig. 3.8(a)). Thus, it is evident that the optimum strength of the hot spot rises with increase in stagnation enthalpy. Further, the increased requirement of energy for a specific amount of drag reduction leads to reduced power effectiveness in both the cases.

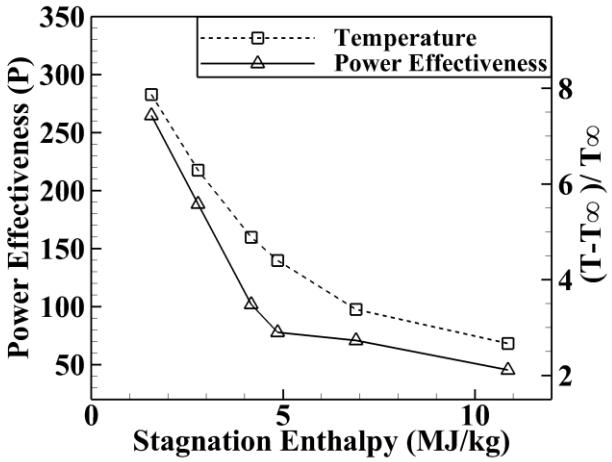

Figure 3.9: Variation of power effectiveness and non-dimensional temperature with stagnation enthalpies for 7.36W of energy deposition for Air medium.

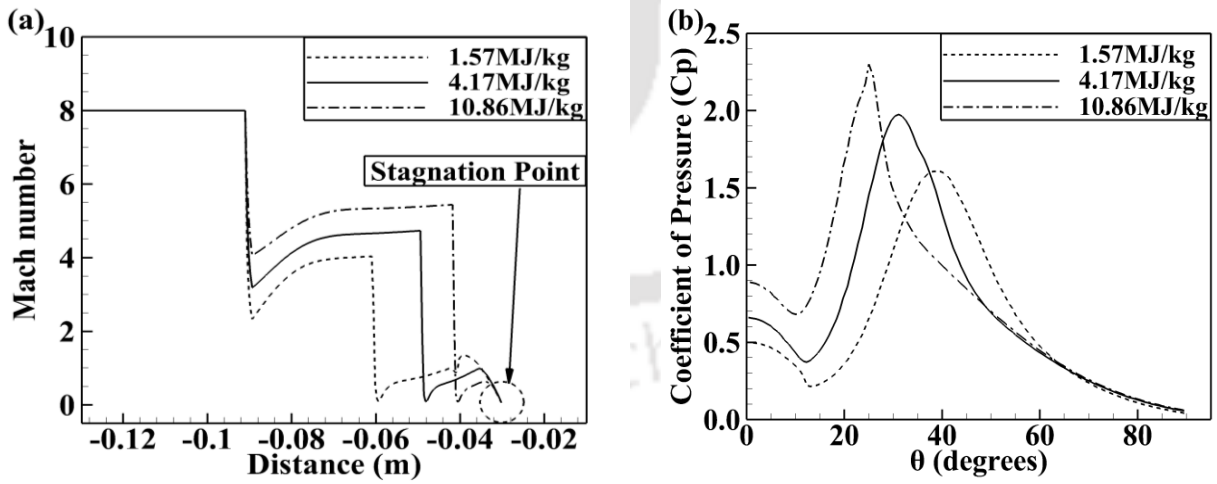

Figure 3.10: Effect of variation in enthalpies for 7.36W of energy deposition for Air medium on (a) Mach number along the stagnation line and (b) Pressure distributions on the surface.

It must also be noted from Fig. 3.8 (b) that, the peak power effectiveness for carbon dioxide medium is always lower than that of air for any stagnation enthalpy. Again, it has its reference with different specific heat variations with temperature of both the mediums. This effect is seen to be dominant at higher enthalpies as well. Due to this effect, optimum strengths of energy spot, for carbon dioxide test cases, are noted to be higher at high enthalpies than those for air flow test cases (Fig. 3.8 (a)). Further, the magnitude of drag reduction is less for carbon dioxide for any of the present enthalpy cases (Fig. 3.11) and it has led to lower magnitude of the peak power effectiveness for Mars flight conditions than that of air (Fig. 3.8 (b)). Larger increase in specific heat with temperature for carbon dioxide medium is again marked responsible here. An important thing to note from Fig. 3.8 (b) is that, there is minor change in peak power effectiveness at higher enthalpies for Martian simulations. This observation can be justified using Eq. 3.1 which defines the power effectiveness. In case of carbon dioxide simulations, the optimum strength of the energy spot increases with increase in stagnation enthalpy (Fig. 3.8 (a)). Therefore, the denominator of the Eq. 3.1 increases but at the cost of lower reduction of drag force component of the numerator (Fig. 3.11). In addition to this, the velocity in the numerator increases with increase in stagnation enthalpy (Fig. 3.11) and that leads to the increment in the product of numerator of Eq. 3.1. Due to similar amount of increment in numerator and the denominator, there is minor change in peak power effectiveness for higher stagnation enthalpies in case of Martian simulations. But, in case of air, decrement of drag is higher and rise in velocity is also less. As a result, numerator of Eq. 3.1 decreases at larger rate with increase in stagnation enthalpy of air flow; which in turn reduces the power effectiveness more than the Mars flight conditions. In all, present studies reveal that, though energy deposition bears potential for drag reduction, this method is more effective for Earth atmospher than that of Mars for same freestream conditions. This recommandation is based on the fact that, more amount of energy needs to be deposited for same amount of drag reduction in Mars atmospheric conditions as compared to that of air for any stagnation enthalpy case.

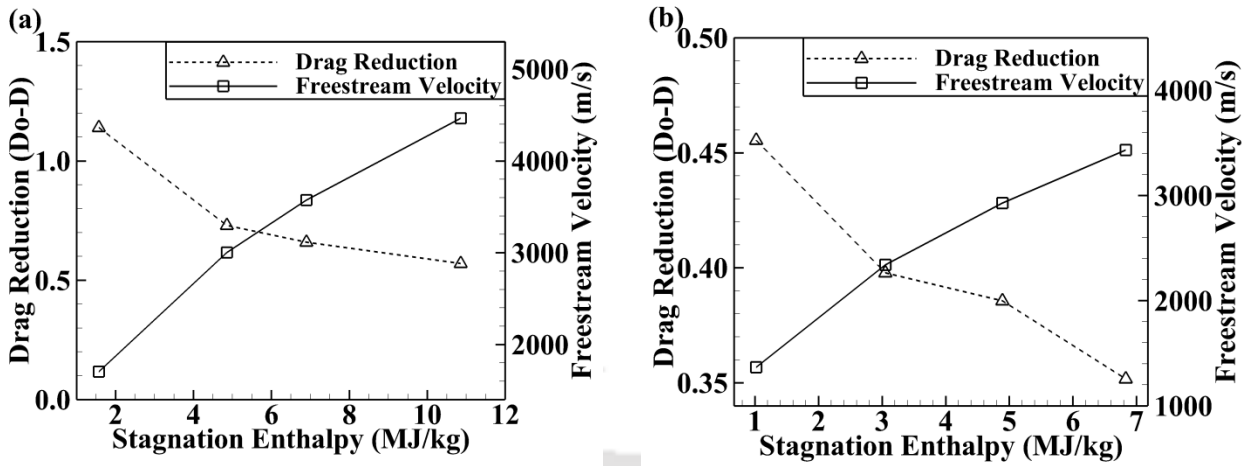

Figure 3.11: Variation of drag reduction and freestream velocity with stagnation enthalpies for (a) Earth Atmosphere and (b) Mars atmosphere.

3.4 Conclusions

The in-house real gas solver is successfully integrated with the golden section search optimization algorithm in order to evaluate the optimum amount of energy required to deposit for maximum power effectiveness. Computations are performed for hypersonic flow over a sphere and it has been found that, there is a demand of higher amount of energy to be deposited for Mars case as compared to the Earth case so as to attain the maximum power effectiveness. Since most of the species recombine before reaching the stagnation point, higher dependence of specific heat of carbon dioxide than air is found to be responsible for this observation. The maximum power effectiveness attained for optimum energy deposition is noted to be lower for Mars case than the Earth flight conditions. Simulations when performed to study the high enthalpy effect, performance of this technique is noticed to be lowered with increase in stagnation enthalpy of the flow for both the cases. Further, Earth conditions are seen to have larger decrement in performance for high enthalpy flight conditions. In all the present studies, potential of this technique in reducing the drag is noted but its effectiveness is marked to be more for hypersonic flights in Earth atmosphere for any stagnation enthalpy case.

Chapter 4 : Assessment of the Transition Criteria for Regular to Mach reflection in Different Flow Mediums at various Freestream Enthalpies.

Overview

This chapter deals with the Mach reflection studies considering real gas effects. Computations are performed for two different flow mediums viz. Earth and Mars atmosphere. Initial computation at lower enthalpy yields Mach reflection in either flow medium. Further, the effect of variation in enthalpy on reflection patterns is investigated, which reveals that with increment in the freestream enthalpy the reflection type changes from Mach to a regular reflection. This change is believed to be due to the noticeable real gas effects at higher enthalpy. Further, to justify the argument, shock polar diagrams are incorporated. These diagrams show that with the rise in enthalpy, the specific heat and Mach number downstream of the incident shock change leading to an increase in the maximum deflection angle of the flow in the region. Thus, flow with higher enthalpy can be deflected with a regular reflection for a comparatively higher value of deflection angle.

4.1 Introduction

In steady supersonic/hypersonic flow, two types of shock reflection patterns can be found [**152**]. They are regular reflection (RR) and Mach reflection (MR). For fixed inlet conditions, the transition from regular to Mach reflection or vice-versa is determined by the incident shock angle. Over the years researchers have shown great interest in determining this transition criterion [**26**,**28**,**29**]. A schematic diagram displaying the Mach reflection phenomena is shown in Fig. 4.1. Contrary to a regular reflection, in Mach reflection, the flow downstream of the reflected oblique shock (R) cannot be turned parallel to the reflecting wall by a single reflected shock causing the formation of Mach stem. Further, the incident shock (I), reflected shock and Mach stem (normal shock) intersect at the triple point from which a slip surface (SS) originates. Here, the flow remains supersonic everywhere except downstream of the Mach stem.

Literature reported findings demonstrate that the previous investigations on MR phenomena mainly focused on evaluating the transitions criteria between RR↔MR [**26**,**27**,**28**], hysteresis effects [**30**,**31**,**32**,**33**], Mach stem height [**34**,**35**,**36**,**37**,**38**] etc. however, most of these investigations are limited to perfect gas assumption and only handful of them accounted for the real gas effects [**43**,**44**]. Furthermore, all these studies are confined to the air medium. Another important observation from the literature review is that the possible high enthalpy effects on the transition criterion for RR↔MR are left untouched. Given this, the present study aims at investigating these phenomena by employing a non-equilibrium/real gas solver. Further, the study is performed on Earth as well as Mars atmospheric conditions. For this purpose, inviscid simulations are performed by the real gas solver discussed in Chapter 2. The following sections discuss the results obtained from these simulations.

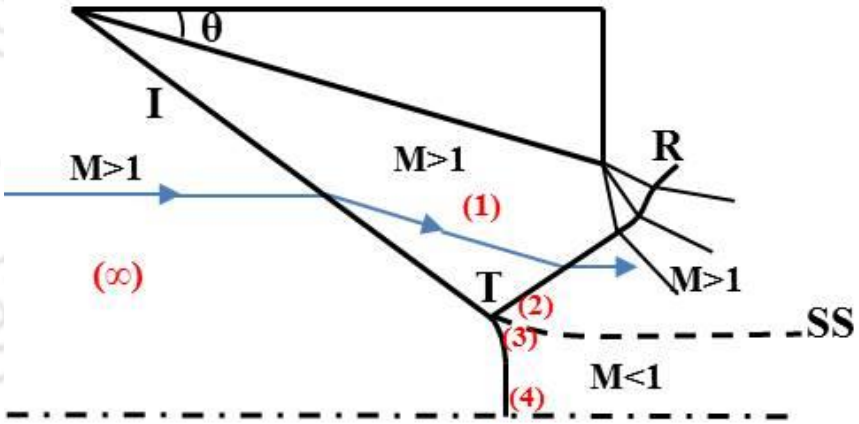

Figure 4.1: Schematic of Mach reflection.

4.2 Results and Discussion

The freestream parameters considered for the simulations in the Earth environment are similar to that considered by Hornung and Robinson [**26**] and are listed in Table 4.1**.** Further, for Mars atmospheric simulations, the freestream pressure, temperatures is kept the same and the Mach number is adjusted to 2.50 to ensure the Mach reflection. The computational domain along with boundary conditions is shown in Fig 4.2. The following sub-sections provide the details of this investigation.

Table 4.1: Freestream conditions used for Mach reflection studies.

Atmosphere	Mach number	Total Pressure (Pa)	Total Temperature (K)	Mass Fraction
Earth atmosphere	2.84	310000	300	N_2- 0.765 O_2- 0.235
Mars atmosphere	2.50	310000	300	CO_2- 0.9685 N_2- 0.0315

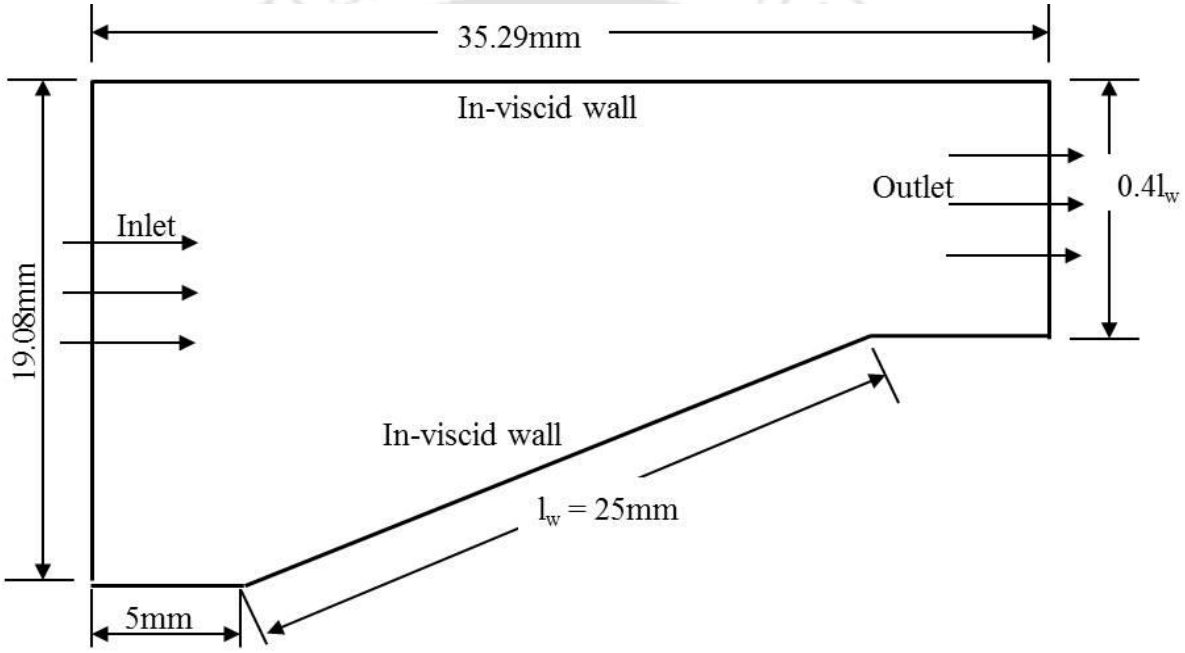

Figure 4.2: Computational domain for Mach reflection study.

4.2.1 Flow fields

A shock polar diagram with Air (γ=1.4) as flow medium is shown in Fig. 4.3 (a). Here, the points in the figure resemble the regions marked in Fig. 4.1. The freestream flow is represented by the freestream polar (M_∞=2.84) at zero deflection angle (θ=0). The flow in the region (1) is parallel to the wedge surface, hence point (1) is marked at θ=21.3^0 (wedge angle) in M_∞ polar, and from this point, M_1=1.82 polar is drawn. Further, Point (2) must be in M_1 polar; point (3) must be in M_∞ polar. However, point (2) and (3) must co-locate as they are separated by a slip surface. Therefore, the point (2) and (3) are marked at the intersection of M_1 and M_∞ polar. Furthermore, the flow in the region (4) is subsonic and parallel to the reflecting wall. Hence, point (4) is marked

at the interaction of zero deflection line and subsonic M_∞ polar. Similarly, the shock polar for Mars atmosphere (γ=1.28) is shown in Fig. 4.3(b). From the figures, it evident that the M_1 polar does not intersect the zero deflection line in either of the cases. This indicates that, for the present freestream conditions, the flow in the region (1) cannot be turned to its original direction (θ=0) by a single reflected shock and hence, a Mach reflection shall occur.

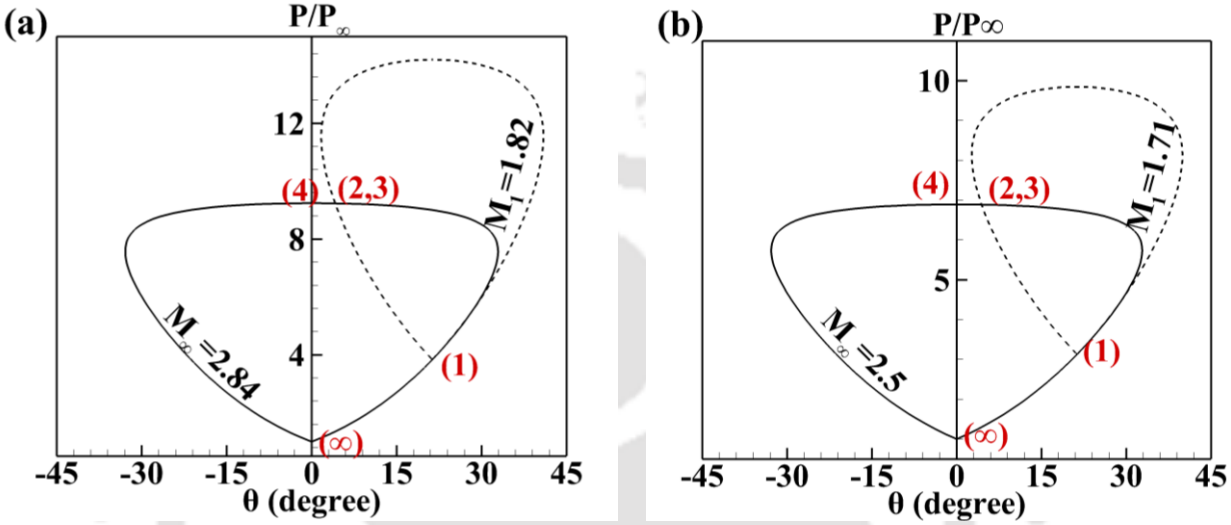

Figure 4.3: Shock polar diagram (a) with M_∞=2.84 and γ=1.4; (b) with M_∞=2.5 and γ=1.28.

Initially, the simulations are carried out for Earth atmospheric conditions. To eliminate the effects of grid size, simulations with three different grids, 240x100, 395x130 and 450x160 were performed. The surface pressure obtained and residue history of all these grids is shown in Fig. 4.4 (a) and (b) respectively. Here, the Fig. 4.4(a) indicates that, not much change is visible after the 395x130 grid resolution and hence, this mesh size is considered for further simulations. Further, the density gradient contour obtained from the same simulation is shown in Fig. 4.4 (c). Here, the attached oblique shock gets inevitably formed at the compression corner and gets reflected. However, the maximum deflection angle (19.62º) of the flow behind the oblique shock is smaller than the wedge angle (21.3º). Thus, this reflected shock cannot turn the flow parallel to its original direction of its own. Hence, a Mach stem emerges and a triple point is formed. Furthermore, from this triple point, a slip surface originates. The reflected shock further interacts with the expansion fan centered at the trailing edge of the wedge and gets deflected. Finally, this shock gets reflected from the bottom wall. The flow remains supersonic except behind the Mach stem. All important flow features such as oblique shock, reflected shock, Mach stem, slip line, expansion fan are well captured by the simulation. Further, the Mars atmospheric simulation also yields the Mach

reflection. The pressure distribution along the bottom surface is plotted in Fig. 4.5 (a). Here, the first pressure ratio jump (≈3.25) is due to the oblique shock at the leading edge of the wedge. Secondly, as the flow relaxes across the expansion corner (trailing edge of the wedge), the pressure ratio reduces to around 1.4. Further, the pressure ratio again increases (≈5.5) at the impingement location of the reflected shock. It is important to note that, for this case, the reflected shock impinges the bottom surface very near to the expansion corner which restricts the complete expansion of the flow. The same fact can be noticed from the density gradient contour plotted in Fig. 4.5 (b). Further, in the same figure, all the important flow features can be noticed.

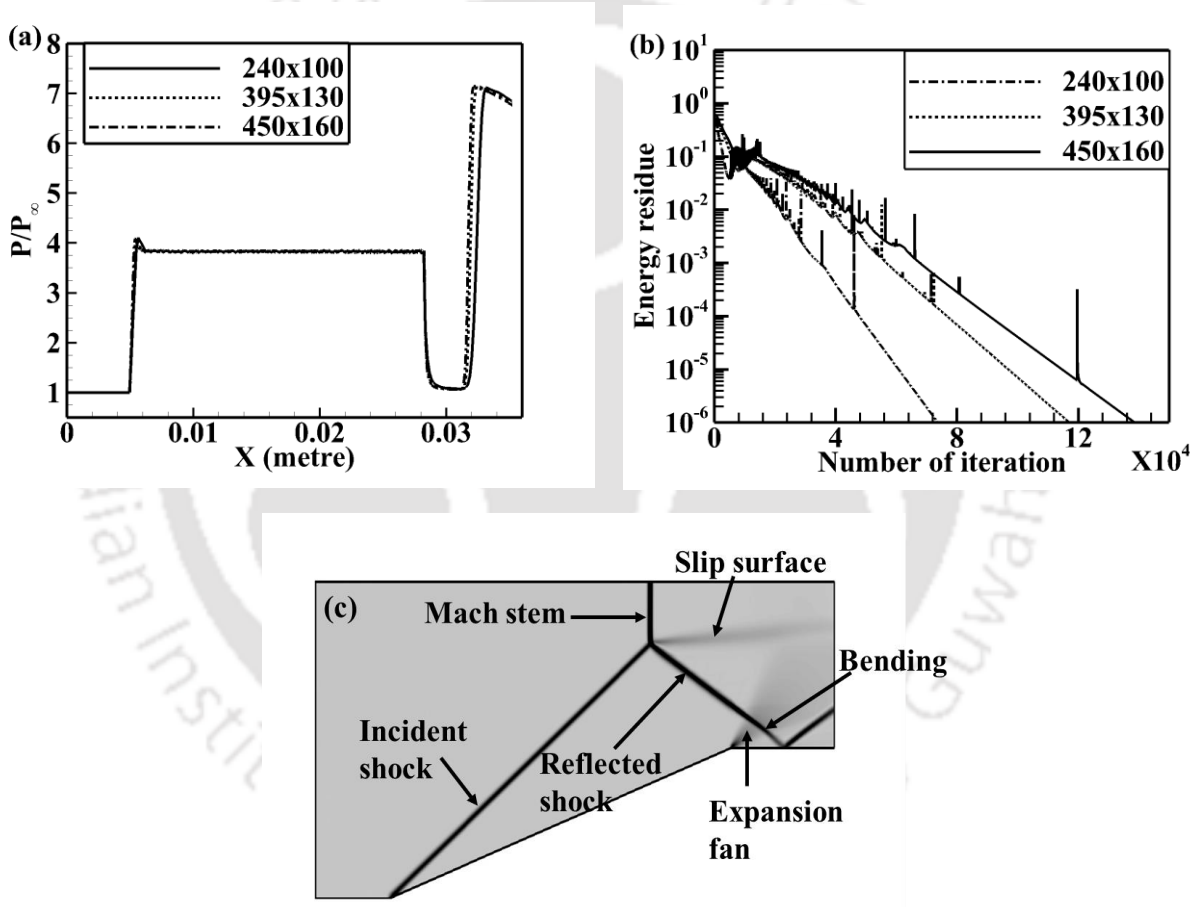

Figure 4.4: Outcomes of Earth atmospheric simulation (a) surface pressure variation (b) residue history and (c) Density gradient contour.

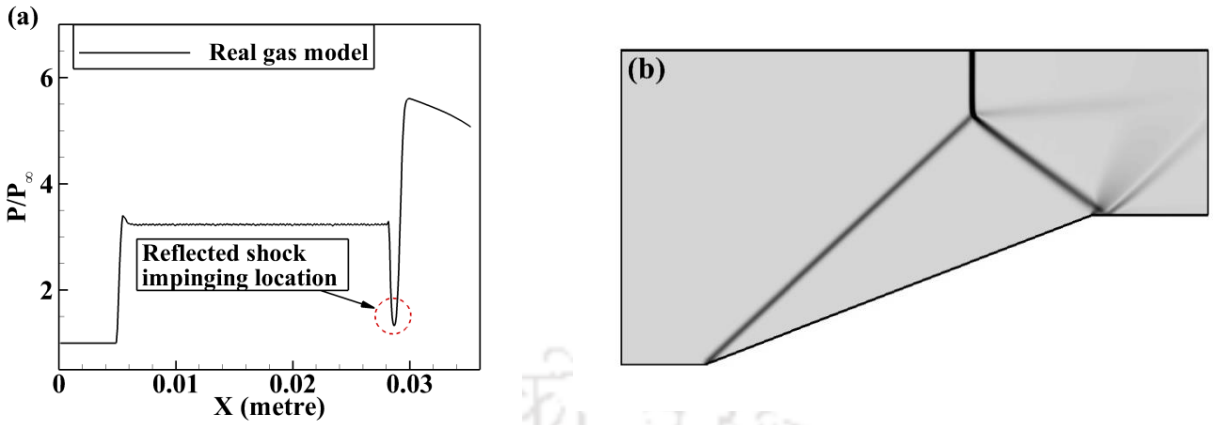

Figure 4.5: Outcomes of Mars atmospheric simulation (a) surface pressure variation and (b) Density gradient contour.

4.2.2 Effect of freestream stagnation enthalpy

The investigation is continued to determine the effects on the shock structures due to change in the freestream enthalpies. For simulations with Earth atmospheric conditions, it is varied from 0.30 MJ/kg to 2.42 MJ/kg and for Mars simulations; it is varied from 0.18 MJ/kg to 0.68MJ/kg. Here, the variation in the enthalpy is achieved by changing the freestream temperatures only. Figure 4.6 shows the density gradient contours for the Earth atmosphere flow model at different enthalpies. For the first two enthalpies (0.30 MJ/kg and 0.79 MJ/kg) Mach reflection is evident. However, the transition from Mach to regular reflection occurs as the enthalpy is increased to 1.32 KJ/kg. An additional increase in the enthalpy yields a regular reflection. Further, it is observed that for Mach reflection cases the Mach stem height (H_{st}) decreases with an increase in enthalpy ($H_{st0.30}$=3.72mm; $H_{st0.79}$=3.20mm). Another fact is the shifting of Mach stem and incident shock impinging location towards downstream with the increase in enthalpies. This fact is also evident from the surface pressure plot for the top wall shown in Fig. 4.7(a). Here, the pressure jump location indicates the shock impinging point. Again, the surface pressure distribution for the bottom wall is plotted in Fig. 4.7(b). An important point to note here is that since for the last two enthalpies (1.32 MJ/kg and 2.42 MJ/kg), the reflected shock doesn't impinge on the wall; so there is no second pressure jump for these two enthalpies. Another observation is the shifting of reflected shock impinging location with the increase in enthalpy. Similar observations are noted from the density gradient contour (Fig. 4.8) obtained from Mars atmospheric simulations as well. However, it is observed that the transition for Mars atmospheric

conditions occurs at a comparatively lower value of enthalpy. Further, the surface pressure distributions on the upper and bottom wall are plotted in Fig. 4.9. The trends observed are similar to that of Earth atmosphere outcomes. From Fig. 4.9(b), it can be noted that for 0.24 MJ/kg case, the reflected shock impinges at a distance from the expansion corner. Thus, unlike the 0.18MJ/kg case, the flow is completely expanded across the expansion corner resulting in a decrease in pressure ratio to unity. Furthermore, the different parameters such as Mach numbers in behind the incident shock (M_1), reflected shock (M_2) and the Mach stem (M_3), the incident shock angle (α), the reflected shock angle (β), the Mach stem height (H_{st}), the slip line angle (θ_s), and the spread angle of the expansion fan (θ_{sExp}) obtained from the simulations are summarized in Table 4.2.

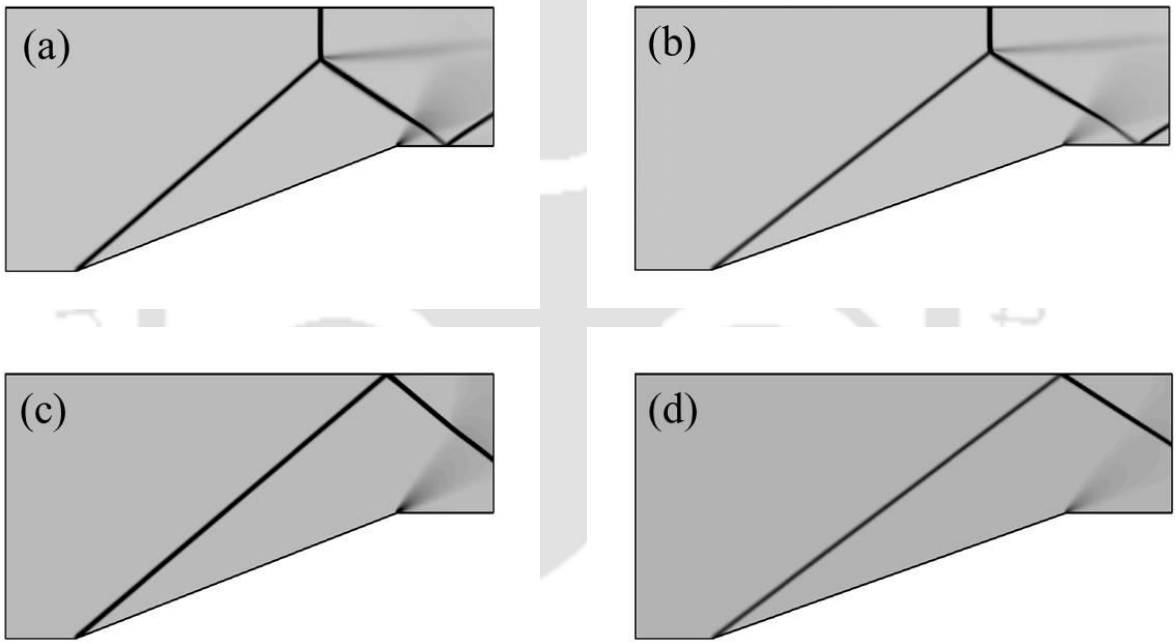

Figure 4.6: Density gradient contours at different enthalpies for Earth atmosphere (a) 0.30 MJ/kg (b) 0.79 MJ/kg (c) 1.32 MJ/kg and (d) 2.42 MJ/kg.

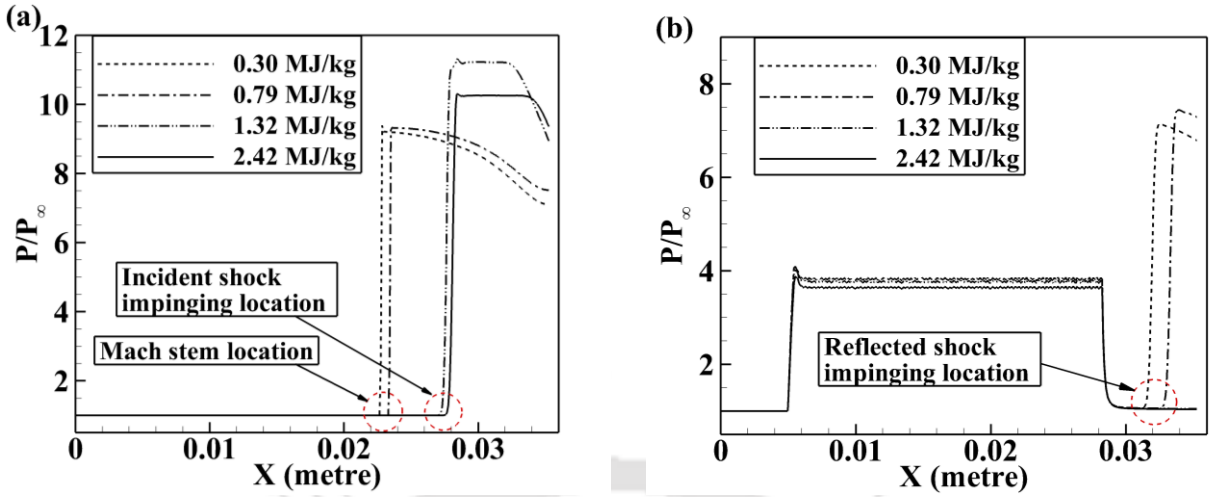

Figure 4.7: Surface pressure distribution obtained at different enthalpies from Earth Atmosphere simulations (a) Top Wall (b) bottom wall.

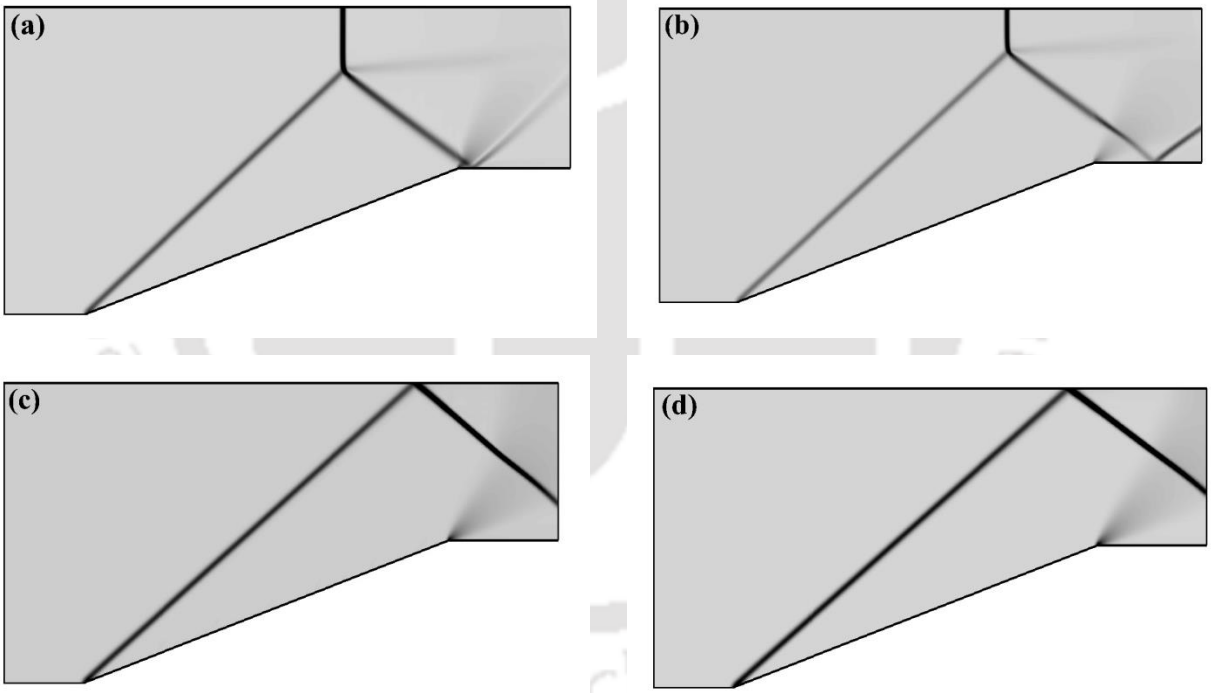

Figure 4.8: Density gradient contours at different enthalpies for Mars atmosphere (a) 0.18 MJ/kg (b) 0.24 MJ/kg (c) 0.39 MJ/kg and (d) 0.68 MJ/kg.

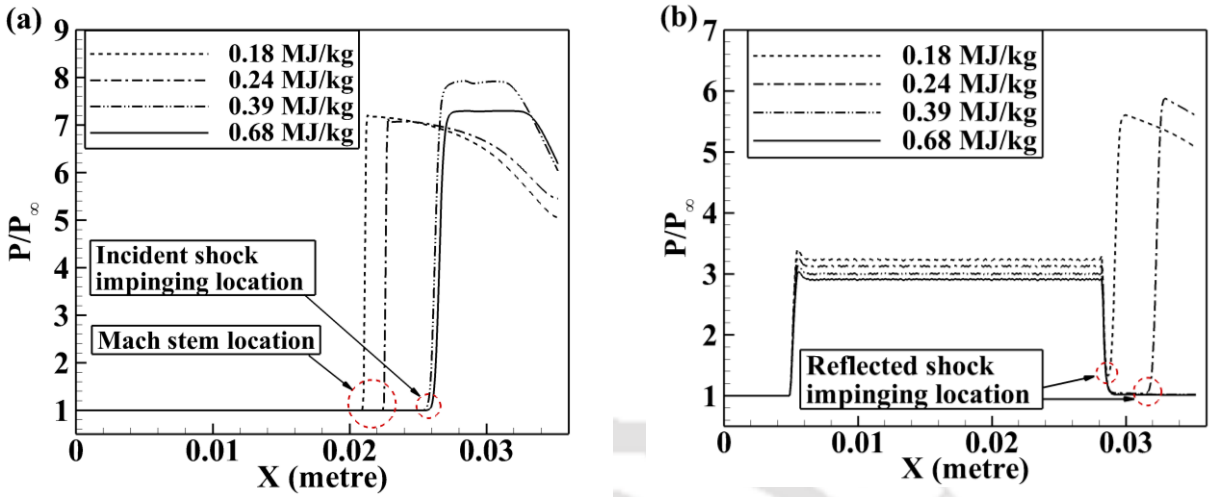

Figure 4.9: Surface pressure distribution obtained at different enthalpies from Mars Atmosphere simulations (a) Top Wall (b) bottom wall.

Table 4.2: Summary of different parameters obtained from present simulations.

Atmosphere	Enthalpy (MJ/kg)	M_∞	M_1	M_2	M_3	α	β	H_{st} (mm)	θ_{Slip}	θ_{SExp}
Earth	0.30	2.84	1.82	1.16	0.49	40.74	33.82	3.72	5.30	40.79
	0.79	2.84	1.83	1.17	0.48	40.56	33.37	3.20	5.19	38.89
	1.32	2.84	1.88	1.02	N/A	40.27	40.00	N/A	N/A	38.51
	2.42	2.84	1.93	1.14	N/A	39.71	35.32	N/A	N/A	35.89
Mars	0.18	2.50	1.70	1.10	0.49	43.03	37.12	3.82	3.97	-
	0.24	2.50	1.74	1.13	0.47	42.75	35.54	2.75	3.22	39.96
	0.39	2.50	1.78	1.01	N/A	42.26	40.84	N/A	N/A	37.45
	0.68	2.50	1.82	1.11	N/A	41.71	37.31	N/A	N/A	35.69

These changes in the shock structures and transition of Mach to regular reflection with enthalpies are attributed to real gas effects. The range maximum flow field temperature (500K to 1200K) in these simulations is not sufficient to cause any dissociation reaction. Hence, only temperature-dependent specific heat contributes for these changes. Here, with increasing enthalpy the specific heat across the first oblique shock rises, resulting in a lower percentage rise in temperature; thus higher approaching Mach number for the reflected shock. This increases the

maximum deflection angle (θ_{max}) of the flow and hence, the transition from Mach to regular reflection occurs [**25**]. This transition can further be explained with the help of a shock polar diagram for the Earth atmospheric condition (Fig. 4.10(a)). Since no dissociation reaction is observed in the present study, the shock polar are obtained using pressure deflection relation valid for perfect gas flow with the local Mach numbers and local specific heat ratio. The local specific heat ratio and Mach number in the region (1) are listed in Table 4.3. From the table, it can be observed that with an increase in enthalpy the Mach number increases whereas the specific heat decreases. This increases in the maximum deflection angle for the region (1) polar (θ_{max1}) is increasing with the increase in enthalpy as shown in the figure (Fig. 4.10(a)). Here, for the 0.32 MJ/kg and 0.79 MJ/kg enthalpy cases, the region (1) polar is not intersecting the zero deflection line indicating the fact that the flow in the region (1) cannot be deflected to its freestream direction by the reflecting shock from the wall. Hence, Mach reflection occurs for these two enthalpies. Additionally, the greater value of θ_{max1} for 0.79 MJ/kg ensures lower Mach stem height for this case. Further, for the 1.32 MJ/kg and 2.42 MJ/kg cases, the zero deflection line is intersected by the region (1) polar. Hence, it is possible for the reflected shock to turn the flow parallel to the wall; thus regular reflection occurs. A similar conclusion can be drawn from the shock polar for Martian atmospheric simulation shown in Fig. 4.10(b).

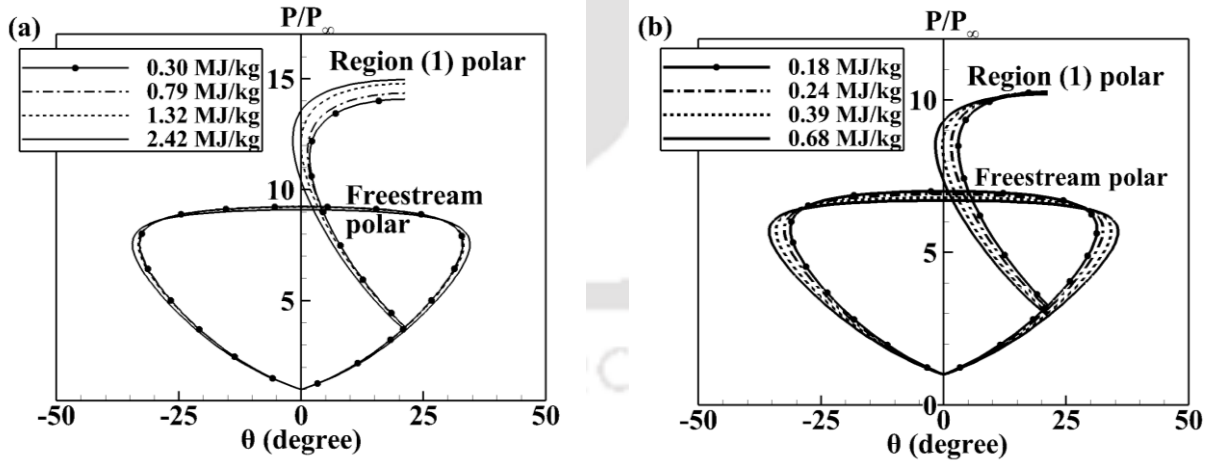

Figure 4.10: Shock polar diagram at different enthalpies (a) Earth atmosphere (b) Mars atmosphere.

Table 4.3: The specific heat ratio and Mach number after the incident shock wave at different enthalpies.

Atmosphere	Enthalpy (MJ/kg)	Specific heat ratio (γ_1)	Mach number (M_1)
Earth	0.30	1.40	1.82
	0.79	1.39	1.83
	1.32	1.36	1.88
	2.42	1.32	1.93
Mars	0.18	1.29	1.70
	0.24	1.26	1.74
	0.39	1.21	1.78
	0.68	1.18	1.82

4.3 Conclusion

The Mach reflection study is successfully carried out by employing the in-house real gas solver. Numerical investigation is performed on Earth and the Martian atmosphere. Simulations at lower stagnation enthalpy confirm the Mach reflection for both the flow mediums. It is noted that the variation in enthalpy has a severe effect on the reflection patterns. In either flow medium, with an initial increase in enthalpy, the Mach stem height decreases and eventually leads to a transition to a regular reflection as the enthalpy is increased further. This transition is due to the prominent real gas effects at higher enthalpies. Further, the shock polar diagram at different enthalpies reveals that, with the increase in enthalpy the maximum deflection angle of the flow behind the incident shock increases; thus, allowing the flow to be deflected parallel to the surface by the reflected shock and thereby causing the transition from MR↔RR. Another observation is the occurrence of the transition at comparatively lower enthalpy for the Mars atmosphere case.

Chapter 5 : Aerothermodynamics Analysis of Different Shock/Shock Interactions Induced by Double Wedge Geometries in Earth and Mars Atmospheric conditions.

Overview

In this chapter shock/shock interactions on different double wedge geometries for different stagnation enthalpies are investigated to explore the detailed physics associated with these interactions. For the purpose, hypersonic flow simulations in Earth and Mars atmosphere by perfect as well as real gas solvers are performed. The reasons behind the transition in interaction types are identified and discussed in detail. It is found that real gas effects are more prominent in the Mars atmosphere and it provides a similar effect as that of decreasing the second wedge angle. Another important observation is the transition in interaction types with variation in stagnation enthalpies.

5.1 Introduction

Shock waves are inherent, whenever supersonic/hypersonic flow encounters any obstruction. In many practical applications, these shock waves are present in multiple numbers. One such case is the shock wave generated due to the wings and fuselage of an aircraft. Furthermore, the presence of multiple shock waves leads to frequent interactions between them. These interactions change the flow field drastically, which may cause serious design issues. Therefore, it is of utmost importance to understand and investigate the effects of these interactions on the flow field. Edney [**48**] was the first scholar to classify these shock on shock interactions into six different types based on his experimental work for flow over a sphere. Later on many researchers performed investigations on different aspects of these interactions.

From the literature, it is clear that most of the studies considered air as the flow medium and only a few attempts have been made for venturing into another medium like Carbon-dioxide [**51**] and Nitrogen [**75**]. Further, limited attention is paid for investigation of shock/shock interaction phenomena including real gas effects [**71**,**72**,**73**,**74**,**75**]. Efforts also lack to provide

detailed insights on the modification of such interaction patterns. In view of these, the present study deals with different Types (IV, V and VI) of shock/shock interaction generated by flow over two-dimensional double wedge geometries. The numerical simulations are carried out for Earth (air) as well as Mars (CO_2) atmospheric conditions. The investigation considers different second wedge angles and stagnation enthalpies where prominent real gas effects are noted. The present study offers a generalized detailed discussion of physics involving different shock/shock interactions. Moreover, the contribution of real gas effects on significant flow field modification is explained. The shock polar diagrams are also presented for better understanding and justification. For the same, along with a perfect gas solver, a separate Euler solver for Earth and Mars atmospheric simulations considering real gas effects have been employed. The details of the results are discussed in the following sections.

5.2 Results and Discussion

The present analysis is centered on the investigation of different shock/shock interactions induced by double-wedge obstruction exposed in the supersonic/hypersonic stream. For the purpose, three different double wedge configurations are considered each for Earth and Mars atmosphere simulations. Here, both the wedges are 25mm in length. Further, the first wedge angle is kept same at 15º for all the cases while the succeeding ramp angles are 50º, 45º, and 35º for Earth atmospheric conditions and 56º, 49º, and 35º for Mars atmospheric conditions. These angles are corresponding to achieve Edney's Type IV, V, and VI shock/shock interaction in perfect gas simulations. Schematic diagrams of interaction Type IV, type V with overall Mach reflection (MR), Type V with overall regular reflection (RR) and Type VI are shown in Fig. 5.1. The freestream conditions used for the present study are listed in Table 5.1 as mentioned by Olejniczak et al. [**62**].

5.2.1 Flow field around the double-wedge geometries

Initially, a grid independence study is carried out for the perfect gas Earth atmosphere flow model. In the study, the chosen double ramp configuration consists of first and second wedge angles of θ_1=15º and θ_2=50º respectively. Further, three different mesh of 265x140, 345x200, and 490x300 quadrilateral elements are considered herein. The invscid simulations are performed for the freestream conditions as mentioned in Table 5.1. The surface pressure distributions and residue

history obtained from these simulations are shown in Fig. 5.2(a) and (b) respectively. It can be seen that not much change is visible for the number of elements more than 345x200. Hence, this grid configuration is chosen to initiate the detailed study of Edney's Type IV shock/shock interaction formed by the prescribed geometry.

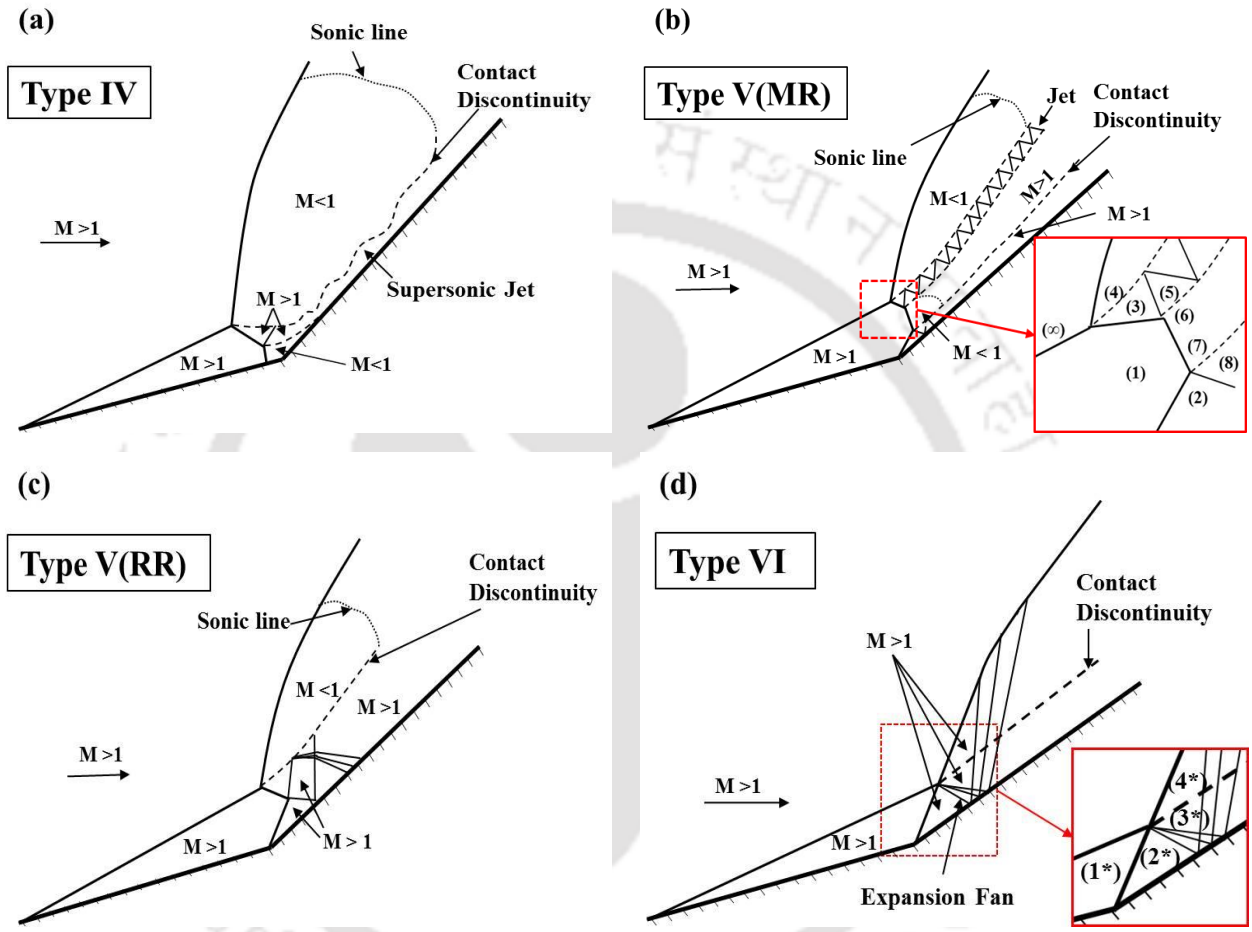

Figure 5.1: Schematic of shock/shock interaction types: (a) Type IV; (b) Type V with overall Mach reflection (MR); (c) Type V with overall regular reflection (RR); and (d) Type VI.

Table 5.1: Freestream conditions used for shock/shock interaction studies.

Atmosphere	Mach number	Pressure (Pa)	Temperature (K)	Mass Fractions
Earth atmosphere	9	89	113	N_2- 0.765; O_2- 0.235
Mars atmosphere	9	89	113	CO_2- 0.9685; N_2- 0.0315

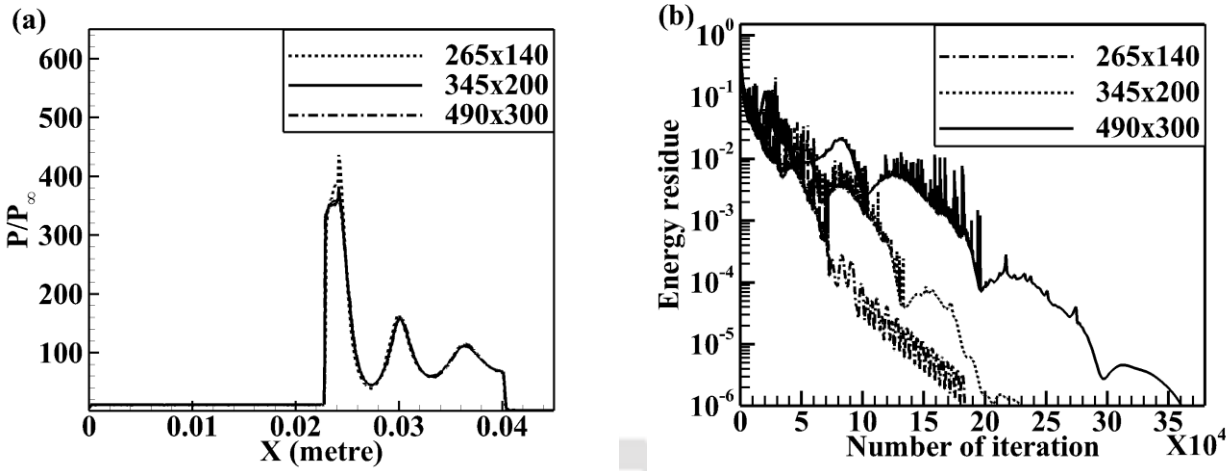

Figure 5.2: (a) Surface pressure distributions (b) residue history obtained with three different grid sizes: perfect gas Earth atmosphere flow model.

The density gradient contours (Numerical Schlieren) obtained from the simulation with the aforementioned conditions and grid are shown in Fig. 5.3(a). It is evident that all the essential flow features like oblique shock, normal shock, bow shock, triple point are captured very well. Here, the first oblique shock inevitably gets formed at the leading edge of the first ramp. Similarly, the bow shock gets developed ahead of the secondary wedge at the upper undisturbed region of oblique shock. It occurs as the turning of the freestream at upstream of the second ramp is not possible by an oblique shock. This bow shock interacts with the first ramp oblique shock and transmits a secondary shock. Further, the detached normal shock also gets created ahead of succeeding ramp in the lower disturbed region at the downstream of the first oblique shock. Here, the detachment happens even at a lower deflection angle value (50º) than the maximum deflection angle [**25**] criteria (56.18º) for detachment at the present condition. This is attributed to the pressure condition imposed by the subsonic region behind the bow shock which must be met by the inboard fluid. Olejniczak et al. [**62**] argued that the transition angle cannot be determined analytically due to the presence of subsonic regions as well as curved shocks and must be found computationally. Moreover, both transmitted secondary shock and normal shock interact with each other. Eventually, two contact discontinuities originate from the interaction points separating the different entropy regions. In between these discontinuities (Fig. 5.3(b)), a supersonic jet is formed. Here, the fluid experiences a series of compression and expansions as it passes through this jet and leads to the undulation of contact discontinuity. The jet is highly curved towards the second ramp

and eventually impinges downstream. It is important to note that the inboard fluid, in the vicinity of the wall, initially passes through the first ramp oblique shock and remains supersonic at downstream. Further, it becomes subsonic behind the normal shock and immediately turns supersonic from jet impingement location. These facts are evident from the Mach contour and surface pressure plot depicted in Fig. 5.4(a). Here, the first and the second pressure peaks are due to the attached normal shock and second ramp respectively. Afterward smaller peaks are seen which are attributed to the waviness in the contact discontinuity.

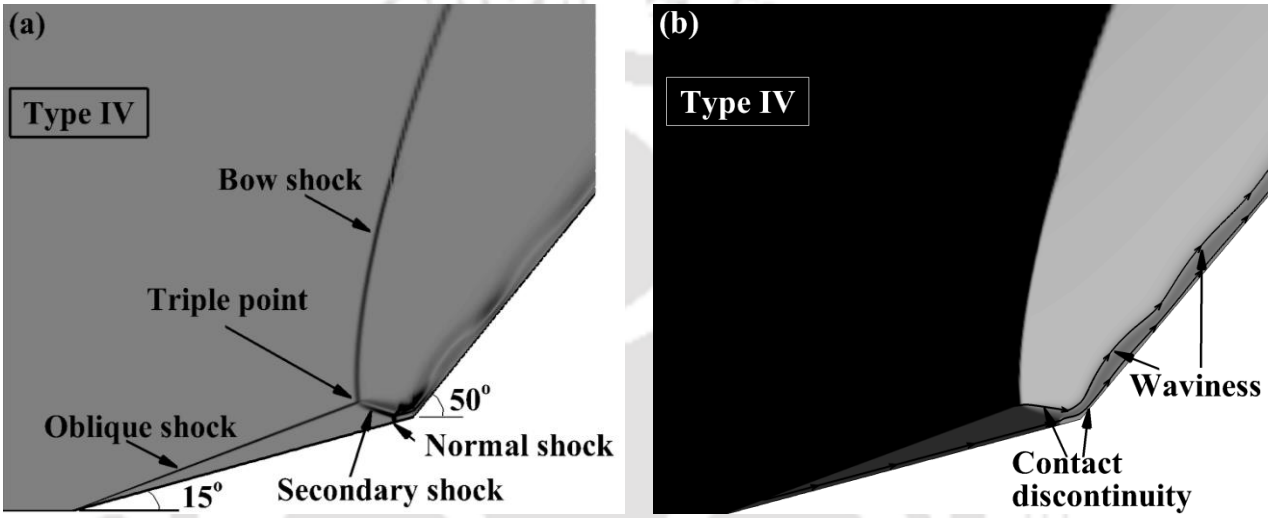

Figure 5.3: Basic flow structures of a Type IV interaction obtained with θ_1=15º and θ_2=50º configuration by perfect gas Earth atmosphere flow model: (a) Density gradient contour; and (b) Entropy contour.

Similar simulations are also performed for the real gas flow model of the Earth atmosphere. The Mach contour along with pressure variations obtained from the real gas flow model is shown in Fig. 5.4(b). It is noted that the shock interaction pattern is the same as obtained from the simulation of the perfect gas model. However, the normal shock height is more and it is very closely located to the second ramp as compared to perfect gas model. Similar to perfect gas model, here also the two pressure peaks due to the normal shock and the ramp seem to form a single jump**.** However, noticeable difference in the width of the peak indicates the fact that for the real gas flow model, the normal shock is more closely located to the ramp. In this case, the rise in specific heat values at the downstream of normal shock and bow shock reduces the shock layer temperature, and thus higher shock layer density, in turn, lesser shock layer thickness is obtained.

These variations eventually lead to the closer appearance of the normal shock wave from the second ramp as compared to the perfect gas model.

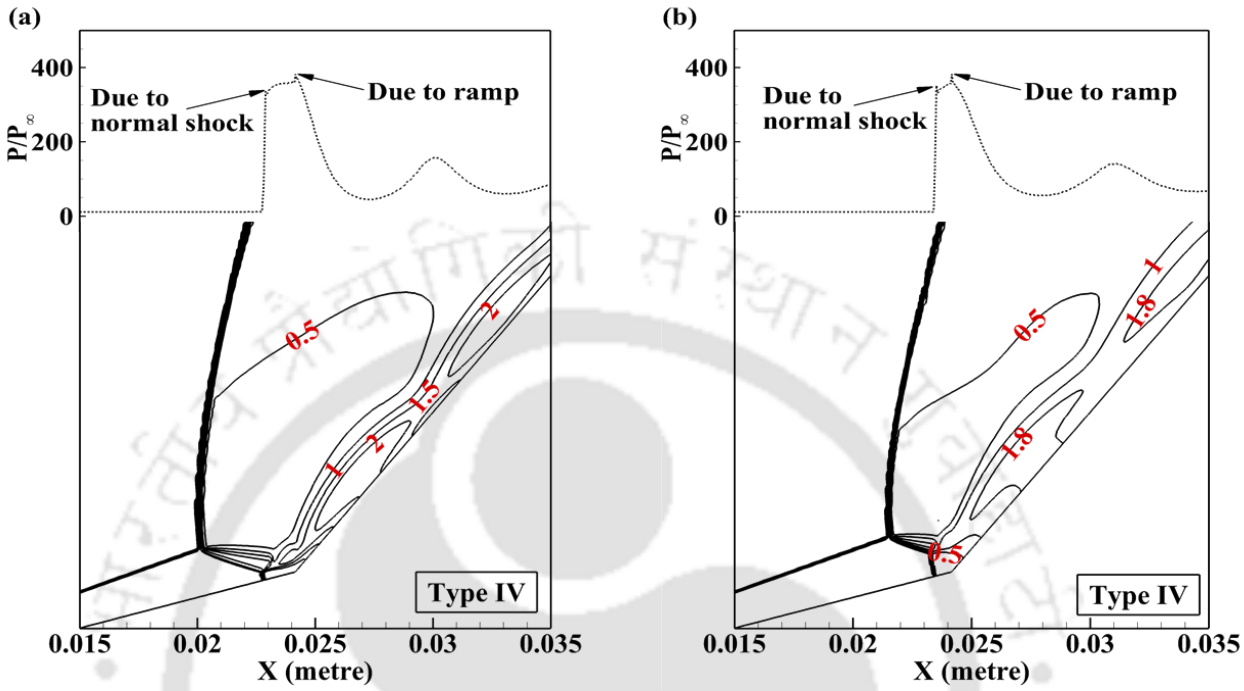

Figure 5.4: Mach contour showing Type IV interaction and surface pressure variation obtained with θ_1=15º and θ_2=50º configuration by Earth atmosphere flow models: (a) perfect gas flow; and (b) real gas flow.

Further, studies are continued for the perfect gas and real gas flow model of the Mars atmosphere with θ_1=15º and θ_2=56º configuration. Here as well, Edney's Type IV interaction is observed for both the flow model simulations as shown in Fig. 5.5. However, just like Earth based simulation, the higher density in the secondary shock layer causes the normal shock to be greater in height and nearer to the second ramp for real gas model. It is noted that both the atmospheric conditions with the real gas model do not show sufficient temperature rise to induce any dissociation reaction. Hence, only the changes in temperature-dependent specific heat values contribute to flow field modification.

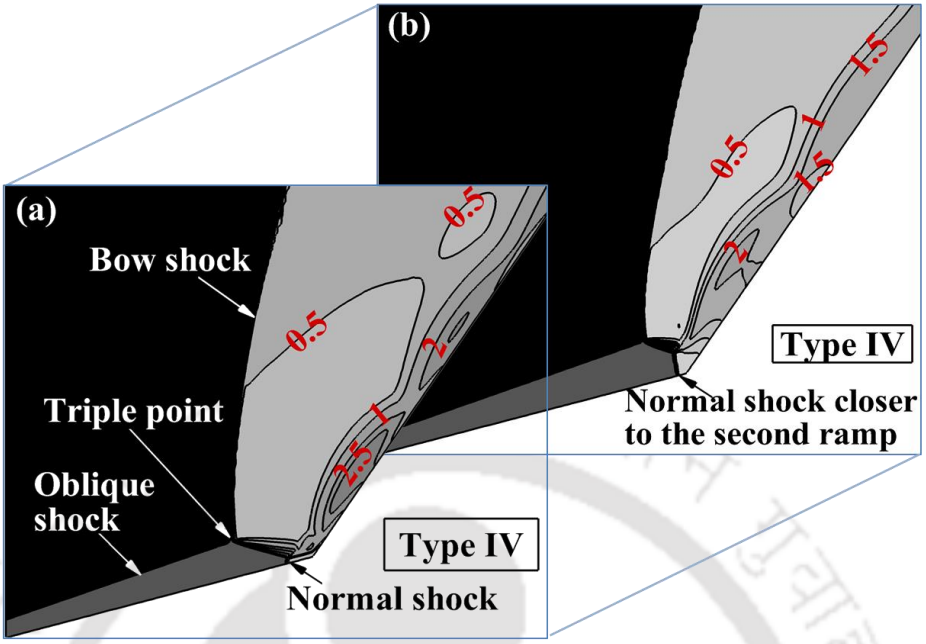

Figure 5.5: Mach contour showing Type IV interaction for θ_1=15º and θ_2=56º configuration obtained by Mars atmosphere flow models: (a) perfect gas flow; and (b) real gas flow.

In the next set of simulations, the second wedge angle is decreased from 50º to 45º while other parameters are kept constant to ensure the Edney's Type V (MR) shock pattern (Fig. 5.1(b)) in the perfect gas Earth atmospheric model. The Mach contour obtained from the simulation for the perfect gas case for Earth shows a change in shock structure compared to Type IV in Fig. 5.6(a). In this case, the oblique shock gets formed ahead of the first ramp and bow shock in the upper undisturbed region. It is important to note that the second ramp angle is within the range to obtain the attached shock. Thus, an oblique shock emerges from the second ramp foot rather than a detached normal shock. Similar to Type IV interaction, the bow, and first oblique shocks interact with each other and transmits a secondary shock. This shock later interacts with the second oblique shock. Further, this interaction includes a Mach reflection as depicted in schematic Fig. 5.1(b). In all, three interaction points are developed from which contact discontinuity originates demarcating the entropy difference regions as shown in Fig. 5.6(b). Similar to Edney's Type IV an under-expanded jet forms in between two upper contact discontinuities.

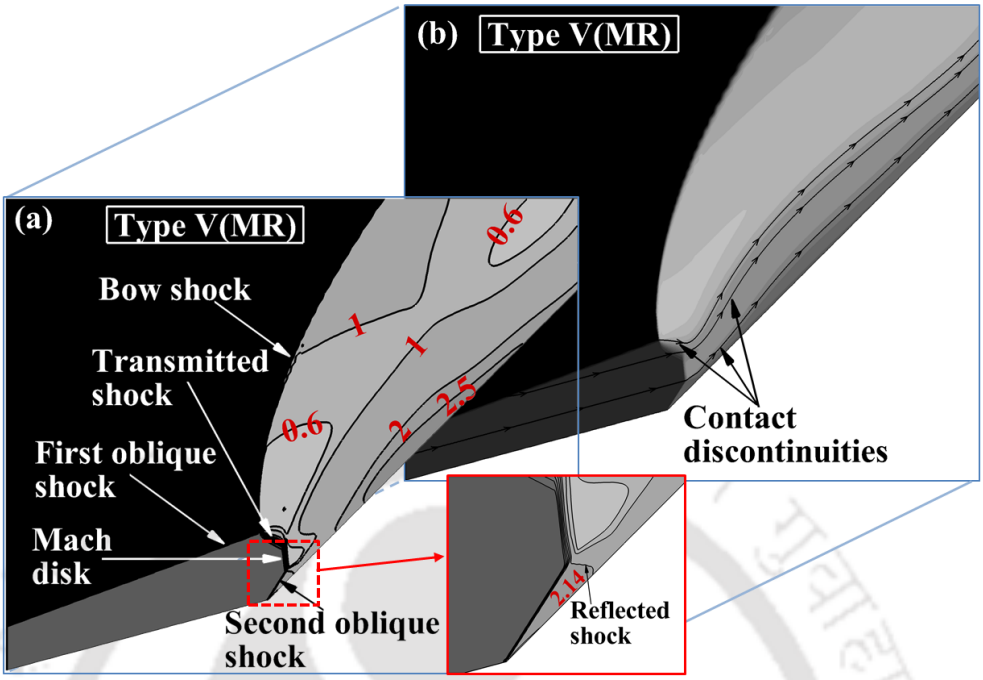

Figure 5.6: Basic Flow structures of a type V (MR) interaction obtained with θ_1=15° and θ_2=45° configuration by perfect gas Earth atmosphere flow model: (a) Mach contour; and (b) Entropy contour.

Further, simulations are continued for the real gas flow model of Earth atmosphere where Type V (MR) interaction is observed. However, from the Mach contour shown in Fig. 5.7, it is evident that the Mach stem is smaller in size and further downstream of the second ramp as compared to perfect gas model. Here, the rise in the specific heat values at downstream of second oblique shock results in lesser temperature rise and hence, higher approaching Mach number (Fig. 5.6 and 5.7) for the reflected shock in case of real gas flow model. This higher Mach number pushes the reflected shock downstream causing the movement of Mach stem away from the ramp foot. This fact can also be observed from the normalized pressure distributions along the wedge surface as shown in Fig. 5.8. Here, the first peak is due to the oblique shock at the second wedge and the largest peak is due to the reflected shock.

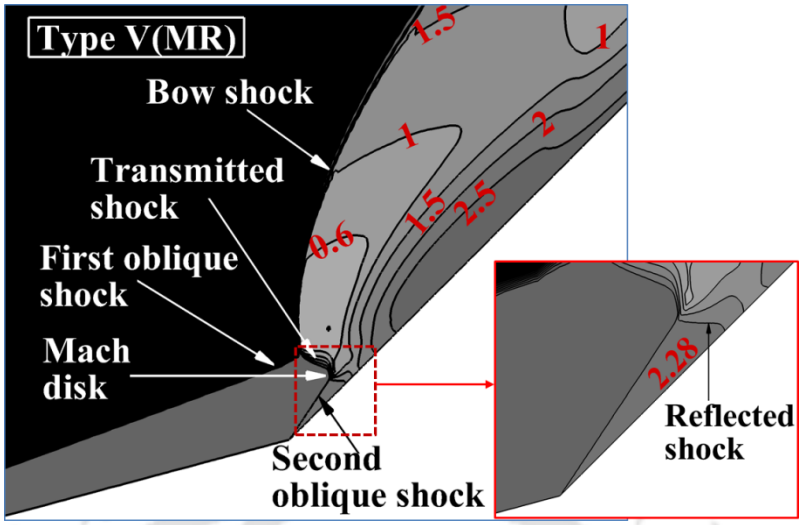

Figure 5.7: Mach contour showing type V (MR) interaction obtained with θ_1=15º and θ_2=45º configuration by real gas Earth atmosphere flow model.

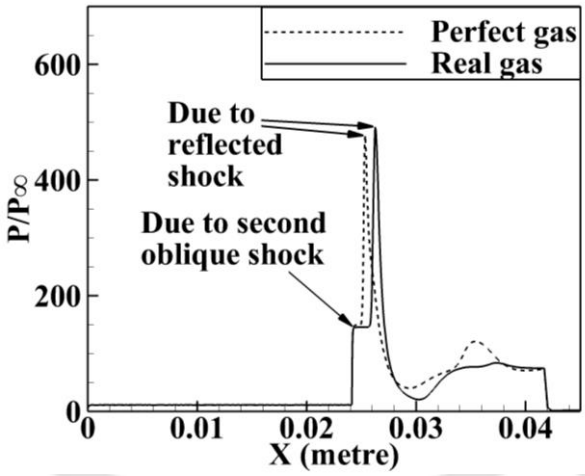

Figure 5.8: Surface pressure distributions obtained with θ_1=15º and θ_2=45º configuration by Earth atmosphere flow models.

Further, simulations are continued for the Mars atmosphere with θ_1=15º, θ_2=49º configuration. An important point to note here from Fig. 5.9 is the appearance of bow shock in the upper part of second wedge even though its angle (49º) is smaller than the maximum deflection angle (49.64º) of freestream flow. This conflict can be explained by the shock polar diagram of Type V interaction shown in Fig. 5.10(a). Here, the points marked in the shock polar correspond to the respective regions shown in Fig. 5.1(b). In Region (1) the flow field is parallel to the first

wedge. Therefore, point (1) is marked at θ= -15º in the freestream shock polar for Mach number, M_∞=9. Starting from this point, the shock polar for Mach number (M_1=5.74) in Region (1) is drawn. Flow in the region (2) is parallel with the second wedge angle so the point (2) is marked at θ= -49º in M_1 polar. Point (3) and (4) are separated by a contact discontinuity so they should co-locate at the intersection of freestream and M_1 polar. Likewise, point (5) and (6) should co-locate at the intersection of M_1 and M_3=3.47 polar; and, point (7) and (8) should co-locate at the intersection of M_1 and M_2=2.38 polar. From the shock polar diagram, it is evident that, as the secondary wedge angle decreases, point (2) move downwards (towards the right) and would lead to Type V interaction with overall regular reflection. Further decrement in second wedge angle eventually leads to a transition from Type V to Type VI. The transition angle can be determined by drawing an isentropic line from point (2) such that it intersects the M_∞ shock polar at its sonic point as shown in Fig. 5.10(b). Below this point, the flow field is completely supersonic and flow can be turned by a single oblique shock. Hence, bow shock turns into an oblique shock; transmitted shock disappears, and results into type VI interactions. The idea behind the isentropic expansion line is that in Type VI interaction (Fig. 5.1(d)) region (3*) and (2*) are separated by an expansion fan and hence, an isentropic expansion line originating from point (2*) must connect point (3*). Another point is point (3*) and point (4*) must co-locate at M_∞ shock polar. A shock polar diagram of Type VI corresponding to Fig. 5.1(d) is shown in Fig. 5.10 (c) for detailed insights. Nevertheless, the wedge angle corresponding to point (2) in Fig. 5.10 (b) is the transition criterion for Type V to VI. For the present study, this value is found to be 43.08º.

Furthermore, for the present simulations, the second wedge angle is much higher than the critical transition angle (43.08º). Therefore, the perfect gas model generates a Type V (MR) interaction and is shown in Fig. 5.9(a). However, the shock structure for the real gas flow model shows drastic change and resembles a Type V (RR) interaction as shown in Fig. 5.9(b). Similar to Earth atmosphere, the higher post shock Mach number in the immediate downstream of the second oblique shock ensures a regular reflection of the reflected shock and restricts the formation of Mach disk [**74**]. Hence a Type V interaction with overall regular reflection is obtained. In other words, this flow model demands a greater second wedge angle to obtain the Type V interaction with Mach Disk (MR), Xiong et al. [**74**].

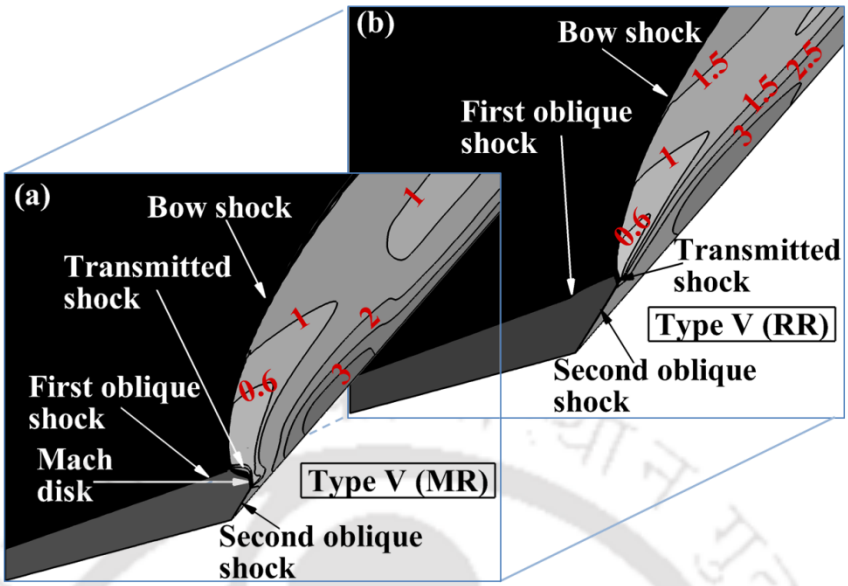

Figure 5.9: Mach contour obtained with θ_1=15º and θ_2=49º configuration by Mars atmosphere flow models: (a) perfect gas flow; and (b) real gas flow.

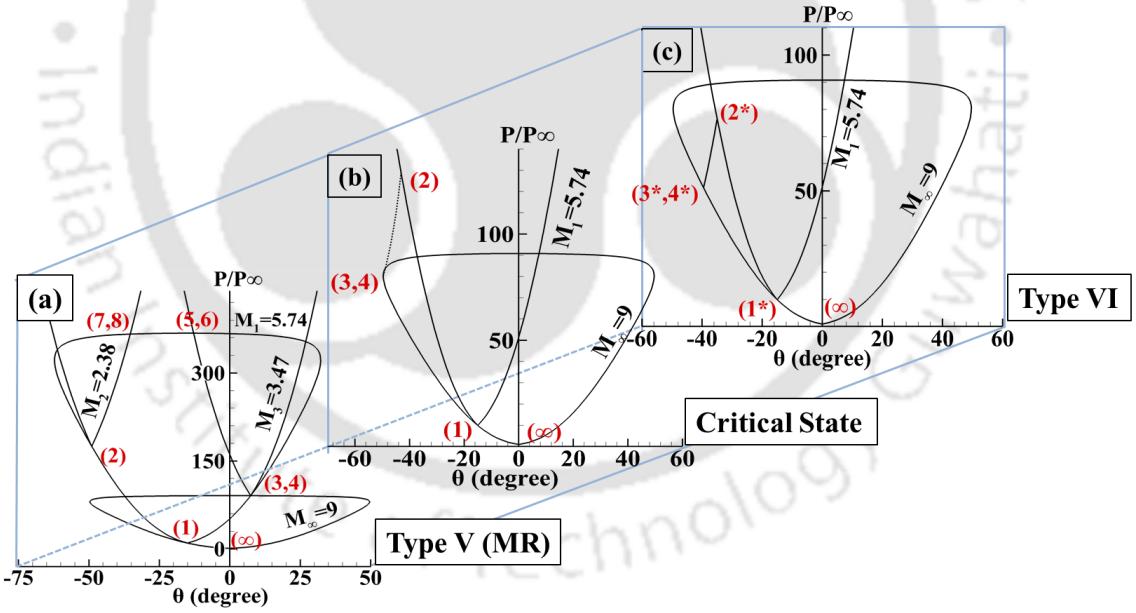

Figure 5.10: Shock polar diagram of different interaction for M = 9, γ= 1.28: (a) Type V with θ_1=15º, θ_2=49º; (b) Critical state between type V and VI; and (c) Type VI with θ_1=15º, θ_2=35º.

As the second wedge angle is further decreased to 35º, the interaction type changes to Type VI interaction. All the important flow features like first wedge oblique shock, second wedge oblique shock, transmitted oblique shock, and contact discontinuity are clearly captured by the density gradient contours for the perfect gas Earth atmosphere model shown in Fig. 5.11(a). In addition to the transmitted shock, an expansion wave also emerges from the interaction point of two incident shocks. This expansion wave gets reflected from the surface of the second ramp and hits the transmitted oblique shock at downstream location causing it to turn downwards (Fig. 5.11(a)). Further, it is observed that the density gradient contour shown in Fig. 5.11(b) obtained from the real gas model in Earth atmosphere shows no distinct difference compared to the perfect gas flow model. Additionally, the surface pressure distribution shown in the same figures reconfirms that no significant difference is present between the models. Similarly, the perfect and real gas flow models of the Mars atmosphere also demonstrated a Type VI pattern with no significant difference in Fig. 5.12. It is worth mentioning that the pressure jump due to the second wedge for perfect gas model is found to be 76.97 which is in excellent agreement with the pressure ratio (76.64) obtained in the Type VI shock polar analysis (Fig. 5.10 (c)).

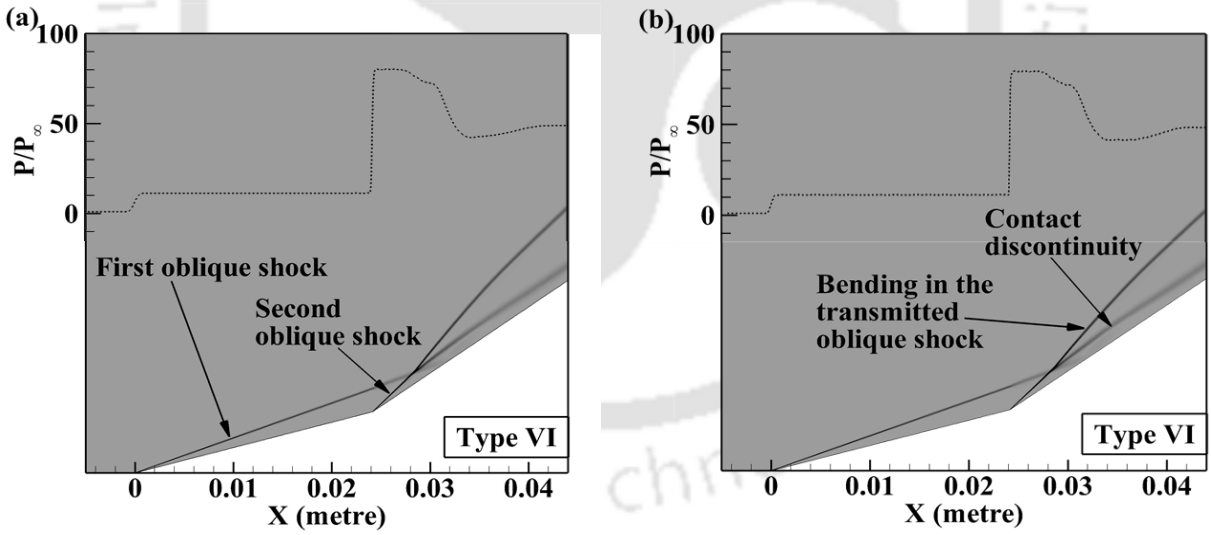

Figure 5.11: Density gradient contour showing Type VI interaction and surface pressure distribution obtained with θ_1=15º and θ_2=35º configuration by Earth atmosphere flow models: (a) perfect gas flow; and (b) real gas flow.

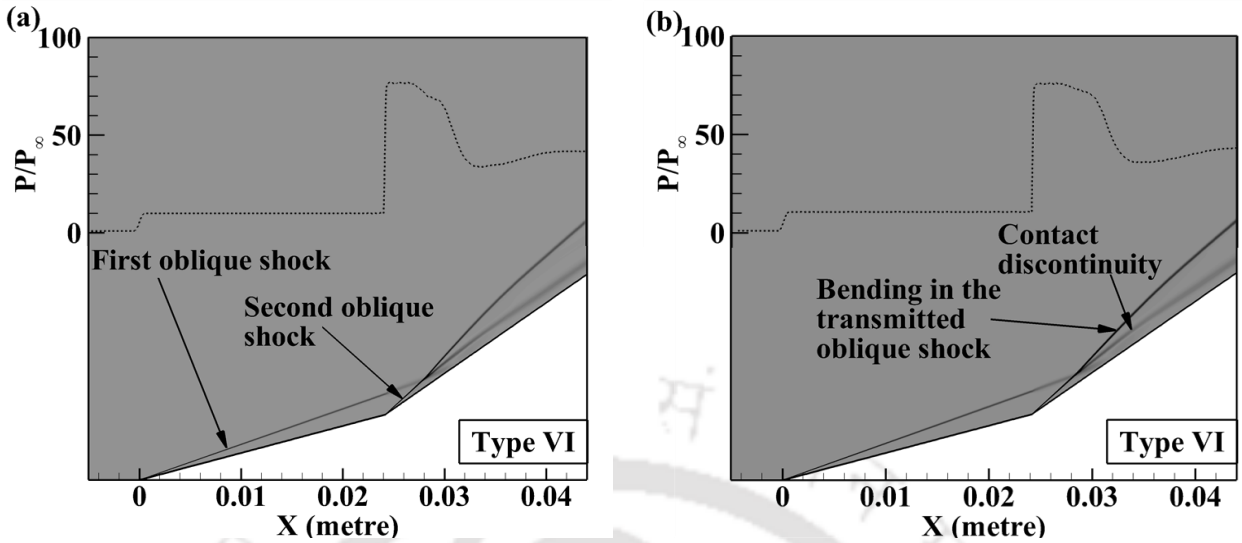

Figure 5.12: Density gradient contour showing type VI interaction and surface pressure distribution obtained with θ_1=15º and θ_2=35º configuration by Mars atmosphere flow models: (a) perfect gas flow; and (b) real gas flow.

In summary, significant differences are observed between the interaction patterns for perfect and real gas models. Here, the real gas effects always tend to attach the secondary wedge shock and reduce the shock layer thickness. This effect is similar to that of decreasing the second wedge angle while keeping other parameters constant for a perfect gas. In other words, due to real gas effects, the real gas flow model demands a higher second wedge angle to yield the same type of interaction as that of the perfect gas flow model.

5.2.2 Effect of freestream stagnation enthalpy

The study has been continued to investigate the effect of stagnation enthalpy. Since the variation in enthalpies does not affect the outcomes of perfect gas models; this section of the study is carried out with only real gas flow model. Simulations are performed at four different stagnation enthalpies each for Earth and Mars cases. The range of freestream stagnation enthalpies considered herein is 1.95 MJ/kg to 10.26 MJ/kg and 1.27MJ/kg to 6.34 MJ/kg for Earth and Mars atmospheres respectively. This variation in enthalpies is accomplished by varying the freestream temperature while keeping all other parameters same as mentioned in Table 5.1.

At first, simulations are performed in the Earth atmosphere for θ_1=15º and θ_2=50º configuration. The Mach contours obtained are shown in Fig. 5.13. At lower enthalpies (1.95 and

3.47 MJ/kg) Type IV interaction is evident. However, as the enthalpy is increased to 6.06 MJ/kg, interaction changes to Type V with overall Mach reflection (MR) and further to Type V with overall regular reflection (RR) at 10.26 MJ/kg. The patterns of surface pressure distribution also indicate the same facts in Fig. 5.14. Here, the pressure jump due to normal shock and compression corner in 1.95 and 3.47 MJ/kg appears to be a single peak. An important point is the location of normal shock is comparatively closer to the second ramp for 3.47 MJ/kg in the type IV interaction. Thus, the span of pressure peak (Fig. 5.14) for 1.95 MJ/kg case is larger than the 3.47 MJ/kg case.

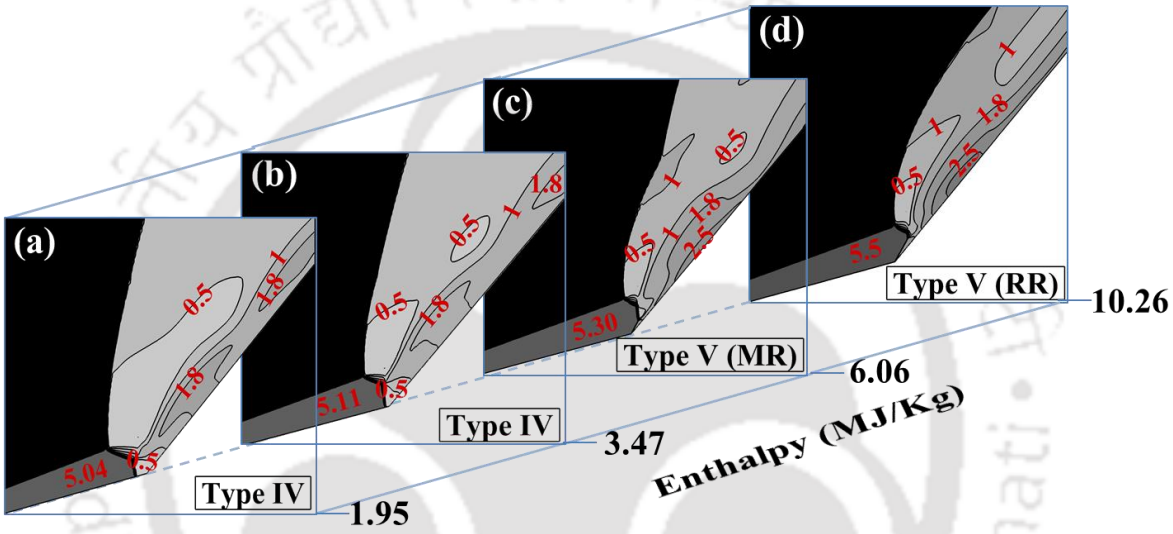

Figure 5.13: Mach contour obtained with θ_1=15º and θ_2=50º configuration by Earth atmosphere flow model at different stagnation enthalpies: (a) 1.95 MJ/Kg; (b) 3.47 MJ/Kg; (c) 6.06 MJ/Kg; and (d) 10.26 MJ/Kg.

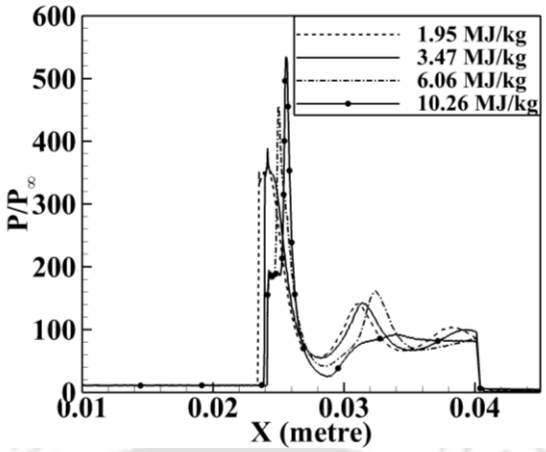

Figure 5.14: Surface pressure distributions obtained with θ_1=15º and θ_2=50º configuration by Earth atmosphere flow model at different stagnation enthalpies.

Here, the decrease in the specific heat ratio with increase in enthalpy is causing higher approaching Mach number (Fig. 5.13) for the second wedge. For example, in the Earth atmosphere, the specific heat ratio downstream of the first oblique shock decreases from 1.40 to 1.38 as the enthalpy is increased from 1.94 MJ/kg to 3.47 MJ/kg resulting in an increase in Mach number from 5.04 to 5.11. Further, as the enthalpy is increased to 6.06 MJ/kg, the specific heat ratio decreases to 1.34, and the Mach number increases to 5.30 and for 10.26 MJ/kg these values are 1.31 and 5.50 respectively. This enhancement in the approaching Mach number increases the maximum deflection angle of the oncoming flow thereby increasing the critical angle for transition of the flow in the region (1) and hence transitions in interaction types. The same fact can be explained with the shock polar diagram at different enthalpies as showed in Fig. 5.15 (a). As the transition can be explained by the shock polar of freestream and region behind the first oblique shock (i.e. region (1)), only these polar are considered herein. In these regions, no dissociation reaction is observed and hence, shock polars are obtained using pressure deflection relation valid for perfect gas flow with the local Mach numbers and specific heat ratio. From the figure, the increase in maximum deflection angle for freestream ($\theta_{max\infty}$) and region (1) polar (θ_{max1}) with enthalpy are evident. This increase in the θ_{max1} of the approaching flow for second ramp, results into greater critical angle of transition between the interaction types. For the first two enthalpies (1.95 MJ/kg and 3.47 MJ/kg) the interaction remains Type IV due to a very small increase in the θ_{max1}. However, the closer appearance of the normal shock for 3.02 MJ/kg case indicates that the increase in θ_{max1} is pushing towards the attachment of the shock at the second ramp foot.

Subsequently, the significant increase in θ_{max1} for 6.06 MJ/kg case enables the attachment of second oblique shock, resulting in a transition from the Type IV to V interaction with MR. Again, for 10.26 MJ/kg case additional increases in θ_{max1} results in the transition from Type V with MR to Type V with RR.

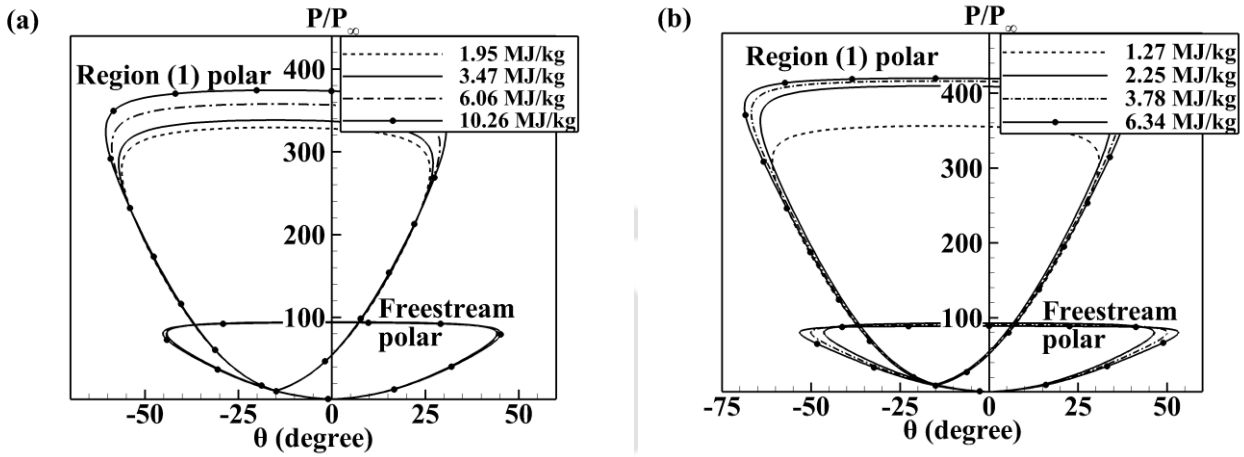

Figure 5.15: Shock polar diagram for different enthalpies with: (a) θ_1=15º and θ_2=50º configuration in Earth atmosphere; and (b) θ_1=15º and θ_2=56º configuration in Mars atmosphere.

Further, the simulations are carried out in the Mars atmosphere with the θ_1=15º, θ_2=56º configuration. The Mach contours are plotted in Fig. 5.16. It is observed that at 1.27 MJ/kg the interaction is of Type IV. As the enthalpy is increased to 2.25 MJ/Kg, interaction changes to Type V (MR) interaction and remain same for the 3.78 MJ/kg case. Though for these two enthalpies the interaction Type is same yet the decrease in shock layer thickness and subsonic region with enhanced enthalpy is evident. In addition, difference in the Mach stem size and location can also be noticed. Again, the increase in enthalpy to 6.34 MJ/kg causes the transition to Type V (RR) interaction. Similar to Earth atmosphere case, the increase in the approaching Mach number (Fig. 5.16) for second ramp results in higher maximum deflection angle (oncoming flow); there by changing the critical transition angle. It is to be noted that, due to the higher sensitivity of specific heat to temperature change in Mars flow condition, results in higher percentage change in the approaching Mach number (18.35% for Mars, 9.13% for Earth) for this case. Figure 5.15 (b) shows the shock polar diagram at different enthalpies for the Mars atmosphere. Here, significant increase in $\theta_{max\infty}$ and θ_{max1} is observed with increase in enthalpy. This consistent increase in maximum deflection angle with enthalpy results in transition from Type IV to Type V (MR)

interaction between 1.27 MJ/kg and 2.25 MJ/kg; and further result in Type V (RR) interaction at 6.34 MJ/kg. It is worth mentioning that, in both flow mediums significant dissociation reaction occurred at higher enthalpies in the downstream region of second ramp. Figure 5.17 displaying mass fraction distribution of oxygen and carbon dioxide along the wall for Earth and Mars atmosphere flow models respectively indicates the occurrence of dissociation.

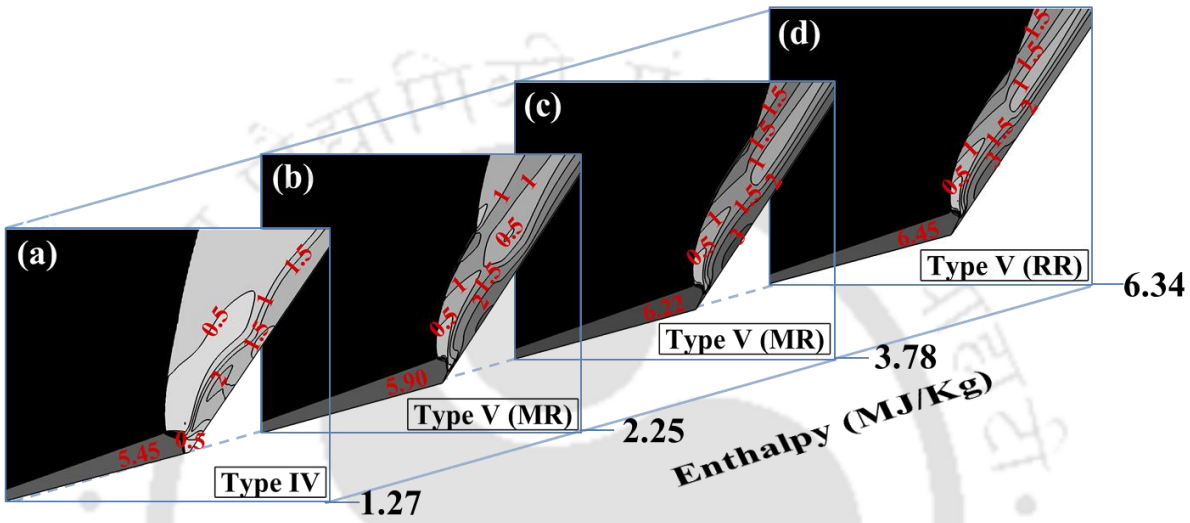

Figure 5.16:Mach contour obtained with θ_1=15º and θ_2=56º configuration by Mars flow model at different stagnation enthalpies: (a) 1.27 MJ/Kg; (b) 2.25 MJ/Kg; (c) 3.78 MJ/Kg; and (d) 6.34 MJ/Kg.

Likewise, the simulations are continued for θ_1=15º and θ_2=45º configuration at the different enthalpies in the Earth atmosphere. Figure 5.18 shows the density gradient contours obtained from these simulations. For the lowest enthalpy, the interaction is a Type V (MR) interaction and as the enthalpy is increased to 3.47 MJ/kg the interaction changes to a Type V (RR) interaction. Further increase in the enthalpy turns the flow fields completely supersonic and the interaction turns into Type VI. Though the additional increase in the enthalpy does not change the interaction type yet noticeable difference in shock layer thickness is evident. The density gradient contours obtained for the Mars atmosphere with θ_1=15º and θ_2=49º configuration are shown in Fig. 5.19. Here, at the lowest enthalpy a Type V (RR) interaction is observed. As the enthalpy is increased to 2.25 MJ/kg the interaction transforms to a Type VI interaction and remains same for additional increase in the enthalpy. However, substantial decrement in the shock layer thickness can be noticed in the same figure. Again, significant dissociation of oxygen and

carbon dioxide is observed at higher enthalpies and hence, these changes in the shock interactions are attributed to collective effects of dissociation reactions and variation of specific heat with temperature.

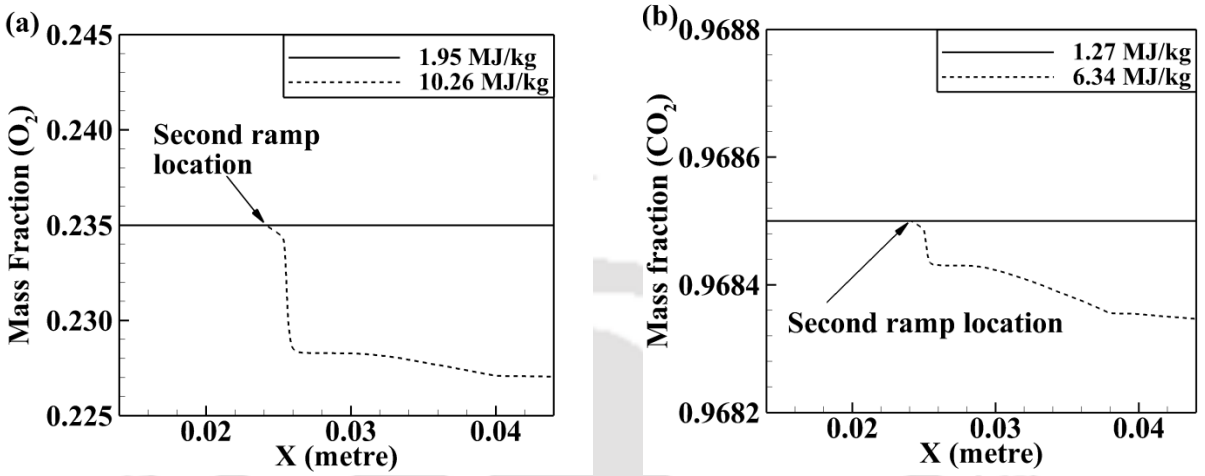

Figure 5.17: Mass fractions of (a) oxygen obtained from θ_1=15º and θ_2=50º configuration by Earth atmosphere flow model (b) Carbon dioxide obtained from θ_1=15º and θ_2=56º configuration by Mars atmosphere flow model.

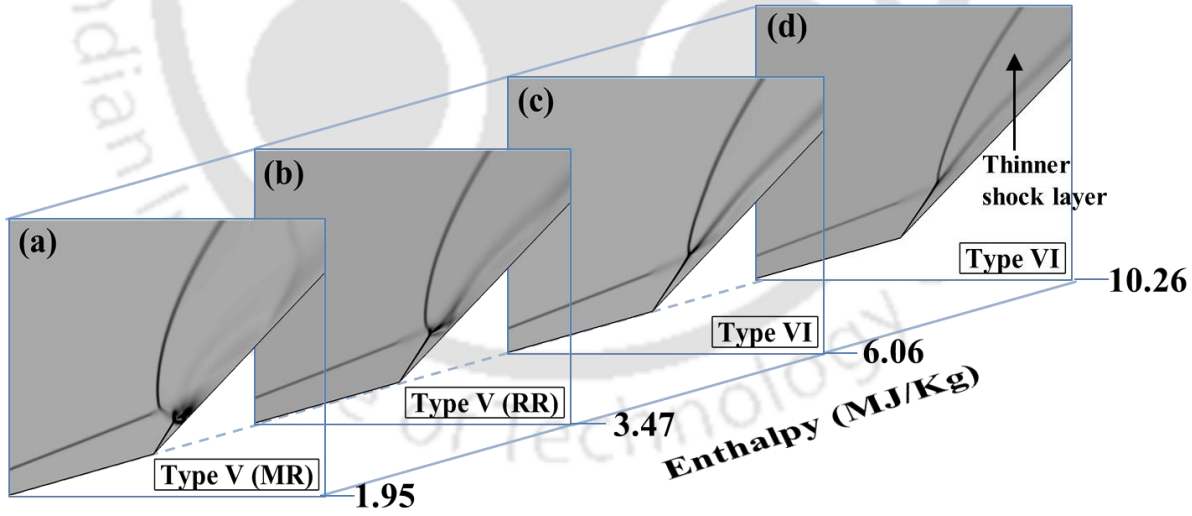

Figure 5.18: Density gradient contour obtained with θ_1=15º and θ_2=45º configuration by Earth atmosphere flow model at different stagnation enthalpies: (a) 1.95 MJ/Kg; (b) 3.47 MJ/Kg; (c) 6.06 MJ/Kg; and (d) 10.26 MJ/Kg.

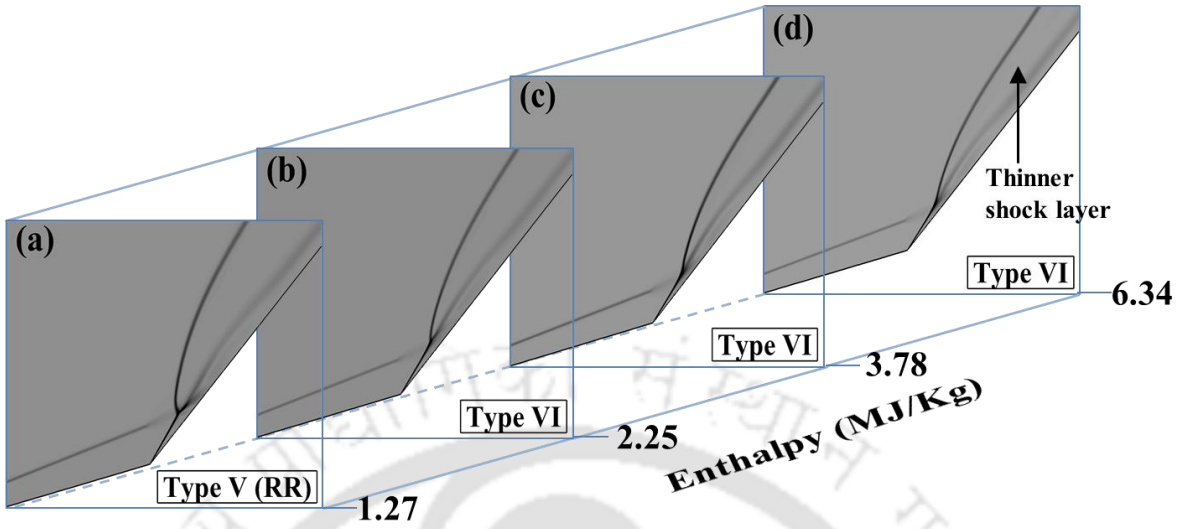

Figure 5.19: Density gradient contour obtained with θ_1=15º and θ_2=49º configuration by Mars atmosphere flow model at different stagnation enthalpies: (a) 1.27 MJ/Kg; (b) 2.25 MJ/Kg; (c) 3.78 MJ/Kg; and (d) 6.34 MJ/Kg.

The investigation is also performed for θ_1=15º and θ_2=35º configuration. For both Earth as well as Mars atmosphere, it is found that the variation in enthalpy does not change the interaction type and it remains Type VI all throughout. However gradual decrease in the shock layer thickness with increase in enthalpy can be noticed for both the flow mediums from the density gradient contours plotted in Fig. 5.20 and 5.21. For this configuration, no prominent dissociation is observed in any of the flow models.

Overall, it is observed that change in enthalpy has significant effects on the shock/shock interactions considered herein. The highest effects are witnessed for θ_1=15º & θ_2=50º and θ_1=15º & θ_2=56º configurations, where the shock interactions change from Type IV to Type V (RR) for the Earth and Mars atmosphere case respectively. Patterns in the outcomes suggest that increase in the stagnation enthalpy leads to the attainment of attached oblique shock in the second ramp, and hence, the transition from Type IV to V interaction occurs. Further increase in enthalpy increases the critical angle for transition leading to a Type VI interaction. Hence, it is observed that, for the same configuration, transition of one interaction type to other occurs with an increase in the stagnation enthalpy.

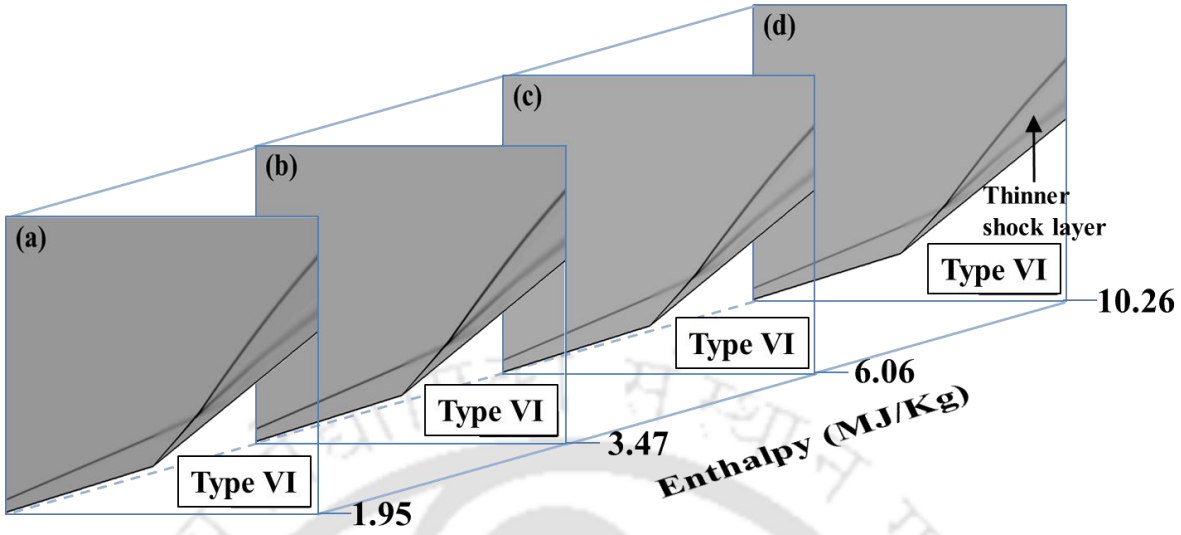

Figure 5.20: Density gradient contour obtained with θ_1=15º and θ_2=35º configuration by Earth atmosphere flow model at different stagnation enthalpies: (a) 1.95 MJ/Kg; (b) 3.47 MJ/Kg; (c) 6.06 MJ/Kg; and (d) 10.26 MJ/Kg.

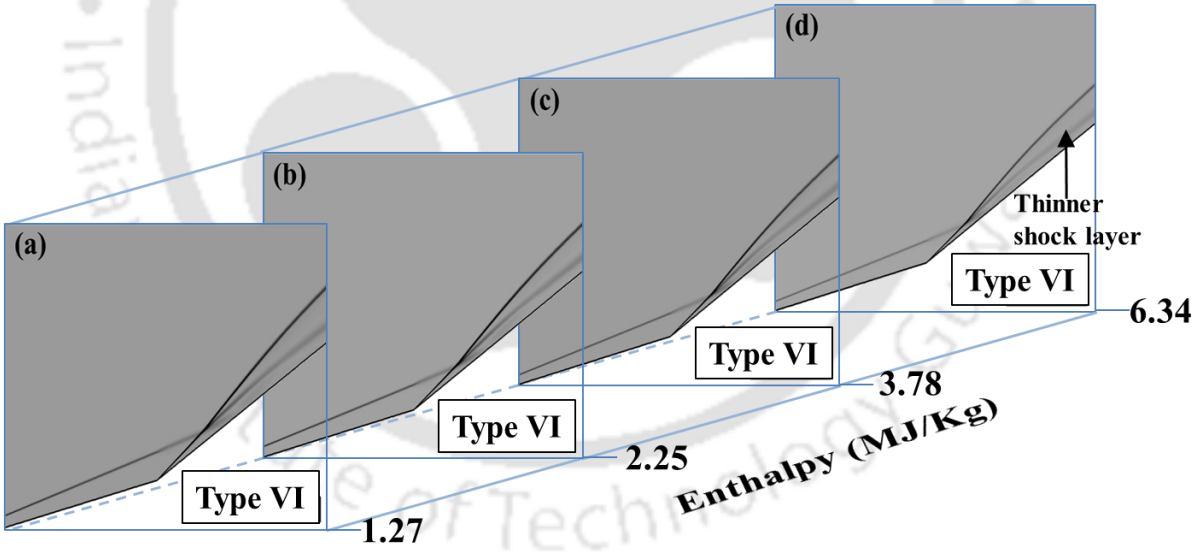

Figure 5.21: Density gradient contour obtained with θ_1=15º and θ_2=35º configuration by Mars atmosphere flow model at different stagnation enthalpies: (a) 1.27 MJ/Kg; (b) 2.25 MJ/Kg; (c) 3.78 MJ/Kg; and (d) 6.34 MJ/Kg.

5.3 Conclusion

An investigation on different types of shock/shock interaction in Earth and Mars atmospheric condition is successfully carried out. Different configurations are used specifically to generate Edney's Type IV, V and VI interactions with the perfect gas solver. Initial comparative study between the outcomes of respective perfect and real gas flow models reveals significant difference in flow structures. For Mars atmosphere models, the interaction type changes from Type V (MR) to Type V (RR) for configurations with second angle 49^0. For Earth atmosphere models, though no change in the type of interaction, yet significant difference in the flow field is observed. Disagreement in the location of normal shock attached to the first wedge in Type IV interaction is noticed for the first configuration. Similarly, in second configuration (Type V (MR) interaction), significant difference in the Mach stem size and location are observed. Based on these trends it can be concluded that, in Earth as well as Mars atmosphere, real gas effects in real gas flow model tends to cause transition between different types of interactions at higher value of second wedge angle as compared to perfect gas model. Further, higher discrepancies in the Mars atmosphere model is attributed to higher dependency of specific heat to temperature change in this particular model. Investigation of variation in stagnation enthalpy reveals that, the interaction types are very sensitive to change in stagnation enthalpies. Significant difference in the flow structures are observed for all configurations in both flow mediums. It is observed that increase in enthalpy tends to transform the interaction patterns to a Type VI. Further, it is concluded that, different enthalpies yield different interaction patterns/types for the same configuration.

Chapter 6 : Assessment of Real Gas Effects on Shock/Expansion Fan Interaction.

Overview

In this chapter, inviscid flow simulations are performed to investigate the real gas effects on shock/expansion wave interactions. Initial perfect gas simulations at low enthalpy capture the flow structures efficiently and outcomes are found to excellent agreement with the inviscid analytical calculations. Further, the simulations with the real gas solver for different enthalpies showed that the variation in enthalpies significantly changes the flow structures. It is observed that an increase in enthalpy has a decreasing and increasing effect on post-shock and post-expansion wave Mach numbers respectively. Another important observation is the decreasing peak pressure ratio with increment in the enthalpy. These effects are marked to be more pronounced for Mars environment.

6.1 Introduction

The design of high-speed aircraft necessitates the proper predictions of flow structures associated with it. These flights often encounter shocks and expansion fans. Further, the shock and expansion waves may interact and complicate the flow structure. Hence, researcher community has performed many investigations associated with this interaction. Based on the literature survey it has been noticed that the presence of shock/expansion fan interaction can significantly affect the boundary-layer separation and can delay the Mach reflection. Further, few researchers also emphasized on flow filed modification caused by this interaction. However, it is noticed that the important aspect of real gas effects in predicting these flow structures is left untouched. Further, these investigations consider only air as the flow medium. In view of this, for accurate prediction of flow structure arising due to this interaction, simulations in Earth, as well as Mars environment with real gas effects are planned for the current study. The investigation is performed for different configurations and at different enthalpies. Further, the influence of the real gas effects on the flow field alteration is discussed with the aid of shock polar diagrams. Thus, the in-house developed real gas (non-equilibrium) solver along with the prefect gas solver mentioned earlier, are employed for the current investigation.

6.2 Results and Discussion

Inviscid simulations are performed to investigate the real gas effects on the flow field involving shock and expansion fan. Two test cases of shock impingement before and after an expansion corner are considered herein as shown in Fig. 6.1. The shock impinging location is at horizontal distance, X_{sh}=13.42 mm from the expansion corner. For both configurations, the expansion corner is at Y=0.0 and X=70mm. The oblique shock is generated using a wedge of 4º and the centered expansion fan is generated with an expansion corner of 2.5º. The freestream conditions considered for both Mars and Earth atmosphere simulations are Mach 8, freestream total pressure 5.38 MPa, freestream total Temperature 800 K (Chung and Lu [**79**]. The detailed discussion about the investigation is described in the following sub-sections.

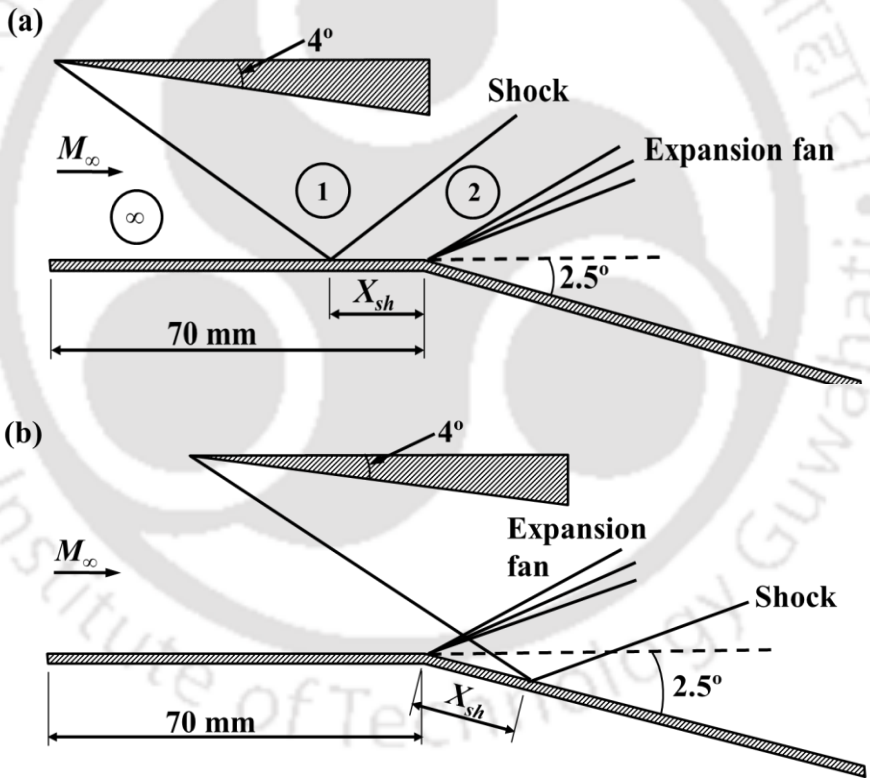

Figure 6.1: Schematic of test cases considered for shock impingement (a) before expansion corner (b) after expansion corner.

6.2.1 Flow fields

To nullify the effects of grid sizes, a grid independence study is carried out prior to an in-depth investigation. For the purpose, simulations with a perfect gas Earth atmosphere flow model

are performed for the shock impingement before the expansion corner case. The surface pressure distribution obtained from three different meshes are plotted along with the analytical pressure distribution [**25**] and is shown in Fig. 6.2 (a)**.** No significant deviation in the results is evident for the 915x80 and 1025x100 grids. Furthermore, the residue history of the simulations with these grids is plotted in Fig. 6.2 (b). Hence, the 915x80 grid size is chosen for the rest of the studies.

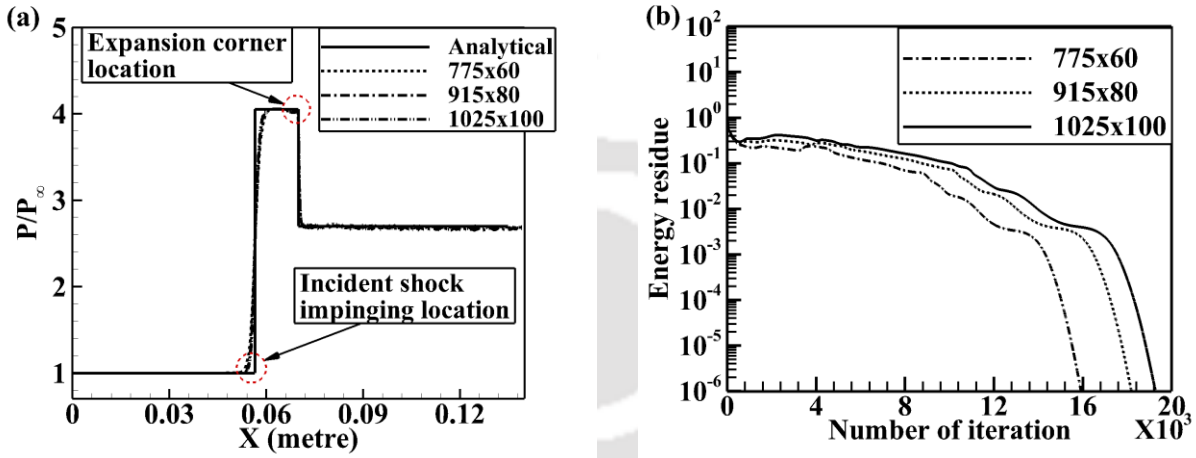

Figure 6.2: (a) Surface pressure distribution and (b) residue history obtained with perfect gas Earth atmosphere model before expansion corner case for three different grids.

The density gradient obtained from the same gas model and geometry is shown in Fig. 6.3 (a). It is evident that all the important flow structures such as incident shock, reflected shock and expansion fan are captured very well. From the Mach contour (Fig. 6.3 (b)), it is visible that the Mach number decreases across the incident oblique shock and reflected shock, which then again increases across the expansion waves. Further, shock impingement and expansion corner location can be visualized by the normalized surface pressure distribution shown in Fig. 6.2**.** The pressure distributions obtained are in good agreement with the analytical predictions. Here, the pressure ratio remains unity until the shock impinges at the wall; across this point, the flow gets compressed due to the incident as well as reflected shock and as a result, the pressure ratio jumps

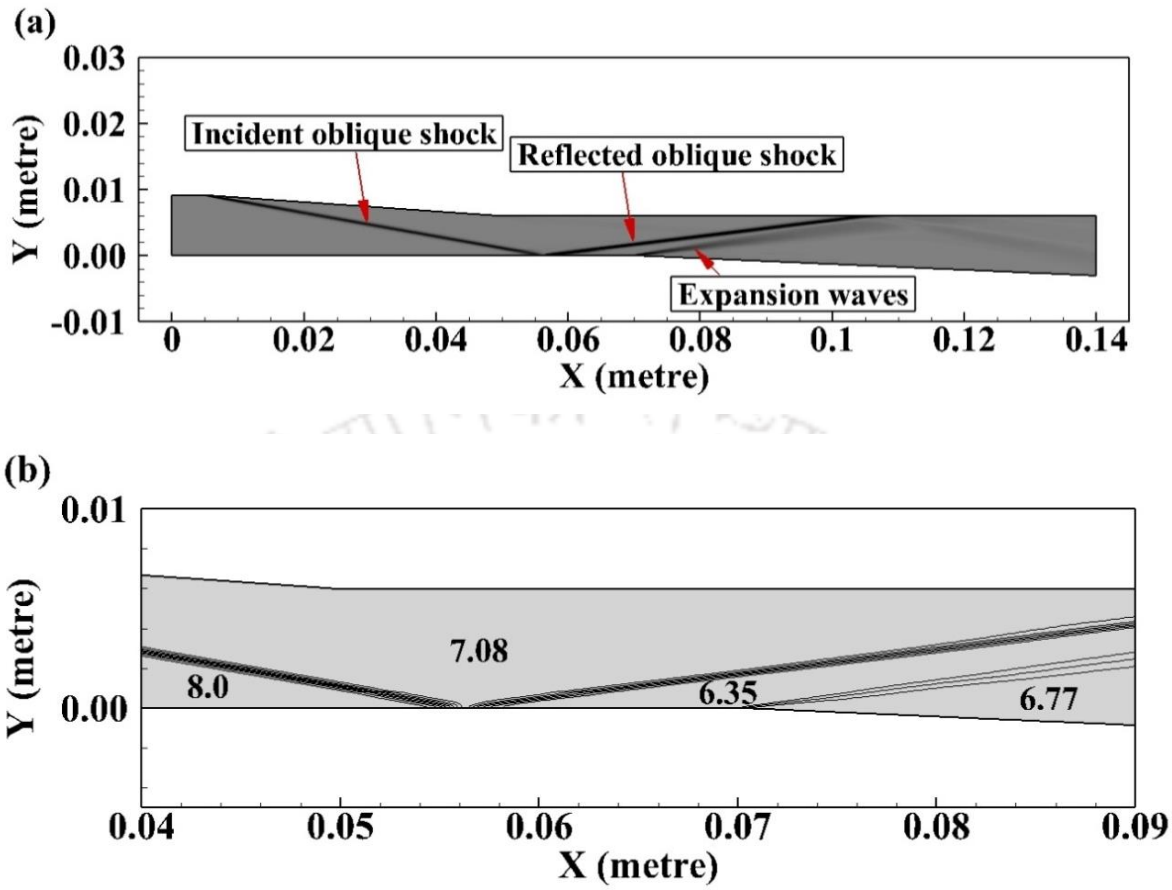

Figure 6.3: Contours obtained with perfect gas Earth atmosphere model before expansion corner case ;(a) Density gradient contour; (b) Mach contour (Enlarge view).

to 4.05; as the flow is relaxed across the expansion corner the pressure ratio drops to 2.70. Similarly, simulations were performed for the Mars atmosphere with the perfect gas solver. The density gradient obtained is shown in Fig. 6.4. All the important flow features are evident in the same figure. Again, the surface pressure distributions are in good agreement with the analytical results [**25**] as shown in Fig.6.5. Here, the peak pressure ratio due to shock impingement is found to be 3.73 and the pressure ratio across the expansion corner is 2.52. In both atmospheric conditions, it is observed that the pressure ratio just upstream of the expansion corner gets reduced by a certain quantity. This shows that the upstream flow is also influenced by the expansion corner.

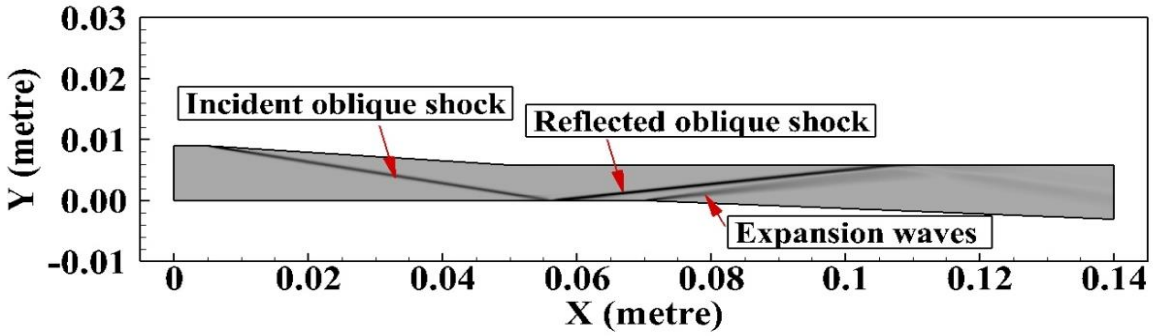

Figure 6.4: Density gradient contour obtained with perfect gas Mars atmosphere model before expansion corner case.

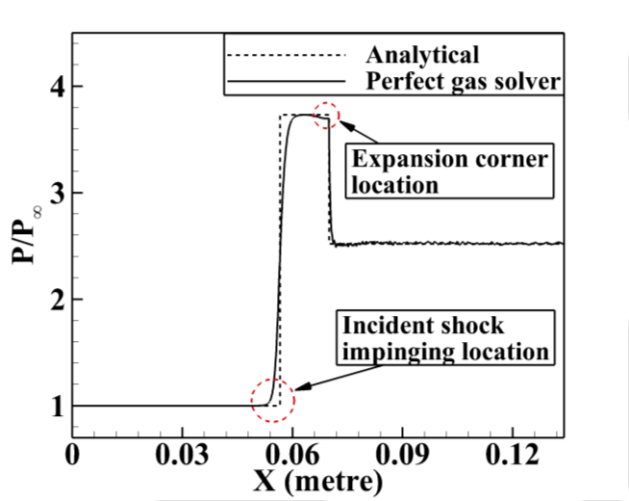

Figure 6.5: Surface pressure distribution obtained with perfect gas Mars atmosphere model before expansion corner case.

The study is continued for the case where shock impinges after the expansion corner. Figure 6.6 shows the density gradient and Mach contour for the perfect gas Earth atmosphere flow model. Here, the incident shock directly interacts with the expansion waves. All the flow structures and the bending of expansion waves due to interaction are clearly evident in the figure. Here, flow in the vicinity of the wall passes through the expansion corner, incident shock, reflected shock. Accordingly, the Mach number increases from 8 to 8.64 across the expansion corner, then it decreases to 7.61 as it passes through the incident oblique shock.

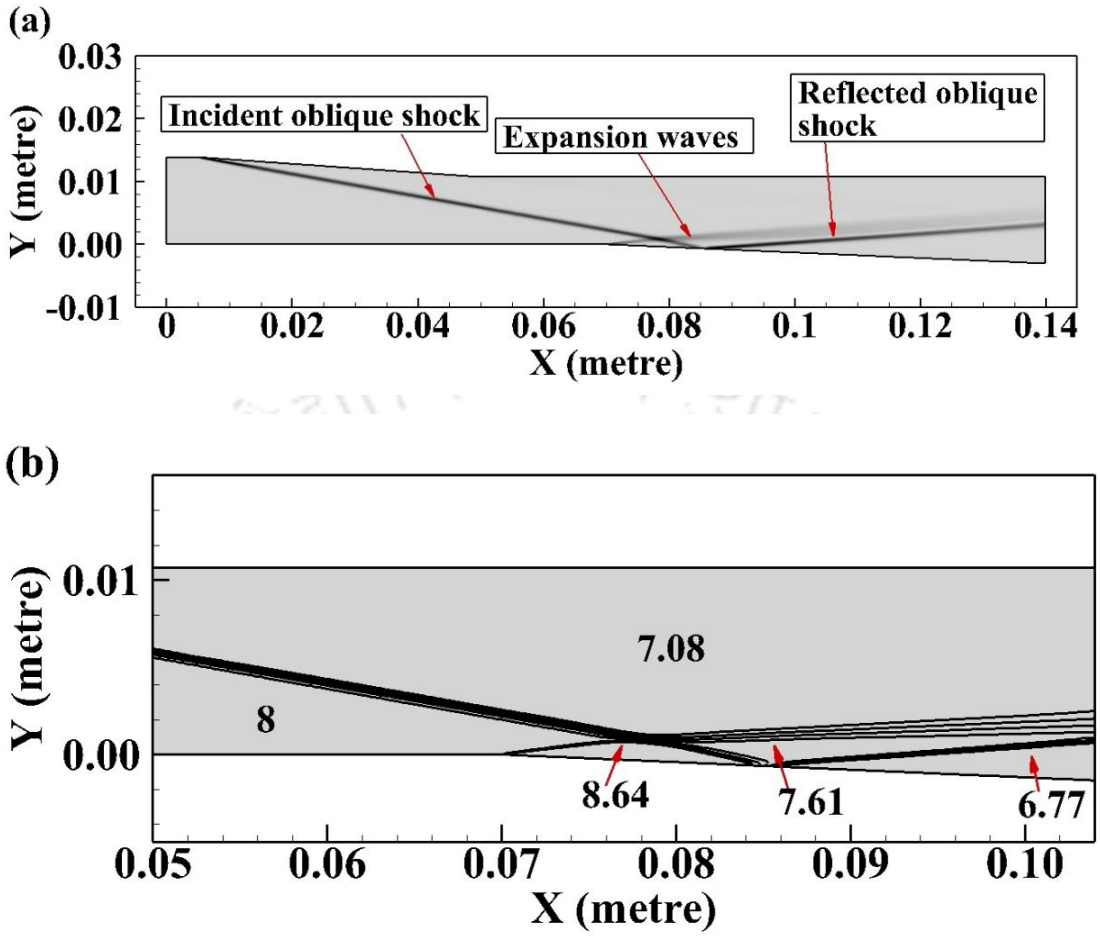

Figure 6.6: Contours obtained with perfect gas Earth atmosphere model after expansion corner case ;(a) Density gradient contour; (b) Mach contour (Enlarge view).

Further, across the reflected shock Mach number is reduced to 6.77. The surface pressure variation obtained from the same simulation is plotted in Fig. 6.7. The pressure ratio decreases sharply to 0.59 as the flow passes through the expansion corner, then between the expansion corner and shock impinging point it remains constant. Across this point, the pressure ratio increases to 2.69 and maintains this ratio downstream. For the same configuration, the simulations are performed for Mars atmospheric conditions. Incident shock, reflected shock and expansion fan are clearly visible in the density gradient contour shown in Fig. 6.8. Furthermore, the surface pressure plot showed in Fig.6.9 shows the same trend as that of the Earth atmosphere case. Here, across the expansion corner, the pressure ratio is decreased to 0.63 and across the shock impinging point it is increased to 2.51.

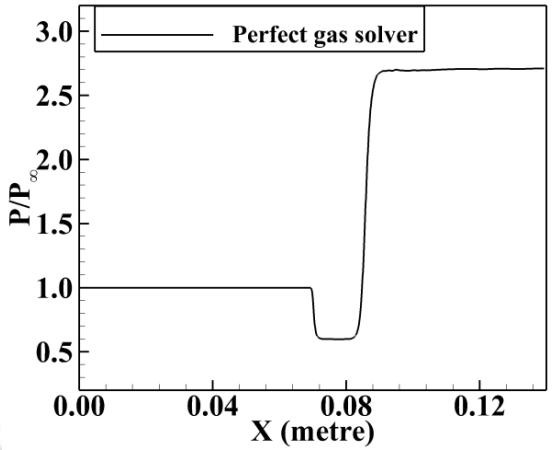

Figure 6.7: Surface pressure distribution obtained with perfect gas Earth atmosphere model after expansion corner case.

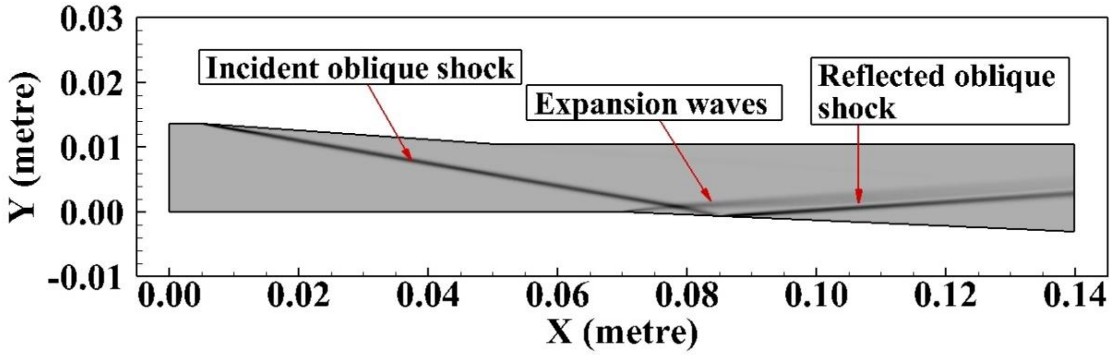

Figure 6.8: Density gradient contour obtained with perfect gas Mars atmosphere model after expansion corner case.

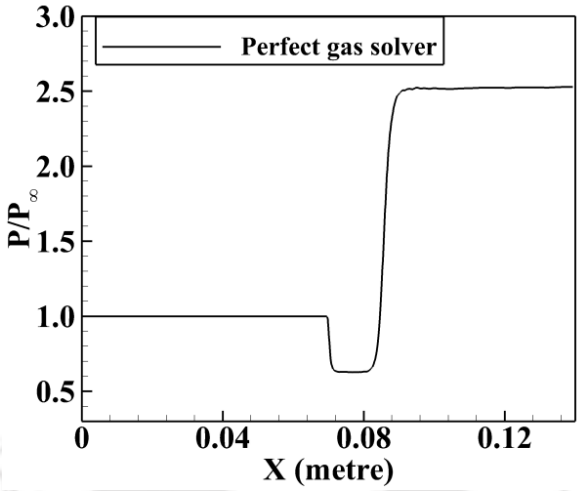

Figure 6.9: Surface pressure distribution obtained with perfect gas Mars atmosphere model after expansion corner case.

6.2.2 Effect of freestream stagnation enthalpy

The study has been continued with the real gas flow solver capable of simulating in Earth as well as Mars atmospheric conditions to investigate the effects of stagnation enthalpy. The enthalpies are varied by changing the freestream temperature only and the rest of the freestream parameters are kept the same as mentioned in the above section**.** For the Earth atmosphere, the enthalpies are varied in a range of 2.09 MJ/kg to 8.24 MJ/kg and For the Mars atmosphere it is varied from 1.37 MJ/kg to 5.14 MJ/kg. The details of these simulations are discussed below.

The simulations are performed with real gas solver at three different enthalpies for the shock impingement before expansion corner case. The Mach contours in Earth and Mars medium are shown in Fig. 6.10 and 6.11 respectively. Here, an increase in the post-shock Mach number across the incident and reflected shock with increasing enthalpy is observed for both flow mediums. The rise in specific heat value with enthalpy results in a lesser percentage rise in temperature. In addition, the specific heat ratios decrease with increasing enthalpy and hence, higher post-shock Mach numbers. Another important observation is the decrease in peak pressure ratio with an increase in enthalpy from the surface pressure distributions plotted in Fig. 6.12. The percentage decrease between the lowest and highest enthalpy is found to be 2.24 % for the Earth atmosphere and 10.59 % for the Mars atmosphere. This is contrary to the fact that, for the same flow deflection angle and specific heat ratio, the pressure ratio should increase with the

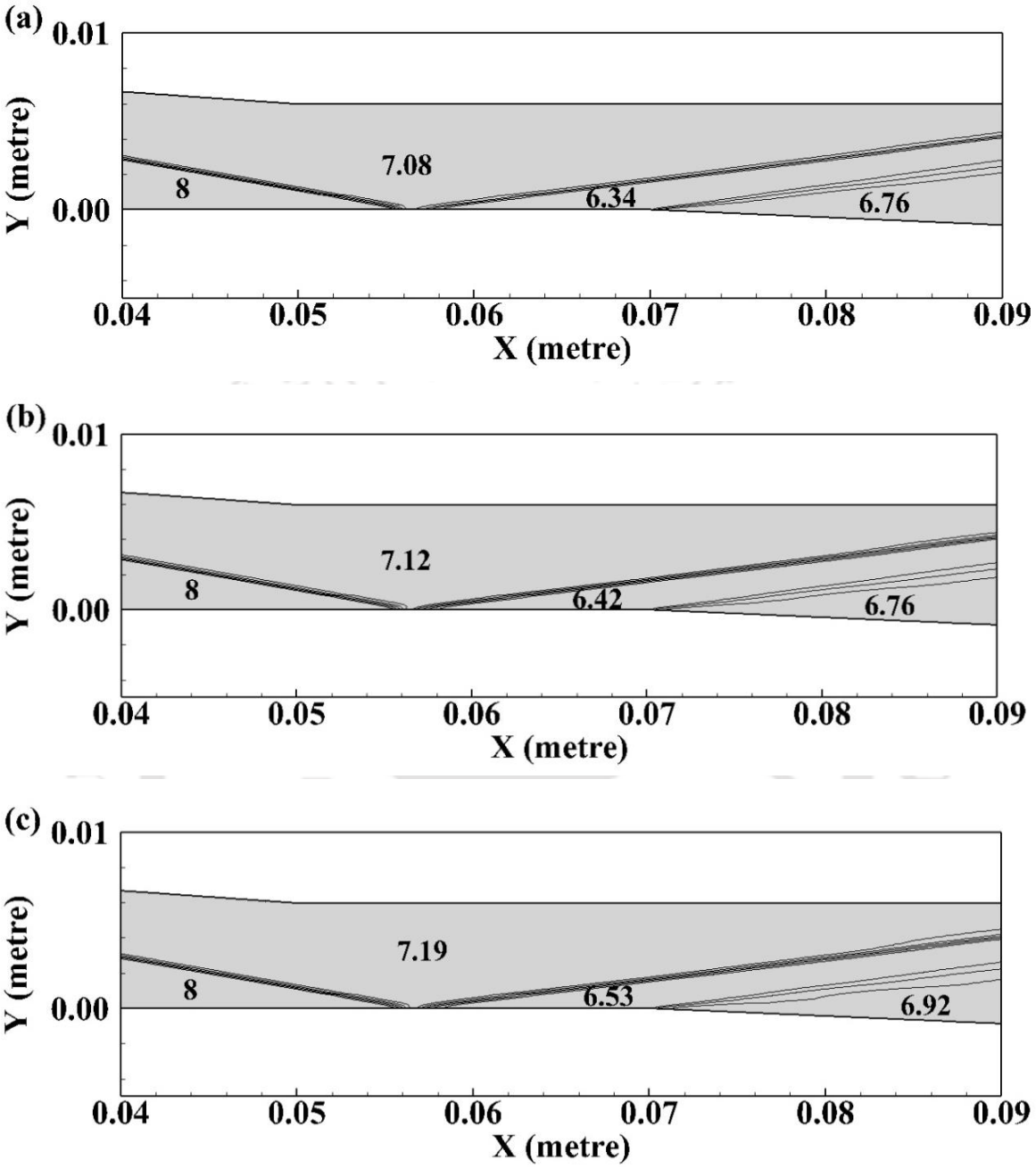

Figure 6.10: Mach contours at different enthalpies in Earth atmosphere. (a) 2.09 MJ/kg (b) 5.55 MJ/kg and (c) 8.24 MJ/kg.

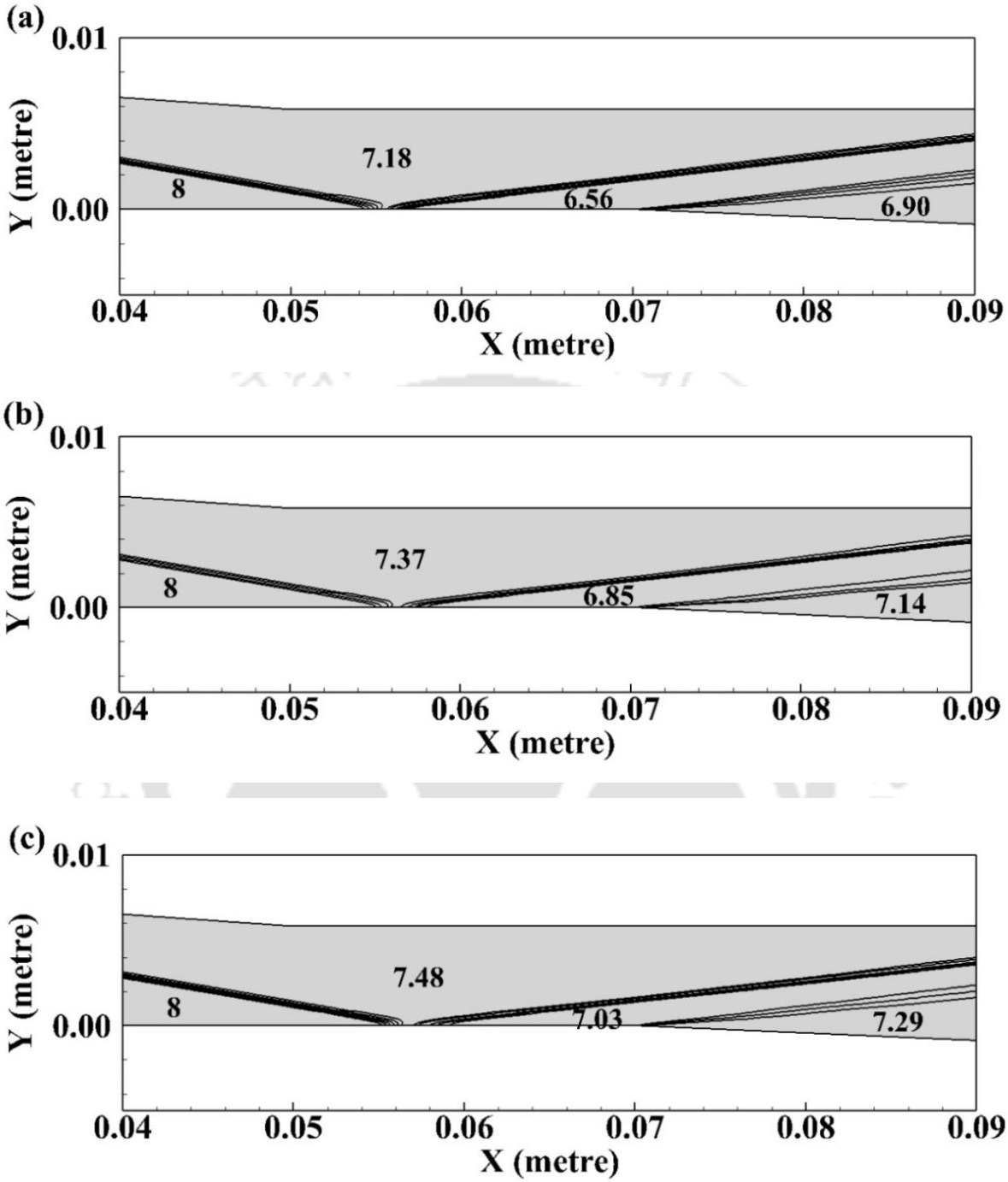

Figure 6.11: Mach contours at different enthalpies in Mars atmosphere for shock impinging before expansion corner. (a) 1.37 MJ/kg (b) 2.64 MJ/kg and (c) 5.14 MJ/kg.

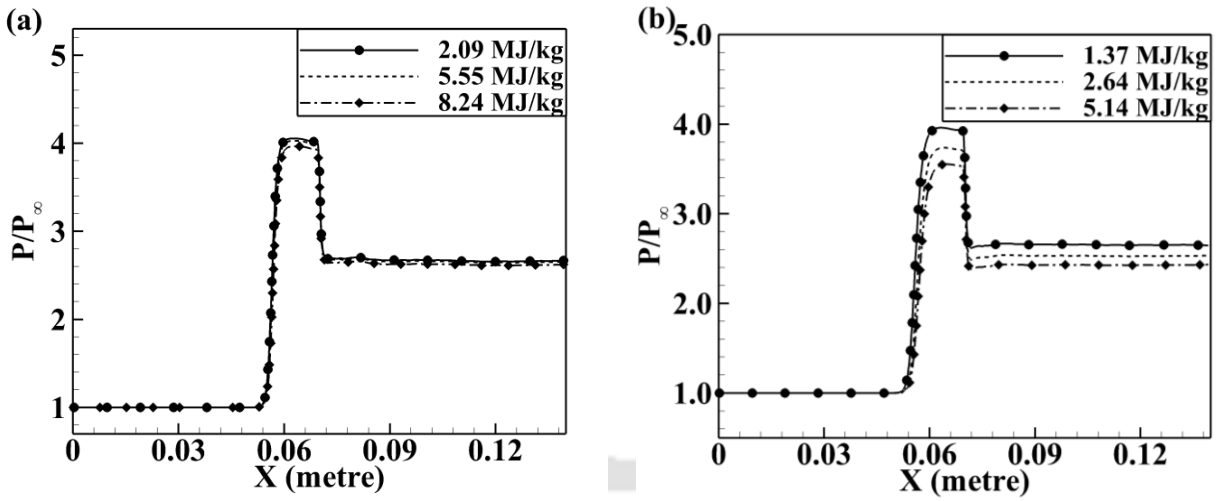

Figure 6.12: Surface pressure distribution at different enthalpies for shock impinging before expansion corner case. (a) Earth Atmosphere (b) Mars atmosphere.

increase in Mach number [**25**]. However, this decrease in the pressure ratio can be explained by the effects of decreasing specific heat ratio with increasing enthalpy, which tends to decrease the pressure ratio. For example, for the air medium, the variation in enthalpy from 2.09 MJ/kg to 8.24 MJ/kg decreases the specific heat ratio across the incident shock from 1.40 to 1.36 thereby increasing the Mach number of the region from 7.08 to 7.19. Hence, it is observed that the change in the specific heat ratio is more dominate than the increase in Mach number for decrease in pressure ratio.

Further, to quantify this observation, pressure deflection diagrams are drawn with the relations valid for perfect gas [**25**] with the local Mach number and specific heat ratio and are shown in Fig.6.13. Here, region (1), region (2) and region (∞) are the corresponding to the regions marked in Fig. 6.1(a). To start with, M_∞ =8.0 polar are drawn. As the flow in the region (1) must be parallel to the wedge, hence point (1) is marked at M_∞ polar at flow deflection angle equal to 4º. From this point, M_1 polar are drawn. The flow in the region (2) must be parallel to the wall. Therefore, point (2) is marked at the intersection of the M_1 polar and zero deflection line. It is clearly evident that the pressure ratio (P_2/P_∞) is lesser at higher enthalpies. Furthermore, the deviation is noticed to be more significant for Mars atmospheric conditions. This is attributed to the fact that, specific heat values change more sharply with the change in temperature for Mars atmosphere.

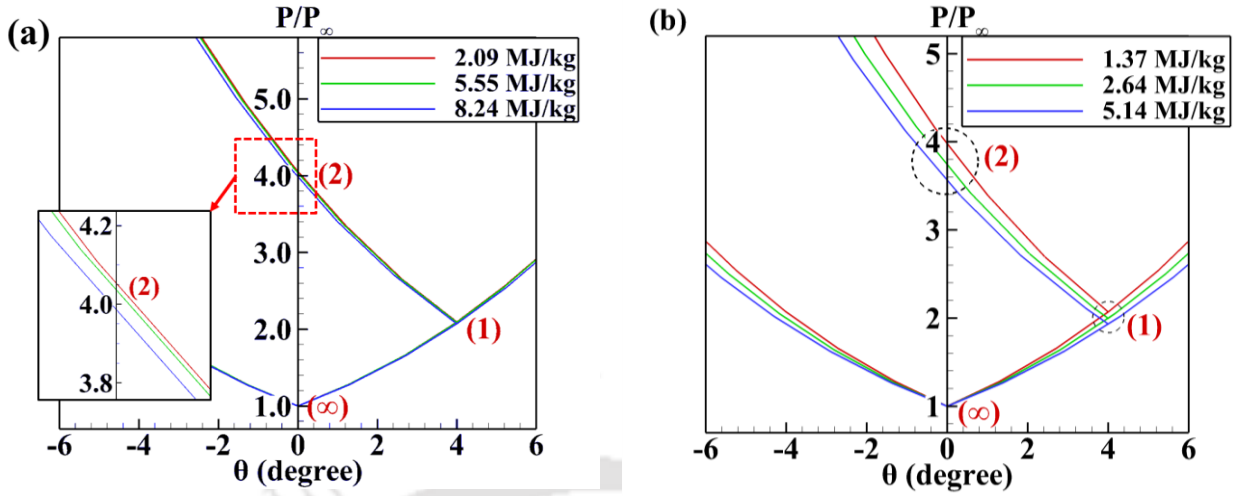

Figure 6.13: Shock polar diagram at different enthalpies for shock impinging before expansion corner case. (a) Earth Atmosphere and (b) Mars atmosphere.

The investigation is continued for shock impingement after the expansion corner with the same solvers. Here, the expansion waves directly interact with the incident shock. The bending in incident shock and expansion waves is evident in the Mach contours shown in Fig. 6.14 and 6.15. Further, it is observed that an increase in enthalpy increases the Mach number across shocks and reduces across the expansion fan. Similarly, the surface pressure distributions plotted in Fig. 6.16 reveals that across the expansion fan the change in pressure ratio is not significant for the Earth atmosphere. However, for the Mars atmosphere, the changes are found to be significant. The percentage reduction in pressure ratio peak for the Earth atmospheric condition is found to be only 1.81% against a reduction of 8.69 % for the Mars atmosphere. Another important observation is that, for the Martian condition the shock impingement location shift downstream with increase in enthalpy. These changes are attributed to the temperature dependent specific heat and reduction in specific heat ratio with enthalpy resulting in the decrease in the pressure ratio. It is important to note that, for all the simulations the flow field temperatures are not high enough to induce any dissociation reaction and hence only the specific heat variation contributes to the real gas effects. Further, the deviations in the results are found more prominent in Mars atmosphere as the specific heat of that gas is more sensitive to temperature variation.

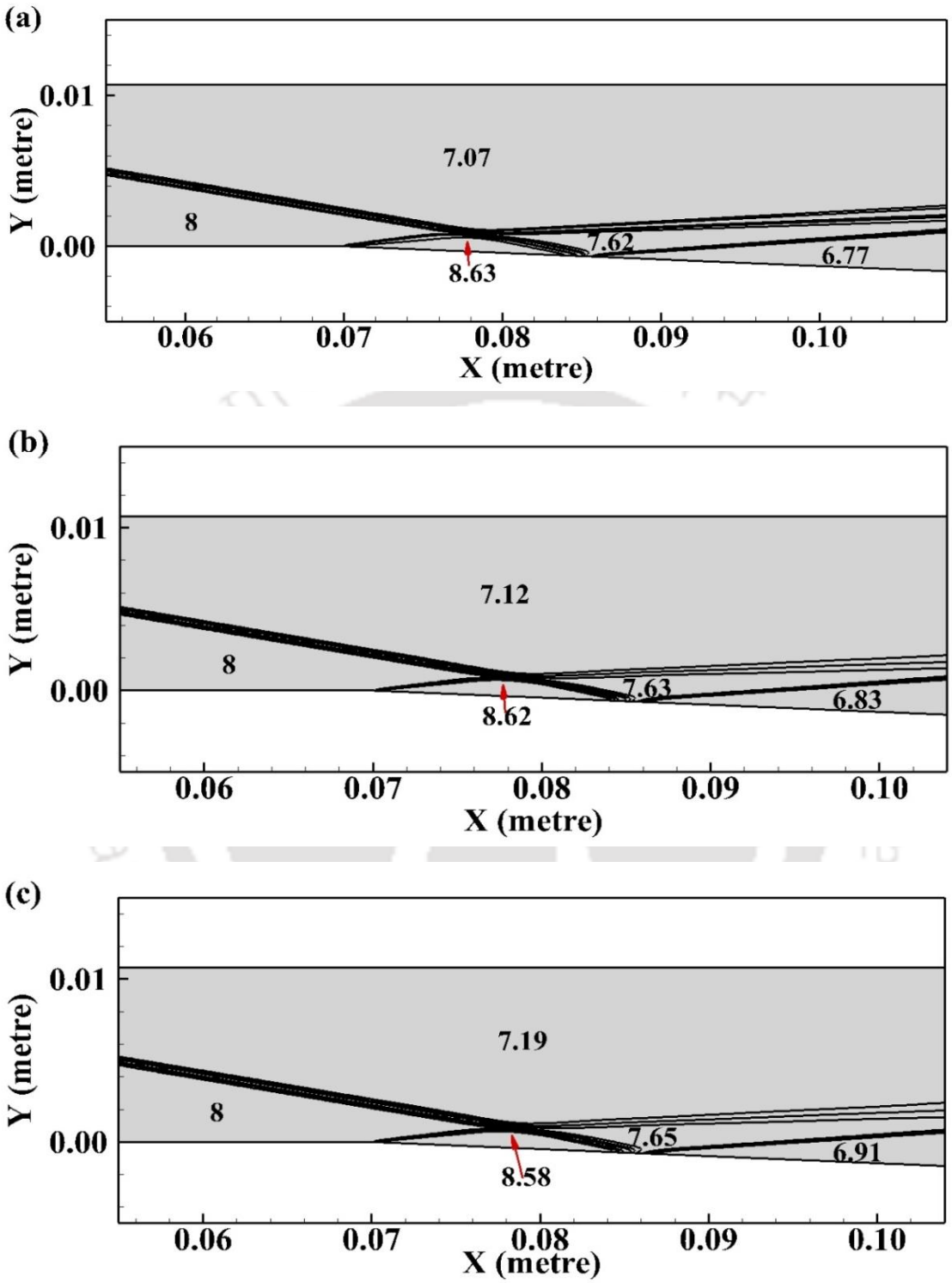

Figure 6.14: Mach contours at different enthalpies in Earth atmosphere for shock impinging after expansion corner. (a) 2.09 MJ/kg (b) 5.55 MJ/kg and (c) 8.24 MJ/kg.

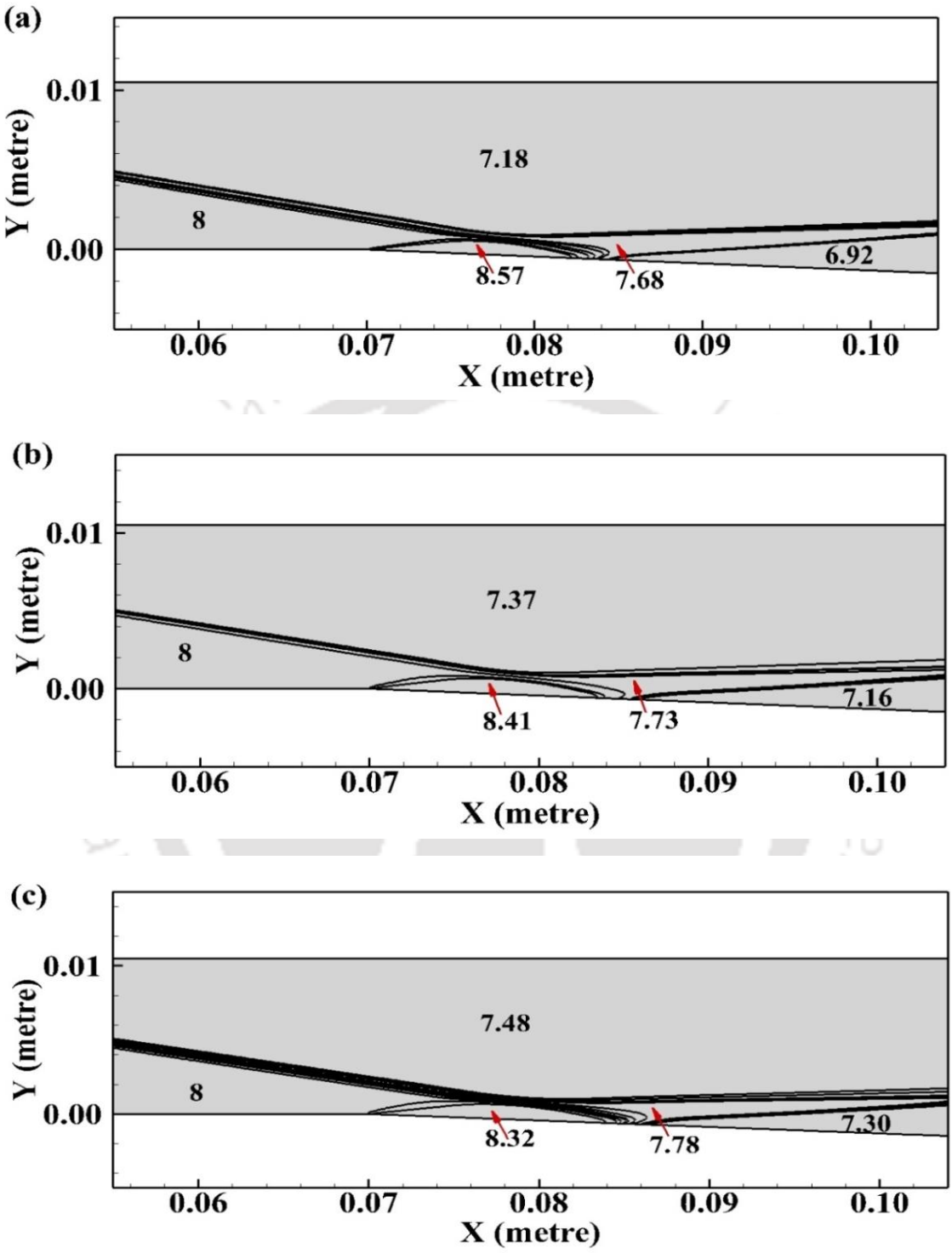

Figure 6.15: Mach contours at different enthalpies in Mars atmosphere for shock impinging after expansion corner. (a) 1.37 MJ/kg (b) 2.64 MJ/kg and (c) 5.14 MJ/kg.

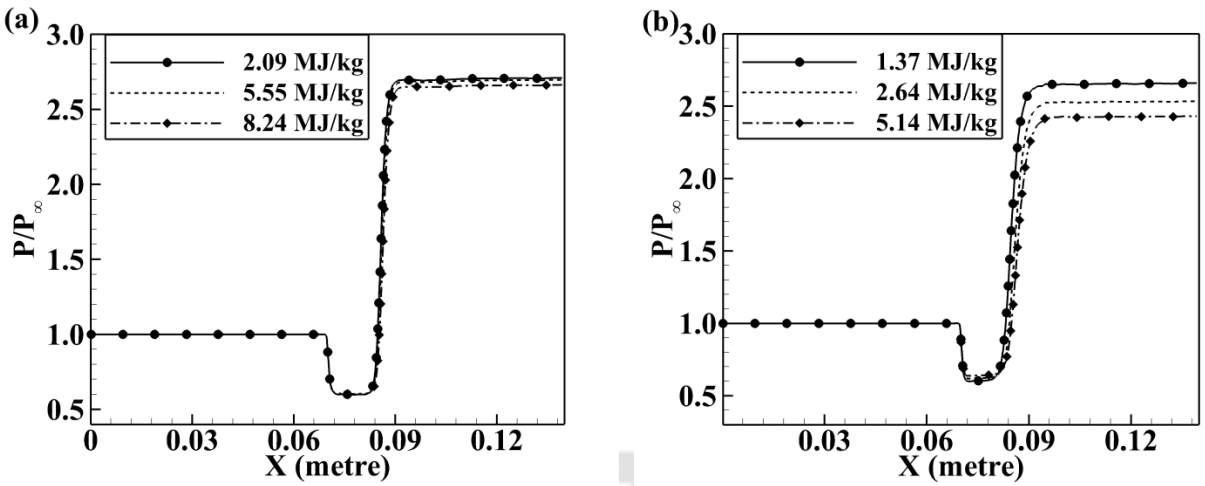

Figure 6.16: Surface pressure distribution at different enthalpies for shock impinging after expansion corner case. (a) Earth Atmosphere and (b) Mars atmosphere.

6.3 Conclusion

An investigation of shock/expansion fan interaction is performed with perfect gas and real gas solvers in Earth and Mars atmospheric conditions. Two configurations with shock impingement (a) before and (b) after expansion corner are considered herein. The perfect gas results are found to be in good agreement with the analytical calculations. Further, the investigations with real gas solvers indicate that variation in the enthalpy causes significant changes in the flow fields. For both the configurations and gas models, it is observed that, increase in enthalpy results in an increase in post-shock Mach number and a decrease in the post-expansion corner Mach number. Further, a reduction in peak pressure ratio is noticed with the increase in enthalpy for all test cases and gas models. Again, these observations are found to be more prominent in Mars atmospheric conditions owing to more temperature-sensitive specific heats. Hence, it can be concluded that, while performing studies including such complicated flow structures the consideration of real gas effects is very important especially for Mars atmospheric conditions.

Chapter 7 : Comparative Studies of Shock Wave Boundary-Layer Interactions in Earth and Mars Atmospheres

Overview

In this chapter, investigations of ramp induced shock wave boundary-layer interaction (R-SWBLI) have been carried out for real gas flows of air and carbon dioxide through hypersonic laminar flow simulations corresponding to Earth and Mars atmospheres. In house developed solver, which accounts for the real gas effects, has been employed for these studies. Effects of various parameters like wall temperature, freestream stagnation enthalpy, freestream Mach number and blunt leading edge are explored on the intensity of shock wave boundary-layer interaction (SWBLI). In either case, increase in separation length is observed with increase in wall temperature and decrease in Mach number as well as freestream stagnation enthalpy. Here, the intensity of alteration is always noted to have higher percentage for Mars gas model. Further, separation length is found to be almost equal for the same wall to total temperature ratio in both the flow mediums. Present study also affirms the fact that the leading-edge bluntness can be used as a tool to reduce the size of separation region in these planetary atmospheres. Revised correlations have been proposed for hypersonic Earth atmospheric flow with real gas effects to predict the extent of upstream influence and separation bubble size. The outcomes of simulations have also helped to device new correlations for these flow features of SWBLI for Mars atmospheric conditions. In all, need for consideration of real gas effects and an exclusive real gas flow solver for Mars atmosphere are the prominent recommendations of current studies.

7.1 Introduction

Shocks and their interactions have been one of the major fields of interest in high speed aerodynamics. Amongst these interactions, shock wave boundary-layer interaction (SWBLI) is of the prime importance as its occurrence is almost unavoidable in most of the high speed vehicles such as aircrafts, missiles, rockets etc. This interaction may lead to undesirable effects in the vicinity of interaction such as boundary-layer separations [**153**,**154**] and higher thermal loads

[**122**,**155**]. To mitigate these issues, many active [**156**,**111**] as well as passive [**103**,**123**] techniques were proposed by various researchers.

In the literature reported findings, it has been noticed that SWBLI was studied either to mitigate its adverse effects, using active as well as passive techniques, or to understand the effect of different parameters. Further, most of these investigations were in Earth atmosphere (air medium) and preferably with perfect gas assumption. But very few researchers accounted the real gas effects on SWBLI. Therefore, it is very important to perform such parametric studies for SWBLI along with the real gas effects and also for other important planetary conditions like Mars. Hence such real gas effects are planned for investigation in Mars atmospheric conditions in order to understand the relative intensity with change in flowing fluid. Growing interest in the Mars exploration [**157**] is the motive behind this objective. In view of this, the effect of parameters like Mach number, wall temperature, freestream stagnation enthalpy, wall to total temperature ratio and leading edge bluntness are studied on the size of boundary-layer separation in Earth as well as Mars atmospheric conditions considering real gas effects. In addition, efforts are also made to revisit and re-correct the previously reported correlations for upstream influence and size of separation region in air medium. Further, similar correlations are proposed to account the Mars atmosphere for the first time. Hence, to achieve the desired goals, in-house finite volume based CFD solver, equipped with reaction modeling and temperature dependent specific heats has been used in the present study. The results obtained are discussed in the following sections.

7.2 Results and discussion

Viscous flow simulations are performed by the in-house real gas flow solver to simulate R-SWBLI. The initial conditions such as freestream Mach number (M_∞), freestream static temperature (T_∞), freestream static pressure (P_∞), freestream per unit Reynolds number (Re_∞) and wall temperature (T_w) considered are listed in Table 7.1. The chosen ramp angle (17º) promotes separation for these freestream conditions. Thus, the opted geometry along with boundary conditions and grid distributions is shown in Fig. 7.1. This geometrical configuration is kept constant throughout the study. Initially, grid independence studies are carried out using three grid combinations as 210x60, 280x100 and 400x200. The details of the grids specifying minimum element size near wall (Δy_{min}), at the leading edge (Δx_{minle}) and at the flat plate-Ramp junction (Δx_{minju}) are shown in Table 7.2. The convergence histories of all the grids considered are plotted

in Fig. 7.2. The computed skin friction coefficient distributions for Earth and Mars flight conditions are shown in Fig. 7.3. Flow separation and reattachment locations can be identified from crossing of the zero line by the skin friction coefficient plot. Here, the difference between the lengths of separation bubble, measured between these cross-overs, can be easily noticed between the result obtained from coarse grid (210x60) and that of medium size grid (280x100). But such discrepancy is very much insignificant with further refinement of the grid. Therefore, the mesh of size 280x100 is chosen to perform detailed studies with SWBLI since such mesh is seen to capture the dynamics of SWBLI properly. The flow is noticed to be separated in both the planetary cases but the length of separation is different. Here, the hypersonic flow over the given configuration encounters growth of boundary-layer along the plate but the flow remains attached for some length of the plate. At the upstream influence location flow becomes pre-warned about the shock. Current ramp angle and Mach number combination imposes such an oblique shock in the flow field which creates sufficient adverse pressure gradient for flow separation for both the freestream mediums. This observation clearly portrays that the mechanism of SWBLI is indeed same in these two cases but the effect is different since it is governed by the flow and wall properties. Therefore, it becomes essential to understand and quantify the difference in each case for a given change in the SWBLI governing parameter.

Table 7.1: Freestream conditions considered for simulations [**122**].

Atmosphere	M_∞	T_∞ (K)	T_o (K)	P_∞ (Pa)	Re_∞ (m^{-1})	T_w (K)	Mass fractions
Earth	6	131.7	1080	199.4345	800000	300	N_2- 0.765 ; O_2- 0.235
Mars	6	178.8	1080	199.4345	766667	300	CO_2- 0.9685 ; N_2- 0.0315

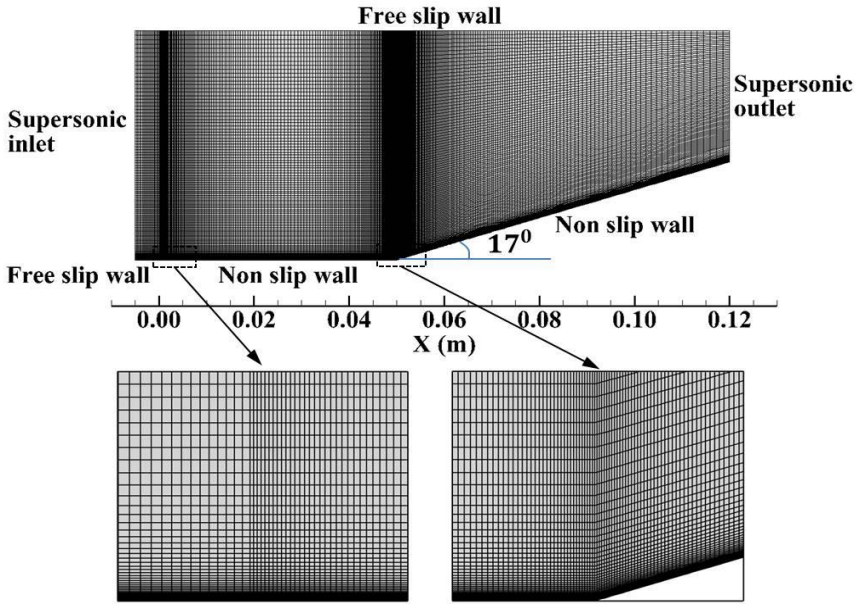

Figure 7.1: Computational domain with boundary conditions and grid distribution.

Table 7.2: Details of grids used for the simulations.

Grid size	Δy_{min} (m)	Δx_{minle} (m)	Δx_{minju} (m)
210x60	3×10^{-5}	3×10^{-4}	2×10^{-4}
280x100	1×10^{-5}	1×10^{-4}	9×10^{-5}
400x200	8×10^{-6}	6×10^{-5}	5×10^{-5}

Now, R-SWBLI is explored with the real gas flow solver for Earth as well as Mars flight conditions to understand the relative effect of different parameters like wall temperature, freestream enthalpy, wall to freestream total temperature ratio, freestream Mach number and leading-edge bluntness. Initially, effect of each parameter is studied and compared for the same wall thermal and freestream conditions for Earth and Mars atmosphere flows except their Reynolds numbers. Later the same effect is again analyzed for same freestream Reynolds number. The outcomes of these simulations are expected to reveal the impact of all the parameters on R-SWBLI and alteration in relative strength with change in flowing fluid or medium. The detailed discussion is presented in the following subsections.

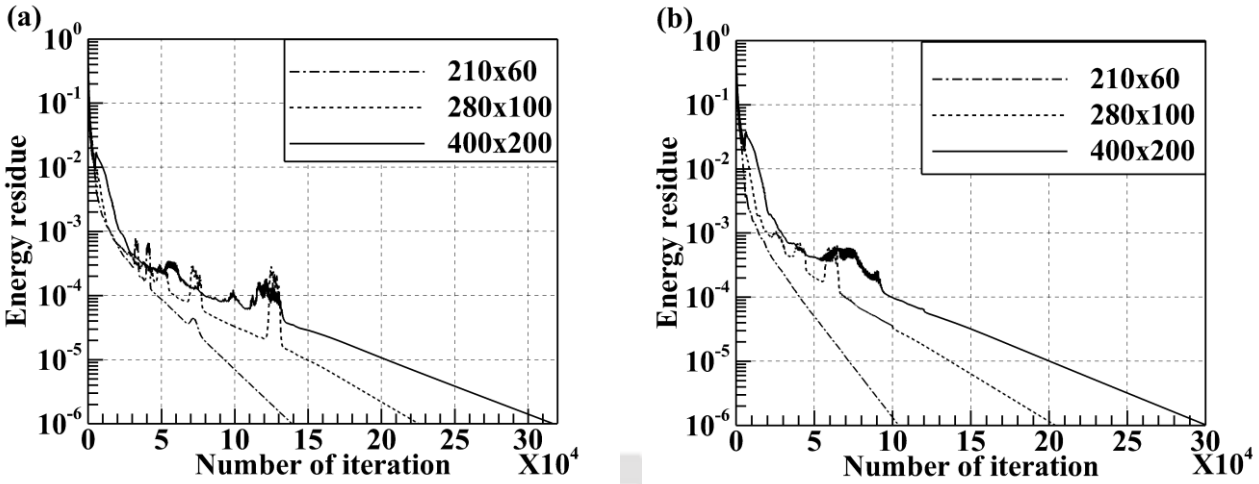

Figure 7.2: Convergence history of different grids considered (a) Earth gas model; (b) Mars gas model.

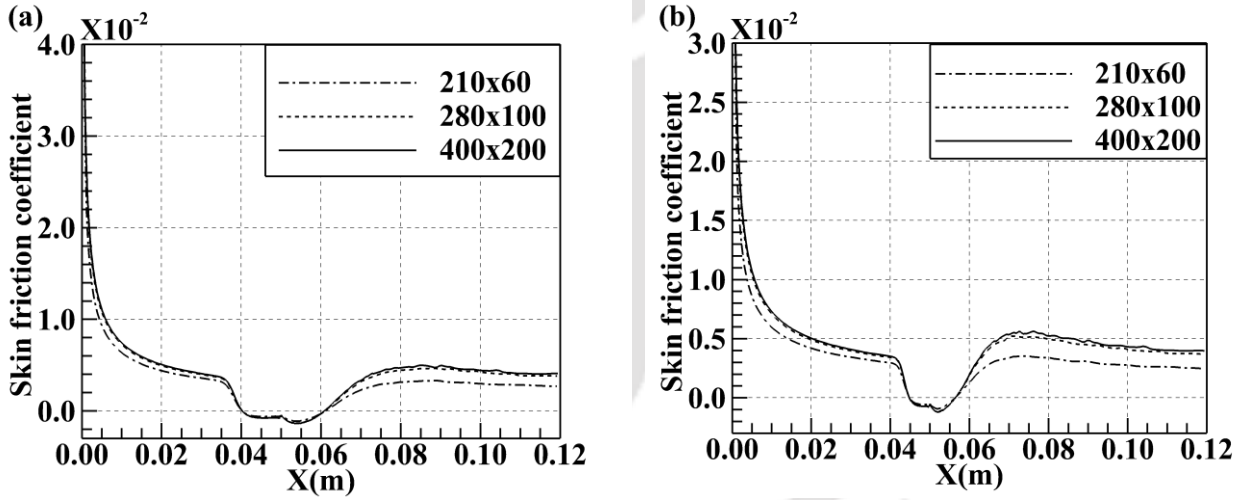

Figure 7.3: Skin friction distribution over the surface of 17º ramp obtained with different grid size (a) Earth gas model; (b) Mars gas model.

7.2.1 Effect of wall temperature

Initial numerical efforts are made to demonstrate the effect of wall temperature on the SWBLI, since this temperature is expected to govern the near wall dynamics of the SWBLI. The investigations are performed for Earth as well as Mars gas flow models with freestream conditions and the geometry as mentioned in the previous section with different wall temperatures as 300K, 500K and 700K. Such wall temperature variation was accounted in the literature [**122**] for

hypersonic flow of air while analyzing the effect of wall temperature on the near wall dynamics of SWBLI. A need has been recognized to capture the effect of wall temperature for hypersonic flow of carbon dioxide flow and to assess its magnitude with that of air. Results of the simulations performed for this objective are presented in terms of density gradient and Mach contour for 700K case in Fig. 7.4(a) and (b) respectively. All the important features like leading edge shock, boundary-layer, separation shock, detachment shock and triple point are captured very well. Another important observation from the Mach contour (Fig. 7.4(b)) is the smaller recirculation for the Mars flow model indicating lesser separation. Further, the obtained wall property distributions are shown in Fig. 7.5, 7.6 and 7.7. For both the real gas flow models, surface pressure distribution depicts the increase in the extent of upstream influence and plateau pressure for higher wall temperature conditions. Most upstream influence locations (x_o) for Earth and Mars cases are 26.07mm and 33.05 mm respectively for the highest wall temperature case (700K). Further, the surface heat flux has similar trend in both the cases and is seen to be decreased with increment in wall temperature. Additionally, more negative region is noted in the skin friction coefficient plot which illustrates the increment in boundary-layer separation length. The calculated separation lengths (L_b) using these plots are mentioned in Table 7.3. Here, the elevated wall temperature results in higher boundary-layer temperature, more viscosity and hence thicker boundary-layer. Consequently, strong interaction occurs between the boundary-layer and the shock wave which in turn leads to larger upstream influence, higher plateau pressure and wider separation bubble. Higher wall temperature results in a lower temperature gradient near the wall and thus, lesser surface heat flux as compared to low wall temperature cases. It must also be noted here that, for the lower wall temperature, the near wall temperature gradient is high and hence the wall heat flux is higher in the attached as well as separated flow regions. This fact along with the lower zone of separation maintains the heat flux variation along the length for lowest temperature at much higher magnitude as compared to other choices of higher wall temperatures. As a result of such segregation, plot of heat flux variation for each case does not intersect and can be seen separately unlike pressure and skin friction variations.

Further, it is interesting to note from the polynomial fit expression for specific heat of air and carbon dioxide (Martian atmosphere) that the rise in specific heat is more for carbon dioxide in comparison with air for same amount of temperature increment. This fact clearly suggests that the carbon dioxide flow would experience lesser rise in boundary-layer temperature than that of

air. Therefore, due to lower temperature rise inside the boundary-layer, the viscosity, being dependent on temperature, experiences lesser increment in case of carbon dioxide than the air. For this reason, weaker SWBLI is noted through the absolute values of all important flow features like upstream influence, separation length and distribution of wall properties in case of carbon dioxide as the flowing medium. This fact is clear from Table 7.3, where it can be seen that, for Earth gas model, the absolute separation length increases by 16.65mm for rise in wall temperature from 300K to 700K. In the same range of wall temperature change, amount of separation length raises by 12.34mm for Mars gas model. But this adverse effect is around 80% for Earth and 110.77% for Mars in this range of wall temperature rise. In summary, higher wall temperature provokes more percentage change in the boundary-layer separation for Mars atmospheric condition as compared to Earth, which can be taken as indication of stronger interaction.

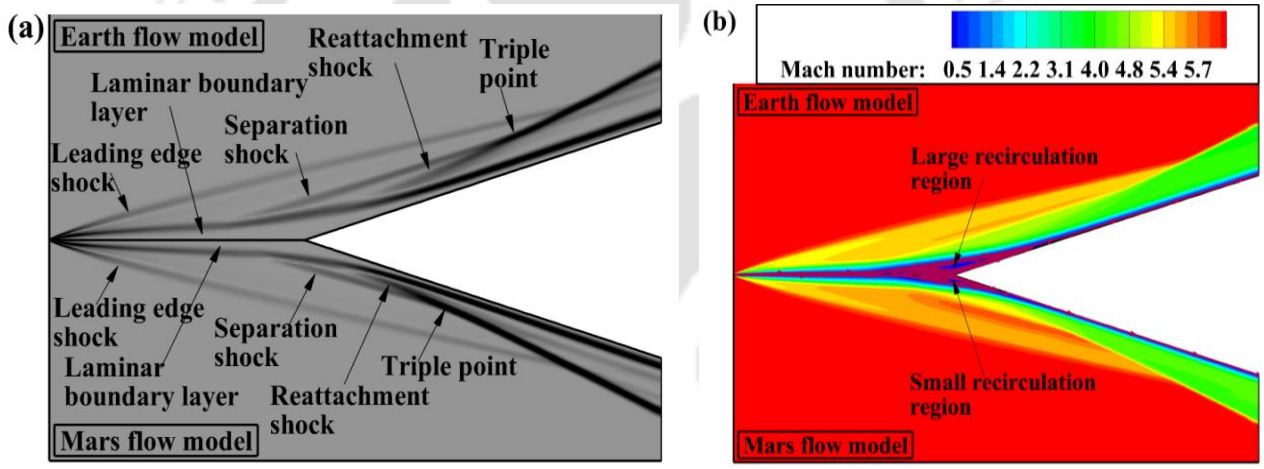

Figure 7.4: Different contours obtained from 700K wall temperature case (a) Density Gradient contour; (b) Mach contour.

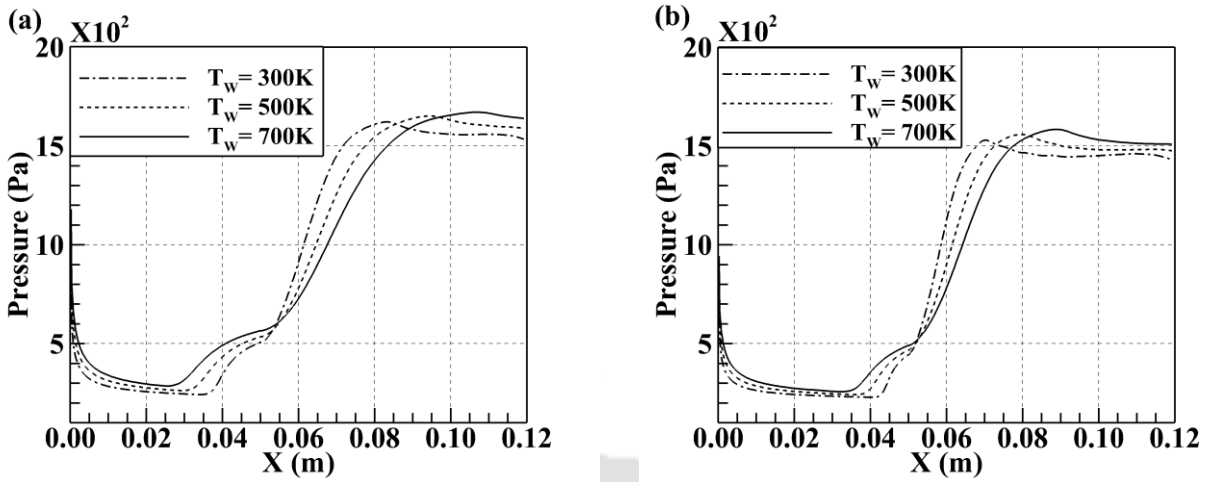

Figure 7.5: Effect of variation of wall temperature on pressure distribution for (a) Earth gas model; (b) Mars gas model.

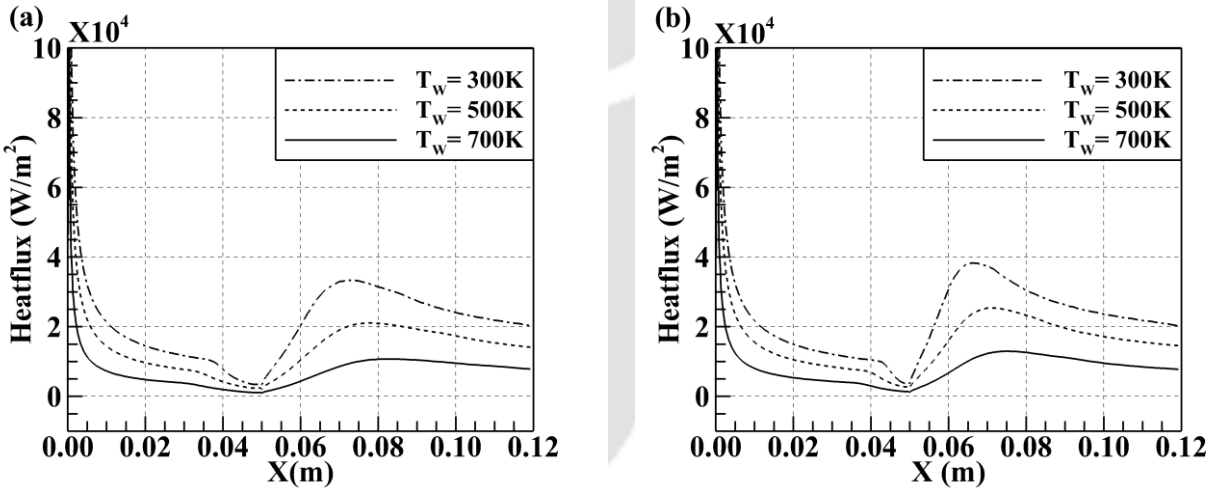

Figure 7.6: Effect of variation of wall temperature on heat flux distribution for (a) Earth gas model; (b) Mars gas model.

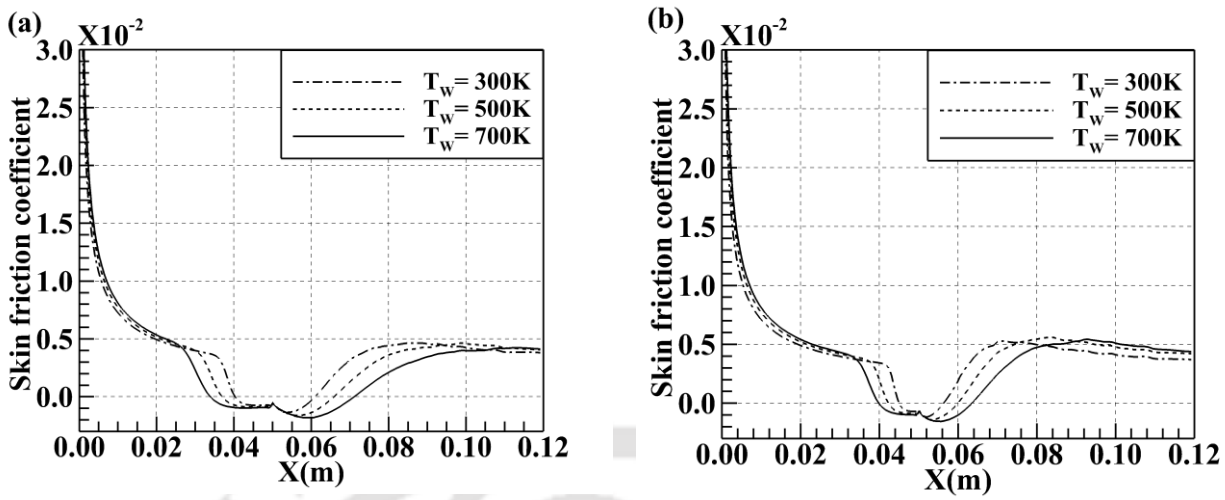

Figure 7.7: Effect of variation of wall temperature on skin friction distribution for (a) Earth gas model; (b) Mars gas model.

7.2.2 Effect of freestream enthalpy

In this section, the role of freestream total enthalpy along with the real gas effects is examined on the flow field modifications. For the same, three freestream total temperatures (T_o) of 1080K, 1400K and 1800K are considered, while the other parameters like Mach number, Reynolds number and wall temperature are kept unaltered. The variation of skin friction coefficient along the wall, obtained from the simulations with Earth and Mars gas model is shown in Fig. 7.8. It reveals that the separation bubble length gets reduced with the increment in the freestream total enthalpy for both the planetary conditions. The reason behind this observation is the enhancement of freestream kinetic energy with higher freestream total enthalpy or total temperature which supplies greater momentum to the approaching boundary-layer fluid against the adverse pressure gradient imposed by the configuration. As a consequence, lesser separation is noted for both the gas flow models (Table 7.3**)**. It is worth to mention that the real gas effects become prominent at higher enthalpy due to sharp rise in specific heat values. This increment is relatively more with Mars gas model compared to the Earth gas model. Hence its assistance is more for Earth than Mars atmosphere to reduce absolute value of separation, which are 8.08mm and 6.89mm respectively when the stagnation temperature is increased from 1080K to 1800K. But, Mars gas model shows 39.78% decrement while Earth gas model shows 28.41% reduction for this change in total temperature. It may be noted that, no contribution of dissociation reactions is

observed in any case. Hence, it is summarized that the higher stagnation enthalpy, as well as real gas effects, alleviate the boundary-layer separation significantly for either gas flow models and the percentage change is more prominent for Mars gas model.

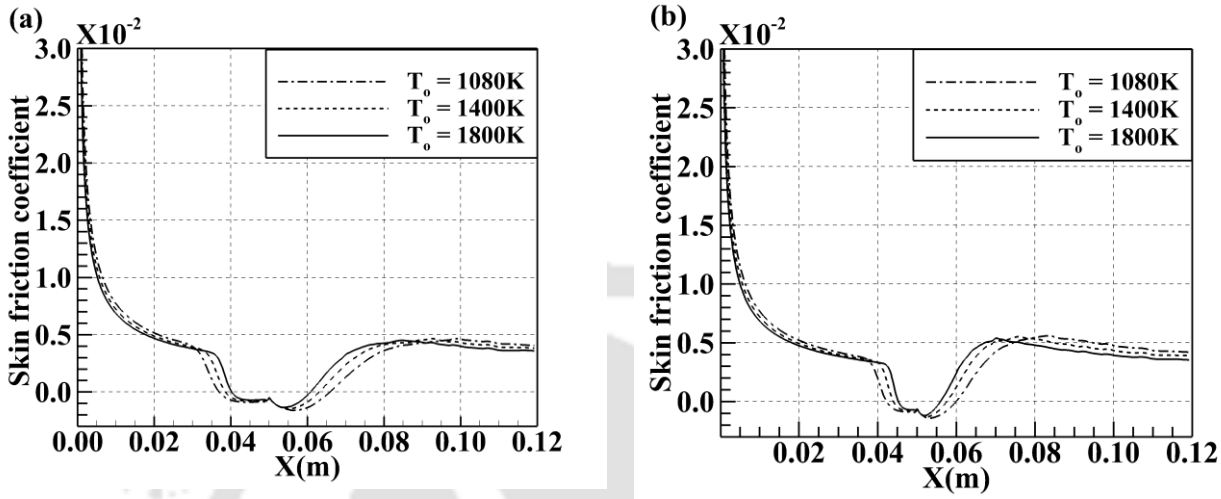

Figure 7.8: Effect of variation of freestream enthalpy on skin friction distribution for (a) Earth gas model; (b) Mars gas model.

7.2.3 Effect of wall to freestream total temperature ratio

The wall to freestream total temperature ratio (T_w/T_o) is another vital parameter for SWBLI. In the earlier studies [**122**], it was marked that the non-dimensional wall properties remain identical for the same value of T_w/T_o ratio in perfect gas flow cases (constant specific heats) for Earth atmosphere. The wall temperature affects the flow properties inside the boundary-layer while the freestream stagnation temperature influences the boundary-layer edge properties. Therefore, it is essential to revisit these findings in the presence of real gas effects for Mars as well as Earth atmospheric conditions. Hence, two different cases of the same T_w/T_o ratio with different wall temperatures as 500K and 833.33K are considered herein. These cases correspond to total temperature of 1080K and 1800K respectively. Further, the Reynolds number and Mach number are kept constant as mentioned in Table 7.3. The variation of skin friction coefficient in these cases is shown in Fig. 7.9. The results of both real gas flow models also demonstrate the similar trend of wall properties for same T_w/T_o ratio. In these cases, separation lengths are observed to be same and around 28mm and 17mm for Earth and Mars flow conditions respectively. Therefore, the present study reaffirms the earlier finding even in the presence of real gas effects and for Earth

as well as Mars atmospheric conditions. Hence it is recommended to include the T_w/T_o parameter in well-established correlations in order to develop the better insight of SWBLI.

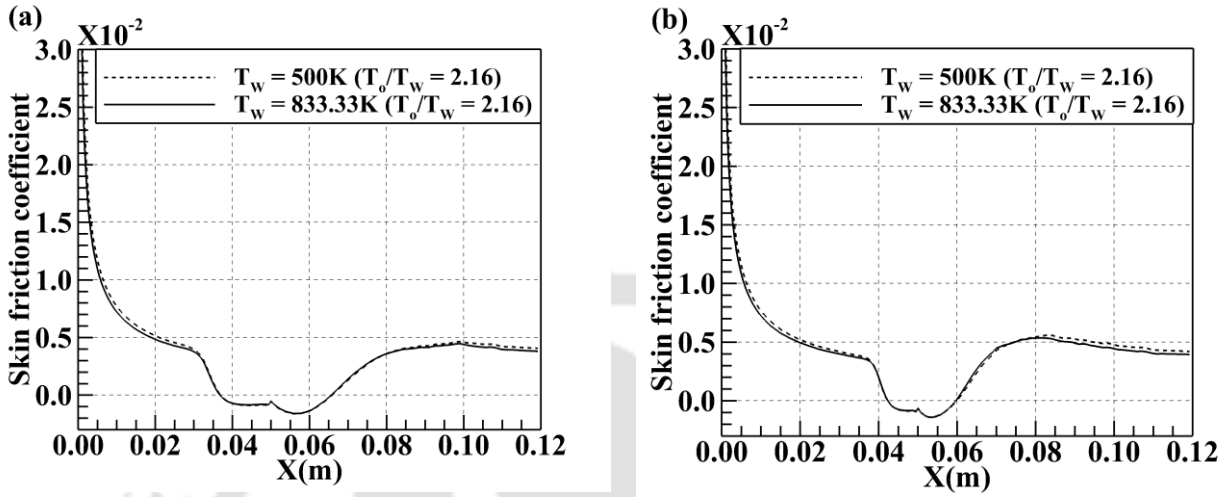

Figure 7.9: Effect on skin friction distribution when the ratio between total and wall temperature is kept constant for (a) Earth gas model; (b) Mars gas model.

7.2.4 Effect of Mach number

Simulations are continued to study the influence of freestream Mach number on SWBLI. Here, three Mach numbers (6, 7 and 8) are considered to perform the investigations for both the cases with the other properties like freestream temperature, Reynolds number as well as wall temperature as constant (Table 7.3). The surface pressure and skin friction distribution for these cases are plotted in Fig. 7.10 and 7.11. It clearly demonstrates the lesser upstream influence, lower plateau pressure and lesser separation length at higher Mach number for both the gas flow models. In the present cases, higher Mach number leads to more freestream kinetic energy and momentum against the impedance offered by ramp configuration. Consequently, weak shock wave boundary interaction occurs. This result clearly demonstrates that the separation length is inversely proportional to the freestream Mach number. Hence, for both the planetary conditions, more freestream Mach number yields lesser separation of boundary-layer. This amount is 11.45mm or 40.26% for Earth and 10.61mm or 61.25% for Mars when freestream Mach number is increased from 6 to 8. Thus, the intensity of separation decrement is higher in percentage for Mars than Earth gas model with increase in Mach number.

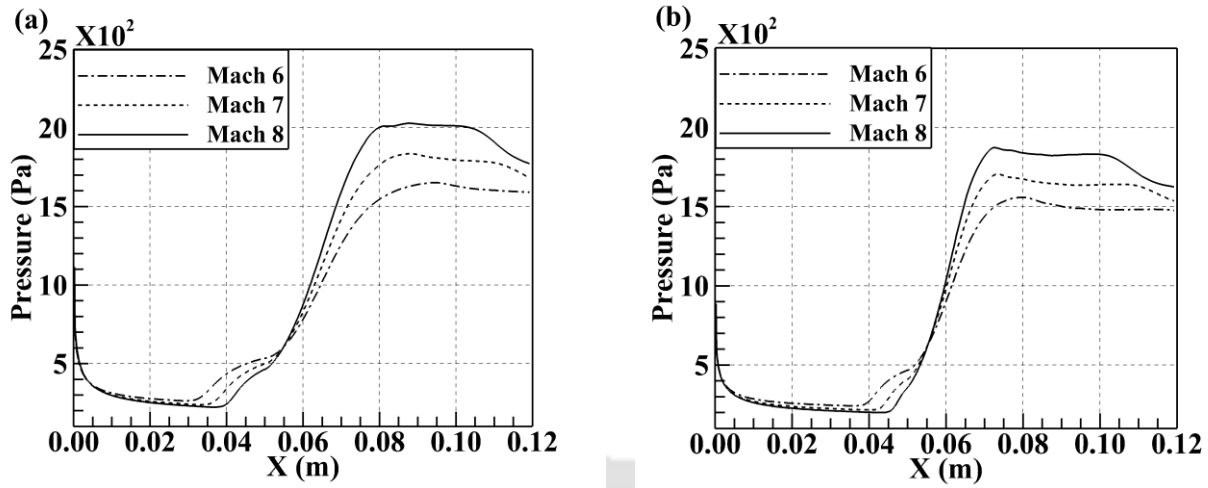

Figure 7.10: Effect of variation of freestream Mach number on pressure distribution for (a) Earth gas model; (b) Mars gas model.

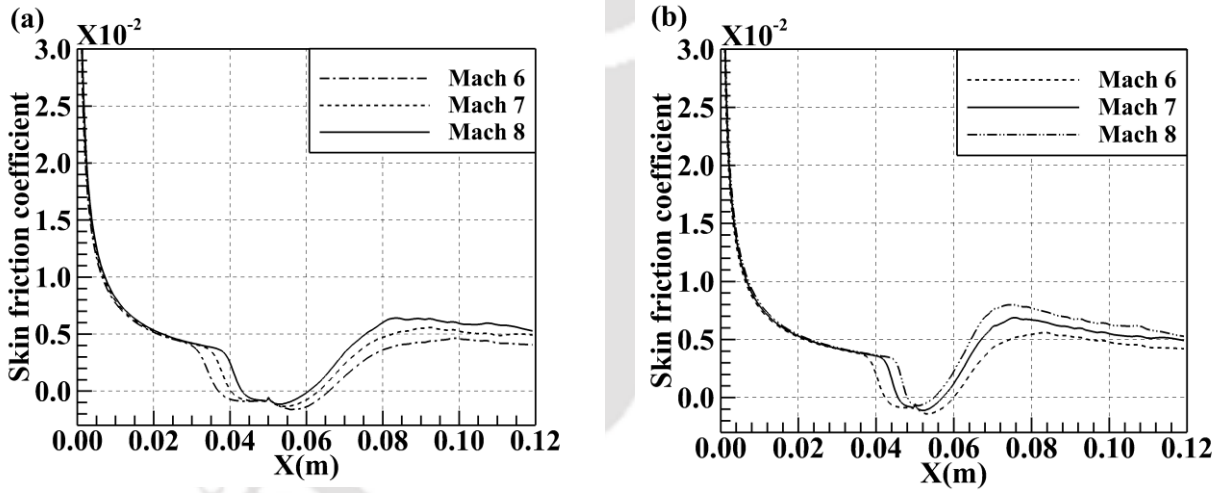

Figure 7.11: Effect of variation of freestream Mach number on skin friction distribution for (a) Earth gas model; (b) Mars gas model.

7.2.5 Effect of leading edge bluntness

The blunted leading edge is one of the most widely discussed boundary-layer separation control strategies. This technique assures separation control only if the bluntness is more than the required minimal value (equivalent radius) for a given freestream conditions. A schematic diagram of R-SWBLI with a blunt leading edge is shown in Fig. 7.12. Leading edge bluntness replaces the attached sharp leading edge shock with the detached bow shock. This leads to alteration in the

flow properties like Mach number, pressure, temperature, density etc. in the leading edge region. Further, it modifies the boundary-layer separation length as the stream gets convected towards the ramp.

The earlier reported studies with blunt leading edge were limited by perfect gas assumption for Earth flight conditions [**123**]. Hence it is really important to evaluate its performance in the presence of real gas effects as well as for Mars atmospheric conditions. Therefore, same numerical strategy is used, while the freestream Mach number is kept as 6 and total temperature as 1080K in either case. Here, the blunt leading edge radius (r) of 2.5mm has been adopted keeping rest of the geometry the same as described earlier. Further, the grid of size 360 x 85 is employed to perform the simulations which assured the grid independent results. The details of the grid used for the present simulations are provided in Table 7.4. The results obtained from these simulations are shown in Fig. 7.13 and 7.14. In the Fig. 7.13, surface property distribution clearly shows prolonged over pressure region ahead of the upstream influence location (x_o = 38.81mm for Earth and x_o = 41.25mm for Mars) as compared to the base sharp leading-edge case. This over pressure region helps to delay the downstream adverse pressure gradient. The skin friction coefficient also depicts downstream shift of separation point and upstream shift of re-attachment point. Lowering of separation size can be justified due to swallowing of the boundary-layer by entropy layer. The thicker entropy layer possesses stream wise vorticity as per the Croco's theorem which transfers the streamwise momentum to the boundary-layer and stabilizes it. This momentum exchange results in the reduction of separation bubble length for both gas models as shown in Fig. 7.14. In case of Earth gas model, the separation bubble size decreases from 20.36 mm for sharp leading-edge case to 11.43mm for blunt leading-edge of radius, 2.5mm. This blunt edge helps Mars gas model to reduce the separation from 11.14mm to 8.38mm. Hence present work shows that the blunt leading-edge radius of 2.5mm provides the boundary-layer separation control for both Mars and Earth flight conditions.

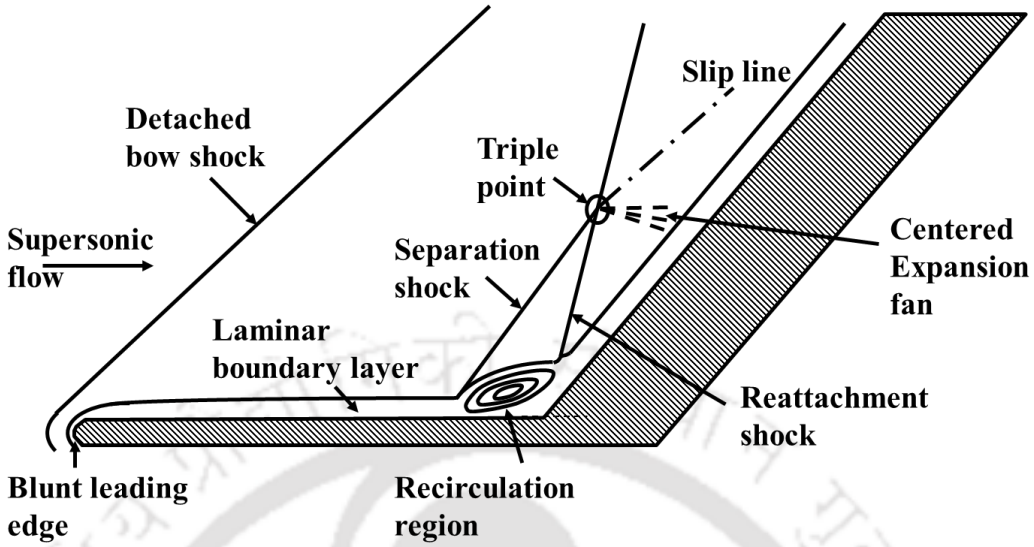

Figure 7.12: Schematic diagram of a ramp induced SWBLI with blunt leading edge.

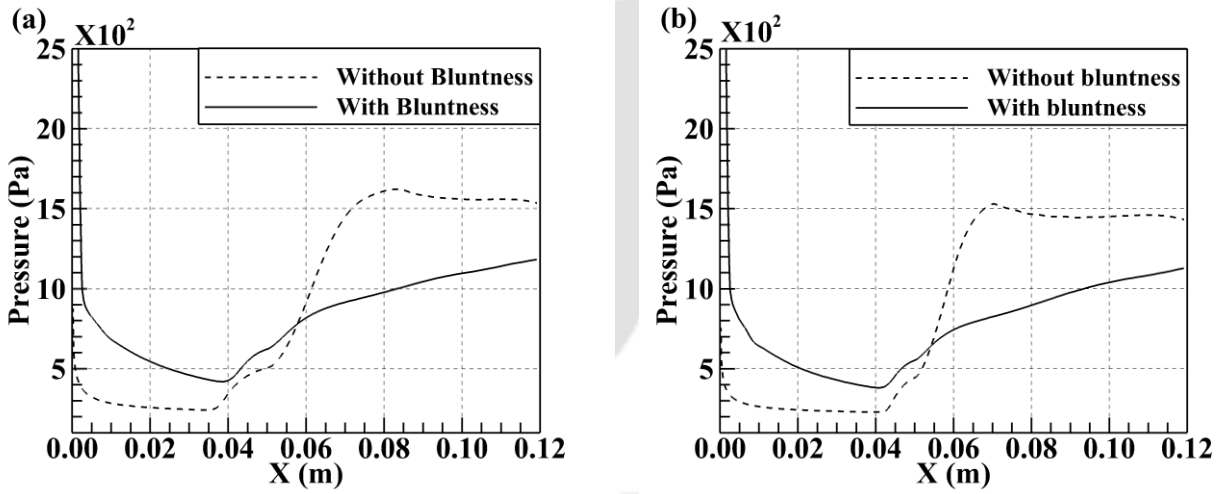

Figure 7.13: Comparison of pressure distribution over the ramp surface with and without leading-edge bluntness for (a) Earth gas model; (b) Mars gas model.

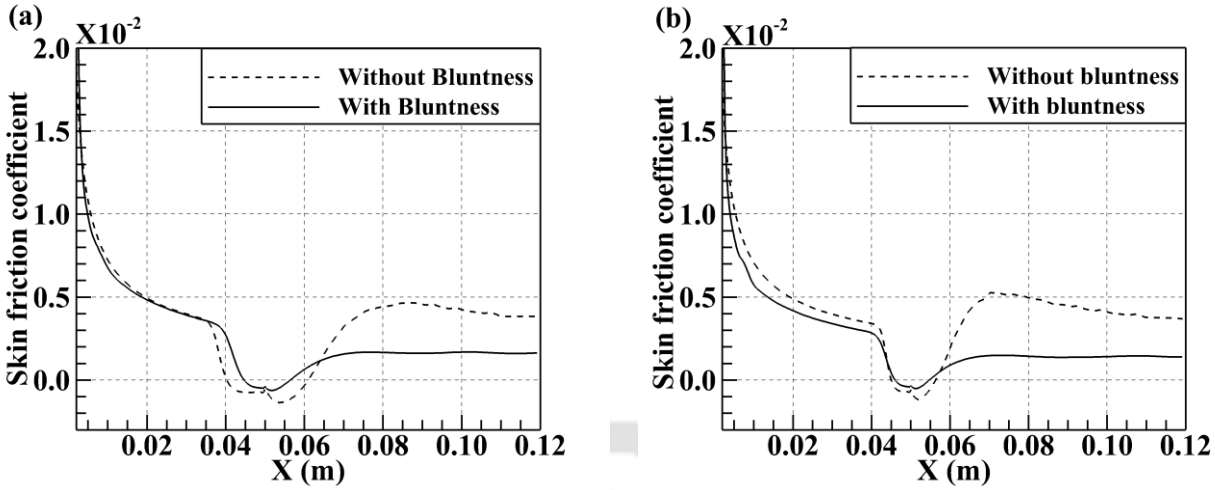

Figure 7.14: Comparison of skin friction distribution over the ramp surface with and without leading-edge bluntness for (a) Earth gas model; (b) Mars gas model.

Table 7.3: Summary of the parametric study

Atmosphere	Parameter	M_∞	Re_∞ (m^{-1})	T_0 (K)	T_w (K)	r (mm)	L_b (mm)
Earth	Wall temperature	6	$8x10^5$	1080	300	0.0	20.36
		6	$8x10^5$	1080	500	0.0	28.44
		6	$8x10^5$	1080	700	0.0	36.65
	Freestream enthalpy	6	$8x10^5$	1080	500	0.0	28.44
		6	$8x10^5$	1400	500	0.0	24.36
		6	$8x10^5$	1800	500	0.0	20.36
	Mach number	6	$8x10^5$	1080	500	0.0	28.44
		7	$8x10^5$	1422	500	0.0	22.72
		8	$8x10^5$	1817	500	0.0	16.99
	Wall to total temperature ratio	6	$8x10^5$	1080	500	0.0	28.44
		6	$8x10^5$	1800	833.33	0.0	28.50
	Leading edge	6	$8x10^5$	1080	300	0.0	20.36
		6	$8x10^5$	1080	300	2.5	11.43

Mars	Wall temperature	6	$7.667x10^5$	1080	300	0.0	11.14
		6	$7.667x10^5$	1080	500	0.0	17.32
		6	$7.667x10^5$	1080	700	0.0	23.48
	Freestream enthalpy	6	$7.667x10^5$	1080	500	0.0	17.32
		6	$7.667x10^5$	1400	500	0.0	13.35
		6	$7.667x10^5$	1800	500	0.0	10.43
	Mach number	6	$7.667x10^5$	1080	500	0.0	17.32
		7	$7.667x10^5$	1405	500	0.0	11.36
		8	$7.667x10^5$	1780	500	0.0	6.71
	Wall to total temperature ratio	6	$7.667x10^5$	1080	500	0.0	17.32
		6	$7.667x10^5$	1800	833.33	0.0	17.02
	Leading-edge	6	$7.667x10^5$	1080	300	0.0	11.14
		6	$7.667x10^5$	1080	300	2.5	8.38

Table 7.4: Details of grids used for the simulating with leading edge bluntness.

Grid size	Δy_{min} (m)	Δx_{minle} (m)	Δx_{minju} (m)
360x85	$1x10^{-5}$	$2x10^{-5}$	$7x10^{-5}$

7.2.6 Effect of governing parameters for same Freestream Reynolds number

From the above discussion it is noticed that the percentage change in separation length is higher for Mars gas model and hence, Mars atmospheric simulations are performed with the same Reynolds number as that of Earth atmospheric simulations i.e 800000 m^{-1} to ensure the same trend for this case as well. It is worth mentioning that, this change in Reynolds number is achieved by altering freestream pressure and keeping all the other parameters same as mentioned in the previous sections. Such simulations are performed for different wall temperature, freestream stagnation enthalpy and freestream Mach number. The distribution of skin friction coefficient, obtained from these simulations, for each case, is shown in Fig. 7.15. The separation lengths predicted for these cases are summarized in Table 7.5. It is observed that the percentage increase in the separation length for increase in the wall temperature from 300K to 700K is 102.07 % for

Mars as against 80% for Earth atmospheric conditions. Again, the simulations for different freestream stagnation enthalpy or total temperature reveal the increase in separation length by 40.56% for Mars gas model as that of 28.41% for Earth gas model when the total temperature is increased from 1080K to 1800K. Further, the increase in the Mach number from 6 to 8 results in decrease in the separation length by 61.78% for Mars atmosphere simulations while 40.26% decrement is observed for Earth atmosphere simulations for the same Mach number range. Hence, authors are of view that, the percentage deviation in the separation length is higher for the Mars atmospheric conditions than that of Earth atmospheric conditions and this conclusion is consistent for same or different freestream Reynolds numbers.

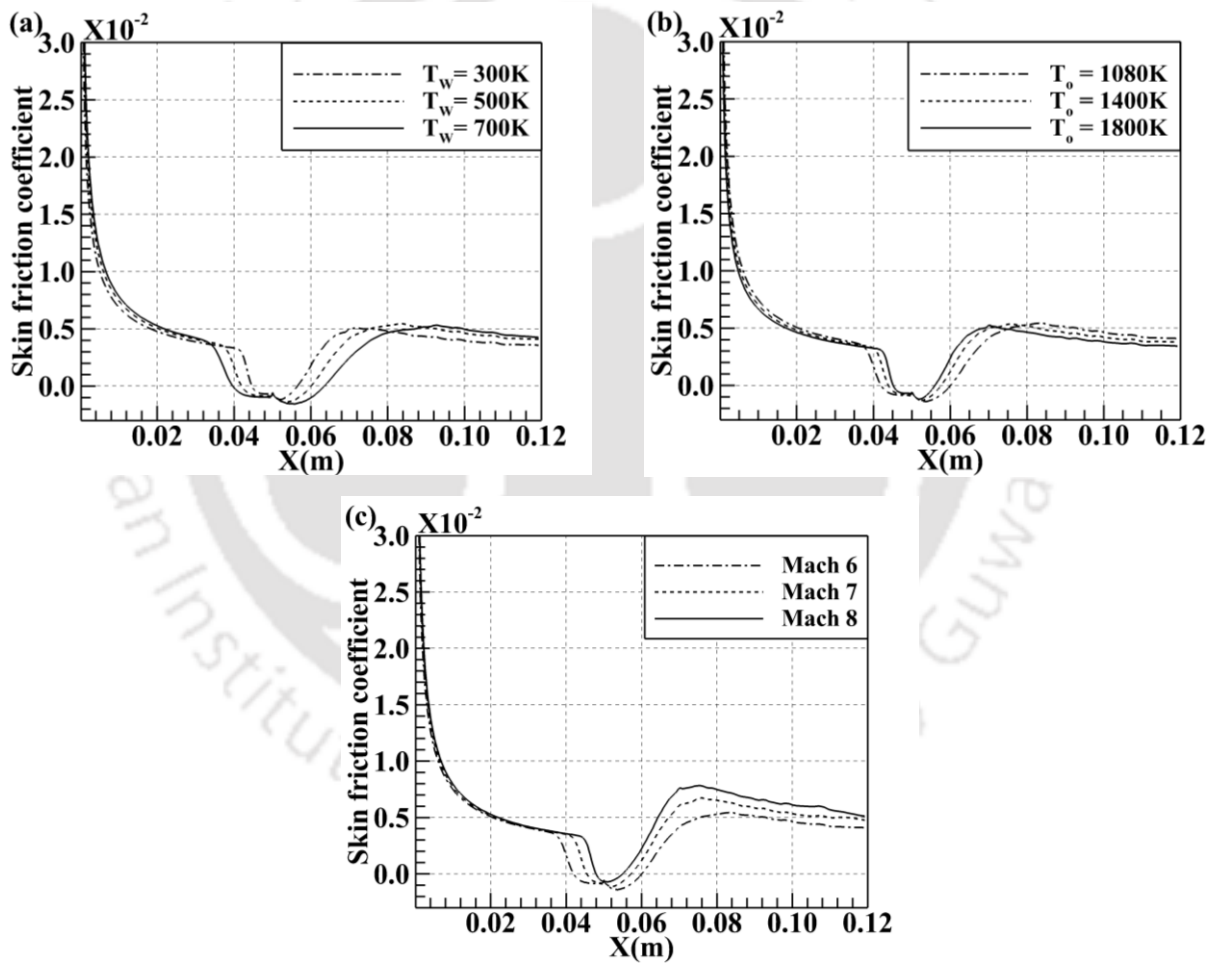

Figure 7.15: Skin friction distribution obtained by Mars gas model with $\boldsymbol{Re_\infty = 8x10^5 m^{-1}}$ at different (a) wall temperature, (b) Freestream enthalpy and (c) Mach number.

Table 7.5: Summary of parametric study performed by Mars gas model with $\boldsymbol{Re_\infty = 8x10^5 m^{-1}}$

Parameter	M_∞	Re_∞	T_0	T_w	r	L_b
		(m^{-1})	(K)	(K)	(mm)	(mm)
Wall temperature	6	$8x10^5$	1080	300	0.0	11.62
	6	$8x10^5$	1080	500	0.0	17.95
	6	$8x10^5$	1080	700	0.0	23.48
Freestream enthalpy	6	$8x10^5$	1080	500	0.0	17.95
	6	$8x10^5$	1400	500	0.0	13.62
	6	$8x10^5$	1800	500	0.0	10.67
Mach number	6	$8x10^5$	1080	500	0.0	17.95
	7	$8x10^5$	1405	500	0.0	11.59
	8	$8x10^5$	1780	500	0.0	6.86

7.2.7 Assessment of correlation for upstream influence and separation bubble size

In addition to the parametric studies, results from the in-house solver are also used to assess the correlations for upstream influence and separation bubble size proposed by John and Kulkarni [**124**]. The details of these studies are discussed in the following sub-sections.

7.2.7.1 Analysis of extent of upstream influence

There are many correlations proposed by several researchers to relate the upstream influence with various governing parameters such as Mach number, wall temperature etc. However, for the present study the correlation proposed by John and Kulkarni [**124**] has been considered since it accounts most variables which govern the SWBLI. This expression is given by Eq. 7.1.

$$\frac{L_{ui}}{\delta_o} = F_{ui}\frac{\sqrt{Re_{x_o}}}{M_o^3\sqrt{C_w}}\left(\frac{P_3}{P_1} - 1\right)\beta^* \tag{7.1}$$

Where,

$$\beta^* = \left(\frac{T_w}{T_o}\right)^m \left(\frac{T_\infty}{T_o}\right)^n$$

Here, δ_o is the boundary-layer thickness at the upstream influence location (x_o). Further, L_{ui} is the extent of upstream influence which is the distance measured from ramp foot to the upstream influence location. M_o is the Mach number at the edge of boundar-layer and the term C_w is the Chapman-Rubesin parameter calculated with wall temperature. Pressure ratio P_3/P_1 is the inviscid pressure jump across the attached oblique shock. The proportionality constant F_{ui} is calculated by fitting the Eq. 7.1.

The data points from the present studies for Earth atmosphere are plotted (Fig. 7.16(a)) according to the above mentioned correlations with m=0.59 and n=0.28. Excellent prediction with linear trend can be observed for all the data points with R^2 value 0.9951. The proportionality constant F_{ui} is found to be 5.36 as against 6.15 reported by them [**124**]. This is because their estimate is based on the perfect gas assumption which shows much deviation if used for the present prediction. This observation demands the need for the proposed correction in the correlation if the real gas effects are to be accounted. Further, it is known that no such correlation exists for Mars atmosphere; here efforts are extended to device the same. Therefore, the results of present simulations are used to get the correlation for upstream influence for Mars atmospheric conditions. Same variables are considered as the governing parameters, hence the Eq. 7.1 when opted to fit the data of Mars atmosphere, the values of m and n are noted to be 0.63 and 0.67 respectively. Excellent prediction is observed using this correlation with R^2 value of 0.9904 for F_{ui} as 6.71 (Fig. 7.16(b)).

7.2.7.2 Analysis of separation bubble size

Among many correlations available in the open literature the below mentioned correlation (Eq. 7.2) proposed by John and Kulkarni [**124**] has been taken into consideration for the present study since it accounts influence of most of the variables.

$$\frac{L_b M_0^3}{x_0\sqrt{Re_{x_0}}} = F_{lb}\left(\frac{P_3}{P_2}\right)^2 \beta_{lb} \qquad (7.2)$$

Where,

$$\beta_{lb} = \left(\frac{T_w}{T_e}\right)^m \left(\frac{T_e}{T_0}\right)^n$$

Here, L_b is the separation bubble size; F_{lb} is the proportionality constant. In this correlation P_2 is considered to be equivalent to incipient pressure, P_{incp} [**158**]and is calculated using the triple deck solution proposed by Inger [**159**]. Further, T_e is the Temperature at the boundary-layer edge.

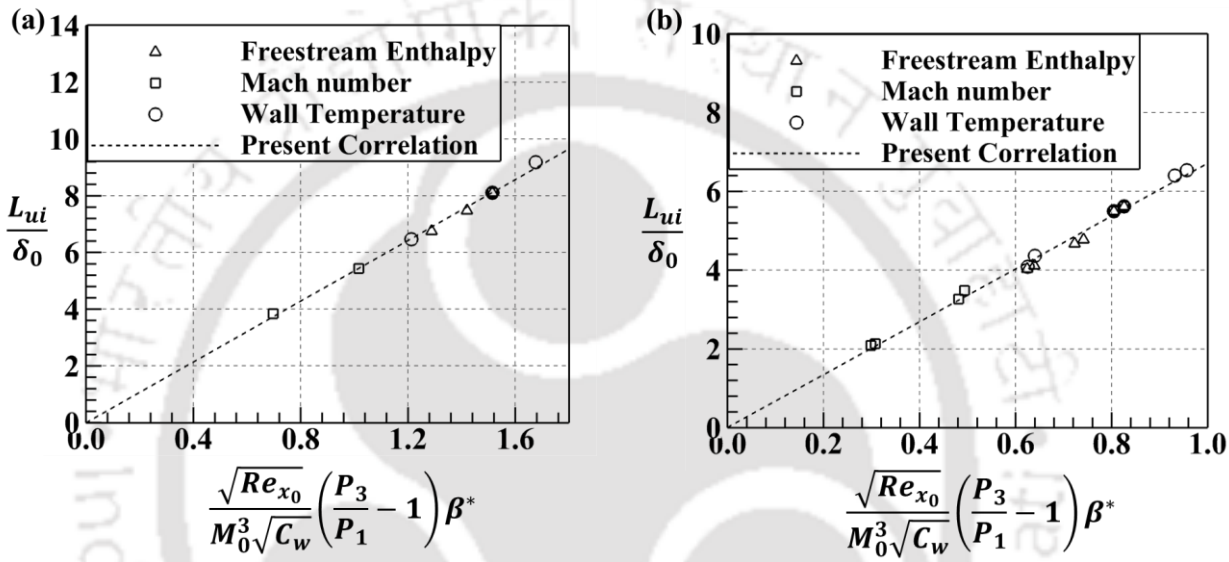

Figure 7.16: Correlation for extent of upstream influence (a) Earth gas model; (b) Mars gas model.

The data points from the present simulations for Earth atmosphere are fitted according to the above correlation and the fit is shown in Fig. 7.17(a). The trend line shows an excellent fit for the values of *m* and *n* as 1.11 and 0.75 respectively with the R^2 value 0.9856. Slight alteration in the proportionality constant for the perfect gas (F_{lb}=0.13) and the present simulation (F_{lb}=0.121) is observed. Thus, it can be noted here that the real gas effects are insignificant, for the given range of simulations, so as to introduce deviation from the estimates made using perfect gas assumption. As mention earlier, due to scarcity of explorations in Mars atmosphere and again with real gas effects, no such correlation has been reported for separation length for hypersonic Mars atmospheric flow. Therefore, the data obtained from present simulations is extended to arrive at a correlation to estimate for extent of separation. Eq. 7.2**,** which accounts most of dependent variables for separation length, has been used again for this case also. Such correlation for Mars

atmosphere is noted to have m=1.16 and n=1.44. This plot of the correlations is shown in Fig. 7.17(b). The proportionality constant F_{lb} is found to be 0.22. Again, excellent prediction can be observed.

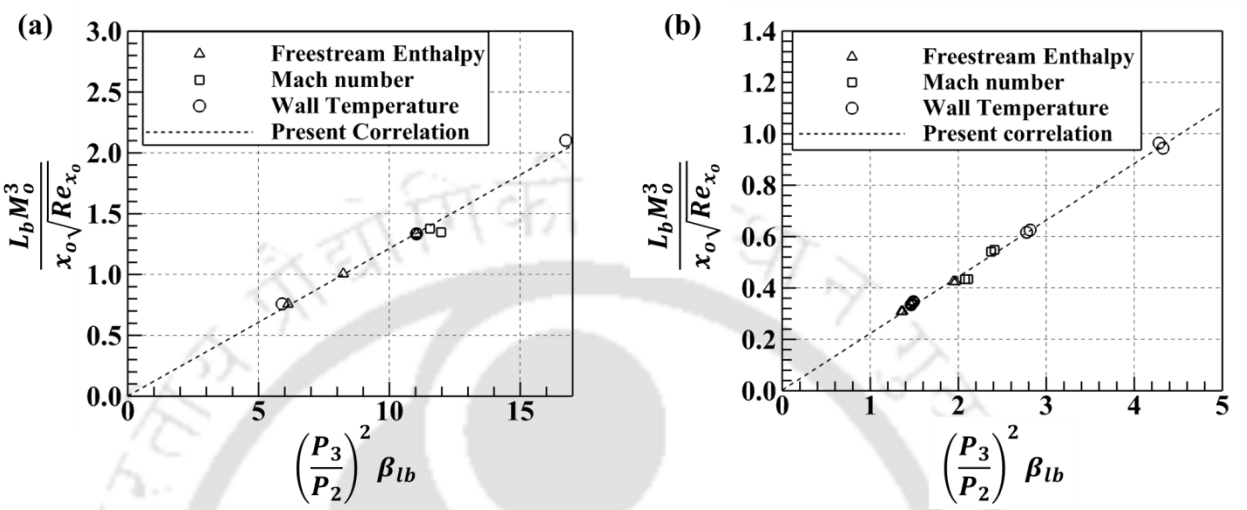

Figure 7.17: Correlation for separation bubble size (a) Earth gas model; (b) Mars gas model.

7.3 Conclusion

Effect of various parameters on R-SWBLI in laminar hypersonic flow has been successfully investigated for Earth and Mars atmospheric conditions. Parametric study has been carried out for working mediums of Earth and Mars atmospheres respectively using in-house real gas flow solver. Increment in separation size by 110.77% for carbon dioxide and 80% for air has been noted for the wall temperature increment from 300K to 700K at freestream Mach number of 6. When stagnation temperature is increased from 1080K to 1800K, there is 39.78% and 28.41% decrement in separation length for Mars and Earth gas models respectively. Similarly, increment in freestream Mach number has reduced the extent of separation by 61.25% and 40.26% for these flow models respectively. Thus, in either case, it has been observed that separation length increases with increase in wall temperature while it decreases with increase in Mach number and freestream stagnation enthalpy. Further, wall to total temperature ratio is confirmed to be a governing parameter and sufficiently large leading edge bluntness as separation control technique for both the mediums without perfect gas assumption as well. Noting these points, existing correlations for prediction of upstream influence length and extent of separation are corrected for air and new correlations are successfully proposed for Mars atmospheric conditions. These

correlations are expected to give better predictions in the present range of freestream and wall conditions for the flat plate ramp configuration. Further, more simulations would be performed to increase the envelope of these correlations. Thus, present studies advocate the use of real gas solvers in case of SWBLI studies for hypersonic flows in Earth as well as Mars atmosphere.

Chapter 8 : Conclusion and Scope of future works

8.1 Conclusion

In the present investigation, energy deposition based drag reduction, shock and its interactions and SWBLI phenomena have been numerically studied. For the same, a finite volume-based non-equilibrium/real gas CFD solver, capable of handling Earth as well as Mars atmospheric conditions, has been developed and validated with various literatures reported test cases. These cases involve analytical, numerical as well as experimental results. After the successful validation, the solver is employed for the detailed investigation of various high-speed flow phenomena at low and high enthalpy conditions. The major results of these investigations are as follows:

8.1.1 Conclusions about energy deposition technique based studies

The Golden section search method is integrated with the in-house real gas flow solver to assess the optimum energy deposition corresponding to the peak power effectiveness. The hypersonic flow simulations in the Earth and Mars atmospheres reveal that the amount of energy required to attain the peak power effectiveness is more for the latter. This is because of the comparatively more dependence of specific heat on temperature for Mars atmospheric medium. Another important observation is the lesser peak power effectiveness corresponding to the optimum amount of energy deposition for Mars atmospheric case. Further, the performance of this technique is found to be reduced with an increase in enthalpy. This decrement is found to be more pronounced in the air (Earth atmosphere) medium. Overall, it is noticed that the energy deposition based technique for drag reduction is effective for both the flow mediums. However, it is more suitable for Earth atmospheric medium.

8.1.2 Conclusions about Mach reflection studies

Inviscid simulations are performed in Earth and Mars atmospheric conditions for the Mach reflection study by the in-house developed real gas flow solver having the reaction kinetics of Earth and Martian atmosphere. The low enthalpy simulations reveal the Mach reflection patterns

in both the flow mediums for the given freestream conditions and configuration. However, drastic changes in the reflection patterns are noted as the freestream enthalpy is varied. It is observed that the initial increase in the freestream enthalpy tends to decrease the Mach stem height leading to transition to a regular reflection as the enthalpy is sufficiently increased. The prominent real gas effects at higher enthalpy are believed to responsible for this transition. Here, with the increase in enthalpy, the maximum deflection angle of the flow in the immediate downstream of the incident shock increases, thereby changes the transition criterion for MR↔RR. To support this argument shock polar are also incorporated. Another important observation is that this transition occurs at comparatively lower enthalpy for the Martian atmospheric condition.

8.1.3 Conclusions about shock/shock interactions studies

Different types of shock/shock interaction patterns are successfully investigated in Earth and Martian atmospheric conditions. Here, different double wedge geometries are considered explicitly to obtain Type IV, V and VI interactions for perfect gas conditions. Substantial differences in the flow patterns are observed through the respective perfect gas and real gas simulations. In Mars atmospheric conditions, for a configuration ($\theta_2 = 49^0$), the interaction type is observed to be type V (MR) for the prefect gas model as against a type V (RR) for the real gas model. In Earth atmospheric conditions, for a configuration ($\theta_2 = 50^0$) significant difference in normal shock location is observed. Similarly, for a configuration ($\theta_2 = 45^0$), disagreement in the location and size of the Mach stem is also noted. Hence, based on these trends it can be said that, for both the flow mediums, the real gas flow model demands a comparatively higher second wedge angle for transition among the different interaction types. Further, the real gas flow simulations at different enthalpies reveal different interaction types for the same configuration. It is noted that, for either flow medium, the rise in freestream enthalpy tends to make the interaction to type VI interactions. These changes in the flow patterns are attributed to the prominent real gas effects at higher enthalpies.

8.1.4 Conclusions about shock/ expansion fan interaction studies

Shock/expansion fan interactions for two different configurations viz. shock impingement before and after expansion corner have been successfully performed. For the same, perfect as well as real gas flow simulations are carried out in Earth and Martian atmospheric conditions. The

perfect gas based outcomes at lower total temperatures are found to be in good agreement with the analytical calculations. The real gas simulations at different enthalpies indicate the increment in post-shock Mach number and decrement in post-expansion wave Mach number with the rise in enthalpy for all gas models and configurations. Further, it is noticed that the peak pressure ratio decreases with an increase in enthalpy for all cases. These observations are more pronounced in Mars atmospheric case. The higher sensitivity of the specific heat with temperature variation for this gas model is believed to be the reason behind this observation. Therefore, it is concluded that real gas effects should be considered, especially in Martian condition, for investigations of complicated flow structure as considered herein, to obtain a more accurate prediction of the flow field.

8.1.5 Conclusions about shock wave boundary-layer interactions studies

A parametric study of ramp induced shock wave boundary layer interaction in laminar hypersonic flow has been carried out successfully. The investigation is performed in Earth and Martian atmospheric mediums using a real gas solver. It is noted that the variation in wall temperature from 300K to 700K results in 110.77% and 80% increments in separation length for Mars and Earth atmospheric case respectively. Further, the increase in stagnation temperature from 1080K to 1800K and Mach number from 6 to 8 leads to decrease in the separation lengths. These reductions are noted to be 39.78% and 61.25% for the Mars flow model and 28.41% and 40.26% for the Earth flow model respectively. Therefore, in either flow model, it has been noted that the separation length is directly proportional to the wall temperature and inversely to the Mach and stagnation enthalpy. Furthermore, the wall to total temperature ratio is verified to be a governing parameter and a sufficiently large leading bluntness as flow separation control method for both the mediums with real gas effects as well. These results are further used to correct the existing correlations for Earth atmospheric conditions for prediction of upstream influence location and extent of separation, and new correlations for Mars atmospheric conditions are successfully proposed. Thus, in the case of SWBLI studies for hypersonic flows in the Earth and Mars atmosphere, present studies advocate the use of real gas solvers.

8.2 Scope of future works

The present investigations have provided a useful understanding of different shock interactions and energy deposition based drag reduction. However, these studies have raised various questions in their respective fields. Hence, some tasks are needed to be undertaken to address the following queries.

- The present solver is capable of solving two-dimensional axisymmetric problems. The solver can be extended for a three-dimensional domain. Hence, making it possible to analyze different 3-D aspects in high-speed flows. Besides, the turbulence modeling can also be integrated to improve the solver's ability to solve turbulent flow problems.
- The present studies consider the optimization of the amount of energy deposition required for peak power effectiveness. Similar optimization study can be performed for other drag reduction strategies such as spike-based drag reduction technique as the amount of drag reductions depends on various parameters viz. length, shape and location of the spike.
- The in-house real gas solver is discretized explicitly except for the source term. This results in higher computational time. Hence, one of the immediate possible extensions of the present work is to reduce the overall computational time by incorporating implicit discretization schemes and as well by parallelization of the solver.
- The present studies have accounted temperature dependent specific heats. Further studies can be undertaken with two temperature model based simulations with present solver.

Publications

Journals

1. D. Das, S. Desai, and V. Kulkarni, "Real Gas Effects for Shock/Shock Interaction in Earth and Mars Atmospheres".(*Under review in the "Journal of Spacecraft and Rockets"*)
2. D. Das, S. Desai, and V. Kulkarni, " Transition of shock reflection at Higher Enthalpies for Earth and Mars Atmospheres". (*Under review in the Journal of "Acta Astronautica"*)
3. D. Das, S. Desai, and V. Kulkarni, "Shock/Expansion Fan Interaction with Real Gas Effects for Earth and Mars Atmospheric Conditions". (*Under review in the "*Journal of Aerospace Engineering*"*)
4. D. Das, S. Desai, and V. Kulkarni, "Comparative Studies of Shock Wave Boundary-Layer Interactions in Earth and Mars Atmospheres". (*Accepted in the journal of "Proceedings of the Institution of Mechanical Engineers, Part G: Journal of Aerospace Engineering"2021)*
5. D. Das, S. Desai, V. Kulkarni and H. Gadgil, "Performance assessment of energy deposition based drag reduction technique for Earth and Mars flight conditions," *Acta Astronautica*, vol. 159, pp. 418-428, June 2019.

References

[1] J. D. Anderson Jr., *Hypersonic and high-temperature gas dynamics*, 2nd ed.: McGraw-Hill, 2006.

[2] T. Nakamura and K. Fujii, "Probabilistic transient thermal analysis of an atmospheric reentry vehicle structure," *Aerospace Science and Technology*, vol. 10, pp. 346-354, March 2006.

[3] A. Riccio, F. Raimondo , A. Sellitto, V. Carandente, R. Scigliano and D. Tescione, "Optimum Design of Ablative Thermal Protection Systems for Atmospheric Entry Vehicles," *Applied Thermal Engineering*, vol. 119, pp. 541-552, June 2017.

[4] V. Menezes, S. Kumar, K. Maruta, K.P.J. Reddy and K. Takayama, "Hypersonic flow over a multi-step afterbody," *Shock Waves*, vol. 14, pp. 421–424, November 2005.

[5] W. Huang, L. Li, L. Yanm and T. Zhang, "Drag and heat flux reduction mechanism of blunted cone with aero disks," *Acta Astronautica*, vol. 138, pp. 168-175, September 2017.

[6] V. Kulkarni, G. M. Hegde, G. Jagadeesh, E. Arunan and K.P.J. Reddy, "Aerodynamic drag reduction by heat addition into the shock layer for a large angle blunt cone in hypersonic flow," *Physics of Fluids*, vol. 20, pp. 1-4, August 2008.

[7] I. S. Rego, P.P. Toro, M. A. S. Minucci, J. B. Chanes Jr, F.J. Costa and A.C. Oliveira, "Calculation of The Vehicle Drag and Heating Reduction at Hypervelocities with Laser-Induced Air Spike," *Journal of Aerospace Technology and Management*, vol. 5, no. 1, pp. 43-48, March 2013.

[8] R. Yadav, G. Velidi and U. Guven, "Aerothermodynamics of generic re-entry vehicle with a series of aerospikes at nose," *Acta Astronautica*, vol. 96, pp. 1-10, 2014.

[9] A. Bibi, A. Maqsood, S. Sherbaz and L. Dala, "Drag reduction of supersonic blunt bodies using opposing jet and nozzle geometric variations," *Aerospace Science and Technology*, vol. 69, pp. 244-256, October 2017.

[10] W. Huang, R. Zhang, L. Yan, M. Ou and R. Moradi, "Numerical experiment on the flow field properties of a blunted body with a counterflowing jet in supersonic flows," *Acta Astronautica*, vol. 147, pp. 231-240, June 2018.

[11] A. A. Zheltovodov and E. A. Pimonov, "Numerical simulation of an energy deposition zone in quiescent air and in a supersonic flow under the conditions of interaction with a normal shock," *Technical Physics*, vol. 58, no. 2, pp. 170-184, February 2013.

[12] O. A. Azarova and D. D. Knight, "An approach of drag force decrease for combined cylinder AD bodies under the action of microwave and laser energy deposition," *Aerospace Science and Technology*, vol. 64, pp. 154-160, May 2017.

[13] Z. Eghlima and K. Mansour, "Drag reduction for the combination of spike and counter flow jet on blunt body at high Mach number flow," *Acta Astronautica*, vol. 133, pp. 103–110, April 2017.

[14] S. O. Macheret, M. N. Shneider and R. B. Miles, "Scramjet inlet control by off-body energy addition: a virtual cowl," in *AIAA paper 2003-32, 41st AIAA Aerospace Sciences Meeting and Exhibit*, vol. 32, Reno, Nevada, 2003, pp. 1-18.

[15] K. Satheesh and G. Jagadeesh, "Effect of concentrated energy deposition on the aerodynamic drag of a blunt body in hypersonic flow," *Physics of Fluids*, vol. 19, pp. 1-4, March 2007.

[16] E. Erdem, L. Yang and K. Kontis, "Drag reduction studies by steady state energy deposition at mach 5," in *AIAA paper 2011-1027, 49th AIAA Aerospace Sciences Meeting including the New Horizons Forum and Aerospace Exposition*, vol. 1027, Orlando, Florida, 2011, pp. 1-20.

[17] D. S. Miller and H. W. Carlson, "On the application of heat and force fields to the sonic boom minimization problem," in *AlAA Paper No. 70-903, AlAA 2nd Aircraft Design and Operation Meeting*, Los Angeles, California, 1970, pp. 1-9.

[18] D. Riggins, H. F. Nelson and E. Johnson, "Blunt-Body Wave Drag Reduction using Focused Energy Deposition," *AIAA Journal*, vol. 37, no. 4, pp. 460-467, April 1999.

[19] Y. Ogino, N. Ohnishi, S. Taguchi and K. Sawada, "Baroclinic vortex influence on wave drag reduction induced by pulse energy deposition," *Physics of fluids*, vol. 21, pp. 1-11, June 2009.

[20] A. R. Sangtabi, A. Ramiar, A. A. Ranjbar, M. Abdollahzadeh and A. Kianifar, "Influence of repetitive laser pulse energy depositions on supersonic flow over a sphere, cone and oblate spheroid," *Aerospace Science and Technology*, vol. 76, pp. 72-81, May 2018.

[21] B. John and V. Kulkarni, "Investigation of energy deposition technique for drag reduction at hypersonic speeds," *Applied Mechanics and Materials*, vol. 367, pp. 222-227, August 2013.

[22] M. A. Ganesh and B. John, "Concentrated energy addition for active drag reduction in hypersonic flow regime," *Acta Astronautica*, vol. 142, pp. 221-231, January 2018.

[23] D. D. Knight, Y. F. Kolesnichenko, V. Brovkin and D. Khmara, "High speed flow control using microwave energy deposition," in *AIAA paper 2008-1354, 46th AIAA Aerospace Sciences Meeting and Exhibit*, Reno, Nevada, 2008, pp. 1-14.

[24] S. Desai, V. Kulkarni, H. Gadgil and B. John, "Aerothermodynamic considerations for energy deposition based drag reduction technique," *Applied Thermal Engineering*, vol. 122, pp. 451-460, July 2017.

[25] J. D. Anderson Jr., *Modern Compressible Flow: with Historical Perspective*, 2nd ed.: McGraw-Hill, 1990.

[26] H. G. Hornung and M. L. Robinson, "Transition from regular to Mach reflection of shock waves Part 2. The steady-flow criterion," *Journal of Fluid Mechanics*, vol. 123, pp. 155-164, 1982.

[27] A. Chpoun, D. Passerel, H. Liz and G. Ben-Dor, "Reconsideration of oblique shock wave reflections in steady flows. Part 1. Experimental investigation," *Journal of Fluid Mechanics*, vol. 301, pp. 19-35, 1995.

[28] M. S. Ivanov, D. Vandromme, V. M. Fomin, A. N. Kudryavtsev, A. Hadjadj and D. V. Khotyanovsky, "Transition between regular and Mach reflection of shock waves: new numerical and experimental results," *Shock Waves*, vol. 11, pp. 199-207, 2001.

[29] F. WU, H. Dai and D. Kong, "Mechanism for the transition from a regular reflection to a Mach reflection or a von Neumann reflection," *Acta Mathematica Scientia*, vol. 36, no. 3, pp. 931-944, 2016.

[30] M. S. Ivanov, S. F. Gimelshein and A. E. Beylich, "Hysteresis effect in stationary reflection of shock waves," *Physics of Fluids*, vol. 7, pp. 685-687, 1995.

[31] M. S. Ivanov, S. F. Gimelshein and G. N. Markelov, "Statistical Simulation of the Transition between Regular and Mach Reflection in Steady Flows ," *Computers & Mathematics with Applications*, vol. 35, no. 1/2, pp. 113-125, 1998.

[32] G. Ben-Dor, M. Ivanov, E. I. Vasilev and T. Elperin, "Hysteresis processes in the regular reflection↔Mach reflection transition in steady flows," *Progress in Aerospace Sciences*, vol. 38, pp. 347–387, 2002.

[33] Y. Tao, X. Fan and Y. Zhao, "Viscous effects of shock reflection hysteresis in steady supersonic flows," *Journal of Fluid Mechanics*, vol. 759, pp. 134-148, 2014.

[34] D. J. Azevedo and C. S. Liu, "Engineering Approach to the Prediction of Shock Patterns in

Bounded High-Speed Flows," *AIAA Journal*, vol. 31, no. 1, pp. 83-90, January 1993.

[35] H. Li and G. Ben-Dor, "A parametric study of Mach reflection in steady flows," *Journal of Fluid Mechanics*, vol. 341, pp. 101-125, 1997.

[36] C. A. Mouton and H. G. Hornung, "Mach Stem Height and Growth Rate Predictions," *AIAA Journal*, vol. 45, no. 8, pp. 1977-1987, August 2007.

[37] B. John, G. Sarath, V. Kulkarni and G. Natarajan, "Performance comparison of flux schemes for numerical simulation of high-speed inviscid flows," *Progress in Computational Fluid Dynamics*, vol. 14, no. 2, pp. 83-96, 2014.

[38] J. Vuillon, D. Zeitoun and G. Ben-Dor, "Reconsideration of oblique shock wave reflections in steady flows. Part 2. Numerical investigation," *Journal of Fluid Mechanics*, vol. 301, pp. 37-50, 1995.

[39] K. Wu, S. K. Raman, V. R. P. Sethuraman, G. Zhang and H. D. Kim, "Effect of the wall temperature on Mach stem transformation in pseudo-steady shock wave reflections," *International Journal of Heat and Mass Transfer*, vol. 147, pp. 1-19, February 2020.

[40] Z. M. Hu, C. Wang, Y. Zhang and R. S. Myong, "Computational confirmation of an abnormal Mach reflection wave configuration," *Physics of Fluids*, vol. 21, no. 1, pp. 1-5, January 2009.

[41] A. N. Semenov, M. K. Berezkina and I. V. Krassovskaya, "Classification of pseudo-steady shock wave reflection types," *Shock Waves*, vol. 22, pp. 307–316, May 2012.

[42] F. Kemm, "On the proper setup of the double Mach reflection as a test case for the resolution of gas dynamics codes," *Computers and Fluids*, vol. 132, pp. 72-75, June 2016.

[43] X. Shi, Y. Zhu, X. Luo and J. Yang, "High temperature effects in moving shock reflection with protruding Mach stem," *Theoretical & Applied Mechanics Letters*, vol. 6, no. 5, pp. 222-225, September 2016.

[44] J. Li and S. Yang, "Thermochemical non-equilibrium effects of shock reflection hysteresis in steady supersonic flows," in *AIAA 2017-2195, 21st AIAA International Space Planes and Hypersonic Technologies Conference*, Xiamen, China, 2017, pp. 1-9.

[45] E. J. I and C. T. Johansen, "Effect of particle momentum transfer on an oblique-shock-wave/laminar-boundary-layer interaction," *Acta Astronautica*, vol. 128, pp. 431-439, December 2016.

[46] D. Knight and M. Mortazavi, "Hypersonic shock wave transitional boundary layer interactions – A review," *Acta Astronautica*, vol. 151, pp. 296-317, October 2018.

[47] M. V. Silnikov, M. V. Chernyshov and V. N. Uskov, "Analytical solutions for Prandtl–Meyer wave–oblique shock overtaking interaction," *Acta Astronautica*, vol. 99, pp. 175-183, July 2014.

[48] B. Edney, "Anomalous heat transfer and pressure distributions on blunt bodies at hypersonic speeds in the presence of an impinging shock," Technical Report in the Aerospace Research Institute of Sweden, 1968.

[49] S. M. Boldyrev, V. Y. Borovoy, A. Y. Chinilov, V. N. Gusev, S. N. Krutiy, I. V. Struminskaya, L. V. Yakovleva, J. Déler and B. Chanetz, "A thorough experimental investigation of shock/shock interferences in high Mach number flows," *Aerospace Science and Technology*, vol. 5, no. 3, pp. 167-178, March 2001.

[50] V. Y. Borovoy, A. Y. Chinilov, V. N. Gusev, I. V. Struminskaya, J. Délery and B. Chanetz, "Interference Between a Cylindrical Bow Shock and a Plane Oblique Shock," *AIAA Journal*, vol. 35, no. 11, pp. 1721-1728, November 1997.

[51] F. D. Hains and J. W. Keyes, "Shock Interference Heating in Hypersonic Flows," *AIAA Journal*, vol. 10, no. 11, pp. 1441-1447, November 1972.

[52] F. Grasso, C. Purpura, B. Chanetz and J. Délery, "Type III and type IV shock/shock interferences: theoretical and experimental aspects," *Aerospace Science and Technology*, vol. 7, no. 2, pp. 93–106., March 2003.

[53] A. Chettle, E. Erdem, and K. Kontis, "Edney IV Interaction Studies at Mach 5," in *29th International Symposium on Shock Waves*, Springer, Cham, 2013, pp. 605-610.

[54] D. Gaitonde and I. S. Shang, "On the Structure of an Unsteady type IV Interaction at Mach 8," *Computers & Fluids*, vol. 24, no. 4, pp. 469-485, 1995.

[55] C. A. Lind and M. J. Lewis, "Computational Analysis of the Unsteady Type IV Shock Interaction of Blunt Body Flows," *Journal of Propulsion and Power*, vol. 12, no. 1, pp. 127-133, February 1996.

[56] S. Yamamoto, S. Kano and H. Daiguji, "An Efficient CFD approach for Simulating Unsteady Hypersonic Shock-Shock Interference Flows," *Computers & Fluids*, vol. 27, no. 6, pp. 571-580, 1998.

[57] Y. B. Chu and X. Y. Lu, "Characteristics of unsteady type IV shock/shock interaction,"

Shock Waves, vol. 22, pp. 225–235, April 2012.

[58] F. Xiao, Z. Li, Y. Zhu and J. Yang, "Hypersonic Type-IV Shock/Shock Interactions on a Blunt Body with Forward-Facing Cavity," *Journal of Spacecraft and Rockets*, vol. 54, no. 2, pp. 504-510, April 2017.

[59] A. Khatta and G. Jagadeesh, "Hypersonic shock tunnel studies of Edney Type III and IV shock interactions," *Aerospace Science and Technology*, vol. 72, pp. 335-352, January 2018.

[60] J. J. Bertin and J. C. Hinkle, "Experimental investigation of supersonic flow past double wedge configurations," *AIAA Journal*, pp. 897-901, July 1975.

[61] F. F. J. Schrijer, F. Scarano and B. W. Oudheusden, "Application of PIV in a Mach 7 double-ramp flow," *Experiments in Fluids*, vol. 41, pp. 353–363, April 2006.

[62] J. Olejniczak, M. J. Wright, and G. V. Candler, "Numerical study of inviscid shock interactions on double-wedge geometries," *Journal of Fluid Mechanics*, vol. 352, pp. 1-25, December 1997.

[63] M. J. Wright , K. Sinha , J. Olejniczak , G. V. Candler , T. D. Magruder and A. J. Smits, "Numerical and Experimental Investigation of Double-Cone Shock Interactions," *AIAA Journal*, vol. 38, no. 12, pp. 2268-2276, December 2000.

[64] G. Ben-Dor, E. I. Vasilev, T. Elperin and A. V. Zenovich, "Self-induced oscillations in the shock wave flow pattern formed in a stationary supersonic flow over a double wedge," *Physics of Fluids*, vol. 15, no. 12, pp. L85–L88, December 2003.

[65] Z. M. Hu, R. S. Myong, C. Wang, T. H. Cho and Z. L. Jiang, "Numerical study of the oscillations induced by shock/shock interaction in hypersonic double-wedge flows," *Shock Waves*, vol. 18, no. 41, pp. 41-51, April 2008.

[66] Z. M. Hu, C. Wang, Y. Zhang and R. S. Myong, "Computational confirmation of an abnormal Mach reflection wave configuration," *Physics of Fluids*, vol. 21, pp. 1-4, 2009.

[67] Z. M. Hu, Y. L. Gao, R. S. Myong, H. S. Dou and B. C. Khoo, "Geometric criterion for RR-MR transition in hypersonic double-wedge flows," *Physics Of Fluids*, vol. 22, no. 1, pp. 1-9, January 2010.

[68] A. S. Durna, M. E. H. A. Barada and B. Celik, "Shock interaction mechanisms on a double wedge at Mach 7," *Physics of Fluids*, vol. 28, no. 9, pp. 1-17, September 2016.

[69] A. S. Durna and B. Celik, "Time-periodic shock interaction mechanisms over double

wedges at Mach 7," *Shock Waves*, vol. 29, pp. 381–399, 2019.

[70] G. Xiang, C. Wang, H. Teng and Z. Jiang, "Shock/shock interactions between bodies and wings," *Chinese Journal of Aeronautics*, vol. 31, no. 2, pp. 255–261, February 2018.

[71] G. Tchuen , M. Fogue, Y. Burtschell, D. Zeitoun and G. Ben-Dor, "Shock-on-shock interactions over double-wedges: comparison between inviscid, viscous and nonequilibrium hypersonic flow," in *26th International Symposium on Shock Waves*, vol. 2, Berlin, Heidelberg, 2009, pp. 1497-1502.

[72] G. Tchuen, Y. Burtschell and D. E. Zeitoun, "Numerical study of the interaction of type IVr around a double-wedge in hypersonic flow," *Computers & Fluids*, vol. 50, no. 1, pp. 147–154, November 2011.

[73] J. Li, Y. Zhu and X. Luo, "On Type VI–V transition in hypersonic double-wedge flows with thermo-chemical non equilibrium effects," *Physics Of Fluids*, vol. 26, no. 8, pp. 1-16, August 2014.

[74] W. Xiong, Y. Zhu and X. Luo, "On transition of Type V interaction in double-wedge flow with non-equilibrium effects," *Theoretical & Applied Mechanics Letters*, vol. 6, no. 6, pp. 282 -285., November 2016.

[75] O. Tumuklu, D. A. Levin and J. M. Austin, "Shock-shock interactions for a double wedge configuration in different gases," in *AIAA paper 2105-1520, 53rd AIAA Aerospace Sciences Meeting*, Kissimmee, Florida, 2015, pp. 1-33.

[76] P. A. Sullivan, "On the Interaction of a Laminar Hypersonic Boundary Layer and a corner Expansion Wave," in *AIAA paper no. 69-137, 7th Aerospace Sciences Meeting*, New York, USA, 1969, pp. 1-10.

[77] W. W. Koziak and P. A. Sullivan, "Interaction of a Laminar Hypersonic Boundary Layer with a Corner Expansion Wave," *AIAA Journal*, vol. 11, no. 8, pp. 1057-1058, August 1973.

[78] Y. T. Chew, "Shockwave and Boundary Layer Interaction in the Presence of an Expansion Corner," *The Aeronautical Quarterly*, vol. 30, no. 3, pp. 506-527, 1979.

[79] K. M. Chung and F. K. Lu, "Hypersonic Turbulent Expansion-Corner Flow with Shock Impingement," *Journal of Propulsion and Power*, vol. 11, no. 3, pp. 441-447, June 1995.

[80] M. E. White and D. A. Aul, "Expansion Corner Effects on Hypersonic Shock Wave/Turbulent Boundary-Layer Interactions," in *AlAA paper 95-6125, AIAA 6th International Aerospace Planes and Hypersonics Technologies Conference*, Chattanooga,

TN, 1995, pp. 1-7.

[81] R. J. Hawboldt, P. A. Sullivan and J. J. Gottlieb, "Interactions Between Shock Wave and Hypersonic Laminar Boundary Layer Near Convex Corner," *Journal of Spacecraft and Rockets*, vol. 32, no. 5, pp. 783-790, October 1995.

[82] H. Li and G. Ben-Dor, "Oblique-Shock/Expansion-Fan Interaction—Analytical Solution," *AIAA Journal*, vol. 34, no. 2, pp. 418-421, 1995.

[83] G. Abate, W. Shyy, C. Segal and C. Anderson, "Gas Dynamic structure of a Shock Wave Undergoing Sudden Expansion, (1998) 1-12.," in *AIAA paper 98-2508, 20th AIAA Advanced Measurement and Ground Testing Technology Conference*, Albuquerque, NM, U.S.A., 1998, pp. 1-12.

[84] K. M. Chung, "Investigation on Turbulent Expansion-Corner Flow With Shock Impingement," *Journal of Fluids Engineering*, vol. 123, no. 1, pp. 139-144, March 2001.

[85] S. R. Sanderson, "Gasdynamic wave interaction in two spatial dimensions," *Journal of Fluid Mechanics*, vol. 506, pp. 187–205, May 2004.

[86] R. Hillier, "Shock-wave/expansion-wave interactions and the transition between regular and Mach reflection ," *Journal of Fluid Mechanics*, vol. 575, pp. 399–424, March 2007.

[87] S. G. Li and Z. N. Wu, Y. Yao, "Shock reflection in the presence of an upstream expansion wave and a downstream shock wave," *Journal of Fluid Mechanics*, vol. 735, pp. 61-90, November 2013.

[88] Y. Zhang, H.J. Tan, Y. Zhuang and D. P. Wang, "Influence of Expansion Waves on Cowl Shock/Boundary Layer Interaction in Hypersonic Inlets," *Journal of Propulsion and Power*, vol. 30, no. 5, pp. 1183-1191, October 2014.

[89] M. V. Silnikov, M. V. Chernyshov and V. N. Uskov, "Analytical solutions for Prandtl–Meyer wave–oblique shock overtaking interaction," *Acta Astronautica*, vol. 99, pp. 175–183, July 2014.

[90] A. S. Narayanan and S. B. Verma, "Experimental investigation of a Mach 4 shock-wave turbulent boundary layer interaction near an expansion corner," in *AIAA paper 2015-0112, 53rd AIAA Aerospace Sciences Meeting*, Kissimmee, Florida, 2015, pp. 1-11.

[91] L. Nel and B.W. Skews, "Wind tunnel testing considerations in expansion fan/shock wave interaction studies," *R & D Journal of the South African Institution of Mechanical Engineering*, vol. 34, pp. 26-32, Septembe 2018.

[92] A. Fage and R. F. Sargent, "Shock Wave and Boundary Layer Phenomena Near a Flat Surface," in *Proceedings of the Royal Society of London, Series A: Mathematical and Physical Sciences*, vol. 190, 1947, pp. 1-20.

[93] H. W. Liepmann, "The Interaction Between Boundary Layer and Shock Waves in Transonic Flow," *Journal of Aerospace Sciences*, vol. 13, no. 12, pp. 623–638, December 1946.

[94] C. DuP. Donaldson, "Effects of Interaction Between Normal Shock and Boundary Layer," NACA CB 4A27, 1944.

[95] H. W. Liepmann, A. Roshko and S. Dhawan, "On Reflection of Shock Waves from Boundary Layers," NACA report 1100, 1952.

[96] O. Bardsley and W. A. Mair, "The Interaction Between an Oblique Shock Wave and a Turbulent Boundary Layer," *The London, Edinburgh, and Dublin Philosophical Magazine and Journal of Science: Series 7*, vol. 42, no. 324, pp. 29–36, 1951.

[97] N. H. Johannesen, "Experiments On Two-Dimensional Supersonic Flow in Corners and over Concave Surfaces" , 14,607, Jan. 1952.," *The London, Edinburgh, and Dublin Philosophical Magazine and Journal of Science: Series 7*, vol. 43, pp. 568-580, February 1952.

[98] C. D. Donaldson and R. H. Lange, "Study of the Pressure Rise Across Shock Waves Required to Separate Laminar and Turbulent Boundary Layers," NACA TN 2770, 1952.

[99] D. R. Chapman, D. M. Kuehn, and H. K. Larson, "Investigation of separated flows in supersonic and subsonic streams with emphasis on the effect of transition," NACA TN 3869, NACA Report 1356 1957.

[100] D. M. Kuehn, "Experimental investigation of the pressure rise required for the incipient separation of turbulent boundary layers in two-dimensional supersonic flow," NASA/TIL/6209, Washington, NASA Memo 1-21-59A, 1959.

[101] D. A. Needham, "A heat-transfer criterion for the detection of incipient separation in hypersonic flow," *AIAA Journal*, vol. 3, pp. 781-783, April 1965.

[102] D. A. Needham and J. L. Stollery, "Boundary Layer Separation in Hypersonic flow," in *AIAA Paper no 66-455, AIAA 4th Aerospace Sciences Meeting*, Los Angeles, California, 1966, pp. 1-22.

[103] M. S. Holden, "Boundary-Layer Displacement and Leading-Edge Bluntness Effects on Attached and Separated Laminar Boundary Layers in a Compression Corner. Part II: Experimental Study," *AIAA journal*, vol. 9, no. 1, pp. 84-93, January 1971.

[104] A. W. Bloy and M. P. Georgeff, "The hypersonic laminar boundary layer near sharp compression and expansion corners," *Journal of Fluid Mechanics*, vol. 63, no. 3, pp. 431-447, 1974.

[105] L. H. Back and R. F. Cuffel, "Shock Wave/Turbulent Boundary-Layer Interactions with and without Surface Cooling," *AIAA Journal*, vol. 14, no. 4, pp. 526-532, April 1976.

[106] K. Hayakawa and L. C. Squire, "The effect of the upstream boundary-layer state on the shock interaction at a compression comer," *Journal of Fluid Mechanics*, vol. 122, pp. 369-394, March 1982.

[107] M. Marini, "Effects of flow and geometry parameters on shock-wave boundary-layer interaction," in *AIAA Paper 68-1570*, 1968, pp. 3139-329.

[108] W. Dieudonne, H. L. Boerrigter, and J. M. Charbonnier, "Hypersonic Flow on a Blunted Cone-Flare and in the VKI-H3 Mach 6 wind tunnel," von Karman Institute, Belgium, 1999.

[109] M. S. Holden, "Measurements in laminar regions of shock/shock and shock/boundary layer interaction over cylindrical leading edges, cone/cone and hollow cylinder flare configurations for DSMC/Navier-Stokes code validation," in *AIP Conference Proceedings, 585* , 2001, pp. 699-706.

[110] T. Neuenhahn and H. Olivier, "Influence of the wall temperature and the entropy layer effects on double wedge shock boundary layer interactions," in *AIAA paper 2006-8136, 14th AIAA/AHI Space Planes and Hypersonic Systems and Technologies Conference*, Canberra, Australia, 2006, pp. 1-12.

[111] W. Hongyu, L. Jun, J. Di, Z. Zhibo, T. Mengxiao and W. Yun, "Manipulation of ramp-induced shock wave/boundary layer interaction using a transverse plasma jet array," *International Journal of Heat and Fluid Flow*, vol. 67, no. part A, pp. 133–137, October 2017.

[112] R. Szwaba, P. Kaczynski and P. Doerffer, "Roughness effect on shock wave boundary layer interaction area incompressor fan blades passage," *AerospaceScienceandTechnology*, vol. 85, pp. 171–179, February 2019.

[113] J. E. Carter, "Numerical solutions of the supersonic, laminar flow over a two-dimensional compression corner," in *Proceedings of the Third International Conference on Numerical Methods in Fluid Mechanics. Lecture Notes in Physics*, vol. 19, 1973, pp. 69-78.

[114] R. MacCormack and B. Baldwin, "A numerical method for solving the navier-stokes equations with application to shock-boundary layer interactions," in *AIAA paper 75-1, AIAA*

13th Aerospace Sciences Meeting, Pasadena, California, 1975, pp. 1-6.

[115] C. M. Hung and R. W. MacCormack, "Numerical Solutions of Supersonic and Hypersonic Laminar," *AIAA journal*, vol. 14, no. 4, pp. 475-481, April 1976.

[116] J. C. L. Balleur, R. Peyret and H. Viviand, "Numerical studies in high Reynolds number aerodynamics," *Computers & Fluids*, vol. 8, no. 1, pp. 1-30, March 1980.

[117] D. H. Rudy, J. L. Thomas, A. Kumar, P. A. Gnoffo and S. R. Chakravarthy, "Computation of Laminar Hypersonic Compression-Corner flows," *AIAA Journal*, vol. 29, no. 7, pp. 1108-1113, July 1991.

[118] F. Grasso, G. Leone and J. M. Delery, "Validation Procedure for the Analysis of Shock-Wave/Boundary-Layer Interaction Problems," *AIAA Journal*, vol. 32, no. 9, pp. 1820-1827, September 1994.

[119] F. Grasso and M. Marini, "Analysis of hypersonic shock-wave laminar boundary-layer interaction phenomena," *Computers & Fluids*, vol. 25, no. 6, pp. 561–581, July 1996.

[120] M. Marini, "Analysis of hypersonic compression ramp laminar flows under sharp leading edge conditions," *Aerospace Science and Technology*, vol. 5, no. 4, pp. 257-271, June 2001.

[121] R. Savino and D. Paterna, "Blunted cone–flare in hypersonic flow," *Computers & Fluids*, vol. 34, no. 7, pp. 859–875, August 2005.

[122] B. John, V. N. Kulkarni and G. Natarajan, "Shock wave boundary layer interactions in hypersonic flows," *International Journal of Heat and Mass Transfer*, vol. 70, pp. 81-90, March 2014.

[123] B. John and V. Kulkarni, "Effect of leading edge bluntness on the interaction of ramp induced shock wave with laminar boundary layer at hypersonic speed," *Computers & Fluids*, vol. 96, pp. 177-190, June 2014.

[124] B. John and V. Kulkarni, "Numerical assessment of correlations for shock wave boundary layer interaction," *Computers & Fluids*, vol. 90, pp. 42-50, February 2014.

[125] N. Jahantigh, M. Mirzaei and A. Shadaram, "Interaction between Boundary Layer and Shock in Hypersonic Flows with chemical real gas effects," in *Proceedings of the 4th WSEAS International Conference on Fluid Mechanics and Aerodynamics*, Elounda, Greece, 2006, pp. 68-74.

[126] J. P. Davis and S. Bradford, "Separation length in high-enthalpy shock/boundary layer

interaction," *Physics of Fluids*, vol. 12, no. 10, pp. 2661–2687, September 2000.

[127] M. D. Clemente, M. Marini, S. D. Benedetto, A. Schettino and G. Ranuzzi, "Numerical prediction of aerothermodynamic effects on a re-entry vehicle body flap configuration," *Acta Astronautica*, vol. 65, no. 1-2, pp. 221–239, August 2009.

[128] J. Hao and C. Y. Wen, "Effects of vibrational non equilibrium on hypersonic shock wave/laminar boundary-layer interactions," *International Communications in Heat and Mass Transfer*, vol. 97, pp. 136–142, October 2018.

[129] S. Desai, V. Kulkarni and H. Gadgil, "Separation mitigation using pressure feedback technique for hypersonic shock wave boundary layer interaction," *Part G: Journal of Aerospace Engineering*, vol. 233, no. 10, pp. 3519-3533, August 2019.

[130] S. Desai, V. Kulkarni, and H. Gadgil, "Delusive Influence of Nondimensional Numbers in Canonical Hypersonic Nonequilibrium Flows," *Journal of Aerospace Engineering*, vol. 29, no. 5, pp. 1-10, September 2016.

[131] S. Desai, S. Brahmachary, H. Gadgil and V. Kulkarni, "Probing Real Gas and Leading-Edge Bluntness Effects on Shock Wave Boundary-Layer Interaction at Hypersonic Speeds," *Journal of Aerospace Engineering*, vol. 32, no. 6, pp. 1-12, November 2019.

[132] S. Gordon and B. J. McBride, "Computer program for calculation of complex chemical equilibrium composition and applications," *NASA RP-1311*, 1994.

[133] J.S. Shuen, M.S. Liou, B. VanLeer, "Inviscid flux-splitting algorithms for real gases with non-equilibrium chemistry," *Journal of Computational Physics*, vol. 90, no. 2, pp. 371–395, October 1990.

[134] R. Joarder, "Demonstration of supersonic combustion in a combustion driven shock-tunnel," Indian Institute of Science, Bangalore, India 2009.

[135] M. G. Dunn and S. W. Kang, "Theoretical and experimental studies of reentry plasmas," NASA CR, 2232, 1973.

[136] R. D. Kay and M. P. Netterfield, "Thermochemical Non-Equilibrium Computations for a Mars Entry Vehicle," in *AIAA 28th Thermophysics Conference*, Orlando, FL, 1993, pp. 1-8.

[137] S. Chen, F. Cai, H. Xue, N. Wang and C. Yan, "An improved AUSM-family scheme with robustness and accuracy for all Mach number flows," *Applied Mathematical Modelling*, vol. 77, no. 2, pp. 1065-1081, January 2020.

[138] M. S. Liou and C. J. Steffen, "A new flux splitting scheme," *Journal of computational physics*, vol. 107, no. 1, pp. 23-39, July 1993.

[139] T. Barth and D. Jespersen, "The design and application of upwind schemes on unstructured meshes," in *AIAA, 27th Aerospace science meeting*, Reno, NV, USA, 1989.

[140] V. Venkatakrishnan, "On the accuracy of limiters and convergence to steady state solutions," in *AIAA 93-0880, 31 st Aerospace Sciences Meeting & Exhibit*, Reno, NV, 1993, pp. 1-10.

[141] J. Blazek, *Computational Fluid Dynamics: Principles and Applications*.: Elsevier, 2001.

[142] T. Poinsot and S. Lele, "Boundary conditions for direct simulations of compressible viscous flows," *Journal of Computational Physics*, vol. 101, no. 1, pp. 104 – 129, July 1992.

[143] J. Blazek, *Computational Fluid Dynamics: Principles and Applications*, 1st ed. Baden-Daettwil, Switzerland: Elsevier , 2001.

[144] A. Lafon and H.C. Yee, "On the Numerical Treatment of Nonlinear Source Terms in Reaction-Convection Equations," *AIAA Paper 92-0419*, 1992.

[145] T. R. A. Bussing and E. M. Murman, "Finite volume method for the calculation of compressible chemically reacting flows," *AIAA Journal* , vol. 26, no. 5, pp. 1070–1078, September 1987.

[146] W. Sutherland, "Lii. the viscosity of gases and molecular force," *The London, Edinburgh, and Dublin Philosophical Magazine and Journal of Science*, vol. 36, no. 223, pp. 507–531, 1893.

[147] D. Liao, S. Liu, H. Jian, A. Xie, Z. Wang and J. Huang, "Measurement and Calculation of Shock Stand-off Distances over Hypersonic Spheres in CO2," in *AIAA paper 2017-2124, 21st AIAA International Space Planes and Hypersonics Technologies Conference*, Xiamen, China, 2017, pp. 1-7.

[148] S. G. Mallinson, "Shock Wave/Boundary Layer Interaction at a Compression Corner in Hypervelocity Flows," Aerospace & Mechanical Engineering, UNSW, Australian Defence Force Academy, PhD thesis 1994.

[149] J.Olejniczak and G. V. Candler, "Computation of Hypersonic Shock Interaction Flow Fields," in *AIAA 98-2446, 7th AIAA/ASME Joint Thermophysics and Heat Transfer Conference*, 1998, pp. 1-12.

[150] N. R. Deepak, S. L. Gai and A. J. Neely, "A computational investigation of laminar shock/wave boundary layer interactions," *The Aeronautical Journa/*, vol. 117, no. 1187, pp. 27-56, January 2013.

[151] M. Capitelli and G. Colonna, "High-Temperature Thermodynamic properties of Mars-atmosphere components," in *AIAA paper 2004-2378, 37th AIAA thermo-physics conference*, Oregon, 2004.

[152] G. Ben-Dor, *Shock Wave Reflection Phenomena*.: Springer, 1991.

[153] J. Gou, X. Yuan and X. Su, "Adaptive mesh refinement method based investigation of the interaction between shock wave, boundary layer, and tip vortex in a transonic compressor," *Proceedings of the Institution of Mechanical Engineers, Part G: Journal of Aerospsace Engineering*, vol. 1, no. 1, pp. 12-21, 2001.

[154] W. T. Hou, W. Y. Qiao and H. L. Luo, "Shock-wave/boundary-Layer interaction in a transonic turbine cascade," *Proceedings of the Institution of Mechanical Engineers, Part G: Journal of Aerospace Engineering*, vol. 225 , no. 1, pp. 77-85, 2011.

[155] Z. Zhao, W. Y. Song, Y. L. Xiao and J. L. Le, "An experimental investigation of the cold flowfield in a model scramjet combustor," *Proceedings of the Institution of Mechanical Engineers, Part G: Journal of Aerospace Engineering* , vol. 223, no. 4, pp. 425-431, 2009.

[156] D. Schulte, A. Henckels and R. Neubacher, "Manipulation of Shock/Boundary-Layer Interactions in Hypersonic Inlets," *Journal of Propulsion and Power* , vol. 17, no. 3, pp. 585-590, 2001.

[157] M. Capitelli, G. Colonna, D. Giordano, L. Marraffa, A. Casavola P. Minelli D. Pagano, L. Pietanza and F. Taccogna, "High-Temperature Thermodynamic properties of Mars-atmosphere components," *AIAA Journal* , vol. 2378, pp. 980-989, 2004.

[158] J.P. Davis and B. Sturtevant, "Separation length in high-enthalpy shock/boundary-layer Interaction," *Physics of Fluids*, vol. 12, no. 10, pp. 2661–2687, October 2000.

[159] G.R. Inger, "Scaling of incipient separation in high speed laminar flows," *AIAA Journal*, vol. 33, no. 1, pp. 178-182, June/July 1995.